Universitat de València
Facultat de Física
Departament de Física Atòmica Molecular i Nuclear

Silicon detectors for medical imaging: development of a first Compton probe prototype for improved prostate imaging

TESIS DOCTORAL

Gabriela Llosá Llácer

2005

Dr. CARLOS LACASTA LLÁCER, Científico Titular del C.S.I.C.

CERTIFICA:

Que la presente memoria *Silicon detectors for medical imaging: development of a first Compton probe prototype for improved prostate imaging* ha sido realizada bajo mi dirección en el Departamento de Física Atómica, Molécular y Nuclear de la Universitat de València por Dña. Gabriela Llosá Llácer, y constituye su tesis para optar al grado de doctora en Física por la Universitat de Valéncia.

Y para que conste, en cumplimiento de la legislación vigente, firmo el presente Certificado en Burjassot a 10 de Noviembre de 2005

Fdo: Carlos Lacasta Llácer

Visto bueno del tutor:

Fdo: D. Manuel Ramón Cases Ruiz.

Contents

List of Figures

List of Tables

Introduction

The discovery of electron-hole pair production in germanium junctions by α particles in the 1950s was the starting point for the use of semiconductor detectors in nuclear physics for very precise measurements of gamma ray energies, from a few keV up to 10 MeV. Their use in high energy physics began in the 1970s, when telescopes of several layers of silicon detectors were employed for beam monitoring. In the 1980s, they were first employed for the measurement of particle trajectories, and since then they have been employed in most of the high energy physics experiments built in the last 20 years, from large colliders to fixed target experiments, or spectrometers for space detectors. Their success has grown along with the progress of micro-electronics. Most progress has been made towards a faster signal processing with a good signal-to-noise ratio. Some of the characteristics that are the basis of the success of the silicon detectors, making them excellent devices for both energy and position measurements are linearity, excellent energy resolution, speed of the order on 10 ns, spatial resolution of 2-3 μm, flexibility of design, good mechanical properties, and tolerance to high radiation doses.

Nuclear medical imaging is a field that can be enormously benefited by the use of silicon detectors. In current single photon emission computed tomography (SPECT), the detection and determination of the direction of the photons is done by mechanically collimated scintillator detectors, for which resolution and efficiency are inversely coupled. The use of silicon sensors makes possible to implement a novel method of electronic collimation, known as Compton imaging, that has been successfully employed in Compton telescopes. Mechanical collimators are replaced by a detector where photons are Compton scattered, to be subsequently photoabsorbed in a second detector. With this method, both the efficiency and the spatial resolution of the Compton detector can be enhanced simultaneously. Silicon detectors are the optimum choice for the scatter detector.

One of the possible applications of this technique, the development of a probe for prostate imaging, is particularly interesting. Prostate cancer is the second cancer most common among men, but the imaging detectors currently employed are not adequate for early stage prostate cancer diagnosis. The prostate probe can bring significant advantage over existing devices, according to the results of simulation studies that have been performed.

The development of a clinical prototype to validate the results of the simulations is underway. A first prototype of a prostate probe has been built. The aim is to demonstrate the possibility of operating a multimodule scatter detector employing a stack of thick silicon sensors to increase the efficiency, an essential step for the development of the Compton probe. Thick silicon sensors and their associated readout electronics have been developed for this application. This work describes the development process and the first

results obtained with the prototype.

The dissertation is organized in six chapters. The first one is a brief introduction to medical imaging. Chapter 2 explains in detail the Compton imaging principle, and the factors affecting the performance of Compton devices. A brief overview of the main characteristics of silicon detectors is given in chapter 3. Chapter 4 is a summary of the simulation results obtained at the University of Michigan previous to the prototype development. In chapter 5, the development process, description and calibration methods of the detectors are described in detail. Chapter 6 presents the results obtained with the prototype.

Chapter 1

Medical imaging

1.1 Medical Imaging

Nuclear medical imaging involves those techniques in which a compound labeled with a radioactive source is administered to the patient, and the gamma radiation coming from the body is detected to form an image. The radioactive compound, known as radiotracer, must be chosen such that it accumulates in the organ under study. When the radioactive element decays, the emitted photons traverse the body and are detected with a position sensitive device. The radiotracer distribution in the patient's body can be reconstructed, providing information about metabolic processes. Nuclear imaging has become of outstanding importance in neurological diseases, heart diseases and oncology. Other forms of medical imaging such as X-ray imaging, or X-ray computed tomography (CT), ultrasound and magnetic resonance imaging (MRI) provide information about the physical structure of the organs[1] [1].

Planar X-ray (radiography), and X-ray CT are based on the different absorption of X-rays when they traverse different types of tissues. In CT, projections around the patient are recorded, and a computer processes the information to create an image. It has the disadvantage that soft tissue, such as internal organs, is relatively transparent to radiation. A *contrast agent* can be administered to the patient to enhance the contrast of the organ to be imaged.

In ultrasound (US) or echography, and 3D ultrasound, high frequency sound waves are sent out, and the signal reflected in the organs is used to create the image. The imaging procedure requires the probe, known as transducer, to be in physical contact with the surface of the object to be imaged. Ultrasound ecography has several advantages: it is radiation-free, the acquisition device is relatively inexpensive and fairly transportable, and it is a real-time modality. However, the quality is poor compared to other modalities.

MRI is based on the measurement of changes in the magnetic properties of the hydrogen nuclei (protons) found in cellular water, whose distribution depends on the tissue type and whether the tissue is healthy or diseased. It uses a strong magnetic field to polarize the nuclei, pulsed electromagnetic fields known as gradients, and radio waves to excite the protons and produce the image in the region of interest. Excellent spatial resolution

[1] MRI can also be employed as a functional imaging technique. Research is ongoing in this field.

is obtained.

Although these techniques can provide accurate morphological information, they are limited in their ability to provide biologic information and they are therefore considered complementary to emission tomography. The combination of the anatomic images with the biological information in a single image, known as multimodality, is an active research field.

In nuclear imaging, two main modalities can be distinguished depending on the type of radioactive source that is employed. Single photon imaging employs radionuclides that decay by single gamma ray emission, including scintigraphy or SPECT. In positron emission tomography (PET), positron emitters are used. Positrons annihilate with the electrons in the tissue, giving two 511 keV photons. Both modalities make use of the mathematical technique of computed tomography.

1.1.1 SPECT

SPECT is the most widely nuclear imaging technique currently employed. In SPECT systems (fig 1.1), single photons emitted by the radiotracer are detected in a gamma camera head. It differs from planar scintigraphy in the fact that in SPECT the camera head rotates around the patient and data of the same anatomic location are acquired in different projections, providing a more precise display of tracer accumulation. Images are reconstructed in a way similar to CT, using backprojection algorithms. Dual and triple-headed cameras are employed to increase the sensitivity.

The gamma or Anger camera [2] (fig 1.2), is a two dimensional position sensitive detector consisting of a scintillator crystal optically coupled to a set of photomultiplier tubes (PMTs). A collimator is placed between the detector and the patient to determine the direction of the gamma ray. NaI(Tl) is virtually the only material used in gamma cameras. CsI(Tl) is employed in experimental devices using photodiode readout, and new scintillators are under investigation.

When a photon interacts in the crystal, the PMTs that are close to the interaction position detect the scintillation photons produced in the interaction, and the position and energy deposited can be determined. The thickness of the crystal determines the efficiency of the camera. The attenuation length of NaI(Tl) is 4 mm for the 140.5 keV photons emitted by ^{99m}Tc, the radioisotope most commonly employed in SPECT. Therefore a NaI plate of 9-12 mm thick provides nearly complete absorption for 140.5 keV photons. A typical Anger camera has 9% FWHM energy resolution, and 3.5 mm FWHM intrinsic position resolution (for a tightly collimated point source at the surface of the crystal) at this energy [3].

A collimator consists of a hole or array of holes in a lead plate, and is the element determining the performance of the Anger camera. Photons that are not travelling in the desired direction are absorbed in the collimator. Different types of collimators are employed depending on the application, trying to optimize the performance. Some widely used types of collimators are shown in fig 1.3. A typical parallel hole collimator is made from cast lead with hexagonal cross section holes arranged in a honeycomb fashion. For holes with diameter w and length L, separated from its neighbours by a lead septum of thickness t (typically 0.2 mm), the spatial resolution is given by

Figure 1.1: *SPECT system with two imaging heads at 90 degrees to each other.*

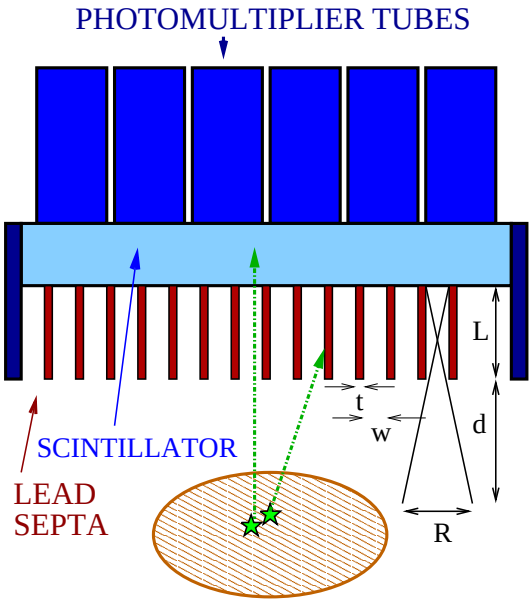

Figure 1.2: *Gamma camera consisting of a scintillator crystal coupled to a set of photomultipliers. Lead septa restrict the direction of the incoming photons.*

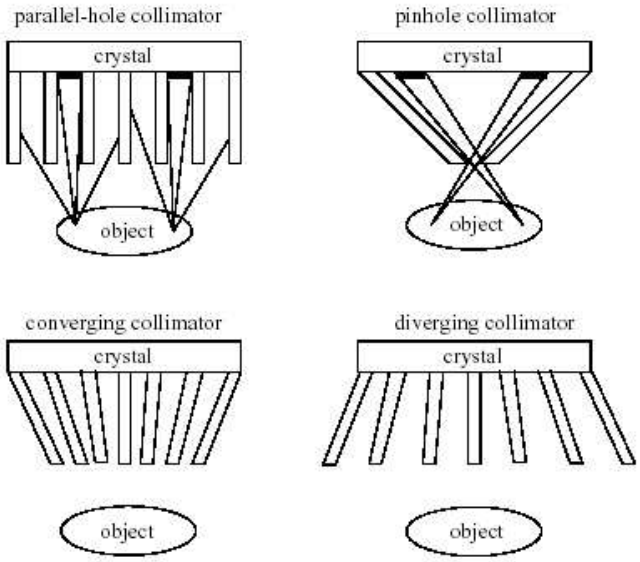

Figure 1.3: *Different types of collimators.*

$$Resolution = 2\frac{w}{L}(d + \frac{L}{2}),$$

where d is the distance from the collimator surface to the object being imaged. The resolution scales linearly with the ratio w/L. L is typically 1-3 cm and d is typically tens of cm, so the resolution increases roughly linearly with the distance d from the collimator. Resolution can be therefore increased reducing w/L. However, this results in a reduction of the efficiency, that is given by

$$Efficiency = (\frac{w}{2L})^2,$$

decreasing quadratically with w/L. For a typical *general purpose* collimator, the spatial resolution is 6.2 mm FWHM at a distance of 5 cm, and the efficiency is 0.023%.

The main limitation of SPECT is therefore given by the fact that spatial resolution and efficiency are inversely coupled and an increase in one implies a decrease in the other. In order to obtain a reasonable resolution with a collimator, the efficiency is low.

In addition to ^{99m}Tc, other commonly used isotopes are ^{201}Tl (135 keV and 167 keV), and ^{123}I (159 keV), for which the Anger cameras have a good performance. At higher energies, thicker septa are necessary, and the performance of the gamma camera decreases.

The most frequent use of SPECT is for studies of myocardial perfusion for assessing coronary artery disease and heart muscle damage following infarction. Cerebral perfusion studies are also widespread, with applications including cerebrovascular disease, dementia, seizure disorders, brain tumors and psychiatric disease. Oncology is a third important application of SPECT, showing accumulation in cancerous cells and allowing to visualize both primary and metastatic lesions.

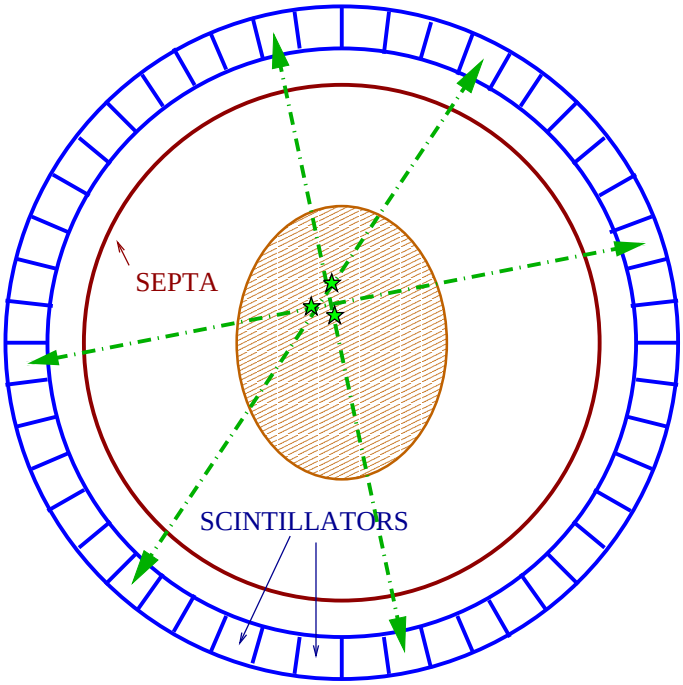

Figure 1.4: *PET system consisting of a planar ring of scintillators coupled to PMTs and working in time coincidence with the detectors on the opposite side of the ring.*

1.1.2 PET

PET has experienced an important development in the last years [4]. This technique employs radioisotopes that are positron emitters, being ^{18}F, ^{11}C, ^{15}O, ^{13}N the most common ones. The positron interacts with the surrounding tissue and annihilates with an electron, producing two 511 keV photons simultaneously travelling in opposite direction. A typical PET detector (figs 1.4 and 1.5) consists of a planar ring of small photon detectors coupled to PMTs and working in time coincidence with the detectors on the opposite side of the ring. If two photons are detected in coincidence, the annihilation point is considered to lie in the line connecting the two interaction positions. The method of employing time coincidence between two detectors to determine the photon direction is known as *electronic collimation*, and implies a considerable benefit in efficiency over mechanical collimation.

BGO is the scintillator most commonly used for PET. The crystal thickness determines the efficiency of the detector. As its attenuation length is 1.2 cm for 511 keV gamma rays, 30 mm thick BGO crystals provide nearby complete absorption.

Resolution and efficiency are in general better that those for SPECT. A typical PET detector module has 20% FWHM energy resolution, 2 ns FWHM timing resolution and 5 mm FWHM position resolution.

Limitations of this technique include attenuation in the tissue, higher than for SPECT because the two photons must traverse twice the amount of tissue, and degradations of the resolution due to the acolinearity of the two photons and the effects of the depth of interaction in the crystal. Some of the drawbacks of the method are its higher cost, and the fact that the most commonly used radiotracers need on-site cyclotron facilities to be

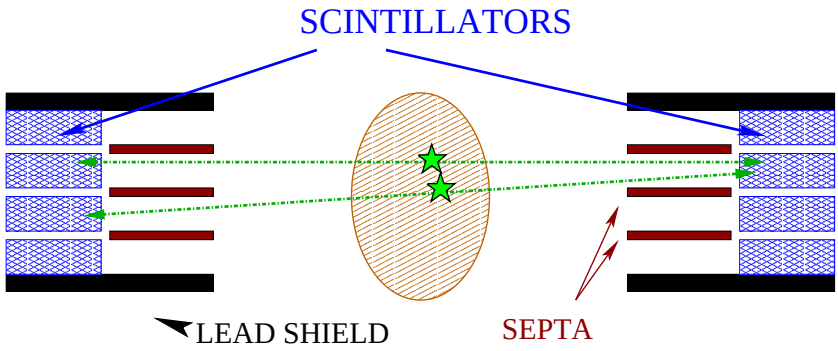

Figure 1.5: *Side view of a PET system. Septa are employed to determine the planes from which the photons are emitted.*

Figure 1.6: *PET tomograph.*

produced.

PET (fig 1.6) has major clinical applications in oncology, neurology and cardiovascular disease. For most applications, 18F-fluorodeoxyglucose (FDG), a sugar analog, is the tracer of choice. The uptake of FDG reflects glucose metabolism in tissues. PET's most widespread application has been for detection and staging of cancer, through whole-body FDG studies. FDG is also used diagnostically in several neurodegenerative diseases and dementia, epilepsy and psychiatric disorders.

1.1.3 Compton imaging

Compton imaging is a variety of SPECT where mechanical collimators are replaced by a first detector in which the photons interact by Compton scattering. The scattered photons are then photoabsorbed in a second detector that can be a conventional gamma camera (figs 1.7 and 1.8). This type of electronic collimation eliminates the resolution-efficiency tradeoff imposed by mechanical collimators, allowing to improve both simultaneously

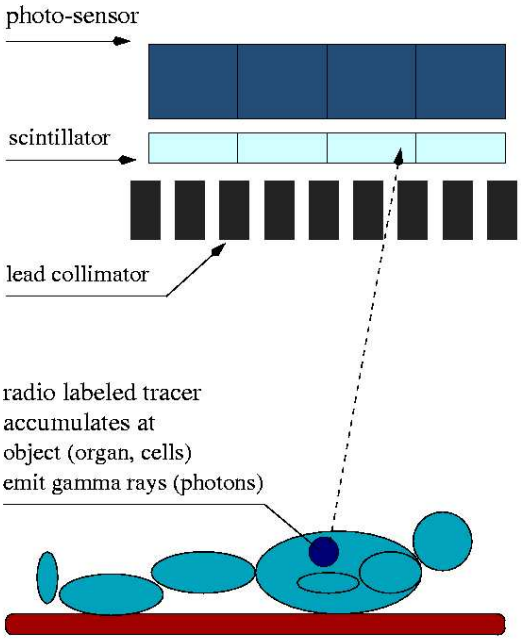

Figure 1.7: *Conventional SPECT: The direction of the photons emitted by the radiotracer is determined by mechanical collimators that couple the resolution and efficiency of the system.*

under the adequate conditions. The principle of Compton imaging will be explained in detail in next chapter.

Silicon detectors are the best option for the scatter detector, and hence their application to Compton imaging can be of great interest. This implies the development of detectors with the adequate characteristics to improve the performance of Compton detectors, and imposes new technological challenges.

The principal advantage of Compton imaging is the efficiency enhancement compared to mechanically collimated devices for a given spatial resolution, but there are also other signifficant advantages. The performance of Compton detectors improves with gamma-ray energy, and therefore high energy radiotracers can and should be employed in order to minimize the scattering and absorption inside the body. This also enables the development of new radiotracers based on different isotopes with a variety of different chemical and decay properties, that have previously been excluded by the fact that the gamma camera performance deteriorates substantially at higher energies.

The main drawback of this method is that the emmision point of the gamma ray is no longer constrained to a line of finite thickness. Instead, for each event, a conical shell can be determined in which the source is restricted to lie, and the intersection of multiple cones generated by several events is necessary to estimate the source position. This implies less information per photon detected, and it must be compensated by the gain in efficiency.

In Compton imaging, the field of view is no longer limited by the collimator, and Compton detectors can image a rather large field of view, even with a small size detector.

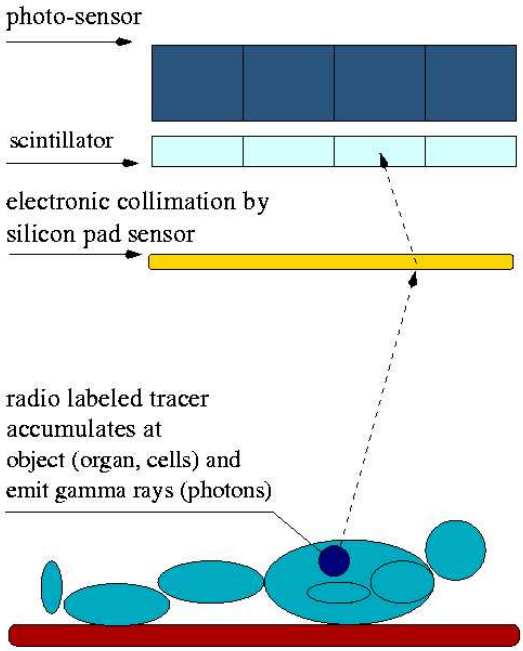

Figure 1.8: *Compton imaging: Mechanical collimators are replaced by silicon detectors in which photons are electronically collimated by Compton scattering.*

However, this also means that photons outside the region of interest are detected at a cost of increasing noise in the image and introducing image artifacts. This effect has to be taken into account when reconstructing the images, and a more complete discussion of the problem is presented in chapter 4.

The possibility of developing a Compton camera for clinical use, in the same way as current PET and SPECT, has been long studied [5,6,7,8,9]. Unfortunately, the technical difficulties imposed by this method will not allow Compton Cameras to be available for clinical use in the near future.

More direct applications of the Compton imaging technique can in the short term offer considerable benefits in medical imaging. Examples of these applications are the development of a probe for high performance scintimammography [10], a very high resolution PET for small animals [11], or a probe for prostate imaging [12], that is the subject of this thesis.

Chapter 2

Compton imaging

In this chapter, the principle of Compton imaging and the factors affecting the performance of Compton detectors are described. These factors will determine the requirements of the scatter and absorption detectors.

The algorithm employed for image reconstruction is also outlined. Finally, a summary of the most relevant developments in Compton imaging is presented.

2.1 Physics of Compton interactions

In Compton scattering, the interaction takes place between an incident photon and an electron from the detector material. The principle of Compton detectors is based on the fact that in the interaction the photon transfers only a portion of its energy to the recoil electron, escaping afterwards. If a second detector is placed such that the scattered photon is absorbed, position and energy can be determined in two points along its trajectory, and information about the point from which the incoming photon was emitted can be obtained.

At the energies relevant for medical imaging, Compton scattering and photoelectric absorption are the two dominating processes [13, 14]. Photoabsorption dominates for low energy gamma rays, and its probability increases rapidly with the atomic number of the material (Z). Compton scattering is the most probable interaction for materials with low atomic number, and for the energy range from hundreds of keV till 5-10 MeV, where pair production starts to dominate.

A good understanding of the physics of Compton interactions is essential for the optimization of the Compton detector performance. Figure 2.1 shows the interaction kinematics. The angle at which the photon is deflected depends on the incoming photon energy and the energy transfer. If the electron is considered at rest, the expression that relates the energy of the scattered photon with that of the incident photon and the scattering angle can be obtained from conservation of energy and momentum

$$E' = E_0 - E_e = \frac{E_0}{1 + \alpha(1 - cos\theta)}. \tag{2.1}$$

In this equation, E_0 is the initial energy of the photon, E' is the energy of the scattered photon, θ is the scattering angle, E_e is the energy of the recoil electron in the scatter detector, and $\alpha = \frac{E_0}{m_0 c^2}$, where m_0c^2=0.511 MeV is the rest-mass energy of the electron.

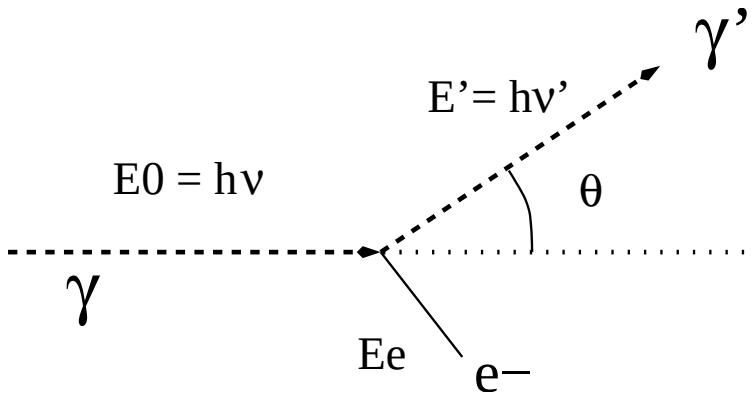

Figure 2.1: *Kinematics of Compton scattering*

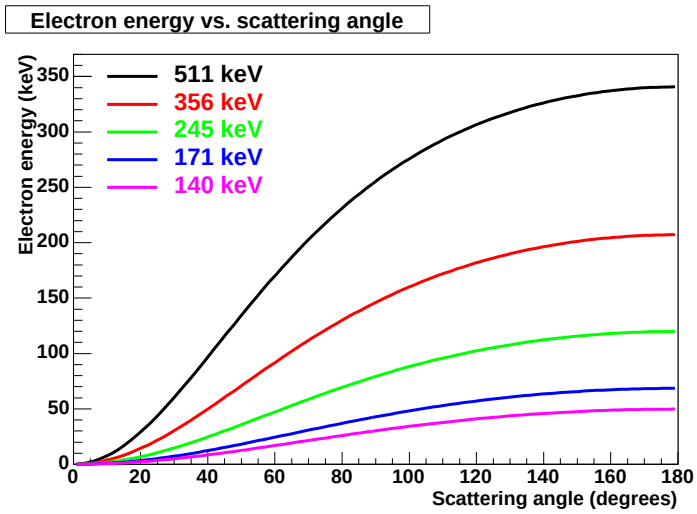

Figure 2.2: *Recoil electron energy versus gamma-ray scattering angle for different values of the incoming photon energy.*

In case that the energy of the incoming photon is known, the scattering angle can be determined by measuring the electron energy in the scatter detector. The electron energy is represented in fig 2.2 versus the scattering angle for different energies of the incoming photon. The energy range corresponding to a given angle interval is smaller for lower energies of the incoming photon. The minimum energy that can be measured determines the minimum scattering angle, that will therefore be smaller if high energy sources are employed.

Regarding the kinematics of the process, it can be seen that for small scattering angles very little energy is transferred, irrespective of the incident photon energy. The high energy transfers correspond to the case of big scattering angles, close to 180º when the photon is scattered in a direction opposite to the incoming direction. The maximum energy transfer, corresponding to the case when the photon is backscattered ($\theta \approx 180º$),

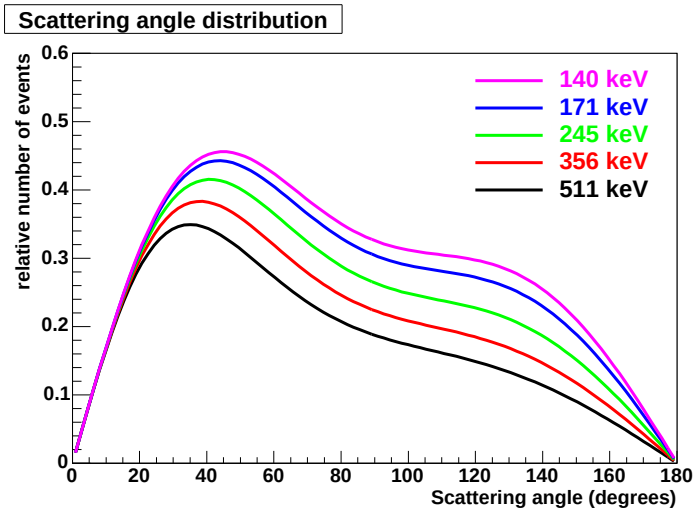

Figure 2.3: *Scattering angle distribution for different values of the incoming electron energy.*

is given by

$$E_{e_{max}} = (E_0 - E')_{max} = E_0(\frac{2\alpha}{1+2\alpha}). \tag{2.2}$$

As a consequence, the energies of the scattered photon range from E_0-$E_{e_{max}}$ to E_0[1]. For energies of the incoming photon below 50 keV, the energy of the scattered photon does not differ much from the incident energy. At these low energies, the interaction tends to Rayleigh (coherent) scattering, which does not change the energy of the scattered photon, but only deflects it.

The double-differential cross section for the Compton scattering process is given by the Klein-Nishina formula

$$\frac{d\sigma}{d\omega} = \frac{r_e^2}{2}\frac{1}{[1+\alpha(1-cos\theta)]^2}\left(1+cos^2\theta+\frac{\alpha^2(1-cos\theta)^2}{1+\alpha(1-cos\theta)}\right), \tag{2.3}$$

where r_e is the classical electron radius (r_e=2.817940 fm).

The integration of the Klein-Nishina formula gives the total probability per electron for a Compton scattering to occur

$$\sigma_c = 2\pi r_e^2\left\{\frac{1+\alpha}{\alpha^2}\left[\frac{2(1+\alpha)}{1+2\alpha}-\frac{1}{\alpha}ln(1+2\alpha)\right]+\frac{1}{2\alpha}ln(1+2\alpha)-\frac{1+3\alpha}{(1+2\alpha)^2}\right\}. \tag{2.4}$$

The angular distribution of photons for a unit solid angle is plotted in fig 2.3 for different values of the incoming photon energy. As the photon energy increases, low scattering angles are more favoured, and the distribution shows a higher anisotropy.

[1]In practice, since the detectors will be operated in coincidence, the maximum energy measured in the absorption detector is limited by the minimum energy that can be measured in the scatter detector.

If the distribution is plotted as a function of the recoil electron energy, the characteristic form of the Compton continuum corresponding to all possible scattering angles is obtained. The maximum energy, known as the *Compton edge* is given by equation 2.2.

The Klein-Nishina formula is derived considering free electrons at rest. In real situations, the electrons involved in the interaction are bound to a nucleus and have non-zero momentum. This causes the rounding-off and slope in the Compton edge of measured spectra compared to the abrupt drop predicted by the formula.

The effect caused by the momentum distribution of the electrons is known as *Doppler broadening*. Instead of a fixed energy for a given scattering angle, scattered photons show an energy distribution about the value predicted by equation 2.1. Doppler broadening depends on the detector material, increasing with the atomic number, and on the atomic shell of the detectors. The outer shell electrons have less binding energy and orbital momentum, causing smaller broadening in comparison to the inner shells. For a given material, the effect is bigger for large scattering angles and decreases with increasing energies of the incident photon as $\frac{1}{E_0}$.

The double-differential cross section derived by Ribberfors [15, 16], equation 2.5, describes the Compton scattering cross section at subshell n. It includes the Compton profile $J_n(p_z)$, that represents the pre-collision electron momentum distribution, being p_z the pre-collision electron momentum along the scattering vector. It depends on the atomic number of the material, the subshell of the specified electron and the binding effects of neighbouring atoms. The total double differential cross section is obtained by weighting each individual term by the specific subshell electron density and summing over all subshells.

$$\frac{d^2\sigma_n}{d\theta dE'_r} = \frac{\pi r_0^2 sin\theta}{E_r}\left(\frac{E'_r}{E_r} + \frac{Er}{E'_r} - sin^2\theta\right)\left(\frac{p_z J_n(p_z)}{1 - \frac{E'_r}{E_r} + \frac{E_r}{m_0 c^2}(1 - cos\theta)}\right). \tag{2.5}$$

Compton profiles have been both calculated [17] and measured [18]. The distribution follows a Lorentzian shape pulse with prominent tails, that is narrower for higher energies.

Doppler broadening is given by the detector material chosen, and will impose a physical limit in the scattering angle uncertainty. A comparison for different detector materials is described in [19, 20]. Doppler broadening is lower for silicon than for Germanium and CZT. Figure 2.4 shows the distribution for these three semiconductor materials for ^{99m}Tc (140.5 keV) at a nominal scattering angle of 60º. Of the studied materials, only diamond has lower Doppler broadening than silicon.

2.2 Compton Imaging

Figure 2.5 illustrates the principle of Compton imaging. Photons coming from a radioactive source are Compton scattered in a first (*scatter*) detector, and then absorbed in a second (*absorption*) detector that is operated in time coincidence with the scatter detector. By this method, photons are electronically collimated, without restricting their incoming direction as mechanical collimators do. As a result, the efficiency can be increased compared to conventional SPECT for a given spatial resolution.

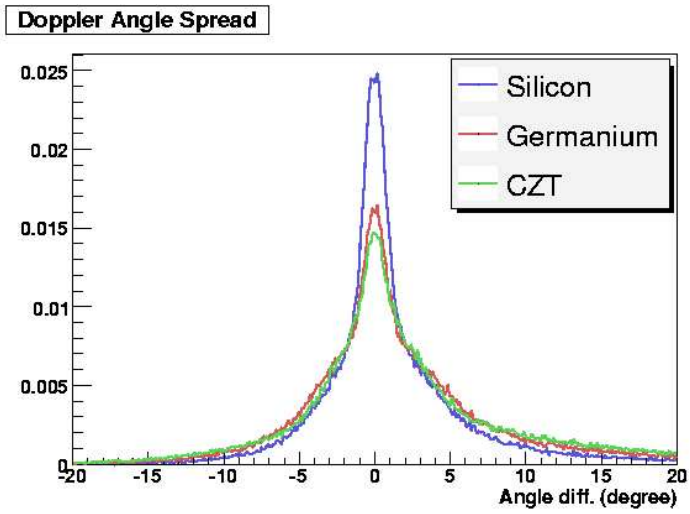

Figure 2.4: *Difference between the nominal scattering angle of 60º and the measured one for ^{99m}Tc due to Doppler broadening.*

From the energy deposited in both interactions (or the energy transferred in the Compton interaction if the energy of the incident photon is known), the scattering angle can be calculated from equation 2.1 as

$$cos\theta = 1 - m_0c^2\left(\frac{1}{E_0 - E_e} - \frac{1}{E_0}\right). \tag{2.6}$$

Since the momentum vector of the recoil electron is unknown, it is not possible to find out the direction of the incoming photon. However, determining the interaction positions in both detectors allows to reconstruct a cone with half angle given by the scattering angle of the event, its vertex given by the interaction point in the first detector, and the axis given by the straight line connecting the interaction points in both detectors (Fig 2.6). The point from which the photon was emitted is then restricted to lie in the conical shell, and from the intersection of the cones generated in several events, the source position can be determined (Fig 2.8).

This method of obtaining the source location results in a more complex image reconstruction procedure than the one employed for mechanically collimated systems, and the gain in efficiency is thus obtained at the expense of a higher computational cost.

The performance of Compton detectors depends on the characteristics of both scatter and absorption detectors, as well as on the detector geometry, and has been thoroughly studied. The improvement in efficiency and spatial resolution over mechanically collimated SPECT is therefore not guaranteed. The final performance of the device will be strongly determined by the detector characteristics.

2.2.1 Spatial resolution

The spatial resolution of the Compton detector depends on the precision in reconstructing the cone, that is affected by the spatial resolution of both detectors, the uncertainty in the scattering angle, and also by the geometry of the device.

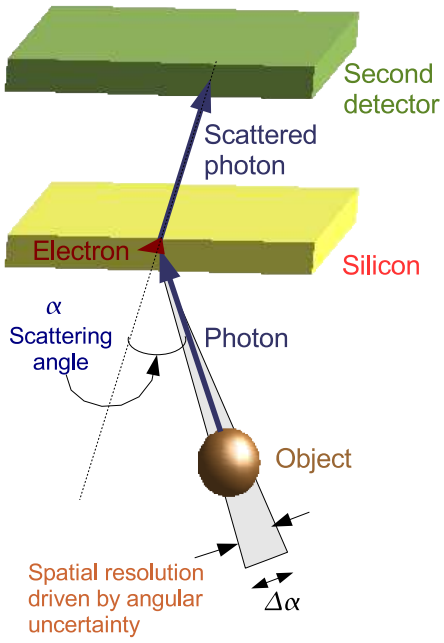

Figure 2.5: *Compton imaging principle. Incident photons are electronically collimated by Compton scattering in a first (scatter) detector, and subsequently absorbed in a second (absorption) detector.*

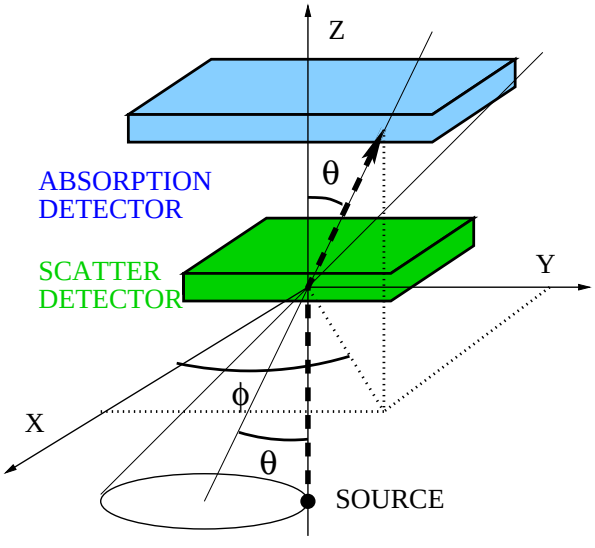

Figure 2.6: *Reconstructed cone from the interaction points in both detectors and the photon scattering angle θ for a photon emitted along the Z axis. The azimuthal angle ϕ defines the interaction plane.*

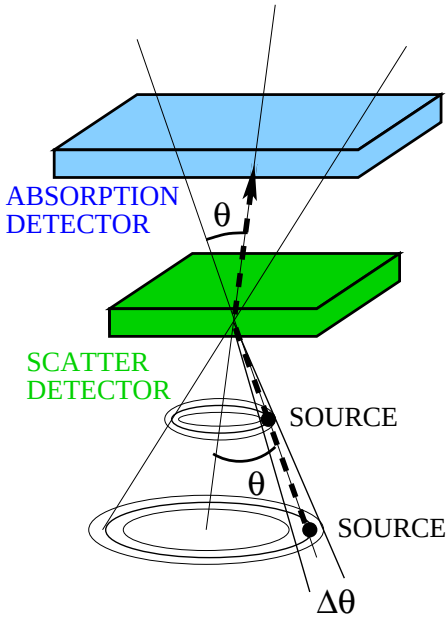

Figure 2.7: *Angular uncertainty of the reconstructed cone aperture at different distance from the source to the scatter detector.*

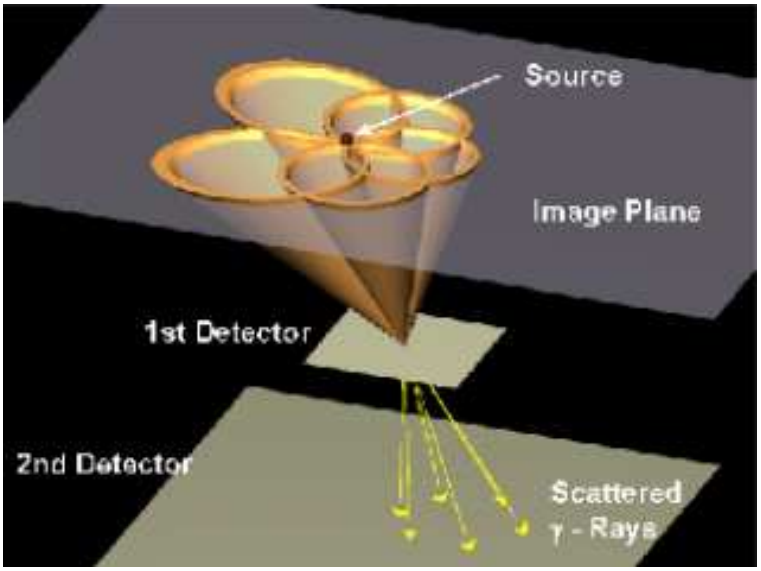

Figure 2.8: *The source position is determined by the intersection of several cones.*

The spatial resolution of the absorption detector affects the uncertainty in the orientation of the cone axis, while the spatial resolution of the scatter detector affects both the orientation of the axis and the position of the cone vertex. However, these effects can be minimized, as it will explained later in this section.

For optimized spatial resolution of the scatter and absorption detectors, the key parameters that determine the spatial resolution of the Compton detector are the uncertainty in the scattering angle and the distance from the scatter detector to the source. The angular uncertainty results in a spatial uncertainty when the intersection of the cone and the image plane is determined. For a given angular uncertainty, a larger distance induces a bigger spatial uncertainty (fig 2.7). Therefore, to achieve an adequate spatial resolution, the scatter detector should be placed as close as possible to the source, and the uncertainty in the scattering angle must be minimized.

The uncertainty in the scattering angle is determined by the accuracy in the measurement of the energy in the scatter detector, as well as the intrinsic Doppler broadening. The influence of the energy resolution of the detector in the scattering angle uncertainty can be obtained from equation 2.1 and is given by

$$\Delta\theta = \frac{m_0 c^2}{sin\theta(E_0 - E_e)^2}\Delta E_e.$$

The sine function in the denominator results in a larger uncertainty for scattering angles close to 0^o and 180^o. The $\frac{1}{E_0}$ dependence makes that for higher energies the uncertainty becomes smaller, resulting in a better performance of the Compton detector.

This can be exploited to image high energy radiotracers that can be very useful in some cases, such as the use of ^{131}I for cancer therapy, and to reduce the effects of multiple scattering and attenuation. The use for SPECT is now restricted to low energy radiotracers due to the worse performance of mechanically collimated devices at high energies.

In fig 2.9 the angular uncertainty is plotted versus the scattering angle for two different

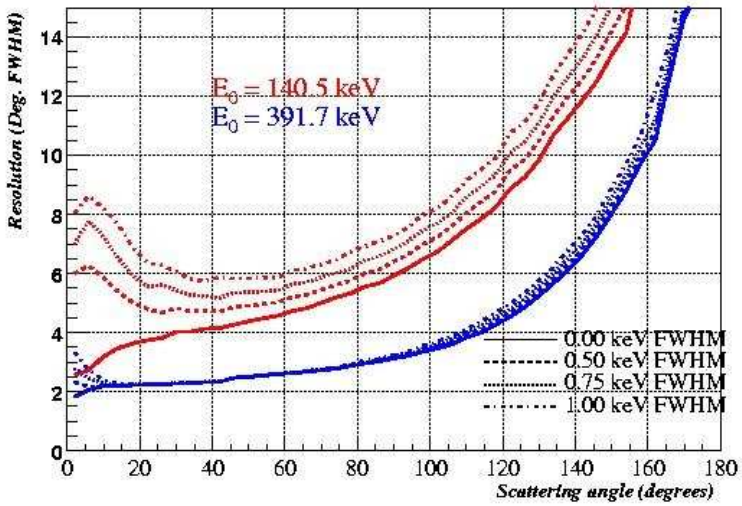

Figure 2.9: *Angular uncertainty versus scattering angle for two different energies and for different values of the energy resolution of the scatter detector. The lowest values are obtained for high energies and low scattering angles. The effect of energy resolution is more significant at lower photon energies.(Adapted from Hua et al, 1999 [21], © IEEE 1999.)*

values of the incoming photon energy (140.5 keV of ^{99m}Tc and 391.7 keV of ^{113m}In) and for different values of the energy resolution of the scatter detector. The influence of Doppler broadening has also been considered. The solid lines correspond to perfect energy resolution, and the angular uncertainty is due to Doppler broadening only. As it was explained in the previous section, the effect is smaller for higher energies and for lower scattering angles, which are therefore the most favourable for Compton imaging. The dashed/dotted lines include the angular uncertainty due to the energy resolution of the scatter detector. It can be seen that at high energies, its effect is almost negligible in an angle range between 20° and 90°-120°, whereas for low energies it can have a significant effect. It is interesting to note that an angular uncertainty of 2° corresponds to a spatial resolution of 3.5 mm FWHM at 10 cm distance from the source to the scatter detector.

The energy resolution of the scatter detector should therefore be minimized. The noise not only affects the angular uncertainty but, also determines the minimum angle that can be measured with a sufficiently low noise occupancy. For ^{99m}Tc, the mean energy deposited for a 15° scattering angle is 1.29 keV. If signals about this energy are to be measured with low noise occupancy (3σ), the corresponding energy resolution of the scatter detector should be approximately 1 keV FWHM [5].

The spatial resolution of the Compton detector depends on the spatial resolution of both the scatter and absorption detectors, and on their relative distance. The effects of these factors have been analytically evaluated for a parallel plate Compton detector [22, 23].

For a given distance from the scatter to the absorption detector, the resolution of the Compton detector improves with the spatial resolution of both detectors. The dependence is linear with the scatter detector spatial resolution. Considering the absorption detector

spatial resolution, a variation with the scattering angle can be observed for small relative distances, while it becomes uniform for bigger distances.

For a given spatial resolution of the scatter and absorption detectors, an improvement of the spatial resolution of the Compton detector is observed if their relative distance is increased, and the influence of the spatial resolution of the individual detectors becomes smaller.

The effects of the spatial resolution of the scatter and absorption detectors are therefore minimized when the distance between them is increased. The value at which this happens depends on the detector geometry.

To summarize, scatter and absorption detectors with good spatial resolution can relatively easily be selected, and their effect on the spatial resolution of the Compton detector can be be further minimized if an adequate geometry is chosen increasing their relative distance. In that case, the spatial resolution for a given distance to the source is determined by the uncertainty in the scattering angle, that depends on the scatter detector energy resolution and Doppler broadening. Therefore, for a given geometry, the scatter detector is the key in the performance of the Compton detector. However, for a given angular uncertainty, its effect on the spatial resolution of the detector is smaller if the scatter detector is placed close to the source. This will be taken into account in the design of the prostate probe to obtain a high spatial resolution.

These factors affecting the resolution of the Compton detectors have to be considered in the requirements that the scatter and absorption detectors must fulfil, that will be discussed in the following sections.

2.2.2 Efficiency

The detection efficiency depends on the joint probability of a Compton interaction in the scatter detector, followed by an escape and interaction in the second detector. Therefore it will depend on the size, type and geometry of the two detectors, and it will be determined by the probability of Compton interaction in the scatter detector, depending on the Compton cross section and detector thickness, and by the solid angle subtended by the scatter and absorption detectors, which is determined by the geometry and will be discussed in section 2.3.3.

The fact that several events are necessary to obtain one point in the image space must also be taken into account when comparing the efficiency of Compton detectors and conventional mechanically collimated devices. For an equal number of detected photons, collimators outperform Compton detectors. However, for a Compton detector the sensitivity can be increased without degrading the resolution.

Studies have been carried out [19] to estimate how much larger the sensitivity must be to be comparable to that of a collimated camera. A quantity defined as *decoding penalty* estimates the gain in sensitivity that Compton detectors must have to perform as a parallel collimated camera. If the decoding penalty is unity, the two have the same estimated performance and each detected photon carries the same amount of information for both cameras. This quantity has been calculated for a Compton camera and a collimated gamma camera, for a disk source at different values of the photon energy. At 140.5 keV (^{99m}Tc) a penalty around 40 is obtained for a 7.5 cm disk source, and therefore the

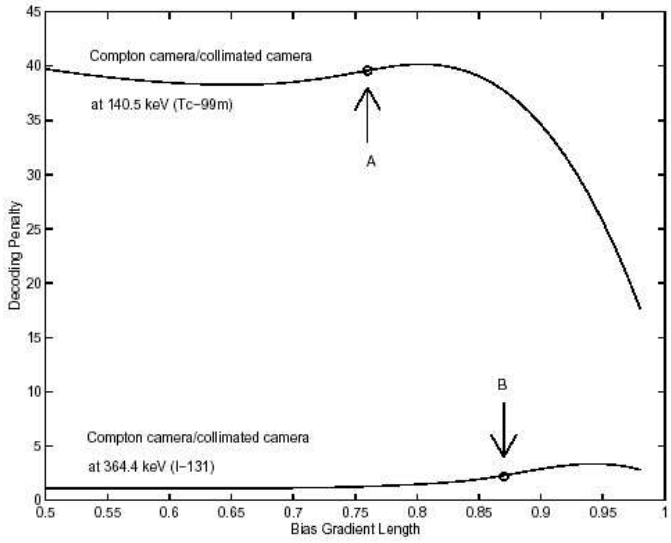

Figure 2.10: *Decoding penalty calculated for a 7.5 cm disk source for two sources and different spatial resolution. (Adapted from Hua et al, 1999 [21], © IEEE 1999).*

Compton cameras must have 40 times higher raw sensitivity to have a performance similar to parallel hole collimated cameras. In contrast, at 364.4 keV (^{131}I), the sensitivity need to be only twice (see fig 2.10).

The calculated decoding penalty decreases if the disk size is reduced, and the Compton camera is already better for a 3.75 cm diameter disk. The potential sensitivity advantage of the Compton camera for the geometries considered in the study is around 30 times the sensitivity of the collimated camera with a technetium collimator, and around 20 with the ^{131}I collimator.

If the efficiency of the Compton camera is further improved, gains in performance can be even higher.

2.3 Detector requirements

The detector requirements are determined by the factors that affect spatial resolution and efficiency, explained in the previous section.

2.3.1 Scatter detector

An appropriate choice of a scatter detector is essential in the development of a Compton detector. For the scatter detector, a single Compton interaction followed by an escape of the scattered photon is desired, together with a good determination of the interaction position and the scattering angle. The main requirements are therefore a high probability of Compton interaction, an adequate spatial resolution, and an excellent energy resolution, that affects the determination of the scattering angle. The probability of having a Compton interaction increases linearly with the atomic number of the material, while the photoabsorption cross section depends on Z^n, where n is between 4 and 5 depending

on the photon energy. Materials with low Z are therefore required. Solid state detectors (silicon, germanium) or gaseous detectors (Ne, Xe, Ar) could be good candidates for the scatter detector.

The main advantage of solid state detectors is that the ionization energy is very small (3.6 eV for Si, 2.9 eV for Ge) compared to the typical value of 30 eV for gaseous detectors. The number of carriers generated per unit of radiation energy absorbed is therefore much larger, reducing the statistical fluctuations, and better energy and timing resolution can be achieved. In addition, their higher density results in a higher efficiency for photon detection. One of their disadvantages is the difficulty in growing large pieces of semiconductor material with the required purity, and the thickness of a practical detector is limited by the increased leakage current and full depletion voltage that must be applied, and a degradation of the timing properties, as it will be explained in chapter 3. The depth resolution is also worse in thick detectors.

Among solid state detectors, several reasons make silicon the preferred option. Although the Compton cross section is smaller than that of germanium reducing the efficiency, the ratio of Compton to total cross section is higher (fig 2.11). The probability of double Compton scattering is also sufficiently low. Besides, germanium has the disadvantage that cryogenic cooling is necessary, while silicon has a good energy resolution at room temperature.

Another factor to consider is Doppler broadening. Diamond has the lowest Doppler broadening. Detectors based on natural diamond are being considered as an alternative to ionization chambers and silicon diodes. Unfortunately, few natural diamonds are suitable for use as detectors and the properties of individual diamonds can vary. In the last years, detectors based on diamond grown by chemical vapour deposition (CVD) have been developed for high energy physics and are being evaluated for medical imaging. However, this technology is still under development [24, 25, 26].

Silicon has the lowest Doppler broadening after diamond. The fabrication of silicon sensors follows now a standard process. Their development has achieved a high level of maturity and stability, that comes parallel to the improvements on the development of the electronics employed for their readout. Their increased use for high energy physics has also made the cost decrease. These reasons make silicon the optimum choice for the scatter detector [27].

2.3.2 Absorption detector

The aim of the second detector is to photoabsorb the scattered photon. Materials with high density and atomic number for efficient gamma ray absorption, avoiding Compton interactions, are therefore required.

The requirements of the second detector for a Compton detector are closer to those for PET detectors than for SPECT [28]. In SPECT, a high light yield is essential to have a good spatial and energy resolution, and photon energies are lower than in PET. Unlike these two techniques, in Compton imaging photons absorbed in the second detector have a wide range of energies, almost up to the incoming photon energy as explained in section 2.1, and they are higher than in SPECT if high energy isotopes are employed. The stopping power must therefore be high.

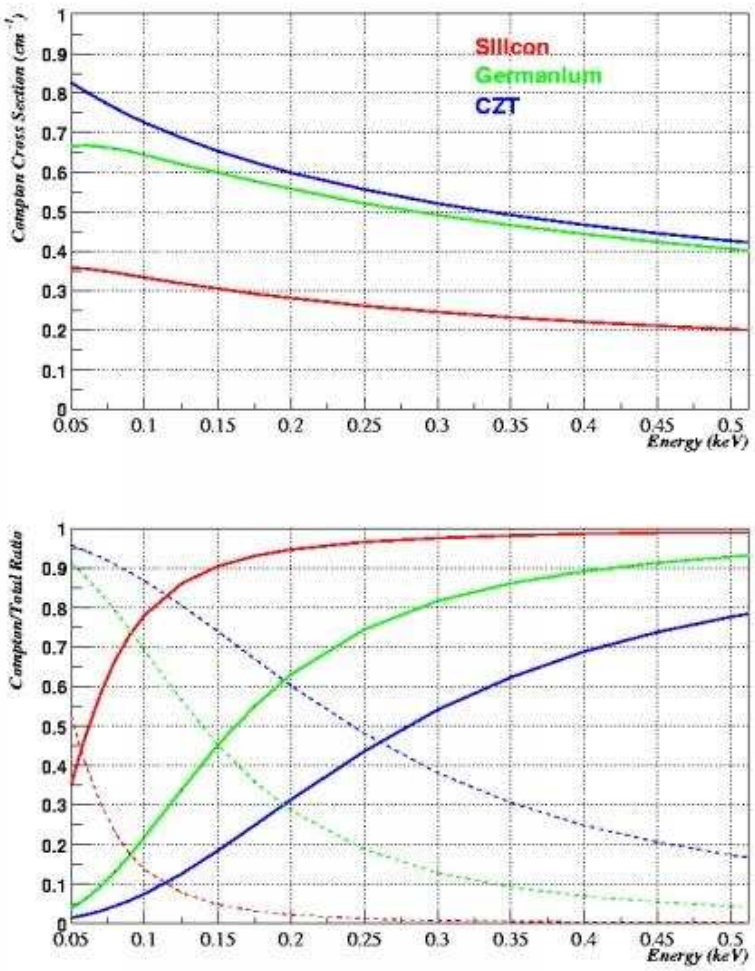

Figure 2.11: *Up: Compton cross section for three semiconductor materials. Down: Compton (solid line) and photoabsorption (dashed line) to total cross section ratio.*

Electronic collimation requires a good timing resolution, in order to allow short coincidence windows and reduce the rate of accidental coincidences. Random events become increasingly important when imaging high activities. High countrate capability is essential to avoid pile-up and reduce the rate of accidental coincidence events and dead time, especially when the second detector views directly the source, increasing the rate of direct photons on the second detector.

If the energy of the radioisotope employed is known, the scattering angle can be calculated from the energy deposited in the scatter detector and only the interaction position in the second detector needs to be calculated. However, when the incident gamma-ray energy is known, the best estimate of the energy transferred in the Compton interaction, ΔE_e, is obtained from the energy measurements in both detectors E_e and E'. If the energy resolution of the scatter and absorption detectors are σ_s and σ_a respectively, the uncertainty in ΔE_e is given by [5]

$$\sigma_{\Delta E_e} = \sqrt{\frac{\sigma_s^2 \sigma_a^2}{(\sigma_s^2 + \sigma_a^2)}}.$$

A good energy resolution also ensures a precise calculation of the total energy of the event as the sum of the energies deposited in both detectors, facilitating the rejection of accidental coincidences and events scattering in the patient. If radioisotopes emitting gamma rays of different energies such as ^{111}In (171 keV and 245 keV) are employed, it must be possible to separate the contributions from different photopeaks to ensure a precise image reconstruction.

Scintillator materials are adequate candidates for a second detector. The ideal scintillator would have high stopping power, high luminosity (light yield), short decay time, no afterglow and low cost. A high detection efficiency is necessary in any medical imaging detector. In addition, a short attenuation length and a high probability of photoabsorption are desired to minimize resolution degradation caused by penetration and Compton scattering in the scintillator [29, 30, 31].

The decay lifetime affects both timing resolution and dead time. If multiple decay lifetime components are present, the dead time is influenced most by the slowest decay component. Timing resolution is determined by the scintillation photon intensity immediately after excitation (I_0). The fastest decay component usually has the largest effect on I_0. The luminosity affects the timing, spatial and energy resolution. The higher the number of photons generated, the less the errors due to statistical fluctuations. For a given decay time, a higher luminosity yields a higher initial intensity I_0, and therefore better timing resolution. On the other hand, scintillators must transmit scintillation light efficiently. Improvements concerning energy, time and position resolution are generally at the expense of efficiency.

The ideal scintillator that combines all these properties is still being searched for. For the time being, a wide variety of well known and recently developed scintillators [32,33,34] allows one to select the one that best matches the main requirements of each application. Table 2.1 shows a list of scintillator properties.

Existing gamma cameras can be an adequate second detector for a Compton detector. NaI(Tl), which has long been the standard scintillator for SPECT, has a high light yield,

Material	Luminosity (photons/MeV)	Density (g/cm^3)	Decay time (ns)	Wavelength (nm)
NaI:Tl	40000	3.8	230	410
CsI:Tl	66000	4.5	800	550
$Bi_4Ge_3O_{12}$ (BGO)	8000	7.1	300	480
Lu_2SiO_5:Ce (LSO)	26000	7.4	40	420
Gd_2SiO_5:Ce (GSO)	8000	6.7	60	440
$YAlO_3$:Ce (YAP)	21000	5.5	30	350
$LuAlO_3$:Ce (LuAP)	12000	8.3	18	365
$LaCl_3$:Ce	46000	3.86	25 (65%)	330
$LaBr_3$:Ce	61000	5.3	35 (90%)	258

Table 2.1: *Main properties of several scintillator detectors.*

and the emission wavelength matches the sensitivity of the PMTs quite well. Crystals of large size can be grown relatively easily and its cost is low.

BGO and LSO are more adequate for high energy gamma rays because of their good detection efficiency and large probability of photoelectric effect for 511 keV photons (about 40%), given their higher atomic number. BGO has been traditionally employed for higher energy photons. However, the light yield is lower, resulting in lower resolution and response time. LSO has a good detection efficiency, higher light yield and shorter response time than BGO. Its main drawback is that large crystals have inhomogeneities in the light production and decay time, afterglow and a natural background activity. Besides, gamma-ray resolution is poorer than expected on the basis of the light yield. GSO is similar to LSO, with the advantage that the Ce concentration and therefore the decay time can easily be varied.

Detector development in general and scintillator development in particular for medical imaging are in full progress. There is a strong interest in the introduction of new dense high atomic number inorganic scintillation crystals with a high light yield and a fast response. Compton detectors would obviously benefit from these improvements. The research is focused on Ce^{3+} doped scintillators expecting a high light yield, and a time response in the 25-100 ns range, as well as improved energy resolution. Lu^{3+} is another option for doping, but it has two disadvantages, its high price and the presence of the radioactive isotope ^{176}Lu.

LuAP:Ce has an attenuation length similar to BGO, but a higher light yield and faster response time, providing an excellent time resolution. Its main disadvantage is that the energy resolution is relatively poor, primarily due to strong scintillation-light absorption. Also the crystal-growing process is complicated.

$LaCl_3$:Ce and $LaBr_3$:Ce have shown up as very promising materials. They provide a high light yield, fast response excellent resolution and very good time resolution, although the attenuation length and photoelectric fraction are lower than in the previous case.

The replacements of PMTs with solid state photodetectors such as avalanche photodiode arrays (APDs) would significantly alter the requirements of the scintillators. The lower signal-to-noise ratio compared to PMTs would require higher luminosity and initial intensity in order to achieve the adequate timing and energy resolution. The quantum

efficiency is significantly higher, and better energy resolution may be achievable. They also have good quantum efficiency in a different wavelength range (400-900 nm rather than 300-500 nm), and therefore it would be possible to use scintillators that emit at much longer wavelengths.

Advances in solid state detectors also offer interesting possibilities for the second detector. CdTe and CZT, with average atomic numbers of 50 and 49.1 and densities 5.85 and 5.78 g/cm^3 respectively, present the advantages of excellent energy, position and timing resolution. In addition, their detection efficiency is comparable to NaI(Tl) and CsI(Tl). CZT detectors have been proposed for medical imaging applications [35, 36, 37, 38]. Their main drawback is the high cost, and the fact that they are not as widely available as scintillators. Also, the number of readout channels is larger, and their smaller dimensions compared to currently employed scintillators require an increased number of detectors for a similar angle coverage. Thick CZT and CdTe detectors with good 3D position resolution are being investigated [39, 40, 41].

2.3.3 Geometry

The application of the Compton detector will determine its geometry. However, geometry affects resolution and efficiency of the Compton detector, and it must be optimized taking these parameters into account for a good detector performance.

The influence of the parameters that define the Compton detector on the resolution has been studied for different geometries: a planar detector, cylindrical or conical configuration, or different configurations of a planar detector [42, 22, 43]. The studies agree in the factors already mentioned in section 2.2.1. The resolution improves when the source is placed close to the scatter detector, and the distance from the scatter to the absorption detector is increased. However, this also has consequences in the efficiency of the detector. If the first detector is placed close to the source, the solid angle is also increased, and a higher efficiency is obtained. On the contrary, placing the absorption detector further results in a smaller angle coverage with the corresponding decrease of the efficiency. This loss can only be compensated by increasing the area of the absorption detector, and therefore the cost.

Other factors must be considered when designing the scatter detector. Increasing the thickness of the detector also enhances the probability of interaction and therefore the efficiency. However, the probability of photoabsorption, and double Compton scattering are also increased. Multiple Compton interactions in the first detector require determining the sequence of interactions to reconstruct the event. A thickness of 10-12 mm of silicon has been found to be the optimum to maximize the efficiency for single Compton events [5, 23], and will be employed for the Compton probe.

To achieve the desired thickness with 300 μm thick silicon sensors, a large number of detectors would be required. The number of readout channels and electronics is then increased, causing problems of scattering materials, and heat generated by the electronics. The use of thick silicon sensors would reduce the number of detectors necessary to achieve the desired efficiency.

Other considerations should also be taken into account in the geometry of a Compton detector. Placing the second detector to absorb those photons with lower scattering angles

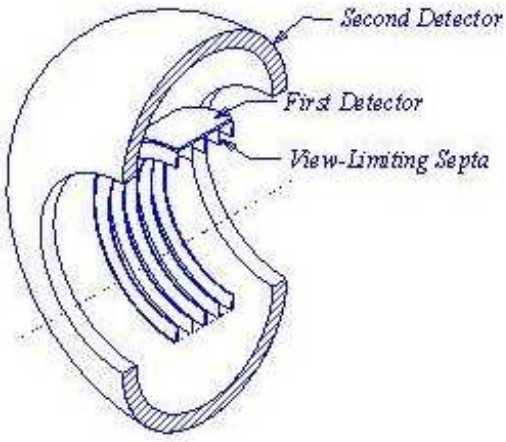

Figure 2.12: *Double ring Compton Camera*

will improve the spatial resolution of the device. It should also try to prevent photons from hitting directly the second detector, adding some shielding in the way from the source to the absorption detector, or carefully selecting their relative position.

The geometry of the detector will also affect the image reconstruction. Angle coverage should be taken into account when selecting the size and position of the detectors. Limiting the scattering angles that are accepted produces artifacts in the reconstructed images, and restricting the angles of the photons coming from the source subtended by the first detector results in a degradation of the depth resolution. For a given size of the scatter detector, this effect is also caused by increasing the distance from the source.

A double-ring or *tyre shaped* Compton camera, with a cylindrical scatter detector surrounded by a cylindrical or tyre-shaped second detector, as the one shown in fig 2.12, is an interesting geometry that fulfils most of the conditions previously mentioned. Its main advantage is the gain in efficiency compared to a conventional gamma camera, about 200 to 400 times better for single scattered events, depending on the source energy (fig 2.13). The main drawback is its high cost compared to simpler options. A number of authors have described the double ring geometry [6, 7, 8, 9].

The application of detector and geometry requirements to the Compton prostate probe will be explained in chapter 4.

2.4 Image reconstruction

Image reconstruction in emission computed tomography aims to determine the unknown distribution of the radiotracer, from which photons are emitted (i.e. the *image*), from the measured data. Numerous methods, both analytical and iterative, have been employed for this task.

An interesting approach is to formulate the image reconstruction as a maximum likelihood (ML) problem. The method has been applied successfully to both emission and transmission computed tomography problems [44, 45].

In the emission problem, the likelihood function representing the physical model of the

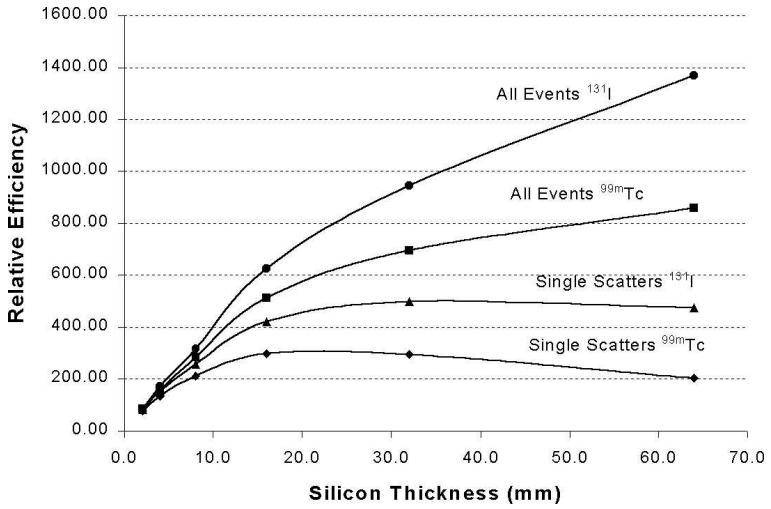

Figure 2.13: *Relative efficiency of a double ring Compton camera with respect to a collimated gamma camera for ^{99m}Tc and ^{131}I (From W.L. Rogers et al. [5])*

photon emission and detector response, is maximized for a set of measured events in which the parameters represent the unknown source distribution. The likelihood function gives an estimation of the probability of obtaining the data that we have actually observed, for a given source distribution. The distribution that maximizes the likelihood is therefore the one that is most likely to produce the observed data, given the physical model represented in the likelihood function. The maximization of the likelihood may be a rather complicated task that can not be accomplished by analytical methods. The expectation maximization algorithm (EM) [46] provides an iterative method of solving the problem.

The maximum likelihood expectation maximization method (MLEM) has several advantages over other methods, such as the possibility to model the underlying physics of the process, positivity constraints, no free parameters and convergence, although it is slow and a high number of iterations may be required.

In the case of the Compton camera, different methods have been proposed [5]. The application of the list-mode MLEM Compton cameras [47] results in a significant computational advantage over approaches using binned projection data.

This method, that has been optimized for the Compton probe [23], has given successful results, and will be employed to reconstruct the images from the data taken with the prototype. A brief description of the method is given next.

2.4.1 Derivation of the list-mode MLEM equation

The maximum likelihood approach tries to estimate the source distribution $\vec{\lambda}$ from the measured data $\vec{y}$. A common way of storing the data (for example in PET) is to discretize the measurement space dividing it into small intervals (*bins*), and to record the number of events y_i detected in each bin i. The vector of measurements is then $\vec{y} = y_1, ...y_N$ where N is the total number of bins.

The emission of photons is assumed to follow a Poisson distribution. The probability of observing y_i events in the i^{th} histogram bin is given by

$$y_i \approx Poisson(\bar{y_i}) = \frac{\bar{y_i}^{yi}}{y_i!} e^{-\bar{y_i}}; i = 1.....N;$$

where $\bar{y_i}$ is the mean value of y_i.

The unknown source distribution $\vec{\lambda}$ is discretized by dividing the distribution in *voxels* (volume elements) or *pixels* if a given plane is considered. The relative intensities of photon emission in each pixel, λ_j, are the parameters to be estimated

$$\vec{\lambda} = \lambda_0, ...\lambda_M,$$

where M is the number of pixels in which the image plane is divided.

Assuming the y_i are independent Poisson random variables, the likelihood can be written as [45]

$$L(\vec{\lambda}) = p(\vec{y}|\vec{\lambda}) = \prod_{i=0}^{N} \frac{\bar{y_i}^{yi}}{y_i!} e^{-\bar{y_i}}.$$

The measurements can be modelled as

$$\bar{y_i} = \sum a_{ij} \lambda_j,$$

where the transition probabilities a_{ij} are the elements of the system matrix that represent the probability that a gamma ray emitted from voxel j is detected in measurement bin i. They depend on geometry and response of the detectors, and are assumed to be known in the model. Effects of attenuation, scattering, accidental coincidences, etc. can also be modelled in the system matrix.

The log-likelihood is generally taken to simplify the maximization problem.

$$l(\vec{\lambda}) = ln\ L(\vec{\lambda}) = \sum_{i=0}^{N} (y_i\ ln \bar{y_i} - \bar{y_i} - ln\ y_i!),$$

and the determination of the parameters is done by solving the equation

$$\hat{\vec{\lambda}} = argmax_{\vec{\lambda}>0}\ l(\vec{\lambda})$$

However, solving the problem in the usual way, maximizing with respect to the parameters, might be a complicated task. A possible option is to employ the EM method. In this method, the measured data are regarded as an *incomplete* data set. In order to apply the EM method, the log-likelihood must be formulated in terms of a *complete* (though unobserved) data set. The measured data are thought as being *embedded* in a larger sample space where the problem is easier to solve. The EM postulates a complete data random vector $\vec{x}$ such that the observed data y_i are a function $h(\vec{x})$ of x_i. Furthermore, if $\vec{y}$ has a probability density function $g(\vec{y}, \vec{\lambda})$, $\vec{x}$ is supposed to have a probability density function $f(\vec{x}, \vec{\lambda})$ with respect to some measure $\mu(\vec{x})$, such that $g(\vec{y}, \vec{\lambda})$ can be recovered by integration

$$g(\vec{y}|\vec{\lambda}) = \int f(\vec{x}, \vec{\lambda}) d\mu(\vec{x}).$$

The choice of the appropriate complete data specification is important. Although there can be many possibilities, often physical considerations suggest a natural definition of $\vec{x}$. A natural choice in this case is to consider x_{ij} the number of photons that are emitted from pixel j and detected in element i

$$\bar{y_i} = \sum_j x_{ij}.$$

The log likelihood of the complete data set can then be maximized by a two-step algorithm. In the first step (E-step), the conditional expectation of the complete data set is obtained. Then (M step) it is maximized by obtaining the derivatives with respect to the parameters and finding the values of the parameters that set them to zero. In the following, the vector notation will be omitted.

The likelihood in terms of the complete data takes the form

$$lnf(x,\lambda) = \sum_i \sum_j (-a_{ij}\lambda_j) + x_{ij} ln(a_{ij}\lambda_j) - ln\ x_{ij}!)$$

Taking the conditional expectation of x_{ij} with respect to y_i and the current vector of parameter estimates λ^n yields

$$E(lnf(x,\lambda)|y,\lambda^n) = \sum_i \sum_j (-a_{ij}\lambda_j) + N_{ij} ln(a_{ij}\lambda_j) + R,$$

where R does not depend on the new λ, and

$$N_{ij} = E(x_{ij}|y_i,\lambda^n) = \frac{a_{ij}\lambda_j^n y_i}{\sum_k a_{ik}\lambda_k^n}.$$

In the M-step, the derivatives are taken,

$$\frac{\partial}{\partial \lambda_j} E(lnf(x,\lambda)|y,\lambda^n) = -\sum_i a_{ij} + \sum_i N_{ij}\lambda_j^{-1},$$

and set to zero, and the equation solved. The combination of the two steps yields a fixed point iterative algorithm

$$\lambda_j^{(l+1)} = \frac{\lambda_j^l}{s_j} \sum_i^M \frac{y_i a_{ij}}{\sum_k^N a_{ik}\lambda_k^l},$$

where $s_j = \sum_i^N a_{ij}$ is the probability that a photon emitted from pixel j would be detected anywhere.

A problem that arises from binning the data is that the number of bins increases exponentially with the number of measurement coordinates, increasing also the computational cost and memory requirements of the reconstruction. It may also result in a loss of information, and a high number of empty bins. Under these circumstances, an alternative mode of data storage, known as list-mode, is more adequate. This is the case of the Compton camera, where the total number of detected events is significantly smaller

than the number of bins necessary to store the data, and binning the data is costly and inefficient.

In the list-mode approach, each measured event is considered a point in a continuous measurement space, rather than as a contribution to a position and energy bin, and a list of the M measured events is stored.

The MLEM expression for the list-mode case can be easily obtained by considering that each event is measured in a unique bin, so that $y_i \to 1$ for each detected particle, and $y_i \to 0$ for the infinite number of possible events not detected in the current measurement. The sum is now performed over the M detected events. In this case s_j is no longer the sum over bins, but the integral over all possible events originating in voxel j

$$\lambda_j^{l+1} = \frac{\lambda_j^l}{s_j} \sum_i^M \frac{a_{ij}}{\sum_k^N a_{ik}\lambda_k^l}. \tag{2.7}$$

In [48, 49], the list-mode expression is originally derived for a set of measurements $\vec{A_1}, ..., \vec{A_M}$ where $\vec{A_i}$ represents the vector of measurements (energies and positions) that characterize the i^{th} event, and $a_{ij} = p(\vec{A_i}|\lambda_j)$ is the probability of measuring an event with coordinates A_i originating in pixel j of the source distribution $\vec{\lambda}$.

2.4.2 Calculation of the model parameters

One difficulty in applying the MLEM algorithm to the Compton camera image reconstruction is to determine the parameters that describe the system response. In the previous section, the parameters that characterize the model are assumed to be known. In practice, estimating these parameters to accurately represent the physical model is a complicated task.

For the Compton camera, the transition probabilities a_{ij} will be given by the integral over the pixel volume of the density function $p(\vec{A'}|\vec{x_0})$ describing the probabilities of an emission from the point $\vec{x_0}$ producing an event $\vec{A'}$, convolved with a function $p(\vec{A_i}|\vec{A'})$ describing the measurement process [47].

$$a_{ij} = \int_{\vec{x_0} \subset V_j} d\vec{x_0} p(\vec{x_0}) \int d\vec{A'} p(\vec{A_i}|\vec{A'}) p(\vec{A'}|\vec{x_0})$$

Here $\vec{x_0} \subset V_j$ indicates that the integral is taken over only those $\vec{x_0}$ in the pixel volume V_j and $p(\vec{x_0})d\vec{x_0}$ is the probability that a particle was emitted in $d\vec{x_0}$ at $p(\vec{x_0})$. $p(\vec{A_i}|\vec{A'})$ can be written as

$$p(\vec{A_i}|\vec{A'}) = p(\vec{x_1}|\vec{x_2}')p(\vec{z_1}|\vec{z_2}')p(\vec{E_e}|\vec{E_e'})$$

where $\vec{x_1}$ and $\vec{x_2}$ are the interaction points in the scatter and absorption detectors, and E_e is the energy transferred to the electron in the Compton interaction, and the integral over A' implies an integral over all possible real collision positions and energy transfers which could have resulted in the measurement $\vec{A_i}$.

We also have

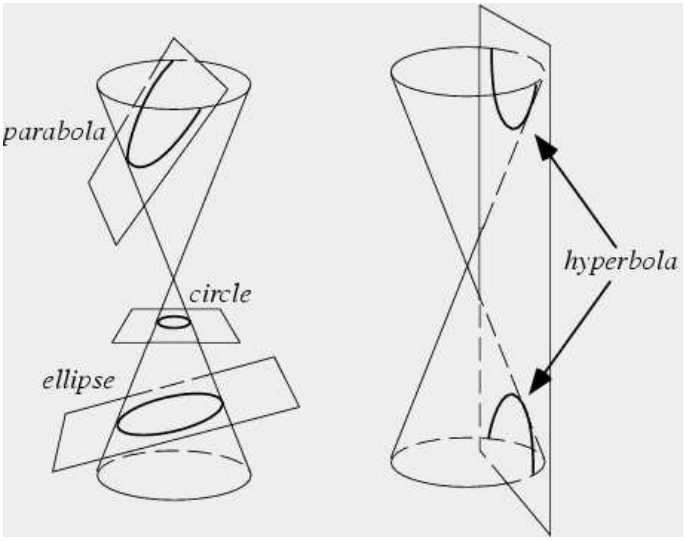

Figure 2.14: *Generation of the conic functions by the intersection of a cone and a plane.*

$$s_j = \int_{\vec{x_0} \subset V_j} d\vec{x_0} p(\vec{x_0}) \int d\vec{A'} p(\vec{A'}|\vec{x_0}),$$

where now the integral over $\vec{A'}$ is the integral over all possible real collisions, independent of the measurements.

A method of estimating the parameters has been developed, yielding good results in the image reconstruction. A first estimation of the image is necessary to initialize the iterative procedure. In [50], a method to compute the initial source distribution λ_0 is developed. The intensities are computed by backprojecting the events into a plane. For each event, the intersection of the reconstructed cone and the image plane is determined. The intersection of a conic surface with the plane $z = z_p$ is given by equation 2.8, where $\vec{n} = (n_x, n_y, n_z)$ is a unit vector in the direction of the cone axis, θ is the scattering angle, and (x_1, y_1, z_1) is the position of the cone vertex, that is, the interaction position in the scatter detector. The solution is a conic function, that can be a circle, an ellipse a parabola or a hyperbola, depending on the relative position of the cone and the plane (fig 2.14). The resulting line represents those points from which photons could have been emitted, and the corresponding pixels in the image plane are then filled. However, the possible emission of photons for a given event is then limited to those pixels intersected by the conic function.

$$[n_x(x - x_1) + n_y(y - y_1) + n_z(z_p - z_1)]^2 = cos^2\theta[(x - x_1)^2 + (y - y_1)^2 + (z_p - z_1)^2] \quad (2.8)$$

To take into account effects of Doppler broadening and energy resolution that broaden the line, neighbour pixels should also be considered. The relative intensities of the pixels that will be filled need to be estimated. This is done by weighting them with a function that depends on the normal distance from the pixel to the conic function, r:

$$f(r) = 0.9\ e^{-\frac{r^2}{2\sigma^2}} + 0.1\ e^{-\frac{r^2}{2(3\sigma)^2}} \quad (2.9)$$

where σ is the standard deviation of the backprojected cone spread function. The cone spread distribution, that is not Gaussian due to the long tails caused by Doppler broadening, can be modelled by adding 0.9 times a gaussian with the computed standard deviation and a 0.1 times a gaussian with three times the standard deviation of the cone spread function. The assumption made that the standard deviation is constant for all energies is valid in the range of energies employed in Compton detectors.

If this procedure is repeated for all measured events, an initial distribution in the image plane is obtained that, in spite of its bad resolution, serves as starting point for the iterations.

The parameters of the system matrix a_{ij} (the probability that a measurement i is due to a photon originating in pixel j) and the sensitivities s_j (the probability that a gamma ray emitted from pixel j is detected anywhere) also need to be determined. Straightforward computation requires numerical integration of the probabilities and density functions describing the interaction and measurement of the two interaction positions and the scattering energy over the areas of the pixels j, the entire first detector and the entire second detector. The procedure is complicated, since it requires detailed knowledge of all system components, and computationally demanding. Instead, a simpler approach has been proposed, yielding good results [51].

In the relative spatial variation of the sensitivities, two effects are assumed to dominate, the solid angle subtended by the scatter detector, and the probability of interaction inside the detector. The absorption detector is supposed to absorb photons scattered in any angle. The sensitivity for a given pixel j can then be calculated from the integration over all rays originating in the pixel and incident on the first detector of the probability that a photon is emitted multiplied by the probability of interaction in the first detector. If the sensitivity in each pixel is assumed to be uniform, since they are small, it can be computed as a sum over the D_1 elements in the scatter detector

$$sj \propto \sum_{k}^{D1} \frac{cos\theta[1 - e^{-\sigma_t z_{jk}}]}{d_{jk}^2}.$$

In this equation, σ_t is the total cross section in the scatter detector, z_{jk} is the path length inside the first detector along the way from the center of pixel j to the center of each detector element k, d_{jk} the distance between the centers, and θ the azimuthal angle measured relative to the centers.

The calculation of the a_{ij} is done only for the pixels intersected in each event. Since the MLEM equation (eq 2.7) is independent of the normalization, only the relative values need to be calculated. This is computed as the product of two factors. The first one takes into account the relative probabilities between the measurements, and the second accounts for the probabilities within the measurements, i.e., the relative probability that the gamma giving rise to measurement i was emitted from pixel j.

The first factor is dominated by the relative differential cross section and the escape probability of the scattered photon in the first detector

$$f(i) \propto e^{(-\sigma_t)z_{12}} \frac{d\sigma_c}{d\Omega},$$

where σ_t is the total cross section in the scatter detector at the scattered photon energy, z_{12} the distance travelled through the first detector along the ray between the first and second collisions, and $\frac{d\sigma_c}{d\Omega}$ the differential Compton cross section, approximated as the Klein-Nisina cross section at the given energy, divided by the square of the distance between the two collisions.

The second factor includes the pixel sensitivities s_j, as well as the resolution loss brought on by Doppler broadening and the energy resolution effect, given by equation 2.9.

The method has been employed for image reconstruction of simulated data and measured data of a previous Compton prototype, and will also be employed in this case. 3D image reconstruction in Compton cameras has been studied [52]. However, image reconstruction in this work will be limited to a plane.

2.5 Main developments in Compton Imaging

Compton imaging of gamma rays is being developed both for medical imaging and astronomy[2], where it is employed in Compton telescopes for medium gamma ray energies. Although some differences exist, mainly due to the smaller energy range in medical imaging and the fact that the energy of the source is known, the same principle is applied. Therefore, research overlaps in many aspects, and it can profit from the advances in the other field.

The development of Compton telescopes occurred earlier. The idea, proposed in 1966 [53] and 1968 [54] for imaging solar neutrinos, was in the 1970's considered for gamma-ray imaging. The work culminated with the development of COMPTEL [55], the first Compton telescope, on board of the Compton Gamma Ray Observatory (CGRO). It consisted of two scintillator detector planes, a liquid scintillator scatter detector, and a NaI absorption detector. The imaging principle is similar to the one employed in medical imaging, and the intersection of the Compton cones gives the position of the gamma-ray source. Due to the higher energies of the photons, pair production also needs to be taken into account.

Silicon detectors have been proposed and used for Compton detectors. A second generation of Compton telescopes (MEGA [56, 57], TIGRE [58, 59]) is under development with the main goal of improving the sensitivity. They utilize arrays of thin position-sensitive silicon detectors as the Compton scatterer. CsI is employed in MEGA as absorption detector. In TIGRE, with a similar original design, arrays of Ge or CZT pixel detectors have been incorporated to improve the performance.

Given the high energy of the incoming gamma-ray, the scattered electron (or the e^+e^- pair created) can traverse several layers of silicon detectors. The key advantage of these telescopes is their ability to track the electron through the silicon and obtain its trajectory for gamma energies higher than 1-2 MeV (below, it is limited by multiple scattering). The direction of the gamma ray can then be restricted to a small segment of the Compton cone, reducing the background and improving the efficiency.

[2]Compton cameras have also been developed for industrial purposes, but this overview will be limited to their employ in physics.

Other types of detectors have also been considered for Compton telescopes, as it is the case of XENA [60]. A liquid xenon time projection chamber allows to determine the depth of interaction [61,62]. The advantages are excellent 3D position reconstruction, moderate efficiency, and the ability to reconstruct the events to reduce internal background. The key issues in this case are Doppler broadening, interaction energy threshold and relatively poor energy resolution, that may be improved in gas detectors.

Advanced Compton telescopes, based on Si, Ge, CZT and CdTe have been proposed, and prototype development is ongoing in several groups [63,64].

The idea of considering multiple Compton interactions [65] has lead to a new concept of image reconstruction. Several interactions in each event allow to determine the source position with or without the scattered gamma being fully absorbed. This concept allows to improve both the efficiency and the position resolution with respect to previous designs.

Multi-Compton gamma-ray telescope prototypes are being developed. The possibility of reconstructing the event without the gamma being fully absorbed means that high Z materials are not required. The telescope can be entirely constructed with a single detector material. The performance of an instrument using this approach is very dependent on the energy and position resolution achieved. Ge, Si and CZT strip or pixel detectors or possibly high purity gas detectors are good candidates.

One of the approaches [66] consists of a semiconductor Compton telescope based on silicon and cadmium telluride. A stack of double-sided silicon strip detectors is used to record the Compton scatterings. Additional layers of a heavy semiconductor CdTe or CZT are used to absorb the scattered photons. The number of Si and CdTe layers and their ratio should be chosen depending on the energy of interest. The order of the interaction sequences can be reconstructed by examination of the energy-momentum conservation for all possible sequences. A first prototype has been built employing one double-sided strip detector combined with two CdTe pixel detectors.

Other options include telescopes with only one detector material. The three-Compton technique without total absorption requires at least three interactions, the first two being Compton scattering [67]. In addition, a correct ordering of the events is necessary, that can be deduced from the observed energies and positions. The results of ordering algorithms are good for high energies, but less than 65% of the sequences are correctly identified at energies lower than 414 keV, and less than 50% at 185 keV. Prototypes consisting of multilayer detectors with a single detector type have also been developed, both with germanium and silicon detectors 2 mm thick.

The application of the Compton technique to medical imaging was first suggested in 1974 [68], and a possible design for a Compton detector was proposed, with a semiconductor detector as scatter detector based on their *energy resolution, response time and transmission properties.*

The idea was reviewed later, but it was in 1983 when the first Compton detector for medical imaging was built [42,69], showing that photons could be electronically collimated. This prototype used a germanium detector due to its higher Compton cross section compared to silicon, and a scintillator detector. Image reconstruction methods and optimized designs for the scatter detector were also proposed and studied. In a later revision, images of ^{99m}Tc and ^{137}Cs point sources were obtained, with a spatial resolution about 0.7 cm for the ^{99m}Tc source at 4.3 cm from the source, and about 0.5 cm for the ^{137}Cs

source placed 2.6 cm away. The sensitivity was 77 cps when a 78.5 MBq point source was placed 5.9 cm away. A new prototype was built in 1985 with a 4×4 germanium detector array as scatter detector, and in 1990, images of three-dimensional cylindrical phantoms were obtained [70]. Conventional SPECT data were also acquired with the Camera scintillator and a collimator. For a similar spatial resolution, the Compton camera showed sensitivities about an order of magnitude higher for ^{99m}Tc.

The use of Germanium has an important disadvantage: cryogenic cooling is required to achieve good energy resolution. Other materials, have been considered for the scatter detector. The possibility of employing gaseous detectors was already mentioned in the first paper. They provide a higher spatial resolution and a larger field of view, but Doppler broadening is large, and they have the disadvantage of a poorer energy resolution. A Compton prototype was constructed with high pressure xenon drift chamber [71]. In this case, the gas detector acts both as scatter and absorption detector. A spatial resolution of 25 mm FWHM for a ^{99m}Tc point source at 10.5 cm was obtained. The sensitivity is low, and it can only be improved by increasing the gas pressure.

Silicon was again considered in 1988 [72] and a feasibility study was carried out in 1997 to test silicon microstrip detectors as scatter detector. The design, based on the TIGRE telescope, consisted of a stack of double-sided silicon strip detectors and three CsI(Tl) scintillator detectors as absorption detector. The results with a ^{22}Na point source at 10.5 cm distance was 1.5 cm spatial resolution.

In 1998, a prototype was built at the University of Michigan, with a 300 μm thick silicon pad sensor as scatter detector, and a 50 cm diameter ring consisting of 11 NaI(Tl) scintillator modules as absorption detector [73, 74]. Two point sources were tested, obtaining a spatial resolution of 8.2 mm FWHM for ^{99m}Tc and 6.5 mm FWHM for ^{131}I, both at 11 cm from the scatter detector. The sensitivities were 1.8×10^{-7} and 1.2×10^{-6} respectively. Images of point sources superimposed on a uniform disk were also reconstructed, yielding 11.7 mm FWHM spatial resolution for a ^{99m}Tc source.

Research in both fields is currently carried out with the aim of improving the scatter detector. In astronomy, thick silicon, germanium and CZT detectors are being considered for the multi-Compton event detectors. Double-sided silicon strip sensors with an active area of 57 mm × 57 mm and 2 mm thickness have been developed [75]. The energy resolution is 3-4 keV at room temperature for 60 keV gamma rays, and 2.1 keV at -20°C.

Silicon has proven to be the optimum choice for medical imaging, where lower energies are imaged. Different options are being tested for the scatter detector. Silicon drift detectors with low energy resolution have been developed and a Compton prototype has been built [76].

The idea of employing multiple layers is also being considered in medical imaging with the main purpose of enhancing the efficiency. The following chapters will explain the development and results of a multi-layer Compton prototype for medical imaging, with thick silicon pad sensors as scatter detector.

Chapter 3

Silicon detectors

Since silicon detectors will be employed as scatter detector, that is the main element of the Compton detector, a brief overview of the main characteristics of these detectors is given in this chapter.

3.1 Properties of semiconductor materials

Semiconductor materials differ from insulators in the value of the energy gap, E_g, between the conduction and the valence band, that in the case of semiconductors is lower than 5 eV [77, 78]. At 0 K all electrons are in the valence band, participating in the covalent bonding between the lattice atoms, and the conductivity of the material is nonexistent. Due to the small value of the energy gap, at nonzero temperatures the electrons in the valence band can acquire sufficient energy to reach the conduction band. The missing electron in the valence band is known as *hole*, and contributes to the conductivity as a positive charge. The conductivity in these materials is thus due to both types of carriers and it can be expressed as

$$\sigma = q_e(n\mu_e + p\mu_h),$$

where q_e is the electron charge ($q_e = 1.6 \times 10^{-19}$ C), μ_e and μ_h are the mobilities of electrons and holes respectively (for silicon at 300 K $\mu_e = 1350\ cm^2/Vs$ and $\mu_h = 480\ cm^2/Vs$), and n and p are their concentrations. The resistivity of the material is the inverse of the conductivity,

$$\rho = \frac{1}{\sigma} = \frac{1}{e(n\mu_e + p\mu_h)},$$

and is equal to 235 $k\Omega\ cm$ for pure silicon at room temperature.

The generation and recombination of electron-hole pairs is produced in an equilibrium situation. In a pure or intrinsic semiconductor material, the concentration of electrons and holes is the same, and it is given by

$$n = p = n_i = \sqrt{N_c N_v} e^{\frac{-E_g}{2kT}} = AT^{\frac{3}{2}} e^{\frac{-E_g}{2kT}},$$

where N_c and N_v are effective densities of states at the conduction and valence band respectively, k is the Boltzman constant, T is the temperature and $E_g = 1.1$ eV. The concentration of electrons or holes is equal to 1.45×10^{10} cm^{-3} at room temperature. This low number of carriers results in a low conductivity for intrinsic silicon.

The number of free charges can be enhanced by *doping* the material, introducing a small amount of impurities. Atoms from the III group with one electron less, like boron, are known as acceptor impurities, and they introduce an energy level close to the valence band. Atoms from group V like phosphorous or arsenic (donor impurities), have one electron more and they introduce an energy level close to the conduction band.

These impurities are integrated in the lattice, creating an excess of electrons or holes, which are known as *majority carriers*. The semiconductor is then known as extrinsic.

Depending on the type of impurities that have been implanted, the doped silicon can be of n-type, with donor impurities, or p-type, with acceptor impurities. If the level of doping is very high, it is denoted n^+ or p^+ type.

3.2 The PN junction

A PN junction is created by implanting a large number of impurities of one type on the surface of a silicon wafer of the other type, changing by this the sign to the doping in a region, and creating regions with opposite doping type that are in contact [79]. The electrons are then free in the n-type, and the holes in the p-type, and both types of carriers diffuse. If they reach the other side of the junction, they recombine with the free charges of the opposite sign. This process leaves behind a net possitive charge on the n side, and a net negative charge on the p side that generate an electric field which is opposed to the diffusion process. The diffusion continues until the electric field is strong enough to balance it, creating a stable state in which a thin layer at the p-n boundary is left without free carriers. The layer is called *depletion region*. If charge is deposited in the depletion layer by a passing particle or a photon, the built-in potential will make the charges drift outside the depletion region, creating an induced electric signal. The junction will act as a detector, but with a very poor performance.

If an external voltage is applied, the p-n junction will show interesting applications as a diode. When positive voltage is applied to the p side of the junction with respect to the n side (forward biasing), the potential will attract both electrons from the n side and holes from the p side across the junction, and the conductivity will be greatly enhanced for small values of the voltage.

If the junction is reverse biased, the natural potential difference is enhanced and it is the minority carriers that are attracted accross the junction. Given that their concentration is relatively low, the reverse current across the diode is quite small. The reverse biased junction can act as a detector, and its properties will be described next.

The depleted region grows with the potential applied, following the relationship

$$V = \frac{q_e}{2\epsilon}(N_a W_a^2 + N_d W_d^2), \tag{3.1}$$

where $\epsilon = \varepsilon_r \varepsilon_0$ is the dielectric constant, N_a and N_d are the concentrations of acceptor and donor impurities and W_a and W_d represent the width of the depletion layer on the

respective side of the junction, being d= W_a+W_d the total depletion layer.

If the doping level on one side of the junction is much higher than on the other side, the depleted region will extend almost entirely on the side with the lowest doping level, and its width is approximately given by

$$d \approx \sqrt{\frac{2q_eV}{\epsilon N}}. \tag{3.2}$$

The depletion layer can be extended up to the full thickness of the silicon detector, that is then *fully depleted*. The previous equation can also be written as a function of the resistivity of the doped semiconductor, ρ_d, as

$$d \approx \sqrt{2\epsilon V \mu \rho_d}. \tag{3.3}$$

One would like the largest depletion width possible for a given depletion voltage, and for that the resistivity should be as high as possible. The resistivity is limited by the purity of the semiconductor material before the doping process. Thick sensors need higher voltages to achieve full depletion, and this can result in a practical limit for the detector thickness, since the high voltages necessary for their correct operation can produce excessively high electric fields.

Because of the fixed charges that are built up on either side of the junction, the depletion region exhibits some properties of a charged capacitor. When the reverse bias voltage is increased, the depletion region grows thicker and the capacitance represented by the separated charges decreases. The value of the capacitance per unit area is

$$C = \frac{\epsilon}{d} \approx \sqrt{\frac{q_e \epsilon N}{2V}}. \tag{3.4}$$

The capacitance decreases until the detector is fully depleted, and then it remains constant. Therefore, it is possible to deduce the depletion voltage by measuring the capacitance versus the voltage applied.

When reverse bias is applied to the junction, a small current is normally observed. The origins of this *leakage current* are related both to the bulk volume and surface of the detector [78]. There are two sources of bulk leakage current. One is due to the minority carriers, that are generated continuously on both sides of the junction, and are free to diffuse. In most cases, the minority carrier current is small and is seldom an important leakage current source. A second source of bulk leakage current is the thermal generation of electron-hole pairs within the depletion region. This rate will increase with the volume of the depletion region, and it can only be reduced by cooling the material. Silicon detectors of the usual dimensions (300 μm thick) have a sufficiently low thermally generated current to allow their use at room temperature, while germanium detectors, because of the lower energy gap, must be always operated at reduced temperatures.

For a fully depleted detector, the diffusion current is negligible, and the main contribution is given by the generation current

$$Jg = q_e g d \propto q_e g \sqrt{V},$$

where g is the generation-recombination rate and d is the thickness of the depletion layer, which is in turn proportional to the square root of the bias voltage. The value of the current grows with the detector thickness since the depleted volume in which the current can be generated is bigger. The dependence of the generation current with the temperature is approximately given by

$$I_g \approx e^{\frac{-Eg}{2KT}}.$$

Therefore, if the leakage current is measured at temperature T_0, the increase of the leakage current for an increase of the temperature is given by

$$I_g(T) = I_g(T_0)\left(\frac{T}{T_0}\right)^2 e^{\frac{-Eg}{2}\left(\frac{1}{KT}-\frac{1}{KT_0}\right)}. \tag{3.5}$$

Surface leakage current effects take place at the edges of the junction where relatively large voltage gradients must be supported over small distances. Their main source are the ionic charges on and outside the semiconductor surface which affect the electric field distribution close to the surface. They strongly depend on the technology and the geometry of the detector. To limit the surface currents, protecting guard rings are added to the detectors.

3.3 Operation of silicon detectors

A silicon detector is based on the properties of a PN junction. Detectors can be fabricated on both p-type and n-type substrate, being the n-type the most widely used. Several fabrication techniques exist. Ion-implantation is commonly employed nowadays. Detectors are fabricated following the planar process. Boron ions are implanted on the detector to create the p^+ contacts, that are separated from each other and act as independent detectors following a detemined geometry.

In pad and pixel detectors, a matrix of small diodes is produced, and one can obtain two-dimensional information of the particle's crossing point. Phosphorous or arsenic atoms are implanted on the back of the detector, where high positive voltage is applied, to create a n^+ layer. Silicon micro-strip detectors are segmented in long, narrow elements that provide a measurement of one coordinate with high precision. Segmentation of the backplane is also possible to create double sided strip detectors that also provide a second coordinate.

The resolution is determined by the ability of segmenting the detector, that can be of a few microns. It is limited by the diffusion of the charges to a size of $\approx 1\ \mu m$ rms. Resolutions of 2-3 μm can be achieved.

A metal layer on top of the pads is necessary to connect the readout electronics that will collect the signal. In DC coupled detectors, the readout electronics are connected directly to the pads. DC coupling has the advantage of minimizing the magnitude of the electric fields on the silicon surface. However, it has the disadvantage of allowing the flow of the leakage current to the preamplifier. This can be compensated by designing a current source in the readout electronics that provides a current of the same magnitude flowing in the opposite direction. Another possibility is AC coupling, in which the readout goes

through a decoupling capacitor, that must be much larger than the capacitance to the neighbours (typically over 1000 pF) to ensure good signal collection. A widely employed solution consists of integrating a capacitor directly on the detector by implanting a SiO_2 layer that acts as a dielectric between the p^+ implants and the metal layers.

3.3.1 Pulse formation

When energy is deposited by a particle in a silicon detector, electron-hole pairs are produced within a few picoseconds. The electric field present through the active volume makes them drift in opposite directions. The motion of either electrons or holes constitutes a current that will persist until those carriers are collected at the boundaries of the active volume [14]. The necessary energy to create an electron-hole pair, known as *ionization energy* ($\eta = 3.6\ eV$), is largely independent of the energy and type of the incident radiation. The energy deposited is proportional to the energy carried by the particle.

Silicon detectors are operated in *pulse mode*: the total charge Q is recorded, since the energy deposited in the detector is directly related to Q. This operation mode provides information on the amplitude and timing of individual events.

Silicon detectors rely on complete integration of the currents due to both electron and holes, and both types must be fully collected to be a faithful measure of the energy deposited by the particle. The charge collection times are not likely the same for electrons and holes because of differences in drift distance and carrier mobilities, and therefore one of the currents will persist for a longer time than the other.

For bias voltages V higher than the full depletion voltage V_{fd}, the maximum charge collection times can be expressed as [80]

$$t_{max}^{e,h} = \frac{d}{v_{e,h}} ln(1 + \frac{E_{max} d}{V_{od}}),$$

where $v_{e,h}$ is the drift velocity of electrons and holes, d is the detector thickness, V_{od} is the amount of over depletion and E_{max} is the maximum field at depletion, given by

$$E_{max} = \frac{2V}{d}.$$

For a well depleted $300\mu m$ thick sensor (V_{fd}=60 V, V_{od}=30 V), typical values of collection times are 8 ns for electrons and 25 ns for holes. If thick sensors are employed, the distance travelled by the carriers is bigger, and the time is increased. For a 1 mm thick sensor with V_{fd}=140 V, the previous equation yields maximum collection times around 50 ns for electrons and 150 ns for holes. The timing properties of the detectors are degraded if thickness is increased, adding up to the list of reasons limiting the operational thickness of the detectors.

The collected charge as a function of time can be expressed as

$$q(t) = \frac{Q}{2}\left(\left(1 + \frac{V_{od}}{E_{max} d}\right)^2 \left(1 - exp(-\frac{\mu_e E_{max} t}{d})\right) + \left(\frac{V_{od}}{E_{max} d}\right)^2 exp(-\frac{\mu_e E_{max} t}{d})\right) +$$

$$\frac{Q}{2}\left(\left(1 + \frac{V_{od}}{E_{max} d}\right)^2 \left(1 - exp(-\frac{\mu_h E_{max} t}{d})\right) + \left(\frac{V_{od}}{E_{max} d}\right)^2 exp(-\frac{\mu_h E_{max} t}{d})\right).$$

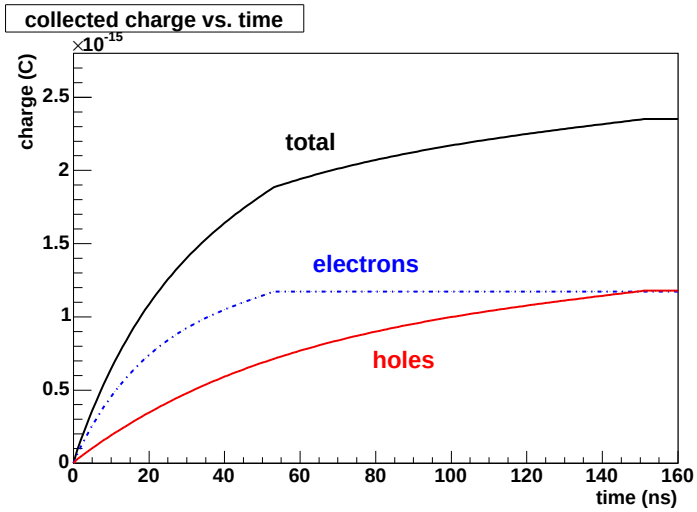

Figure 3.1: *Collected charge as a function of time for a 1 mm thick sensor with V_{od}=30V*

Figure 3.1 illustrates the collected charge as a function of time for a 1 mm thick sensor and $V_{od} = 30V$, for a 45 keV photon. The electron charge remains constant after t^e_{max}, and the hole charge after t^h_{max}, corresponding to a distance d equal to the detector thickness.

The amount of charge deposited is small, and therefore the first element of the readout chain must be a preamplifier to enhance the signal [14]. The preamplifier provides a voltage signal that is proportional to the charge deposited. Preamplifiers can be either *voltage sensitive* or *charge sensitive*. Silicon detectors typically employ charge sensitive preamplifiers to avoid the effects on the output voltage produced by variations in the capacitance with the operating parameters, and to ensure its proportionality to the input charge. In a charge sensitive preamplifier (fig 3.2), the charge is integrated on a feedback capacitor C_f. The output voltage V_{out} is proportional to the total integrated charge in the pulse provided to the input terminals, as long as the duration of the input pulse is short compared with the time constant $R_f C_f$. For an ideal amplifier, it can be written as

$$V_{out} = -\frac{1}{C_f}\int_0^t I_{in}(t)\ dt = -\frac{Q(t)}{C_f}.$$

The output voltage is therefore proportional to the total integrated charge in the pulse provided to the input terminals, as long as the duration of the input pulse is short compared with the time constant $R_f C_f$.

In order to ensure that complete charge collection occurs, preamplifiers are normally adjusted to provide a decay time for the pulse that is quite long (typically 50 μs). If the rate of interaction in the detector is not small, these pulses will tend to overlap one another. Since it is the amplitude that carries the information of the charge deposited in the detector, the *pile up* of pulses that are superimposed on a different residual tail of the previous pulse is no longer a good measure of the event energy.

The ideal solution is to *shape* the pulses in order to eliminate the long tails while preserving the the information carried by the maximum amplitude. CR-RC pulse shaping is the most widespread technique and is performed by sending the signal first through a

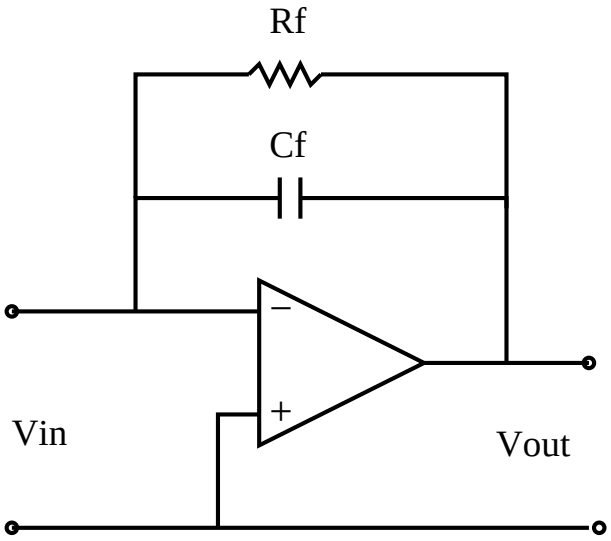

Figure 3.2: *Block diagram of a charge sensitive preamplifier with resistive feedback.*

CR differentiator, where it is filtered at low frequencies, and then through a RC integrator, being filtered at high frequencies, resulting in a improvement in signal-to-noise. One of the undesirable side effects of RC pulse shaping is the presence of an undershoot in the shaped pulse, that returns only very slowly to the baseline. A possible improvement is obtained by adding several RC integration steps, to give the pulse a shape close to a gaussian function (semigaussian). The disadvantage is that the pulses are wider and can more likely run into overlap problems at high counting rates.

The rise time of the pulse in the preamplifier normally corresponds to the charge collection time in the detector itself. If the full amplitude of the preamplifier pulse is to be preserved through the shaping process, the shaping time constants must be large compared to the preamplifier pulse rise time. Because the shaping time constants cannot always be chosen as arbitrarily large, the amplitude of the shaped pulse can sometimes be slightly less than that attainable with very long time constants. The degree to which the infinite time constant amplitude has been decreased by the shaping process is called the *ballistic deficit.*

3.3.2 Energy resolution

The energy resolution of a detector is affected by the intrinsic energy resolution and the noise. The good energy resolution of semiconductor detectors is mainly due to the low value of the ionization energy, typically 3 eV compared to the 30 eV for gas detectors. This results in an increased number of charge carriers for a given amount of energy deposited, and therefore the statistical fluctuations in the number of carriers per pulse become less significant. In addition, a better signal to noise ratio can be achieved.

The statistical fluctuations set a fundamental limit on the energy resolution that can be achieved. In the simplest model, the formation of each electron-hole pair will be considered a Poisson process, and the variation of the number of pairs formed should be given by a standard deviation equal to the square root of the average number formed,

$\sqrt{E/\eta}$.

However, the observed statistical fluctuations are smaller than the predicted value, and the Fano factor is introduced as an empirical constant by which the predicted variance must be multiplied to to give the experimentally observed variance.

$$F \equiv \frac{observed\ statistical\ variance}{E/\eta}.$$

The contribution of the statistical fluctuations to the broadening of the peak in the energy spectrum can be expressed in terms of the equivalent noise charge (ENC), that is defined as the amount of charge that, if applied to the input terminals of the system, would give rise to an output voltage equal to the RMS level of the output due only to noise. It is usual to express this value in units of electron charges, dividing it by the unit charge of an electron. To convert to energy units one must also multiply by the the deposited energy required to generate an electron-hole pair in the detector.

The intrinsic resolution of the silicon sensor is given by

$$ENC_{int} = \sqrt{F\frac{E}{\eta}}. \tag{3.6}$$

The intrinsic resolution combines in quadrature with other sources of peak broadening, like the noise of the system. Noise is an undesired fluctuation that appears superimposed on a signal source. The important sources of noise occur at the beginning of the signal formation chain, where the signal level is at its minimum, and noise undergoes the same amplification as the signal.

The contributions to the noise can be obtained considering n carriers of charge e moving with velocity v through a sample of length l bounded by two electrodes [81]. The induced current i at the ends of the sample is

$$i = \frac{nev}{l}.$$

The fluctuation of this current is given by the total differential

$$< d_i^2 >= (\frac{ne}{l} < d_v >)^2 + (\frac{ev}{l} < dn >)^2,$$

where the two terms add in quadrature, since they are statistically uncorrelated. From this equation it can be seen that the two mechanisms contributing to the noise are velocity and number fluctuations. Velocity fluctuations are due to thermal motion, and originate the *thermal* or *Johnson* noise. They are random fluctuations due to thermal excitations, superimposed on the average drift velocity. The most common example of noise due to velocity fluctuations is the noise of resistors. The noise due to number fluctuations is known as *shot* noise. It occurs whenever carriers are injected into a sample volume independently of one another.

The noise contribution is given by the spectral density, that is the power per unit bandwidth. Both thermal and shot noise have a 'white' frequency distribution, i.e., the spectral power densities do not depend on the frequency f.

In the case of the thermal noise, the spectral density is given by

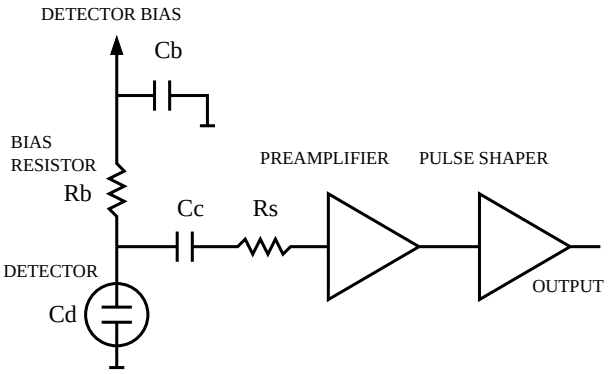

Figure 3.3: *Detector front-end circuit diagram.*

$$\frac{dP_n}{df} = 4kT.$$

where k is the Boltzmann constant, and T is the temperature.

Since $P = V^2/R = I^2R$, the spectral noise density can be expressed as a spectral voltage noise density,

$$\frac{dV_n^2}{df} \equiv e_n^2 = 4kTR,$$

or as a spectral current noise density

$$\frac{dI_n^2}{df} \equiv i_n^2 = \frac{4kT}{R}.$$

The spectral noise density of shot noise is proportional to the average current I,

$$i_n^2 = 2q_eI.$$

Trapping and detrapping processes in resistors, dielectrics and semiconductors can introduce additional fluctuations whose noise power frequently exhibits a $1/f$ spectrum. The spectral density of the $1/f$ noise voltage is

$$e_{nf}^2 = \frac{A_f}{f},$$

where the noise coefficient A_f is device specific and of order 10^{-10}-10^{-12} V^2.

The total noise is obtained by integrating over the relevant frequency range of the system, the bandwidth, and individual noise contributions are added in quadrature.

The noise contributions in a detector can be determined from the analysis of the front-end circuit. A schematic diagram is shown in fig 3.3, where the detector is represented by a capacitor C_d, bias voltage is applied through a bias resistor R_b, and the signal is coupled to the preamplifier through a blocking capacitor C_c. The series resistance R_S represents the sum of all resistances present in the input signal path.

For the noise analysis, the different elements can be represented either as voltage or current noise sources. The leakage current of a detector fluctuates due to electron emission

statistics. This shot noise is represented by a current noise generator in parallel with the detector.

Resistors exhibit noise due to thermal velocity fluctuations of charge carriers. This noise sources can be modelled either as a current or voltage generator. Generally, resistors in parallel with the preamplifier input act as noise current sources, and resistors in series with the input act as noise voltage sources (hence the common expressions of series and parallel noise).

Since radiation detectors typically convert the deposited energy into charge, the system's noise level is conveniently expressed as an equivalent noise charge.

$$Q_n^2 = i_n^2 F_i T_s + e_n^2 F_v \frac{C^2}{T_s} + F_{vf} A_f C^2, \tag{3.7}$$

where C is the total parallel capacitance at the input including C_d, all stray capacitances and the amplifier's input capacitance. F_i, F_v and F_{vf} depend on the shape of the pulse determined by the shaper, and T_s is a characteristic time, for example the shaping time τ.

The first term combines all noise current sources, and increases with shaping time. The second term combines all noise voltage sources and decreases with shaping time, but increases with capacitance. The third term is the contribution of excess $(1/f)$ noise, which is independent of shaping time, but also increases with the capacitance.

Capacitance and shaping time are therefore fundamental parameters determining the electronics noise. At short shaping times, the voltage noise dominates, whereas at long shaping times, the current noise takes over. Minimum noise is obtained when these two contributions are equal. In addition, the different factors depend on the temperature, that also contributes to increase the noise.

For the circuit previously considered, equation 3.7 can be written as

$$Q_n^2 = \left(2q_e I_d + \frac{4kT}{R_b} + i_{na}^2\right) \times F_i \tau + \left(4kT R_s + e_{na}^2\right) \times \frac{C}{\tau} + 4A_f C^2. \tag{3.8}$$

where the contributions to the current noise come from the detector leakage current and resistors in parallel as the bias resistor, while resistors in series, like the resistance of the microstrips in a microstrip detector, contribute to the voltage noise. A pulse shaper formed by a single differentiator and integrator with equal time constants has $F_i = F_v = 0.9$ and $F_{vf} = 4$, independent of the shaping time constant. Increasing the pulse symmetry tends to decrease F_i and increase $F_v = 0.9$, e.g. to $F_i = 0.45$ and $F_v = 1.0$ for a shaper with one CR differentiator and four cascaded RC integrators.

The electronics noise of the preamplifier is described by a combination of voltage and current sources at its input, i_{na} and e_{na}. In a FET amplifier the noise current contribution i_{na} is negligible, and the contribution to the noise is given by

$$ENC_{FET} = \frac{e}{q_e}\sqrt{\frac{4kT2\Gamma}{3g_m\tau}}(Ci + Cd),$$

where e=2.718, Γ is the excess noise factor, g_m is the transconductance, C_i is the input capacitance of the amplifier and C_d is the detector capacitance.

Noise can therefore improved by reducing the detector capacitance and leakage current, judiciously selecting all resistances in the input circuit and choosing the optimum shaping time constant.

3.3.3 Timing

Information on the precise arrival time of the particle is also of particular interest. The accuracy of timing performance depends both on the properties of the specific detector and the type of electronics used to process the signal. The best timing performance is obtained for those detectors in which the signal charge is collected most rapidly. For detectors with equal charge collection time, those that generate the greatest number of carriers per pulse will show superior timing properties [14].

The timing characteristics of a given system depend greatly on the dynamic range (ratio of maximum to minimum pulse height) of the signal pulses. If signal pulses must cover a wide range of amplitudes, timing accuracy is more complicated to achieve.

The most fundamental operation in timing measurements is the generation of a logic pulse whose leading edge indicates the time of occurrence of an input linear pulse. Electronic devices that carry out this function are known as *triggers*. Factors that lead to some degree of uncertainty in deriving the timing signal are always present. Sources of timing inaccuracy are divided into two categories. Those that apply when the input pulse amplitude is constant are called sources of *time jitter*, whereas those effects that derive primarily from the variable amplitudes of input pulses are usually known as *amplitude walk*.

An important source of time jitter is the random fluctuations in the signal pulse size and shape. These fluctuations can arise from several sources. One is the electronic noise added by components that process the linear pulse prior to the trigger time. Another one is due to the statistical fluctuations in the number of carriers that make up the signal, that are reflected in the size and shape fluctuations of the pulse. This effect is greater for small amplitude pulses, when the number of carriers is low so the statistical fluctuations are bigger.

The easiest and most direct triggering method is to determine the time when the pulse crosses a fixed discrimination level. Such *leading edge* timing methods are common, and can be quite effective, especially in situations in which the dynamic range of the input pulses is not large. However, differences on the amplitude or rise time of the pulses can lead to differences in the triggering time (known as *amplitude walk* and *rise time walk* respectively) for pulses with identical time of occurrence, as illustrated in fig 3.4.

Another method, known as *crossover timing*, can greatly reduce the magnitude of amplitude walk, but requires the pulse to have bipolar shape. In that case, in spite of the difference in amplitude, the time at which the waveform crosses from the positive to the negative side of the axis is theoretically independent of the amplitude. Compared with leading edge timing, the amplitude walk is reduced, but at the expense of increased jitter.

A third method known as *constant fraction* timing produces an output signal a fixed time after the leading edge of the pulse has reached a constant fraction of the peak pulse amplitude. This point is independent of pulse amplitude for all pulses of constant shape, reducing the amplitude walk, but with lower jitter than crossover timing.

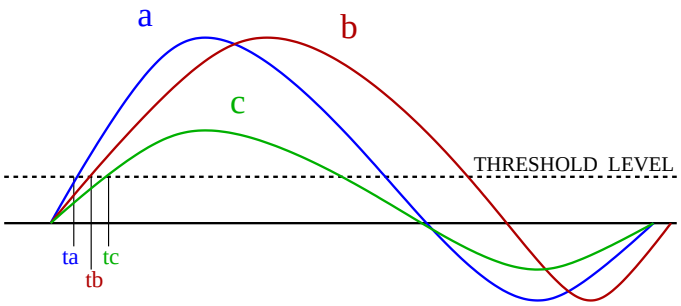

Figure 3.4: *Differences in triggering time with leading edge triggering for three pulses with identical time of occurrence. Pulses a and b have similar amplitude, but different triggering time due to rise time walk. Pulses a and c have the same rise time but different triggering time due to amplitude walk.*

Chapter 4

Compton prostate probe

This chapter is intended to give an overview of the motivations for the development of the Compton prostate probe, and to situate it in a medical imaging context. The development of a Compton probe responds to a necessity of improving prostate imaging for early diagnosis and follow-up of the disease after treatment. Simulations have been carried out to estimate the performance of the Compton probe and its possible improvement over existing devices. Section 4.1 explains the current state of prostate imaging, its problems and limitations. In section 4.2, the results of the simulations conducted to estimate the performance of the prostate probe are summarized. The information and the figures have been obtained from [23].

4.1 Compton probe for prostate imaging

An adequate imaging tool for cancer diagnosis and staging[1] must fulfil the following requirements [82]:

- Detect or confirm the presence of a tumour.
- Provide information about the size or location of the tumour and whether it has spread.
- Guide a biopsy.
- Help plan the therapy (radiation, surgery...).
- Determine whether the cancer is responding to treatment.

Nuclear imaging has become an important diagnostic imaging tool for initial staging of cancer, detection of metastases, evaluation of therapy response and differentiation of post therapy changes from residual or recurrent tumour. Even determination of tumour grade is possible, based on metabolic uptake levels. Its ability to detect cancer is based

[1] Cancer is described both by *grade* and *stage*. Grade describes how closely the tumour resembles normal tissue, based on microscopic appearance. Gleason system, that scores from 2 to 10, is widely used. In this system, the higher the score, the higher the grade of the tumour and the probability to grow more quickly and to spread. Stage refers to the extent of the cancer.

upon elevated tracer uptake in the malignant tissue in comparison to the normal tissue. Unfortunately, situations exist in which their ability to provide the required information is limited.

This is the case of prostate cancer, the second most common malignant cancer in the US after skin cancer, and the second leading cause of cancer death in men, exceeded only by lung cancer. Prostate cancer is rarely seen in men younger than 50 years of age, but the incidence rises rapidly with each decade thereafter. Fortunately, the progress of prostate cancer is slow in most cases, and it can be cured if confined to the prostate gland. Survival rates are excellent when prostate cancer is detected in early stages. Cure rates are as high as 98%. On the contrary, the chances of recovery are drastically reduced when it has spread beyond the prostate. If the disease is locally advanced (it has spread beyond the prostate, but only to nearby regions), it is more difficult to cure, but survival rates can be prolonged for years in many men. Prostate cancer screening is still controversial due to the lack of definitive evidence of benefit. For these reasons, early detection in initial stages, that is based on the ability to detect small tumours, is essential.

The diagnosis of prostate cancer is based on the combined results of a digital rectal exam (DRE) that searches for abnormal areas, bumps, or suspicious tissue in the organ, and laboratory test of prostate-specific antigen (PSA) level in blood. PSA is a protein produced by the cells of the prostate gland whose levels tend to rise when the prostate enlarges. This tumour marker is extremely useful for early detection of prostate cancer and in monitoring patient progression, with a sensitivity[2] about 75% [83]. However, PSA levels can rise due to cancer or benign conditions, such as prostatitis (inflammation of the prostate) and benign prostatic hyperplasia (enlargement of the prostate) resulting in low specificity. Increased PSA levels alone do not provide sufficient information to assess the presence of the disease. If PSA levels continue to rise over time, further tests might be indicated, and in all cases, the presence of cancer must be confirmed by a biopsy. Samples of prostate tissue are removed and viewed under a microscope to determine if cancer cells are present.

Imaging techniques help to assess the presence of the disease, its extent, or whether it has spread to nearby organs (as seminal vesicles or the bladder), or distant areas such as pelvic or abdominal lymph nodes, bones (pelvis or spine ribs) or in the late stages, lungs and liver. Imaging is also employed to determine the point where to take the sample for a biopsy.

The ability to detect tumours in early stages and metastases in neighbouring organs is crucial to the planning of curative therapy, whether surgery, external beam radiotherapy, radioactive seed implants (brachitherapy), hormone therapy (androgen ablation) or cytotoxic chemotherapy (minimally employed for prostate cancer) are adequate. The appropriate option depends on the specific situation. In general, localized cancer is best treated with surgical removal of the prostate gland or radiotherapy. Hormone deprivation therapy is the primary method of controlling metastatic prostate cancer. At present, chemotherapy cannot cure disseminated prostate cancer. Surveillance (also known as watchful waiting) is a reasonable alternative for an older patient or a patient with other serious illnesses.

[2] *sensitivity* is the probability that the test is positive, given that the person has the disease. *Specificity* is the probability that the test is negative, given that the person does not have the disease.

Radical prostatectomy is the most efficient method of avoiding recurrence provided the disease has not spread beyond the prostate gland. However, 30-40% of patients still develop recurrent disease after surgery. Increased morbidity (incontinence and/or impotence) associated with definitive therapies is also significant and must be avoided whenever possible.

If radiation therapy is indicated, knowing the extent of the cancer is essential to determine whether brachitherapy or external field irradiation are adequate and to avoid irradiation in the pelvis area if it can be localized to the prostate bed.

It is also of outstanding importance to be able to assess response shortly after treatment intervention, or to determine the site of recurrence, since patients with isolated local recurrences are the only ones likely to benefit from radiation or other treatment.

Another important issue is to determine the grade or *aggresiveness* of a tumour given that not all cases of early stage disease will progress to clinically relevant disease within the lifetime of the patient. In the cases of clinically insignificant tumours, for which watchful waiting is indicated, the inability to reliably distinguish them in advance from those tumours whose behaviour will be agressive could lead to the adverse consequences of over-treatment. There is a critical need to be able to identify those patients at risk of progression who would benefit from aggressive therapy while sparing low-risk patients the morbidity resulting form aggressive treatment of indolent disease. New techniques based on biologic activity imaging are needed to distinguish between life-threatening and clinically indolent prostate cancer.

X-ray computed tomography (CT), magnetic resonance imaging (MRI) and ultrasound are commonly employed in prostate cancer diagnosis and staging. Each modality has relative merits for distinguishing different features of prostate cancer, but also disadvantages and limitations, and no one technique can consistently provide all the information needed by physicians.

Transrectal ultrasound is the most common technique for imaging prostate cancer, and frequently serves for biopsy guidance. However, ultrasound is not effective as a diagnostic tool because it cannot differentiate well between benign inflammations and cancer. A set of six systematic biopsies may still miss the cancer. More than 20% of patients with cancer require more than two sets of biopsies before the diagnosis is made, risking side-effects. New improvements in imaging that could more accurately determine the areas of malignancy would be of great value.

Ultrasound is also employed for screening together with DRE and PSA tests. However, it lacks both the sensitivity and specificity to be effective as a diagnostic tool (sensitivity of 42% and specificity of 68% [84] or 71% to 92% for prostatic carcinoma and 60% to 85% for subclinical disease [85]). The sensitivity of ultrasound can be enhanced with color/ power Doppler ultrasound or contrast enhancement methods. Functional imaging with color Doppler ultrasound depicts flow within the prostate gland and can locate tumours that are otherwise invisible. A sensitivity of 90% and specificity of 75% have been obtained with power Doppler transrectal ultrasonography [86]. These techniques enhance the sensitivity, but still lack sufficient specificity.

Images of the prostate can also be obtained employing contrast-enhanced CT or MRI to identify the lesions. X-ray CT is among the earliest imaging technologies used for prostate cancer staging, but due to its low sensitivity together with low specificity, its

value is limited. It is used to look for abnormally enlarged lymph nodes where cancer may have spread.

The primary goal of MRI imaging for prostate cancer has been to detect extracapsular spread of tumour. Endorectal coil MRI is accurate in detecting seminal vesicle invasion and extracapsular extension of prostate cancer (96% and 81% respectively [87]). Within the same exam, MRI can also be used to assess cancer that has spread to the pelvic lymph nodes in close proximity to the prostate and to the bony pelvis.

However, it has demonstrated high sensitivity but low specificity in determining tumour location within the gland. Localization of cancer within the prostate is subject to error because of factors such as post-biopsy hemorrhage, chronic prostatitis, BPH hiperplasia, intraglandular dysplasia, trauma and therapy [88, 89].

A recently developed imaging technique, magnetic resonance spectroscopic imaging (MRSI) is used to assess cancer-related metabolic changes in the prostate gland. It has been found to improve detection, localization and staging of prostate cancer, as well as to detect recurrent disease after therapy [90]. One limitation is its relatively poor spatial resolution. Also, it is technically demanding requiring specialized software and expertise in its operation. In combination with MRI, metabolic information reflecting cancer physiology from MRSI complements morphologic information from high-resolution MRI to discriminate cancer from surrounding healthy tissue and necrosis. This technique is under investigation.

In conclusion, the methods that define anatomical structures are only marginally successful in revealing the presence and spread of prostate cancer and in many cases, images can not adequately distinguish suspicious prostatic tissue from normal or other non-cancerous tissue. Structural imaging may miss subtle disease sites that potentially can be detected by biochemical functional imaging.

Nuclear imaging techniques are also employed in cancer diagnosis and staging. However, in the case of prostate cancer they have severe limitations.

Bone scintigraphy can be useful in detecting osseous metastases, but the false-positive rate is high, and the modality cannot detect soft tissue or lymph nodal involvement. Arthritis, an old injury and infections or other bone diseases may also produce positive scans. The finding of multiple areas of increased tracer activity throughout the skeleton in a patient with prostate cancer is strongly suggestive of bone metastases, but the significance of a solitary area of abnormal tracer activity may be problematic.

SPECT is employed to identify extraprostatic disease in initial stages and to detect the site of recurrences after surgery. Indium-111 capromab pendetide (In111-Prostascint), a prostate-specific membrane-based monoclonal antibody that can be labelled with ^{111}In is employed. The two gamma rays of this radiotracer have energies relatively high (171 keV and 245 keV) for SPECT. Also, the fact that imaging is done 4-5 days post-injection, requires low resolution collimators to be used in order to achieve sufficient counting efficiency. The images have therefore low resolution (15 mm FWHM at best), and low tumour to background ratio. As a result, small tumours cannot be detected and the exact location within the prostate and its extra-prostatic extension may be difficult to identify. Values of 49-77% sensitivity, and 35-71% specificity for local recurrence in prostatic bed [91] evidence that SPECT studies cannot be used as definitive imaging study in evaluating recurrence of prostate cancer.

PET scanning using the radioactive glucose analog fluorodeoxyglucose (18-F-FDG or FDG) has proven to be a highly accurate imaging test for diagnosing and staging a variety of non-urologic cancer types, but it has not found a significant role in assessing prostate cancer [92, 93]. FDG uptake in the primary prostate cancer is generally low, and may overlap with the uptake in benign prostatic hyperplasia in the normal gland and in the postoperative scar of local recurrence. Activity accumulating in the ureters and bladder may also limit the evaluation of adjacent structures such as the prostate and pelvic lymph nodes. In addition, it suffers from photon attenuation, worse than in the case of SPECT, since the path is longer given that the two emitted photons must be detected, and the probability of attenuation in the pelvic region is high. FDG PET may be employed in the detection of metastatic disease, since it appears to be more useful in the detection of soft tissue metastases.

Present status of prostate cancer imaging is therefore much less than adequate. Three areas in which advances are likely to lead to immediate improvements are detecting and spatially localizing early-stage prostate cancer, identifying those patients for whom treatment is necessary and likely to be curative, and determining the site of recurrent disease and the most appropriate treatment strategy. Real needs remain for an imaging technique that would facilitate proper diagnosis and staging. This is of particular importance in distinguishing patients with local disease from those with locally advanced disease. By accurately staging the disease and recognizing early phases of local spread, complications resulting from over-treatment can be avoided. Techniques that accurately define the anatomic extent of localized prostate cancer are essential.

The development of new radiopharmaceuticals that overcome the main problems of FDG, have renewed the interest for PET. 11-C choline and 11-C acetate show improved uptake levels compared to FDG, and lack of accumulation in the bladder [94,95]. However, their practical clinical use is limited due to the short half-life of ^{11}C, which requires an on-site medical cyclotron for radiotracer production. 18F-fluorocholine, also under investigation, would avoid this problem.

Dedicated PET systems planning to employ these new radiotracers are under development [96, 97, 98]. Their main goal is to improve the efficiency while reducing the cost of the device to make it widely available. However, they do not show significant improvement over whole body PET scans, and the availability is limited by the need of on-site cyclotron facilities.

A prostate probe based on the Compton imaging method can outperform existing devices both in terms of efficiency and spatial resolution. Its ability to detect small tumours in early stages would result in an improved assessment of cancer presence, determination of the local extent of the disease, guidance for biopsy and measurement of early biological effects of therapy. The detector would consist of a silicon probe placed close to the prostate gland working in coincidence with a scintillator second detector.

Extensive simulations have been conducted to estimate the performance of a prostate probe. A summary of the results obtained in the simulations will be given in the next section.

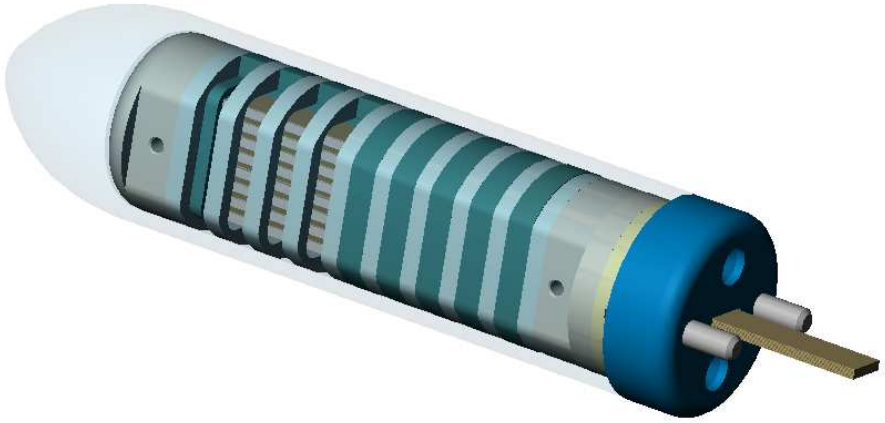

Figure 4.1: *Possible design of the endorectal probe.*

4.2 Simulation results

In order to estimate the performance of the prostate probe, very realistic simulations have been conducted by L. Zhang at the University of Michigan [23, 12, 99]. This section summarizes the results obtained and the expected performance of the Compton prostate probe. Two possibilities have been considered, an external probe, placed beneath the perineum, working in coincidence with a NaI(Tl) absorption detector, and an endorectal probe with two scintillators, above and below the patient. The choice of the second detector material is driven by the fact that NaI(Tl) gamma cameras are widely available, while any other type of absorption detector should be specifically developed, increasing the cost.

In the case of the endorectal probe, more adequate if low energy radiotracers are used, the scatter detector consists of a stack of silicon sensors, 1 cm wide, 4 cm long, and 1 cm thick, to be placed endorectally (fig 4.1). The voxel size is 1 mm^3, and the energy resolution 1 keV FWHM. The absorption detector is composed of two 40 cm $\times$ 40 cm scintillators, 2 cm thick, with a 3 mm FWHM intrinsic spatial resolution and 10% energy resolution. Their position, above and below the patient (fig 4.2), has been chosen for practical reasons, based on the existing gamma cameras. A geometry selecting low scattering angles would yield better results.

The fact that the first detector is less than 2 cm from the prostate results in a very good spatial resolution, since the angular uncertainty induces only a small spatial uncertainty, as explained in section 2.2.1. Another advantage is that the solid angle subtended by the scatter detector is larger, increasing the efficiency for a lower amount of silicon. The main drawbacks are due to its location. Its size is strongly limited, and the temperature of the human body can cause an increase of the leakage current of the silicon detectors and the noise of the readout electronics, degrading the energy resolution, unless cooling is available. Electrical safety becomes also an important consideration in this configuration. Another factor to take into account is the attenuation due to the tissue between the scatter and absorption detectors. To simulate attenuation and scattering in a human body, a digital anthropomorphic phantom, which was created by segmenting a whole-body CT scan (*Zubal* phantom [99]), has been incorporated into the simulation code.

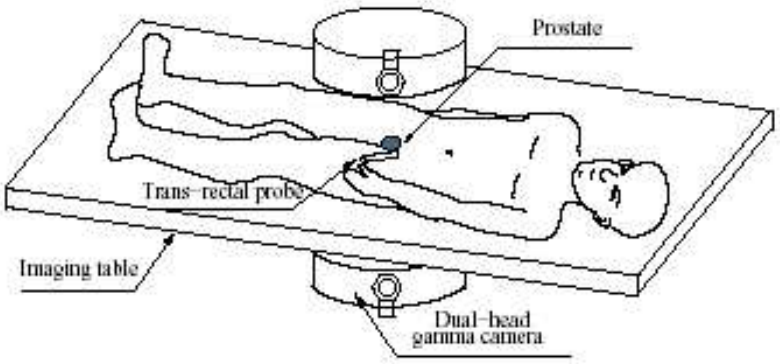

Figure 4.2: *Endorectal probe configuration. The probe works in coincidence with a dual-head gamma camera situated above and below the patient.*

Background due to neighbouring organs has also been considered. The biodistribution of In-111 Prostascint in relevant organs at 5 days post-injection was estimated from patient studies, and employed to initialize the relative concentrations in the phantom.

The MCSIMSPI Monte Carlo code was used to investigate the performance of the endorectal probe in terms of detection efficiency, spatial resolution, and lesion visibility.

Various widely used radionuclides were simulated, in a range of energies from ^{99m}Tc (140.5 keV), ^{111}In (171 keV and 245 keV), ^{131}I (364.4 keV), to ^{11}C (511 keV). The two imageable photopeaks of ^{111}In were simulated independently, and down scattering of the high energy gamma ray on the energy window of the low energy peak was not considered.

The simulations include scattering (Compton and Rayleigh), attenuation, Doppler broadening and spatial and energy resolution of both scatter and absorption detectors. Timing resolution and its effect on random coincidences were not considered. The valid events are those that undergo single Compton scattering in the silicon detector, are absorbed in the scintillator and have total energy deposition within a 20% symmetric energy window.

The absolute detection efficiency is estimated placing an isotropic point source in the prostate of the phantom and calculated as the ratio of valid events to the total number of photons emitted. In the endorectal configuration, the detection efficiency is found to be highest at 171 keV (0.174% for a point source located 1 cm away from the probe front face), and decreases with increasing energy (about 0.13 at 511 keV), due to the strong penetration of high-energy gamma rays and reduced Compton cross-section.

To determine the spatial resolution for each of the energies, an M-shaped array of point sources was located in the prostate at a distance of 1 cm from the probe face. The images (fig 4.3) were reconstructed with a penalized LMML-EM reconstruction algorithm. The distance point-to-point is 1 cm. Spatial resolution considerably better than 4 mm FWHM is achievable over the whole energy range, and it increases rapidly with increasing photon energy due to reduced angular uncertainty resulting from smaller Doppler broadening at higher energy. The estimated FWHM spatial resolution was found to range from 2.8 mm at 141 keV to 1.7 mm at 511 keV.

In the case of the external probe, the proposed configuration for the scatter detector

Figure 4.3: *Reconstruction of a M-shaped array of point sources with the endorectal probe configuration at different energies. From left to right, 140.5 keV (^{99m}Tc) , 171 keV and 245 keV (^{111}In), 364.4 keV (^{131}I), and 511 keV (^{11}C)*

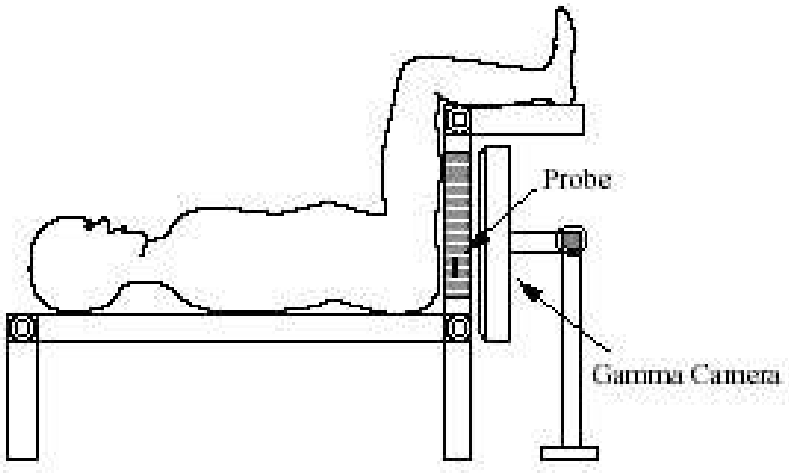

Figure 4.4: *External probe configuration. The probe is placed beneath the perineum, at about 4 cm from the prostate.*

consists of a stack of 4 cm × 4 cm × 1 mm sensors. The patient is lying on a table in a supine position with the legs raised, and the probe is placed beneath the perineum, at about 4 cm from the prostate. One 40 cm × 40 cm × 2 cm gamma camera is placed at a distance of 5 cm from the scatter detector (fig 4.2).

The angular uncertainty is higher than in the previous configuration, due to the larger distance from the scatter detector to the prostate. However, if high energy radiotracers are employed, for which the angular uncertainty is smaller, a reasonably good spatial resolution can be achieved. Although its performance is poorer than the endorectal probe at low energies, it has some advantages. The size of the detectors is not restricted, and it can be increased to enhance the efficiency. It imposes less operational challenges, and cooling becomes less of an issue.

In this configuration, the efficiency is slightly higher than in the endorectal probe due to the increased size of the detectors. It is nearly the same at 141 keV and 171 keV (0.250% for a point source 4.8 cm away from the probe), and it decreases with increasing photon energy. This is about 20 times higher than SPECT systems with a high sensitivity collimator at the same distance. The spatial resolution improves with energy, as in the previous case, ranging from 3.7 mm FWHM at 141 keV to 1.8 mm at 511 keV. The resolution is comparable at high energy, but considerably worse at low energy due to the

	Absolute counting efficiency	Resolution (mm FWHM)
Endorectal Compton probe at 1 cm	1.74×10^{-3}	2.4
External Compton probe at 5.8 cm	1.7×10^{-3}	3.5
Collimated probe at 1 cm	3.2×10^{-4}	2.5
High sensitivity collimator at 10 cm	1.11×10^{-4}	15.9
High resolution collimator at 10 cm	4.00×10^{-5}	10.5

Table 4.1: *Comparison of the results obtained for the prostate probe in both configurations, SPECT with two different collimators and the collimated probe. 10 cm of tissue attenuation is included, except for the collimated probe (1 cm) and the external probe (5.5 cm).*

increased position uncertainty that results from the larger distance to the prostate and the higher angular uncertainty at low energies. As a consequence, to achieve desirable spatial resolution required for identifying lesions of small size, the prostate should be imaged with a radiotracer labelled with nuclides that emit gamma-rays higher than 171 keV.

The results of the simulations have been compared to a SPECT system with different collimators, and with analytical calculations for a mechanically collimated probe of the same size as the Compton probe. For the collimated probe, the efficiency was evaluated at the same spatial resolution as the endorectal probe. The parameters obtained are shown in table 4.1. The values include 10 cm of tissue attenuation except for the collimated probe (1 cm) and the external probe (5.5 cm).

To evaluate the lesion visibility performance, three tumours of different sizes were placed at different positions within a low activity prostate. Different tumour-to-background (T/B) ratios were considered, and two scenarios were evaluated, including or not activity from neighbouring organs. Even in the cases where background from neighbouring organs was considered, small tumours ($\leq$8 mm) with 10:1 T/B ratio were clearly distinguished. To compare with SPECT, the SIMIND code was employed to simulate a SPECT camera, with a NaI(Tl) crystal 50 cm long, 50 cm wide and 0.95 cm deep, a FWHM intrinsic spatial resolution of 4.6 mm and an energy resolution of 10% at 171 keV and 245 keV. Figures 4.5 and 4.6 show the reconstructed images for conventional SPECT and the internal probe. Images in the upper row contain a single 8 mm diameter tumour with a 10:1 tumour to background ratio, while the ones in the lower row correspond to background only. The radiotracer energy is 171 keV for the images in the left column, and 275 keV for those on the right column. In the case of the prostate probe images, the tumour is clearly differentiated from the background-only distribution, in contrast with the corresponding SPECT reconstruction, for which it would be difficult to distinguish from the background. The field of view is 10 cm for the prostate, and 40 cm for conventional SPECT.

Further quantitative analysis using the *non prewhitening matched filter* study demonstrate that the Compton probes exhibit a SNR improvement of 3-3.5 times that of the conventional SPECT for detecting 8 mm and 5 mm tumours.

Concerning the image reconstruction for the Compton prostate probe, two main problems arise that degrade the image. One is the limited angle problem, since the angular sampling of the prostate probe is not complete. The second problem is caused by the

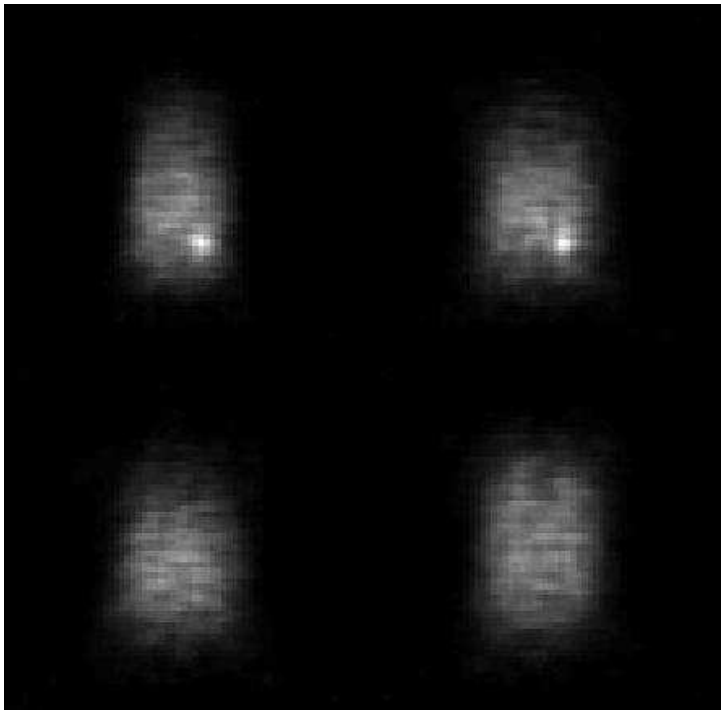

Figure 4.5: *Lesion visibility studies with the Compton probe (10 cm field of view). The 8 mm diameter tumour with a 5:1 (left) or 10:1 (right) tumour-to-background ratio (upper row) is clearly distinguishable from the background only situation (lower row) at 245 keV gamma-ray energy.*

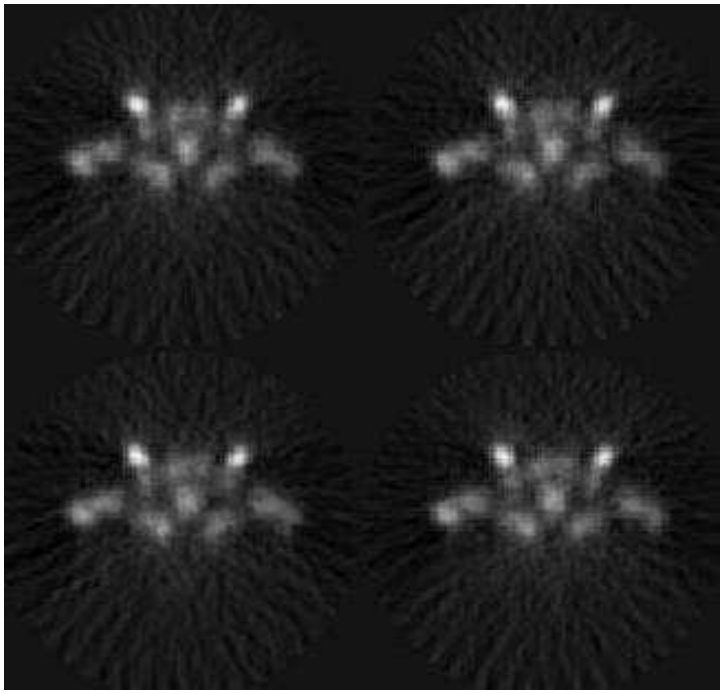

Figure 4.6: *Lesion visibility studies with conventional SPECT (40 cm field of view). The 8 mm diameter tumour with a 5:1 (left) or 10:1 (right) tumour-to-background ratio (upper row) can not be distinguished from the background only situation (lower row).*

activity outside the reconstructed field of view. If the reconstructed field of view is restricted to the prostate, non-prostate activity is considered by the MLEM algorithm as events originated within this limited field of view. This results in background and artifacts in the reconstructed images. Both problems have been studied and solutions have been proposed to improve the image quality.

In the case of the limited angle tomography, a possible solution consists of a Compton camera that can be moved around the target object to acquire complete projection data. The alternative of employing two or more Compton cameras in different positions has also been proposed [100].

For the background due to high activity on nearby regions outside the reconstructed image, a solution has been found by estimating the non-prostate activity with a SPECT system and incorporating it to the M-step of the EM algorithm. Images in fig 4.5 were obtained with this method.

4.3 Conclusion

Current imaging techniques are not adequate in the case of prostate cancer, one of the most common among men. A prostate probe based on Compton imaging offers an alternative that could outperform the methods currently employed. Promising results have been obtained from realistic simulations, that make us believe that an enormous benefit over existing devices can be achieved, both with endorectal and external probe configurations.

The results must now be validated by the development of a clinical prototype. Technical difficulties must be solved, that are more stringent in the case of an endorectal probe. Dense packaging of the detectors is required, and a suitable cooling system for the silicon sensors needs to be developed. Therefore, for the first clinical configuration an external probe will be constructed. The development of a prototype is underway, and a first prototype has been built and tested. The following two chapters will provide detailed explanations of the prototype development and the results obtained.

Chapter 5

Prototype development

The work presented here resumes the Compton imaging experiments carried out at the University of Michigan with a 300 μm silicon sensor as scatter detector. After the successful achievements obtained with the first Compton prototype, C-SPRINT, efforts have aimed at improving the scatter detector. In addition, the general-purpose studies previously performed begin to focus on specific applications, such as a very high resolution PET for small animals [11] and the Compton prostate probe [12]. The main goal of this prototype has been to develop, test and validate thick silicon sensors to be used as scatter detector, as well as to operate several silicon sensors in a stack. The results accomplished are a first step towards the development of a prostate probe clinical prototype.

The use of thick sensors aims to enhance the efficiency of the scatter detector without increasing excessively the number of readout channels. With this purpose, 500 μm and 1 mm thick silicon sensors have been developed and tested. As explained in chapter 3, increasing the thickness of the silicon sensor also results in an increase of the leakage current, and consequently, a degradation of the energy resolution. The development of thick detectors with good energy resolution is one of the main technological challenges in the development of this prototype.

Silicon modules have been produced, employing the new sensors as well as new hybrids and improved versions of the readout electronics. A VME data acquisition system for the silicon modules and a new data acquisition software have also been developed and tested in the last years. Silicon sensors from several manufacturers and different versions of the readout electronics were examined before selecting the final design [101].

In order to test the components in the way they will finally be operated, and to evaluate their performance, a prototype has been constructed with the new modules and scintillators obtained from an existing gamma camera.

Different versions of the prototype and several runs of operation and data taking have served us to understand the properties of the Compton detectors and to optimize the prototype. Each test tried to include the new developments, employ the latest versions of the hardware, correct for the errors found in previous versions and improve the results.

In this chapter, the main characteristics and performance of the components that were employed to build up the final prototype, calibration of the scatter and absorption detectors and prototype assembly and operation, will be described. Next chapter will summarize the results obtained with the prototype in different runs of data taking.

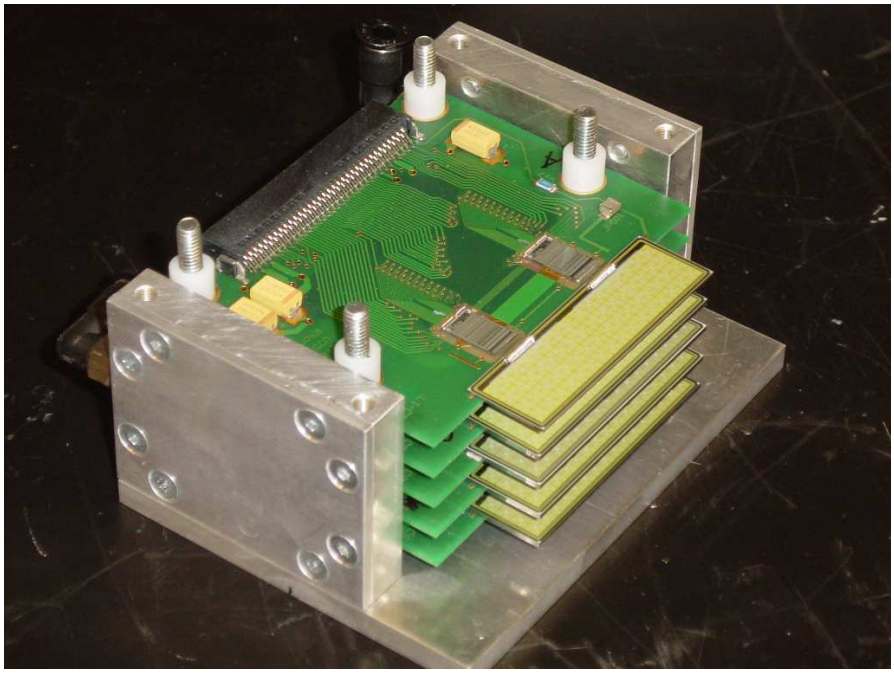

Figure 5.1: *Scatter detector consisting of a stack of silicon modules equipped with thick (one 500 μm and four 1 mm) silicon sensors.*

5.1 Scatter detector

The scatter detector consists of a stack of silicon modules (fig 5.1). Each module is composed of a hybrid that gives support to a silicon pad detector and readout electronics and hosts the signal lines and bias voltage for the detector. The sensors are either 500 μm or 1 mm thick. Each sensor is read out by two self-triggering ASICs, 128 channels each, that are wire-bonded to the side of the silicon detector.

Up to 5 modules can be operated at a time in this prototype. A short description of the components and the performance of the modules is given next.

5.1.1 Silicon sensors

The sensors, produced by SINTEF [102], are p^+n, DC coupled pad sensors, 46 mm long, 14 mm wide and 500 μm or 1 mm thick. Figure 5.2 shows a picture of a sensor before being cut from the wafer. The 256 pads are disposed in a 8×32 array, with a pitch of 1.4×1.4 mm^2, giving a sensitive area of 44.8 × 11.2 mm^2.

The intrinsic spatial resolution resulting from a uniform probability distribution (equation 5.1) for a pitch p=1.4 mm, is good enough to contribute negligibly to the spatial resolution of the Compton detector.

$$\sigma = \frac{p}{\sqrt{12}} = 0.404\ mm \tag{5.1}$$

A cross section of the sensors can be seen in figure 5.3. The pads are 1.39×1.39 p^+ implants on high resistivity n^- silicon, isolated from each other by a 20 μm wide non-

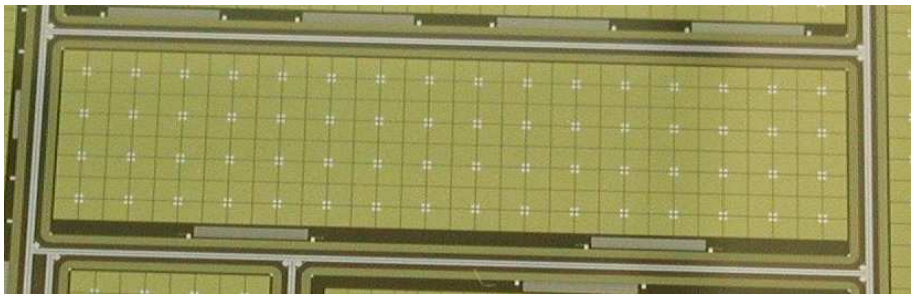

Figure 5.2: *Silicon sensor, 8×32 pads, 46 mm long, 14 mm wide 1 mm thick.*

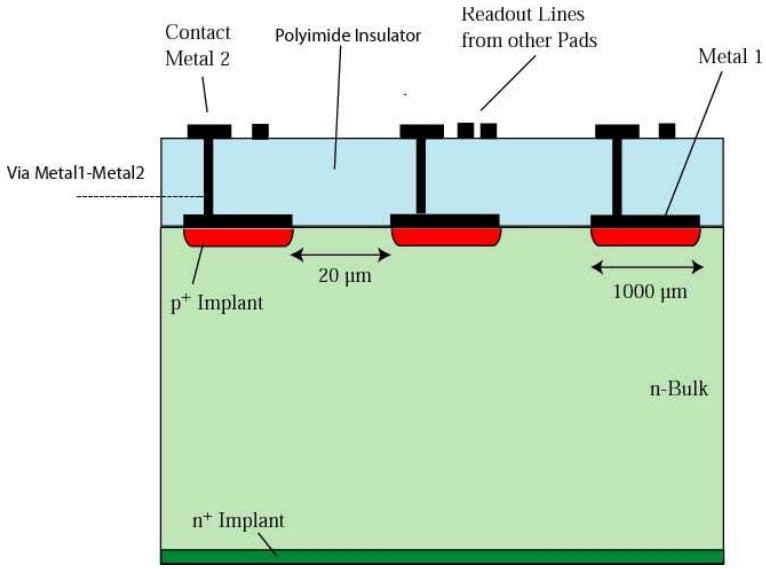

Figure 5.3: *Cross section of a silicon sensor.*

implanted region [103]. Aluminium pads are directly placed on them, and covered by a thin polyimide insulator layer. Double metal technology is employed to route the signals to the bonding pads on the side of the detector. The metal pads (metal 1) are connected to the surface metal contacts (metal2) through a via in the polyimide layer that is filled with aluminium. The readout lines in the surface of the detectors lead the signals to the bonding pads, where they are wire-bonded to the readout ASICs (fig 5.4).

A guard ring structure of p implanted rings with metal on top surrounds the pads and separates the active area from the edges of the detector, in order to prevent the electric field from reaching them. The voltage is gradually degraded from the outermost ring, at the backplane potential, to the innermost one, set to 0 V. A n^+ layer of about 500 nm thickness is created in the backside of the wafer, where the positive bias voltage is applied, to serve as ohmic contact.

The capacitance was measured for different values of the bias voltage. From the fit of the $\frac{1}{C^2}$ versus the bias voltage plot, shown in fig 5.5, a depletion voltage of about V_D=140 - 150 V is inferred. This is compatible with the values obtained with the inflexion point in the I-V curves. This low depletion value indicates a very high resistivity of the silicon material, according to equation 3.3,

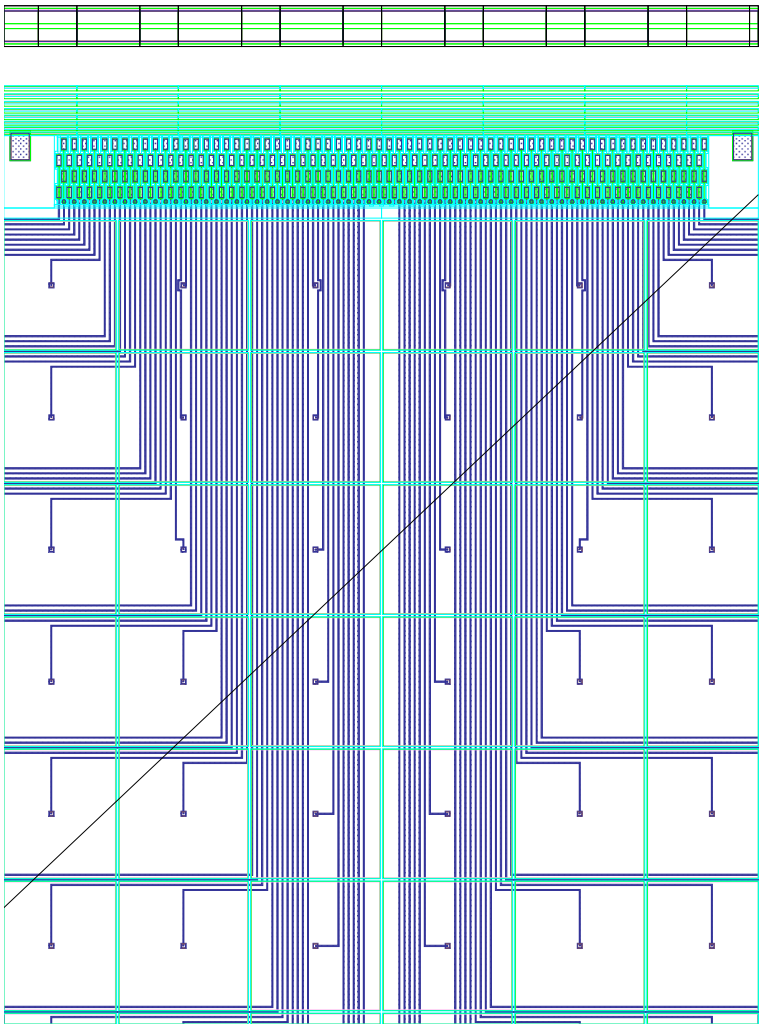

Figure 5.4: *Readout lines routing the signals from the implants to the bonding pads at the edge of the detector.*

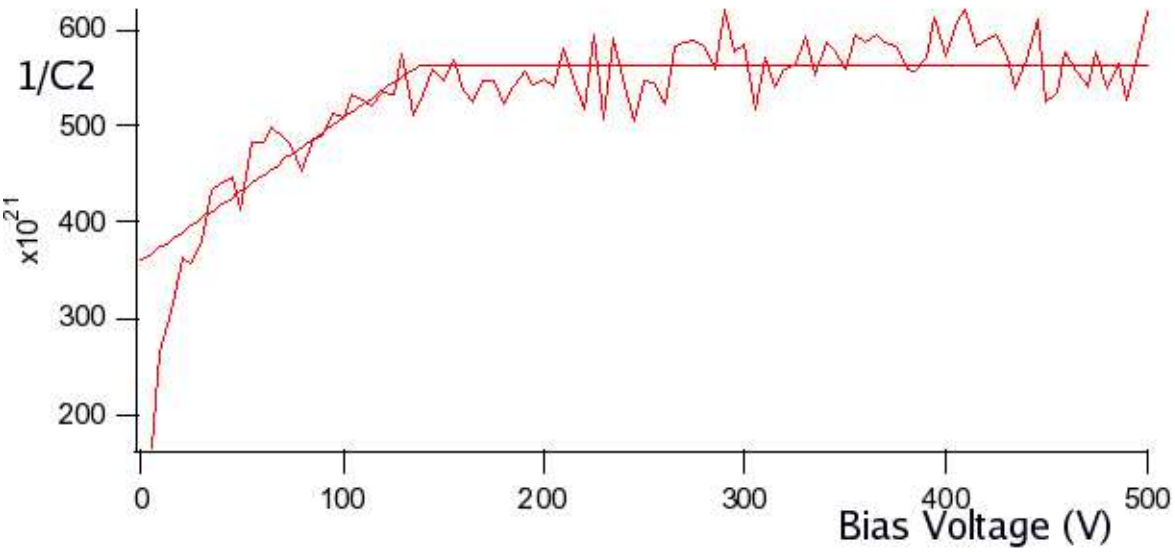

Figure 5.5: *$\frac{1}{C^2}$ as a function of the bias voltage. The point where the slope changes indicates the full depletion voltage of the detectors.*

$$\rho = d^2/2\mu_n\epsilon V_D \approx 200\ k\Omega\ cm,$$

where $1/2\mu_n\epsilon = 31.5k\Omega\times$ 100 V/mm^2 and d=1 mm.

In the case of the 500 μm sensors, the depletion voltage is around 100 V.

The thickness of 500 μm and 1 mm will enhance the efficiency, compared to the 300 μm sensors previously employed. However, an increase of the thickness also raises the leakage current, degrading the energy resolution. Special attention has been put forth in the design of the sensors to keep the leakage current low and avoid this effect. A leakage current between 20 and 50 pA per pad was measured for the 1 mm thick sensors at 400 V, and between 10 and 20 at 300 V for the 500 μm. The leakage current measured on one pad is shown in figures 5.6 and 5.7 as a function of the bias voltage applied to the detector, for different detectors, 1 mm and 500 μm thick respectively. The measurements were done on a corner pad, and grounding the neighbouring ones to avoid contributions from other pads.

The contribution of the diffusion current can be appreciated in the I-V curves for values of the bias voltage lower than the depletion voltage. The effect of diffusion and surface currents is more pronounced in the 1 mm detectors.

5.1.2 Readout electronics

The readout electronics must be fast and self-triggering, provide sufficient timing accuracy and have low noise to avoid degrading the energy resolution of the scatter detector.

Low noise VLSI CMOS ASICs, the *general purpose* VATAGP3 [104] developed by IDEAS [105] is employed as front end electronics for this application. The most important requirements are fulfilled with this version of the chip, although some properties such as

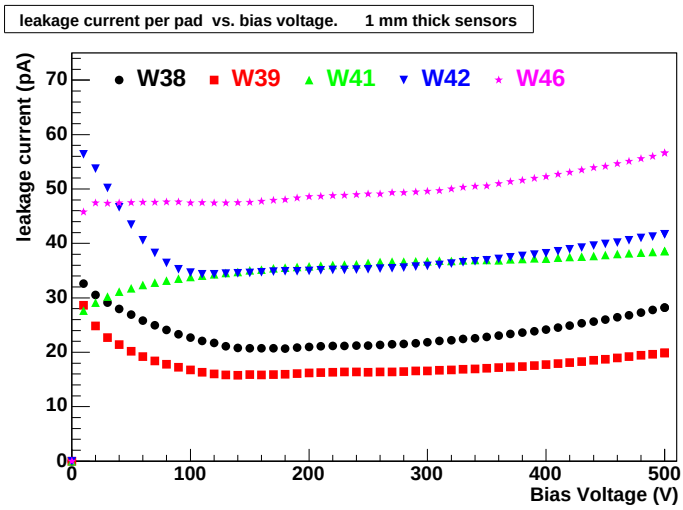

Figure 5.6: *IV curves corresponding to five 1 mm thick silicon sensors.*

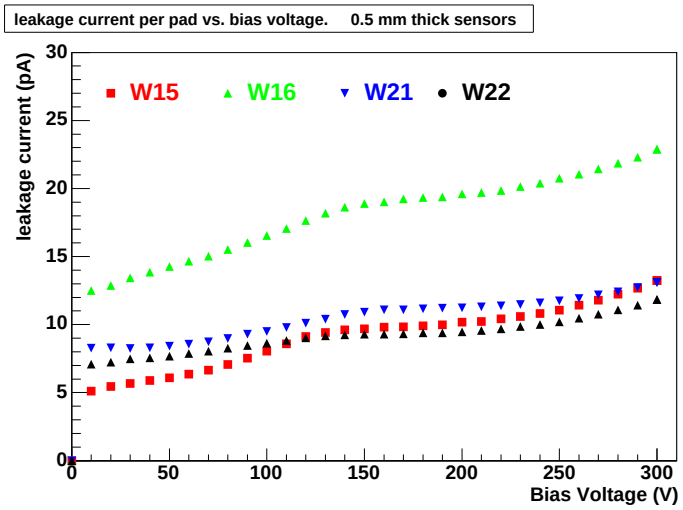

Figure 5.7: *IV curves corresponding to four 0.5 mm thick silicon sensors.*

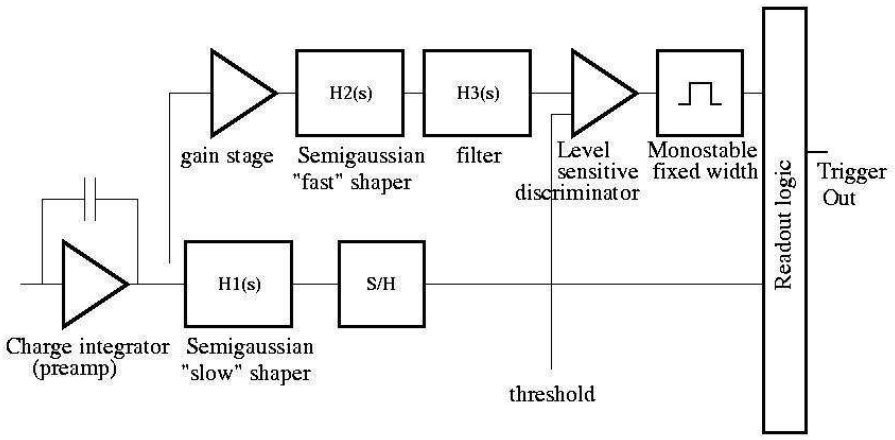

Figure 5.8: *Working principle of one channel of the VATAGP3 ASIC, including a low noise, charge sensitive preamplifier, a semigaussian shaper with adjustable shaping time and multiplexed analog readout. In addition, a fast shaper provides a trigger signal.*

timing performance need to be further improved. Timing resolution is degraded for low energy signals due to time-walk. Time-walk compensation has been included in version 3.1 of the ASIC, that will be employed in future prototypes.

Each chip has 128 channels, and up to 16 chips can be daisy-chained, allowing to read out up to 2048 channels of a detector. Figure 5.8 shows schematically the working principle of the ASIC. Each of the 128 channels includes a low noise, charge sensitive preamplifier, a *slow* semigaussian shaper, sample/hold circuitry and an analog multiplexer (VA part). In addition, a *fast* shaper (around 150 ns shaping time) is followed by a level discriminator and a monostable that produces a trigger signal if the shaped signal exceeds the discriminator reference level set by the user (TA part). The shaping time of the slow shaper is nominally 3 μs, and it can be adjusted. All channels can be read out sequentially thanks to the input and output analog multiplexing system.

Input pads are provided to apply the appropriate control currents and voltages in order to optimize the chip performance. They can also be left unconnected, and the necessary values will be derived from the main control current (MBIAS).

The chip is configured by a control register. The most relevant features are the following:

- Gain stage with three different values of the gain
- chip address for identification if more than one are used
- mask individual channels, to prevent noisy channels from triggering.
- TEST mode to enable response to a calibration input pulse.
- DAC for threshold alignment
- Current compensation
- Three readout modes: SERIAL, SPARSE, and SPARSE WITH ADJACENT.

- Disable late triggers (DLT)

Although the threshold value set to the trigger discriminator is common to all channels of the chip, small differences among channels occur. A 3 bit DAC allows small corrections to be made on the discriminator level for each channel to equalize the threshold value in all channels.

The chip has three possible readout modes. In the SERIAL mode, all channels of the detector are read out, independently of the one that triggered. The readout time for the 256 channels in one module (two chips) is about 240 μs. The dead time becomes excessively large if many channels are read out.

In SPARSE mode only the channel that triggers is read out, increasing significantly the readout speed. The channel address is provided in the data output. In this mode, pedestal and noise calculation required for data analysis, must be obtained prior to data acquisition. A third option is available, SPARSE WITH ADJACENT, where the channel that triggered plus a number of channels on both sides are read out. This number is chosen by the user. In the case of strip detectors, the adjacent channels correspond to adjacent strips that might have collected part of the signal and should be added to obtain the total signal. When employed with pad detectors, adjacent channels in the chip do not always correspond to neighbour pads in the detector. However, reading out neighbour channels has been found to be useful for pedestal, noise and common mode calculation from the data taken.

If a trigger has occurred, the chip has the possibility to disable further triggering by a signal sent by the user (DLT) until the readout is finished, avoiding the interference of the signals produced by a new trigger.

Setting the chip to TEST mode enables the response to a calibration pulse and allows testing the chip to verify the correct performance of all channels before bonding the detector. Both the trigger (TA) and the analog (VA) part of the chip can be tested in a fast and reliable way, and it also makes it possible to characterize the chip features such as the values of the gain for each channel, or to determine the differences in the threshold level and correct for them.

When a trigger signal is sent by the chip, the signals required to start the readout are generated (fig 5.9). After the shaping time, the signal has reached its maximum value, and a sample-and-hold signal goes high. In serial mode, a shift bit and a clock signal enable the analog value of each channel at the output. For each clock, the shift signal is clocked to the next channel until the last channel is enabled and the readout is complete. A shift out signal can be employed as shift in for the next chip if more than one are employed. A disable-late-trigger (DLT) signal can be applied right after the trigger signal to discard all triggers until the readout is finished and a reset signal is sent. This is especially important in the case of high event rates when the probability of having more than one trigger during the readout is higher. Once the readout is finished, the analog output is digitized by a 12-bit ADC and the data stored to be analyzed on a PC.

Figure 5.10 shows the trigger signal and the analog output for 256 channels with a signal in one of the channels. The clock and the hold signal are also shown. The delay between the trigger and the beginning of the analog readout, corresponding to the integration time of the slow shaper, is adjusted to 3.3 μs.

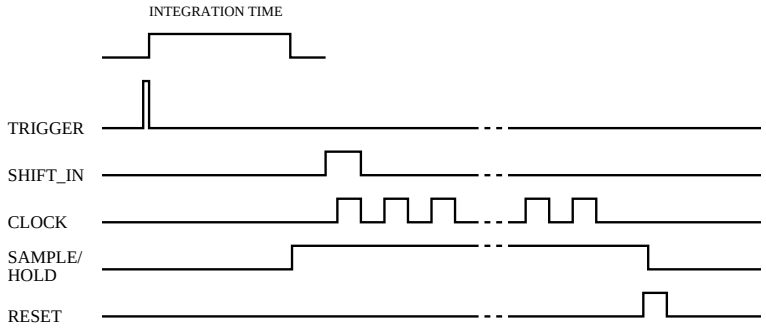

Figure 5.9: *Necessary signals for serial readout mode of the VATAGP3.*

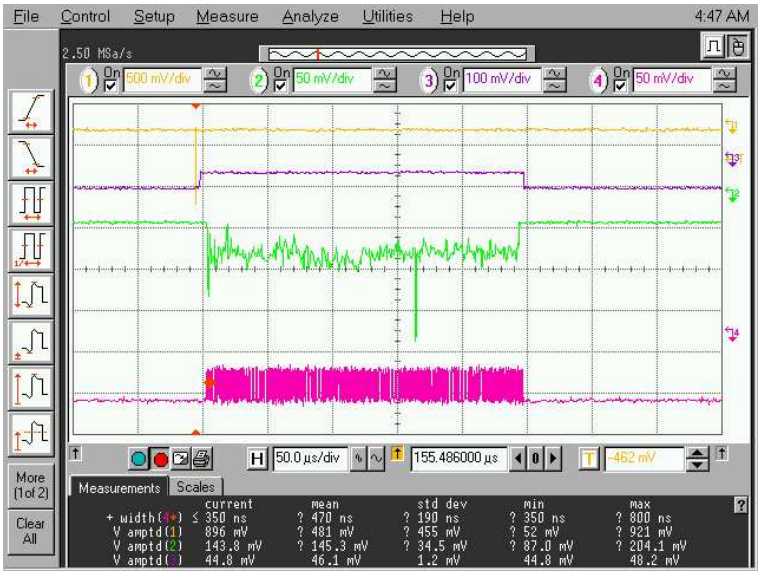

Figure 5.10: *Screenshot of the oscilloscope showing four signals related to the ASICs readout of 256 channels. 1.- trigger signal. 2.- Analog output. 3.-Hold signal. 4.-Clock signal.*

A VME data acquisition system, has been designed for operation and readout of the silicon modules. Two electronic boards are necessary. A VME board controls the data acquisition by means of a FPGA. In an *intermediate* board, the necessary input voltages and currents for the ASICS are generated. A third board (*distribution board*) is used for the operation of more than one silicon module. In this board, the signals generated in the intermediate board are distributed to all the modules. The signal indicating the end of the readout in one module (SHIFT-OUT) is employed as input (SHIFT-IN) for the next one. This way all modules are seen as a single one by the data acquisition system.

The system has the possibility to start the readout by means of an external triggering signal. This feature is essential for the coincidence setup and electronics circuitry necessary to operate the Compton prototype.

5.1.3 Calibration

Optimizing the performance of the silicon modules requires a good understanding of the readout electronics response, both of the analog part (VA) and of the trigger part (TA). Numerous test have been carried out to understand and optimize the performance of the silicon modules. These tests can be performed either with a calibration source of known energy, when a detector is already bonded, or with a calibration pulse, setting the chip to TEST mode. The use of a calibration pulse allows one to verify the correct functioning of the chips prior to bonding the detector, or to perform tests much faster than employing the source.

Results of calibration and testing of the readout electronics will be shown in this section. In the case of the VA part, the aim is to optimize parameters such as noise, that will determine the energy resolution, crucial for the performance of the Compton prototype. In addition, it is necessary to establish a relationship between the energy deposited in the silicon sensor and the output value of the readout system.

The noise in the trigger part is also an essential parameter, since it will determine the minimum threshold that can be set, and therefore the lowest energy that can be measured, determining the possibility of measuring low scattering angles.

VA calibration

The calibration of the analog part of the chip includes the calculation of the the gain factors that relate for each channel the energy transferred to the detector in the particle interaction, and the digitized data from the ADC. The relative differences in the VA gains from one channel to another must be determined and the data corrected with the gain factors in order to obtain the information in terms of energy. Also, the energy resolution of the detector must be determined.

The analysis of the silicon data includes pedestal and common mode subtraction. Clusterization algorithms are also applied. However, at the energies considered, the charge is mainly deposited in one pad. Figure 5.11 shows typical values of the noise for each channel of four detectors. The first one (channels 0-127) is 0.5 mm thick, and the three remaining are 1 mm thick. The noise pattern is correlated to the readout lines on the surface of the detector [106]. Those pads closer to the edge of the detector have more

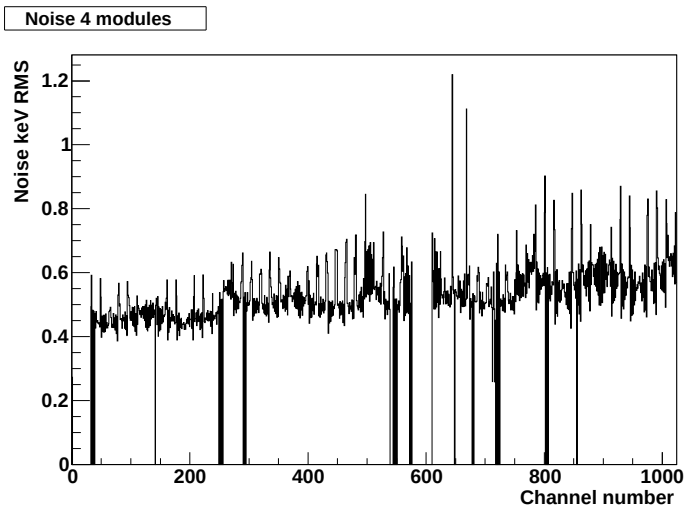

Figure 5.11: *Noise measured for each channel corresponding to four modules.*

readout lines on top, increasing the capacitance and therefore the noise (see fig 5.4).

The energy resolution is an important parameter that greatly influences the resolution of the reconstructed images. The energy resolution is determined by the intrinsic energy resolution of the detector and the electronics noise.

The intrinsic resolution of the silicon sensor is given by equation 3.6. For the 59.5 keV gamma ray of ^{241}Am, its contribution is around 45 e ENC, about 64 e ENC for the 122 keV of ^{57}Co.

As explained in section 2.2.1, the energy resolution of the scatter detector should be around 1 keV FWHM (0.425 keV sigma), which expressed in e ENC corresponds to

$$ENC_{tot} = \frac{425}{\eta} = 118\ e,$$

with η=3.6 eV.

The main contributions to the electronics noise come from the noise in the preamplifier (series noise) and the leakage current of the detector (parallel noise), explained in section 3.3.2.

The preamplifier noise can be parametrized as

$$ENC_{pr} = a + b \times C_{load}[pF]$$

where C_{load} is the total parallel capacitance at the input. The a and b parameters depend on the electronics employed, and can be evaluated by measuring the noise performance of the chip using passive components for a given shaping time. These parameters were measured for the previous version of the chip, that has the same readout structure as the one that is currently employed [107]. The results for two different values of the shaping time are shown in table 5.1. The load capacitance C_{load} is generally around 1 pF, and in our case C_{load} ≈0.8 pF.

The contribution to the noise due to the leakage current of the detector has the expression

$\tau(\mu s)$	a	b
2	88	22
5	68	12

Table 5.1: *Measured a and b parameters of the series noise for two values of the shaping time.*

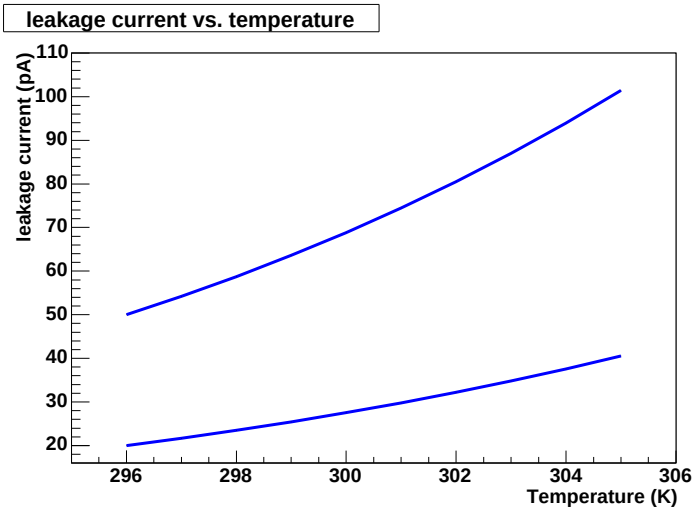

Figure 5.12: *Increase of the leakage current with temperature for initial values of 20 pA and 50 pA.*

$$ENC_{lc} = \frac{e}{q_e}\sqrt{\frac{qI_{lc}\tau}{4}} = 150\sqrt{\frac{I_{lc}\tau}{2\mu s}}.$$

Measurements of the leakage current are shown in section 5.1.1. This measurements were performed at a temperature around 23º C, and the increase of the leakage current due to the heat generated in the operation of the silicon module, given by equation 3.5, must be taken into account. Figure 5.12 shows the increase of a leakage current of 20 pA and 50 pA measured at this temperature.

A temperature around 30º C was measured close to the detectors during operation, and therefore currents from 30 to 80 pA should be considered in the leakage current calculation.

Table 5.2 summarizes the different contributions for three possible values of the shaping time, 2 μs, 5 μs and 3.3 μs that was set to our modules. The main contribution comes from the noise in the preamplifier. Considering all together, a contribution to the energy resolution due to the readout electronics around 115-120 e ENC was calculated for our silicon modules, which is compatible with the noise values previously shown.

An accurate determination of the gains that relate the output data to the energy of the measured signals for all channels is essential. Errors in their determination result in a degradation of the energy resolution that can be appreciated in the broadening of the photopeak when events from all channels are considered.

Gamma sources of known energy are employed for this task. To obtain the ADC value

Contribution	noise (e ENC)		
	τ=2 μs	τ=3.3 μs	τ=5 μs
ENC_{int}	45	45	45
ENC_{pr}	106	-	78
ENC_{lc}	34-42	43-55	53-67
ENC_{tot}	120-123	-	104 - 112

Table 5.2: *Different contributions to the noise for three values of the shaping time*

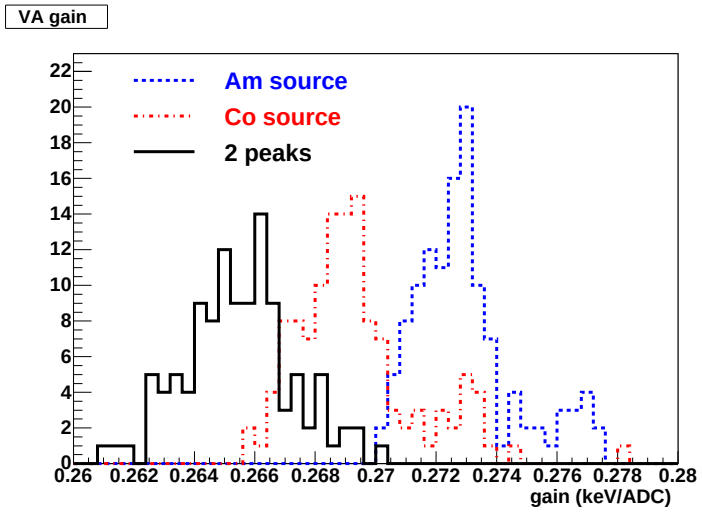

Figure 5.13: *Distribution of gain factors obtained with one energy value (either ^{241}Am or ^{57}Co source) or two values, employing both sources.*

corresponding to the photopeak, the data are histogrammed after pedestal and common mode correction, and the photopeak is fitted with a gaussian function to obtain its mean value. Determining the position of the photopeak for two or more energy values allows to fit a straight line and to obtain the gain as the slope, and a relative offset between the channels.

A simplification can be made assuming that the zero value of the ADC corresponds to zero energy, and no offset exists once pedestals have been subtracted. The gain can then be obtained from just one energy value.

Figure 5.13 shows the distribution of the gains obtained by the first method, employing the two peaks for their calculation, and the second method, employing just one peak of a ^{57}Co source or a ^{241}Am source. Differences of about 2% are found.

A ^{241}Am spectrum has been calibrated calculating the gains with the two methods. The calibration of the data taken with a 1 mm thick detector with one energy value yields an energy resolution of 0.54 keV (1.26 keV FWHM), including data for the 256 channels in the module. If two sources are employed for calibrating the detector, the resolution obtained is 0.5 keV (1.19 keV FWHM), indicating that the calibration is better with this method. However, unless the data can be taken with just one source or the two sources simultaneously, this method is more time consuming than the previous one, and the improvement is not significant for data taking.

Module	resolution (keV sigma)	resolution (keV FWHM)	noise (e ENC)
A	0.495 ± 0.004	1.165 ± 0.009	138
H	0.543 ± 0.002	1.278 ± 0.005	151
F	0.582 ± 0.002	1.370 ± 0.005	162
G	0.616 ± 0.004	1.450 ± 0.009	171
B	0.642 ± 0.002	1.511 ± 0.005	178

Table 5.3: *Energy resolution for 5 silicon modules*

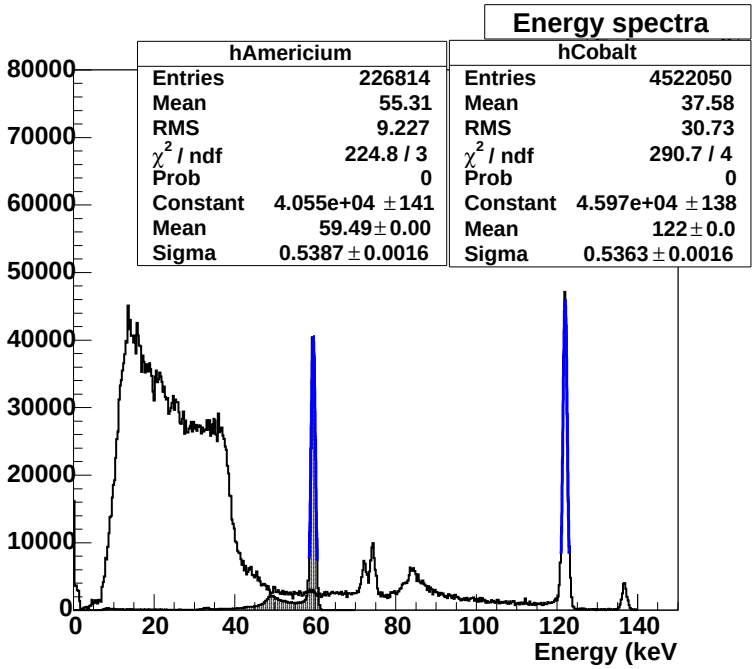

Figure 5.14: *^{241}Am and ^{57}Co energy spectra for a 1 mm thick detector, including data from all 256 channels in the silicon module.*

Table 5.3 shows the energy resolution obtained fitting the 59.5 keV peak of a ^{241}Am spectrum with a gaussian function for 5 silicon modules, four of them 1 mm thick, and one (module A) 500 microns thick. Fig 5.14 shows the ^{241}Am spectrum and a ^{57}Co spectrum measured with one of the 1 mm thick modules, including data taken with all 256 pads of the silicon sensor. In fig 5.15, a ^{241}Am spectrum measured with the 0.5 mm thick detector is shown.

TA calibration

When the chip is set to TEST mode, the calibration inputs, *cali* or *cale*, are enabled, and one of them is selected by the user. The *cali* input contains a $\approx$ 1.0 pF capacitor. For the *cale* input, a 1.8 pF capacitor must be placed close to the chip to prevent pickup.

The channel to be tested is set to TEST mode, and all channels except for that one should be masked. The selected channel is then sensitive to the test signals (a voltage pulse) injected to the calibration inputs.

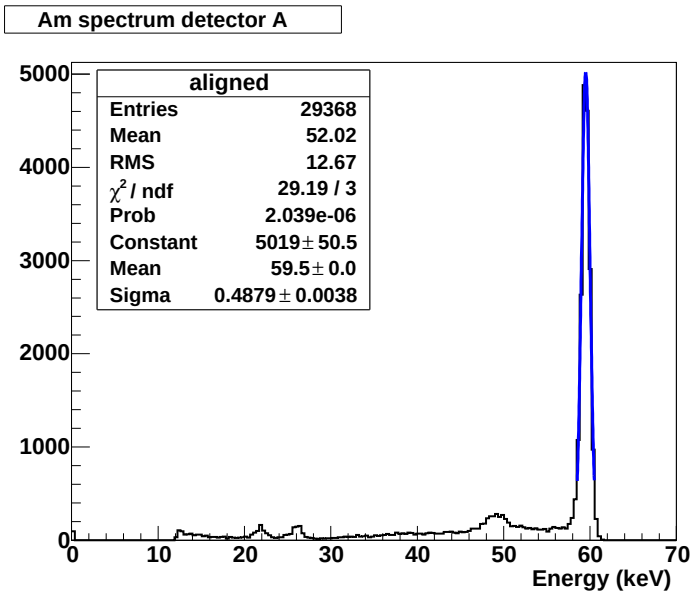

Figure 5.15: *Am spectrum for a 0.5 mm thick detector, including data from all 256 channels in the silicon module.*

The drawback of the method is that the noise in TEST mode is higher than in normal operating mode. It is therefore not possible to set the threshold as low as in the normal mode, and the tests must be carried out at a threshold higher than the lowest possible that will be set for data taking.

The response of the trigger discriminator for a given pulse might vary due to noise or jitter. Hence, a method needs to be established to determine a fixed value as a response for a given pulse amplitude. This can be achieved by studying the response of the chip for a given pulse while varying the threshold level. If the threshold is lower than the pulse, the signal will always be above the threshold level, and the chip will trigger every time the pulse is sent. If the threshold is much higher, the chip will never trigger. But for comparable levels, the noise can determine whether a trigger occurs or not. If a known number of pulses is sent for a given threshold value, and the number of triggers obtained is plotted versus the threshold value, a graph with a characteristic shape known as s-curve is obtained (fig 5.16). Assuming that the noise follows a gaussian distribution, the shape of the s-curve corresponds to the error function, that is the integral of the gaussian function. Its slope is related to the standard deviation of the gaussian function.

$$erfc(x) = 1 - erf(x) = \frac{2}{\sqrt{\pi}} \int_x^{\infty} e^{-z^2} dz; \tag{5.2}$$

where

$$x = \frac{threshold - 50\%\ point}{\sqrt{2}\ noise}$$

The fit of the curve with the error function or complementary error function allows two important parameters to be determined. The slope provides an estimate of the noise of the system, around 6 keV in test mode. The 50% point, value at which the s-curve

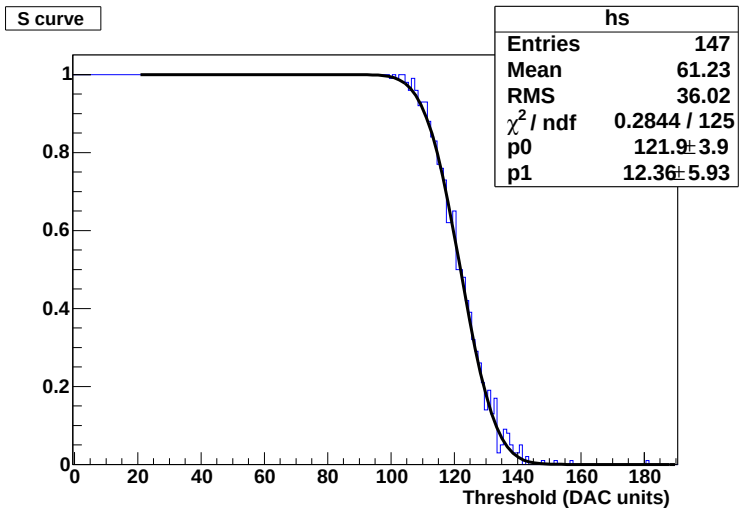

Figure 5.16: *S-curve corresponding to one channel in TEST mode, obtained with a calibration pulse and fitted with a complementary error function. The parameter p0 corresponds to the 50% point, and p1 to the noise.*

reaches half of its height, is independent of the noise, and therefore a good reference value for determining the threshold at which a channel triggers for a given pulse height.

To carry out these tests, the chip was set to TEST mode, channels were selected one by one, and a voltage pulse was sent to the chip through the *cali* input. To determine the point at which the selected channel triggers, a threshold scan is performed setting different values of the threshold and sending 100 pulses in each case. The number of times the channel gives a trigger divided by the number of pulses sent is plotted versus the threshold value. The resulting s-curve is fitted with the error function, and the 50% point obtained from the fit is taken as the value of the threshold at which the channel triggered.

THRESHOLD SPREAD.

As previously mentioned, although the same threshold level is set to the trigger discriminator of all channels in the chip, differences exist in the threshold from one channel to another. If the s-curves are fitted and the 50% points for a given calibration pulse are obtained for all channels in the chip, small variations of the value at which the channel triggers can be appreciated. Figure 5.17 shows these variations for all channels in one module, corresponding to two chips. The pattern and the spread vary from one chip to another. The spread for one chip is within 10 mV, as shown in fig 5.18.

The differences in the threshold cause that the minimum threshold at which the chip can be set while data taking is determined by those channels with higher 50% points. In addition, those channels will have higher noise occupancy, resulting in higher noise in the reconstructed images. The levels should be corrected such that all channels trigger at similar values, and the threshold level of the chip can be lowered. This can be done by a fine adjustment of the threshold that will be explained later.

The pattern is the same for pulses corresponding to energies less than 80 keV. However,

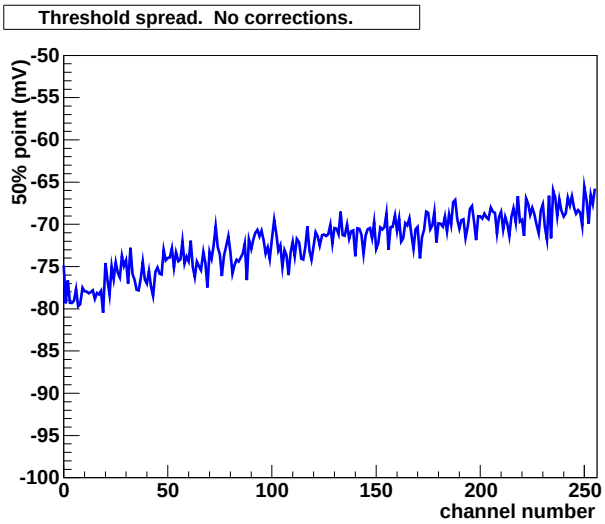

Figure 5.17: *50% points of all channels in two chips for a fixed calibration pulse.*

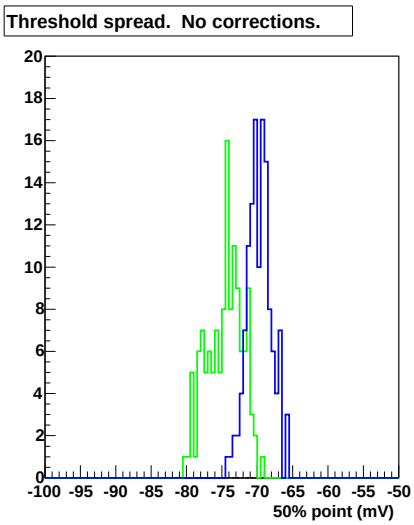

Figure 5.18: *Distribution of 50% points of all channels in two chips.*

differences exist for the 50% points if higher amplitude pulses are employed. If the pulse amplitude is increased, the reference value of the first channels is lower than that of the last channels (fig 5.19), and as the pulse height increases, a larger number of channels show this behaviour. This is due to a nonlinearity in the discriminator response that appears at lower values of the 50% point for the first channels in the chip, as will be explained next.

GAIN

Each channel has a gain stage between the preamplifier and the fast shaper to enhance the signal before it is shaped and discriminated. The gain stage can be enabled or disabled. If enabled, four values of the gain can be set. The first of them implies no additional gain, and the three remaining have different values. All of them invert the signal, so negative thresholds must be set in case it is enabled.

The value of the gain set to one channel can be calculated with the method previously described, finding the level at which the chip triggers for different amplitudes of the input pulse, and plotting them versus the calibrated pulse amplitude. The result for one channel is shown in fig 5.20. The fit of a straight line gives a gain of -1.053$\pm$0.006 mV/keV (23.6$\pm$0.13 mV/fC).

The variations in the values of the gain from one channel to another in one chip have also been studied, resulting in a mean value of -1.043 mV/keV (23.4 mV/fC) and a variation of 0.019 mV/keV in the gain distribution for pulses up to 59.5 keV (figs 5.21 and 5.22). The gain values might slightly vary from one chip to another.

If higher values of the pulse amplitude are considered, a non linearity in the gain is found. The values for two channels in one chip are shown in figs 5.23 and 5.24. This measurements correspond to a module different to the previous one, with a larger threshold range. Two linear ranges can be seen, and the transition point varies from one channel to another, causing the relative variations in the threshold level seen in the previous section.

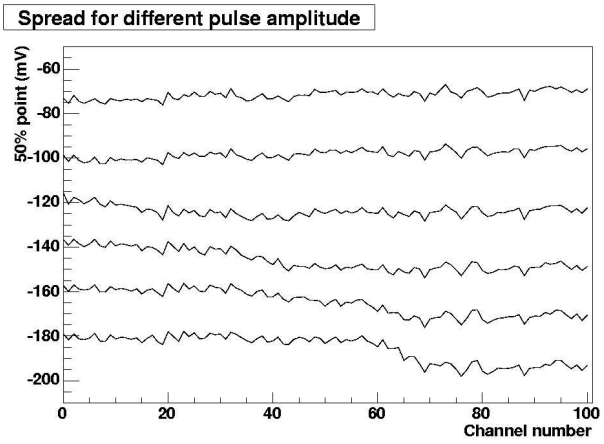

Figure 5.19: *50% points of the first 100 channels in one chip for different amplitudes of the calibration pulse. The upper distributions in the figure correspond to lower pulse amplitude.*

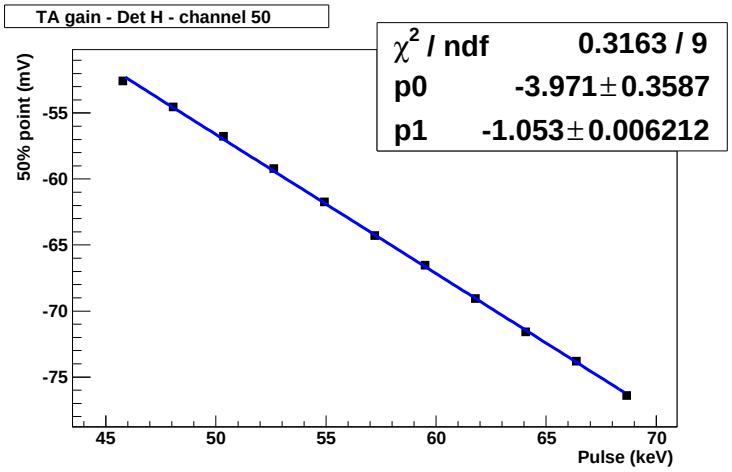

Figure 5.20: *Gain calculation for channel 50.*

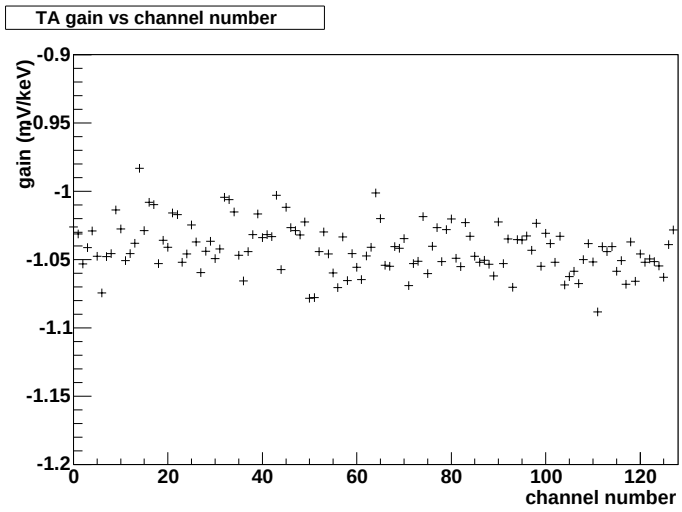

Figure 5.21: *Calculated gain for the 128 channels in one chip.*

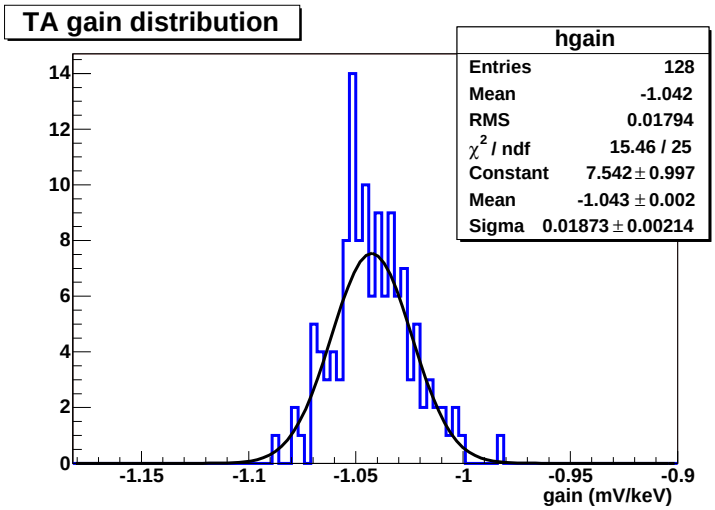

Figure 5.22: *Distribution of calculated gains of the 128 channels in one chip.*

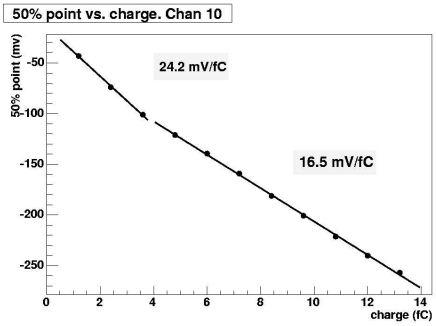

Figure 5.23: *Calculated gain for channel 10. Two linear ranges can be seen, and the transition point varies from one channel to another.*

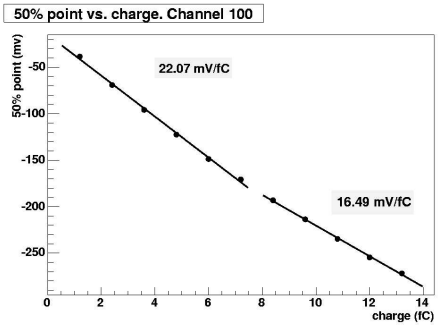

Figure 5.24: *Calculated gain for channel 100. The transition point sepparating two linear ranges appears at higher input charges.*

This effect should be taken into account for high thresholds.

COMPARISON WITH THE SOURCE

In order to validate the method, a ^{241}Am source has been employed to perform the same exercise as explained for the calibration pulse. The advantages of using the source are that the chip can be tested in normal operating mode, and that the noise is lower, allowing to test it at lower triggering values. However, it has two main drawbacks. To perform this test, a detector must be bonded to the chips to provide the triggering signals, In addition, the method is slower, since the rate of the calibration pulse can be much higher than the rate of photons coming from the source.

The procedure is similar to the one previously mentioned. The chip is masked except for the channel to be tested, but in this case it is not set to TEST mode. Instead, the chip is triggered by the signals generated in the detector by the 59.5 keV photons coming from the source. The number of triggers will decrease as the threshold increases. For each threshold value, the number of triggers in a determined time interval is recorded and the s-curve is fitted.

The TA noise can be obtained from the fit of the s-curve. This value will determine the threshold that should be set, and therefore the minimum energy and scattering angle that can be measured, since a high noise occupancy results in an increase of the dead time that reduces the efficiency. Fig 5.25 shows the result obtained for one channel with the ^{241}Am source. The TA noise distribution for all channels in one chip is shown in fig 5.26. The values obtained are close to 1 keV sigma.

The 50% points obtained for each channel with the ^{241}Am source are compared to those obtained with the pulse generator. The result is shown in fig 5.27. The pulse amplitude has been adjusted to trigger at values similar to the ^{241}Am source. The distribution of the differences with both methods is shown in figure 5.28. The agreement is within the errors obtained from the fit of the s-curves, confirming the validity of the method. The same exercise was performed with no source, yielding a similar pattern.

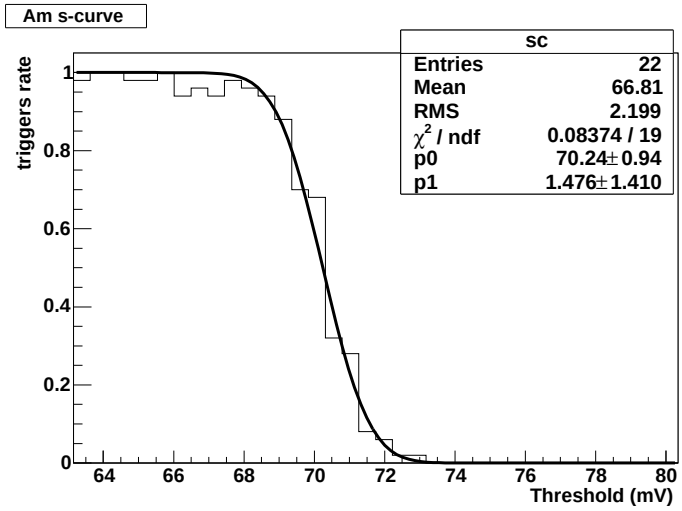

Figure 5.25: *S-curve obtained with a ^{241}Am source. The TA noise is obtained from the fit.*

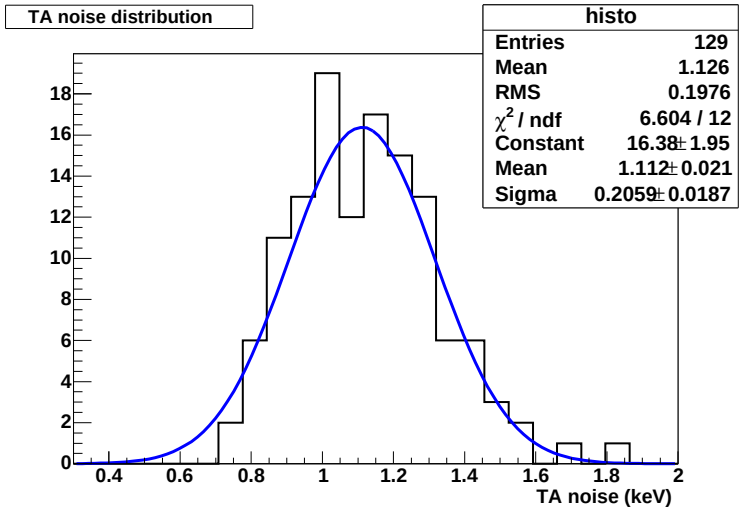

Figure 5.26: *Distribution of TA noise values for all channels in one chip.*

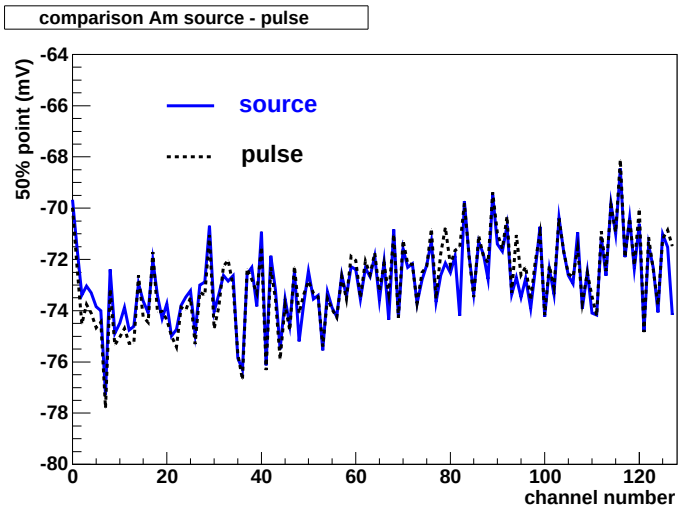

Figure 5.27: *Comparison of the 50% points of all channels in one chip obtained with the calibration pulse and with the* ^{241}*Am source.*

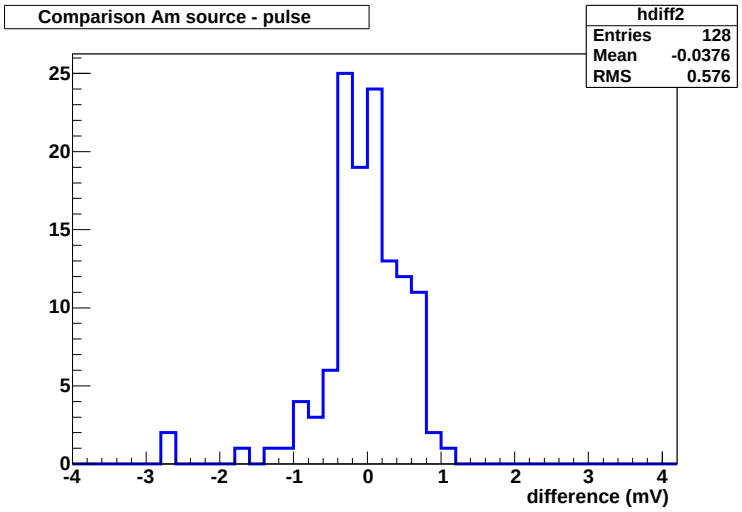

Figure 5.28: *Distribution of the difference for each channel of the 50% points obtained with the calibration pulse and with the* ^{241}*Am source.*

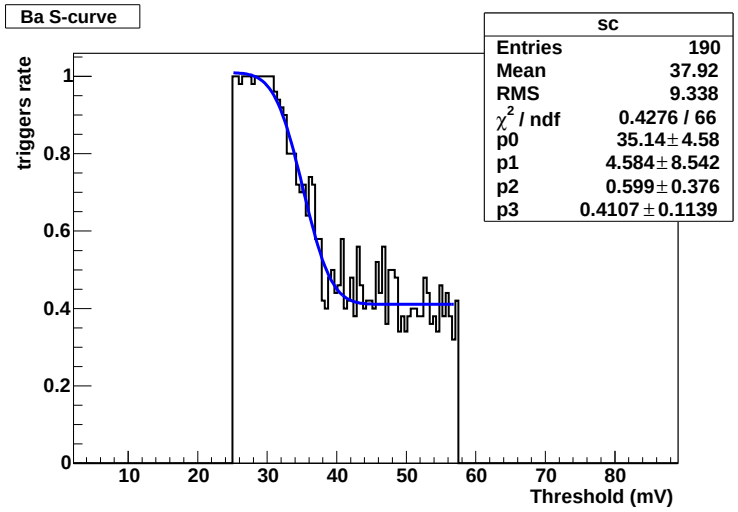

Figure 5.29: *S-curve obtained with the ^{133}Ba source.*

Source	Energy (keV)	50% point
^{133}Ba	31	-35.14
^{241}Am	59.5	-66.27

Table 5.4: *Results of fitting the s-curve obtained with two radioactive sources with the complementary error function.*

The gains obtained with the source and with the pulse generator have also been compared. For one channel, data have been taken with a ^{241}Am source and a ^{133}Ba source. The discriminator response can deviate from linearity for values close to zero, and therefore those measurements with no source have not been considered for the gain calculation.

The ^{133}Ba source has the disadvantage that it emits photons with different energies, and X-rays from the daughter, ^{133}Cs. Table 6.11 in chapter 6 shows the different decay energies from ^{133}Ba.

The 31 keV X-ray was employed to perform these tests, due to the higher rate of photons with this energy. However, contributions from other peaks are also measured. The ^{133}Ba s-curve (fig 5.29) was therefore fitted with the error function plus a flat background. The 50% points measured for one channel with the ^{241}Am and ^{133}Ba source are shown in table 5.4. The calculated gain is -1.09±0.5 mV/keV, compatible with the result obtained with the pulse generator (fig 5.20) -1.053±0.006 mV/keV.

THRESHOLD ALIGNMENT

As previously mentioned, the chip allows one to correct for the small differences among channels in the threshold value. This is done by means of a 3 bit DAC which is set for each channel and whose value is specified to the chip in the control register.

The offset change in the discriminators is achieved by adding or subtracting a current over a resistor. It is proportional to a reference current, which is adjustable, and this value is selected by the 3 bit pattern of each DAC.

The 3 bits allow for 8 possible offsets, two of which are the same and correspond to

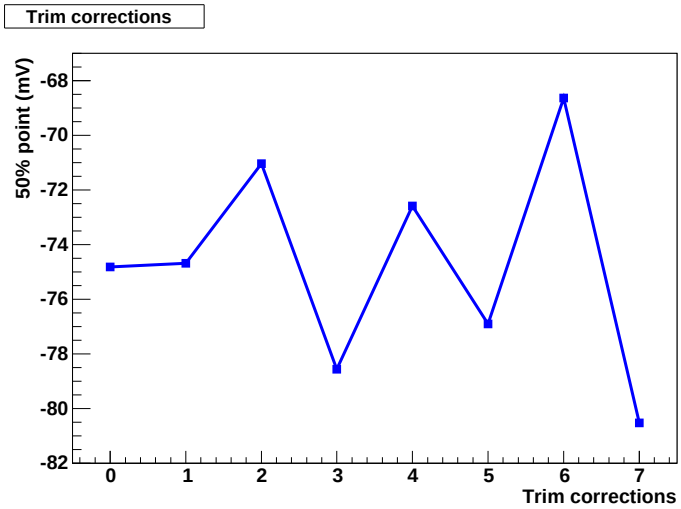

Figure 5.30: *Possible values of the trim corrections, corresponding nominally to the reference value (values 0 and 1)* ± 6, ± 3 *and* ± 9 *mV.*

a correction of 0 mV, the reference threshold value is left unchanged. The 6 remaining possibilities increase or decrease its value. If the reference current is left to be internally generated by the chip, the threshold will be shifted with a nominal step value of 3 mV, the possible correction values being ± 3, ± 6 and ± 9 mV. The 50% points obtained setting the different possible corrections for one channel are shown in fig 5.30.

The trim values are obtained calculating the mean value of the 50% points for all channels in the chip, and finding for each channel the correction that minimizes the spread. However, it must be taken into account that if the net sum of the added and subtracted currents is not zero, a common term offset in the threshold value will occur (figs 5.31 and 5.32) resulting in a shift of the reference threshold value for all channels. Thus, the chip triggers as if a different reference value was applied by the user. The adequate corrections must be such that the currents are compensated.

Figure 5.33 shows the results before and after correcting, when the values of the currents are compensated (*compensated* corrections) and the corrections have been calculated for each chip independently.

Figure 5.34 shows the resulting distributions before and after correcting, where it can be seen that the corrections allow to reduce the spread to within 2-3 mV with the nominal corrections of $\approx \pm 3$ mV steps.

The offset due to the nonzero sum of corrections has been calculated. Data are taken setting to the chip different values of corrections that are not compensated, and generating different values of the offset. The average value of all channels is calculated, and the difference with the average value when no corrections are applied is found in each case. This difference is plotted versus the result of summing the corrections set to the chip (fig 5.35). The fit with a straight line shows its linear behaviour. Further measurements extend the linear range to sums from -1000 to 600 mV.

If, as in our case, more than one chip is necessary for reading out all channels of a detector or several detectors, the threshold level should be as similar as possible for all

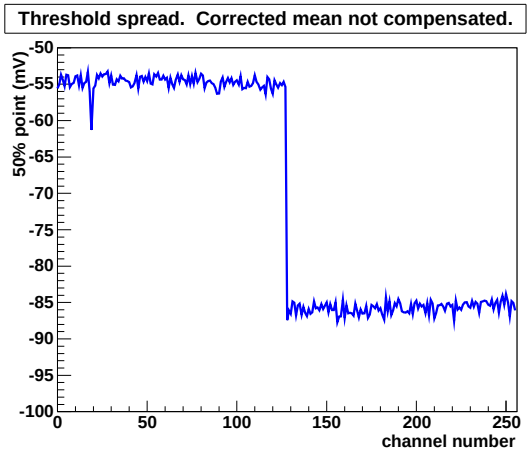

Figure 5.31: *50% points of all channels in two chips for a fixed calibration pulse with non-compensated corrections. An offset is observed.*

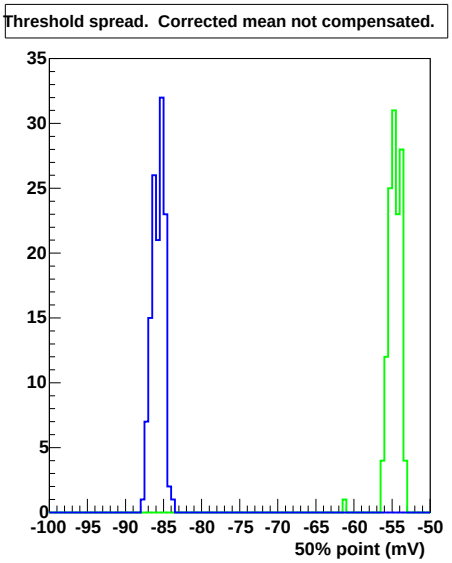

Figure 5.32: *Distribution of 50% points of all channels in two chips with non-compensated corrections.*

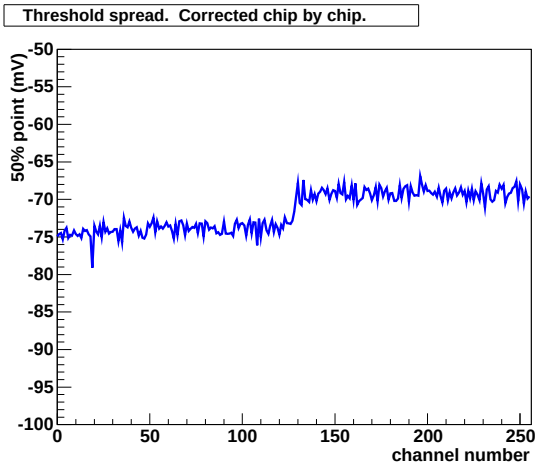

Figure 5.33: *50% points of all channels in two chips for a fixed calibration pulse with compensated corrections.*

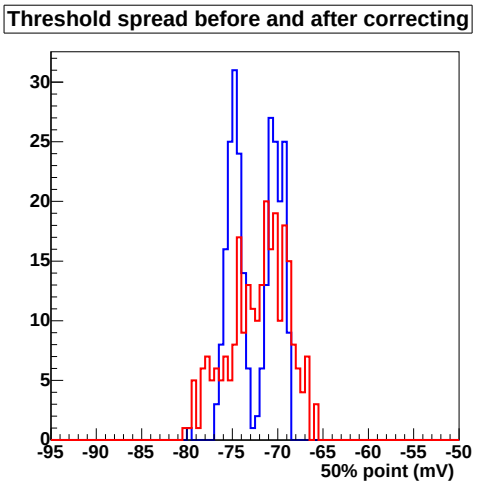

Figure 5.34: *Distribution of 50% points of all channels in two chips before (broad distribution) and after (sepparate peaks) correcting.*

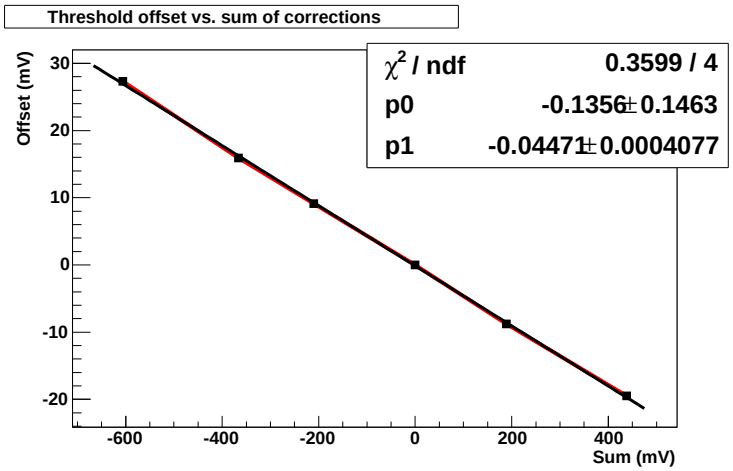

Figure 5.35: *Offset of the threshold value set to the chip versus total sum of trim corrections.*

channels in the module. The corrections have also been calculated considering two chips together, finding the average value of the 50% points of all channels and determining the corrections with respect to this value. The result is shown in figure 5.36. Even if the corrections are applied, a small offset from one chip to the other still occurs. As a consequence, the possibility of setting the threshold level independently for each chip to correct for these small differences is an essential requirement.

5.2 Absorption detector

The absorption detector consists of three scintillator modules situated on both sides and below the scatter detector. The modules (fig 5.37) were obtained from an existing ring tomograph, SPRINT II [108].

The choice of the second detector was driven by availability, and it is far from the optimum. It was originally designed to be employed with a mechanical collimator, and its countrate capability is limited. Its energy resolution is also less than adequate when sources emitting photons of different energies are employed for data taking.

However, it fulfils the basic requirements of the absorption detector. The scattered photons are absorbed and their interaction position can be determined, allowing us to perform the necessary tests satisfactorily.

A high countrate scintillator detector is currently under development and will be employed in the next prototype [109].

5.2.1 Description

The active detector of each of the modules consists of 44 NaI(Tl) bars of dimensions 3 mm × 13 mm × 150 mm. Twenty Hamamatsu photomultiplier tubes (PMTs) are optically coupled to the scintillator bars by means of a 6 mm thick Pyrex window (fig 5.38). The tubes have 38 mm diameter, and they are closely disposed to cover the maximum

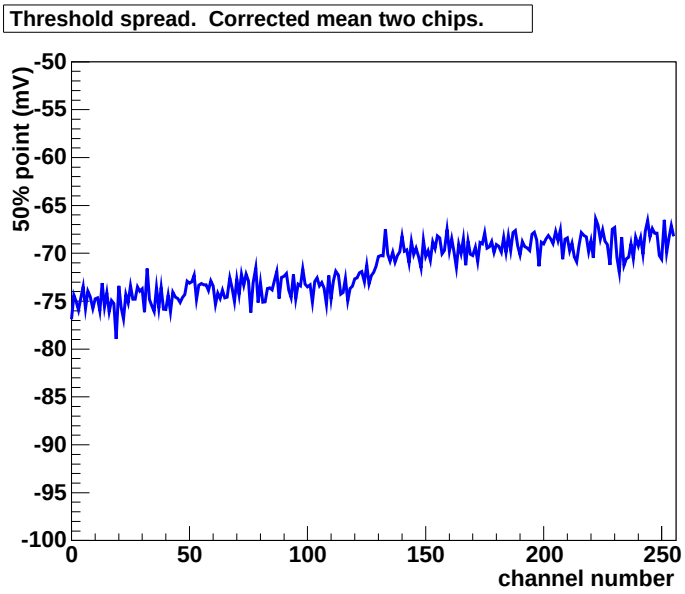

Figure 5.36: *50% points of all channels in two chips for a fixed calibration pulse with corrections calculated considering both chips together.*

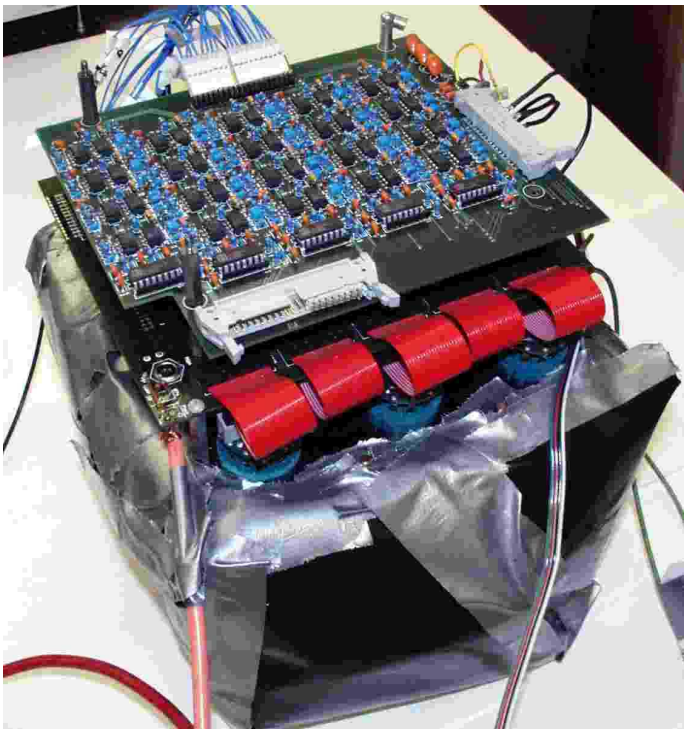

Figure 5.37: *Scintillator module obtained from an existing gamma camera head.*

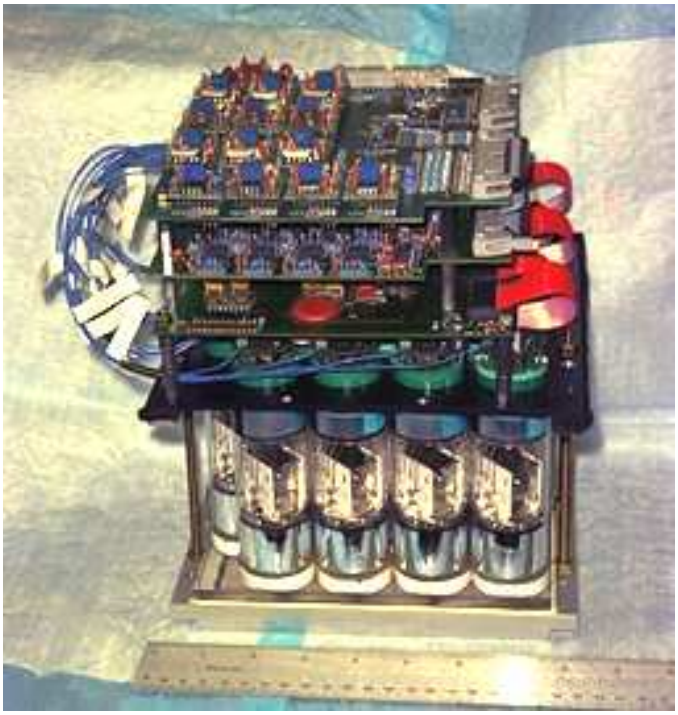

Figure 5.38: *Side view of the scintillator module, where the PMTs can be seen.*

scintillator area. Electronic boards, also integrated in the module, provide the output signals of each of the tubes, as well as the hardware sum of the 20 signals. The sum signal is fed to a constant fraction discriminator (CFD) that provides a NIM pulse at a constant fraction of the input pulse, reducing time walk. The pulse is employed as the trigger signal of the scintillator module. The individual signals of each PMT are fed to a CAEN VME peak sensing ADC for digitization, storage and further processing.

Energy resolution of 7 keV sigma (16.5 keV FWHM) for 122 keV photons and a position resolution about 1.5 mm sigma were measured when calibrating the modules, as it will be explained in the following section.

5.2.2 Calibration

The calibration of the scintillator modules has been done taking data with a gamma source placed in different positions in a regular mesh and studying the response of the scintillator as a function of the position. A set-up has been arranged with two PC controlled stages that move the source to the desired coordinates along the X and Y axis. The source is well collimated to ensure that gamma-rays only illuminate a highly localized region of the scintillator for each source position. The reference frame has been chosen such that the scintillator bars are parallel to the X axis, Y is across the bars, and the centres of the PMTs are disposed as it is shown in fig 5.39. For each position where the source was placed (x_{real}, y_{real}), the energy and the position (x_{calc}, y_{calc}) are calculated and compared with the known values of photon energy and real position.

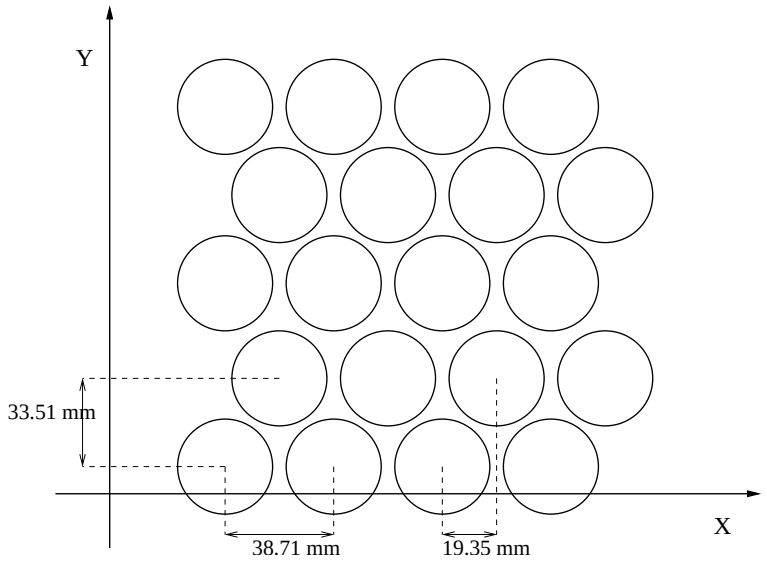

Figure 5.39: *Distribution of the 20 PMTs in the scintillator module.*

Energy calibration

The energy calibration of the detector aims to determine the energy measured at each calibration position (x_{real}, y_{real}) from the response of the PMTs. The total photon energy E_0 is the sum of the energies measured by each of the PMTs, E_i, which is assumed to be proportional to the digitized output of the PMT, ADC_i,

$$E_0 = E_T(x,y) = \sum_{i=1}^{N_{PM}} E_i(x,y) = \sum_{i=1}^{N_{PM}} ADC_i(x,y) \times g_i. \tag{5.3}$$

The gains of the PMTs, g_i, must be determined by the calibration procedure.

To ensure a perfect understanding and a correct energy calibration of the scintillator modules, a geometric model based on solid angle distributions has been developed. The model also takes into account the parameters obtained in the calibration measurements. For a given interaction in the scintillator, the signal given by each of the PMTs, assuming that they are situated in the same positions as in the scintillator, is simulated. Then, the signals of all PMTs are combined to reproduce the scintillator response.

The energy measured by the i^{th} PMT, E_i, is assumed to be a fraction of the total energy of the event, E_T, given by

$$E_i = E_0 \times w_i, \tag{5.4}$$

where w_i represents the response of the PMT to the photon interaction (*light response function* or $LRF_i(x,y)$) calculated at the hit position.

The shape of the light response function of a PMT as a function of the position can be obtained from the calibration data, since the ADC value obtained for a PMT at a given

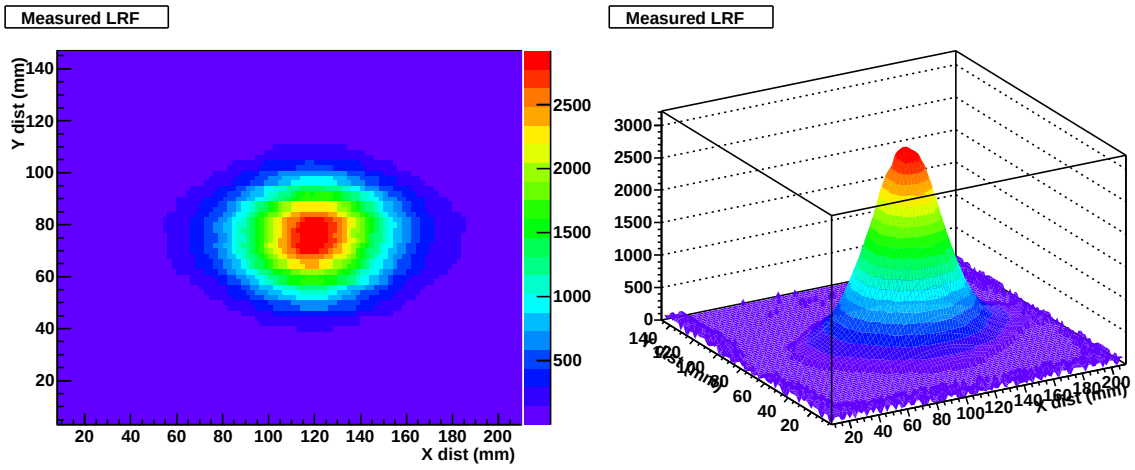

Figure 5.40: *Digitized output of one of the PMTs for all calibration positions.*

position is proportional to the light response function,

$$ADC_i = \frac{w_i \times E_0}{g_i}. \tag{5.5}$$

The values of the ADC measured at each position where the calibration source was placed (x_{real}, y_{real}) are shown in a 2D histogram in fig 5.40 for one of the PMTs.

The maximum value corresponds to the centre of the PMT, and it decreases with the distance to the centre. The resulting peak is a 2D gaussian function with different values of σ_x and σ_y. The maximum of the gaussian varies with the the PMT due to differences in the gain.

The light response function responds to geometrical considerations, and is mainly determined by the solid angle subtended by the area of the PMT from the point that is being considered. However, other factors such as the segmentation of the scintillator, variations in the scintillator surface treatment or a spatially non-uniform photocathode deviate its shape from the solid angle distribution.

The response of a scintillator module with similar characteristics as the ones employed in this prototype has been modelled, taking into account the previous measurements and assumptions. The response of each of the PMTs is simulated as a 2D gaussian function normalized to 1 in the peak and multiplied by the adequate factors to reproduce the measured response of the PMT at each position.

The response of the scintillator to photons interacting in the same positions as the calibration ones, and with the same energy, has been simulated. The total energy of a simulated event can then be calculated for each source position according to equation 5.3 as the sum of the energies measured by each PMT. The result is shown in fig 5.41. According to the model, the difference in the values of the total energy obtained for different positions is mainly due to differences in the geometrical acceptance of the PMTs.

In order to calculate the total energy at each point for the measured calibration data, the gains of all PMTs, g_i, must be determined. Since the total energy of an event is shared among several PMTs, the maximum value measured by one PMT when the source

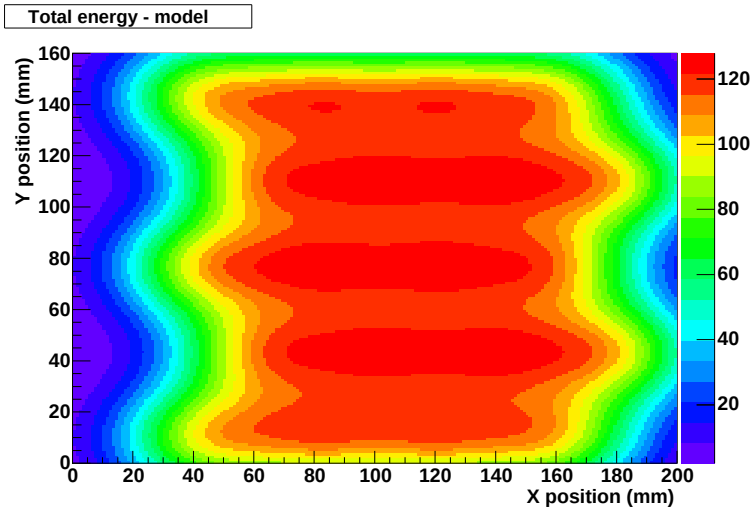

Figure 5.41: *Total energy calculated at each point according to the simulated scintillator model.*

is placed right under its centre does not correspond to the total energy of the event. The fraction of the total energy measured by the PMT when the source is placed at a given calibration point (x_{real}, y_{real}) can be estimated according to equation 5.5. For each PMT, this is done for all calibration points, and the fraction of the total energy obtained in each case is plotted versus the corresponding ADC value (fig 5.42). The gain of the PMT, g_i, is obtained by fitting a straight line.

Once the gains are known, the total energy in each point is calculated following equation 5.3. When the data are considered, a clusterization algorithm is applied to determine those PMTs that give a signal, to be included in the sum. The result for a given position is a nearly gaussian peak, with a standard deviation of 7 keV. The procedure is repeated for all positions, and the mean value of the energy peak is plotted for each position. The result (fig 5.43) reproduces the distribution obtained for the model (fig 5.41), proving that the model accurately represents the response of our scintillator module, and that the dependence of the energy on the position is mainly due to geometrical factors.

This information can be employed to correct for the differences in the total energy with the position, and to obtain similar values in all positions, with a method based on *geometrical considerations*.

According to the model, the differences in the total energy for different positions are due mainly to differences in the geometrical acceptance of the PMTs, represented by the LRF that is in turn related to the solid angle subtended by the PMT. The points where the calculated total energy is maximum correspond to those where the sum of the LRF of all PMTs (and therefore the sum of the solid angles subtended by all of them), is maximum.

At a given point (x, y), the fraction of the total energy measured is proportional to

$$\sum_{i=1}^{N_{PM}} LRF_i(x, y).$$

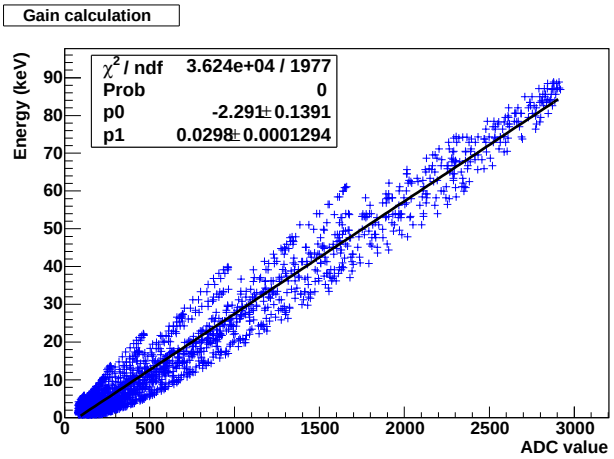

Figure 5.42: *Calculated fraction of the total energy vs. the digitized output for one PMT for all calibration points. The slope of the line resulting of the fit is the gain of the PMT.*

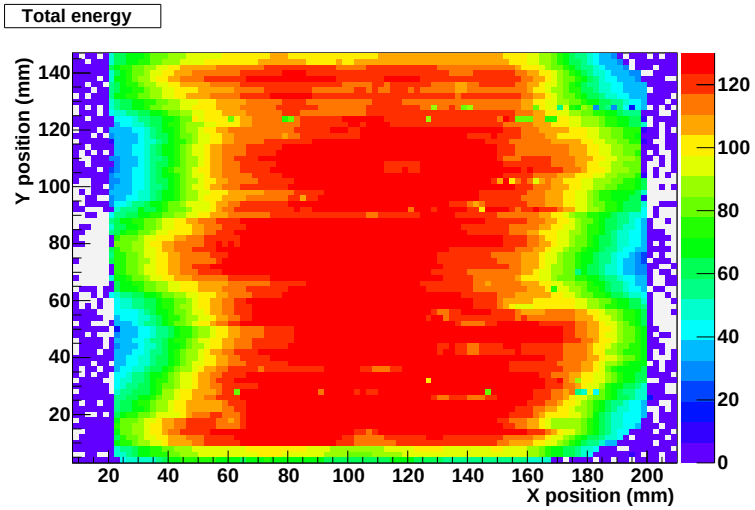

Figure 5.43: *Total energy calculated at each point for the calibration data.*

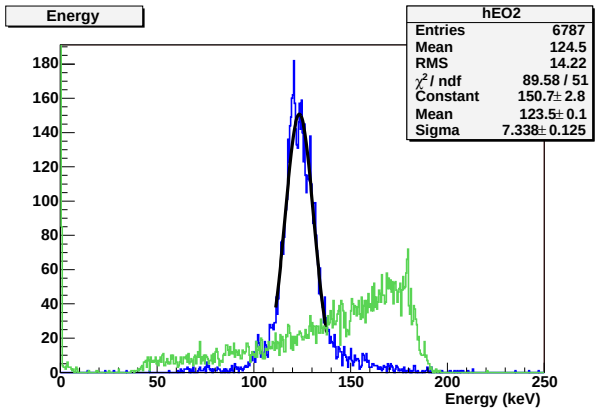

Figure 5.44: *Distribution of calculated total energy for all calibration points, before and after correcting.*

In the regions with full acceptance, close to the centre of the scintillator module, all the energy is measured, and the value of the previous sum is maximum

$$\sum_{i=1}^{N_{PM}} LRF_i(x,y) = LRF_{max} = constant.$$

In the regions where we do not have full coverage, the total energy calculated can be corrected multiplying by a factor that accounts for the lost energy,

$$E_{Tcor}(x,y) = E_T(x,y) \times cf_g(x,y),$$

where

$$cf_g(x,y) = \frac{LRF_{max}}{\sum_{i=1}^{N_{PM}} LRF_i(x,y)}.$$

The distribution of energies before and after correcting with this method for all positions is shown in figure 5.44. The resolution of the corrected peak, 16.5 keV FWHM, is compatible with the energy resolution of the scintillator for one position.

Position determination

In the position calibration, the positions calculated from the measured data (x_m, y_m) are compared to the real values in the regular mesh (x_{real}, y_{real}) where the source was placed. Two methods have been evaluated for the determination of the hit position, the *centroid method*, and the *maximum likelihood* method, the second one yielding better results. However, once the positions are calculated, given that the real positions are known in the calibration, a correction method can be applied to the calculated values to obtain the corrected coordinates (x_{cor}, y_{cor}). The calculation and correction methods will be explained next, and the results will be shown.

In the *centroid method*, the position of a hit (x_m, y_m) is calculated as the weighted average of the positions of the centres of the PMTs that give a signal (x_i^{PM}, y_i^{PM}). The

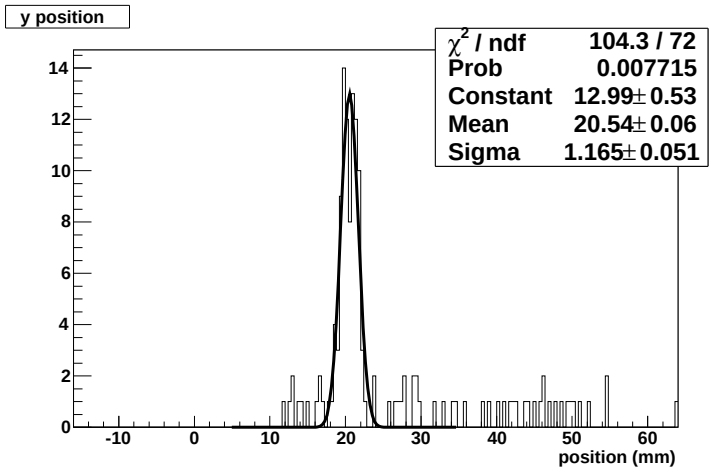

Figure 5.45: *Calculated Y position for one of the calibration points.*

weighting factor f_i corrects for the differences in the gains of the PMTs and other possible differences among them.

$$(x_m, y_m) = \sum_i^{N_{PM}} \frac{((x_i^{PM}, y_i^{PM}) \times ADC_i \times f_i)}{\sum_j^{N_{PM}} ADC_j \times f_j}$$

The positions of the PMT centres must be known or calculated with respect to the calibration reference frame. If, as in our case, the gains of the PMTs are employed as weighting factors f_i, the positions are obtained by the usual method of weighting with the energy collected in the PMT. With this method, the positions can be reconstructed with a statistical error of about 1.2 mm sigma (fig 5.45) for a ^{57}Co source. Figure 5.46 shows both the real and the reconstructed positions, where it can be seen that in the edges of the scintillator, the reconstructed positions are shifted towards the centres of the PMTs, degrading the spatial resolution.

The positions have also been calculated with our model, with the same method. The results, shown in fig 5.47 have the same tendency proving that the response is understood.

If this method is employed to determine the positions, a correction method that determines these deviations and relates the calculated positions to the real ones needs to be applied.

The second method tested for position determination is the *maximum likelihood* method [110]. In a model of the Anger scintillation camera with M photomultipliers placed in the image plane, the scintillation point (X,Y) is assumed to be a uniformly distributed random vector in the object plane. A given scintillation point (X,Y) = (x,y) will cause counts in the M photomultipliers in the image plain, according to a non-homogeneous Poisson process with intensity proportional to the solid angle, i.e., if A is the area of a PMT in the image plane, the conditional probability of k arrivals given a scintillation at (x,y) is given by

$$P_{N_A|XY}(k|x,y) = e^{-w_A(x,y)} \frac{[w_A(x,y)]^k}{k!}$$

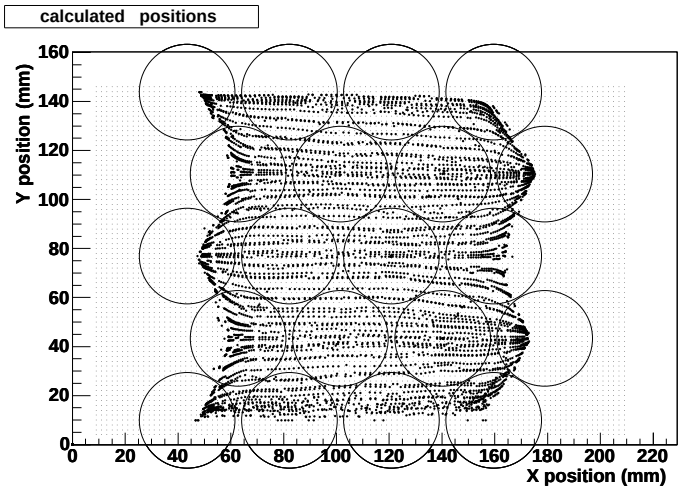

Figure 5.46: *Calculated positions for all calibration points with the centroid method. The regular mesh on the background of the image represents the coordinates of the real calibration points. The circles represent the PMTs at their positions in the scintillator module.*

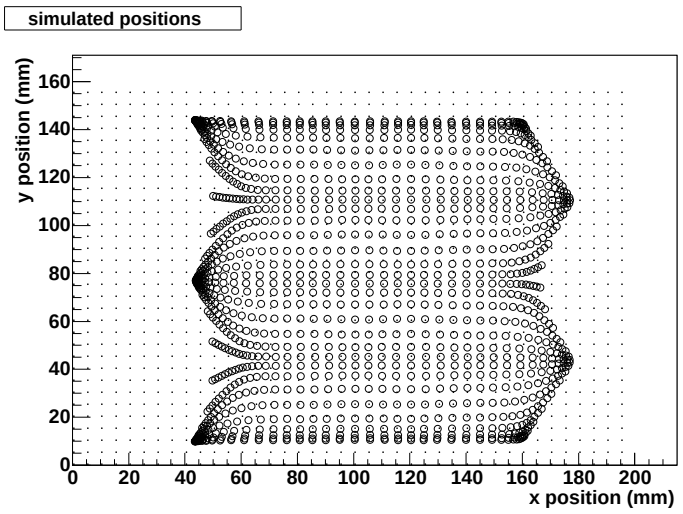

Figure 5.47: *Calculated positions with the centroid method for simulated data.*

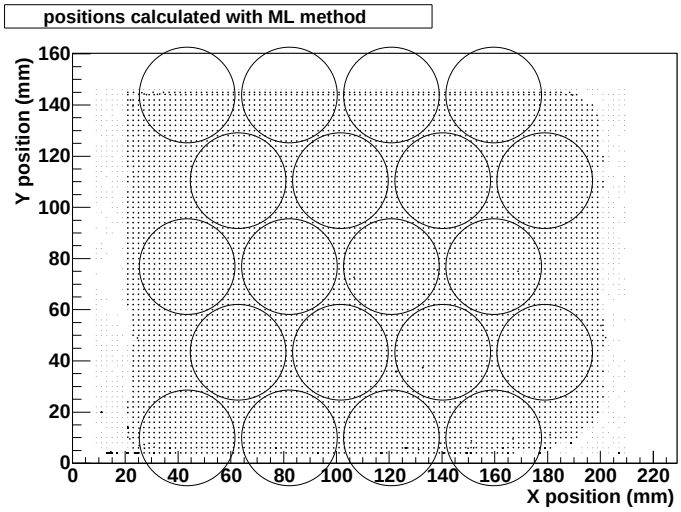

Figure 5.48: *Calculated positions for all calibration points with the maximum likelihood method.*

where N_A is the random variable giving the number of counts in A and $w_A(x,y)$ is the solid angle subtended by A to (x,y). However, as explained in the previous section, the solid angle does not reproduce the real light distribution in the scintillator, and the LRF should be employed instead.

Given the sample values $N_i = n_i, i = 1....M$, the maximum likelihood estimate of the scintillation point (x,y) is given by the value of (x,y) that maximizes the conditional probability

$$P_{N_1....N_M|X,Y}(n_1.....n_m|x,y) = \sum_{i=1}^{M} n_i \;\; ln\; w_i(x,y) - w_i(x,y),$$

$$(x,y)_{ML} = argmaxP,$$

where n_i are the number of counts measured by the i^{th} PMT and w_i is the light response function of the PMT at position (x,y). The maximum value is obtained for the most likely position.

For a calibration performed with 2 mm spacing between the source positions in X and Y, the reconstructed positions perfectly reproduce the real ones (fig 5.48) for almost all the calibrated points. For a calibration with 1 mm spacing in Y and 4 mm in X there are still differences between the real and the calculated positions, and a correction method can also be applied to improve the results. The main drawback of this method is the computation time, much longer than with the previous method.

Position correction

Two methods, the *equation system* method and the *bilinear interpolations* [111, 112, 113] were tested for correcting the positions calculated with any of the previous methods, to obtain values closer to the real position of the source.

The corrections are intended to be applied to the scintillator positions determined from the coincidence data, as it will be done in next chapter. However, for testing purposes they will be applied here to the calibration data. In this case, the point to be corrected (x_m, y_m) is also one of the points of the calibration mesh.

In both methods, the positions of four points in a square that are the closest to the point to be corrected (x_m, y_m) have to be determined from the calibration data. For these four points the calculated positions (x_j, y_j) and the corresponding real values (x_{real_j}, y_{real_j}) with j=1,...4, are found and stored. Then, the correction method is applied.

In the *equation system* method, an equation system of four equations with four unknowns is solved with the x and y coordinates of the four selected points, and the x coordinates of the real positions. The procedure is repeated for the y coordinate.

$$x_{real_j} = Ax_j + By_j + Cx_jy_j + Dx_j^2$$
$$y_{real_j} = Ex_j + Fy_j + Gx_jy_j + Hy_j^2$$

where j=1...4 in each system correspond to the 4 points previously found. Once the 8 coefficients are known, the equations are solved for point to be corrected, (x_m, y_m), giving as a result the corrected coordinates (x_{cor}, y_{cor}).

$$x_{cor} = Ax_m + By_m + Cx_my_m + Dx_m^2$$
$$y_{cor} = Ex_m + Fy_m + Gx_my_m + Hy_m^2$$

The *bilinear interpolations* are the simplest interpolation method in two dimensions. Four points have to be determined from the calibration data, such that

$$x_{11} \leq x_m \leq x_{12}$$
$$x_{21} \leq x_m \leq x_{22}$$
$$y_{11} \leq y_m \leq y_{21}$$
$$y_{12} \leq y_m \leq y_{22}$$

where x_m, y_m are the coordinates of the point to be corrected, and the four points are arranged in the way shown in fig 5.49. Assuming that

$$x_{11} \approx x_{21}$$
$$x_{12} \approx x_{22}$$
$$y_{11} \approx y_{12}$$
$$y_{21} \approx y_{22}$$

the following quantities can be defined:

$$x_1 \equiv \frac{x_{11} + x_{21}}{2}$$
$$x_2 \equiv \frac{x_{12} + x_{22}}{2}$$

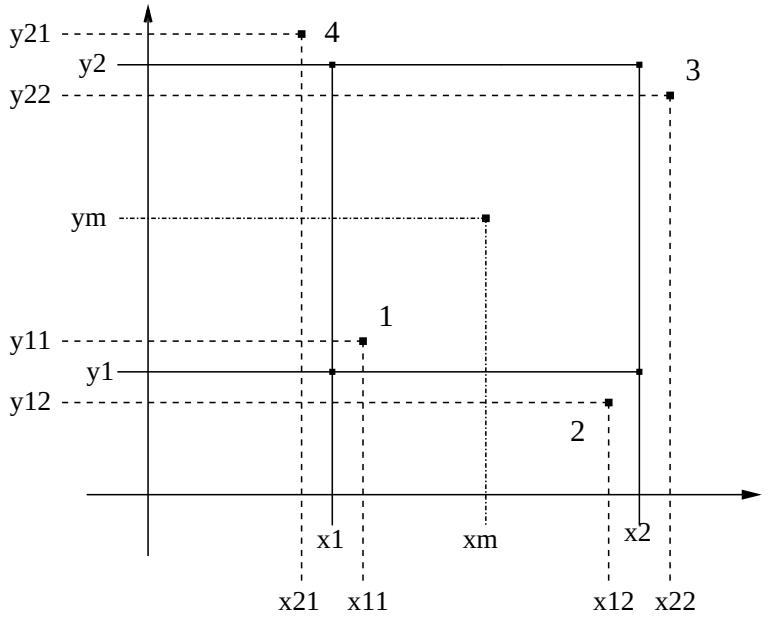

Figure 5.49: *Relative position of the four points considered in the bilinear interpolations position correction method.*

$$y_1 \equiv \frac{y_{11} + y_{12}}{2}$$
$$y_2 \equiv \frac{y_{21} + y_{22}}{2}$$

The corrected position is calculated from the following expression:

$$x_{cor} = (1-t)(1-u)x_{real_1} + t(1-u)x_{real_2} + tux_{real_3} + (1-t)ux_{real_4}$$
$$y_{cor} = (1-t)(1-u)y_{real_1} + t(1-u)y_{real_2} + tuy_{real_3} + (1-t)uy_{real_4}$$

where t and u take values from 0 to 1, and are defined as:

$$t = \frac{x_m - x_1}{x_2 - x_1}$$
$$u = \frac{y_m - y_1}{y_2 - y_1}$$

Both methods have been applied to the positions determined with the centroid method. Although the corrected positions should match exactly the real positions for the calibration data, the correction methods fail when the calculated points corresponding to different positions are too close, as it happens near the edges of the scintillator module. For the central region, the results are satisfactory.

The difference between the real and the corrected position are shown in figures 5.50 and 5.51 for the *equation system* method and the *bilinear interpolations* method respectively, and are summarized in table 5.5, where the results of the standard deviation obtained fitting the peaks with a gaussian function are presented. In both cases, the difference is negligible compared to the statistical error obtained in the previous section (fig 5.45).

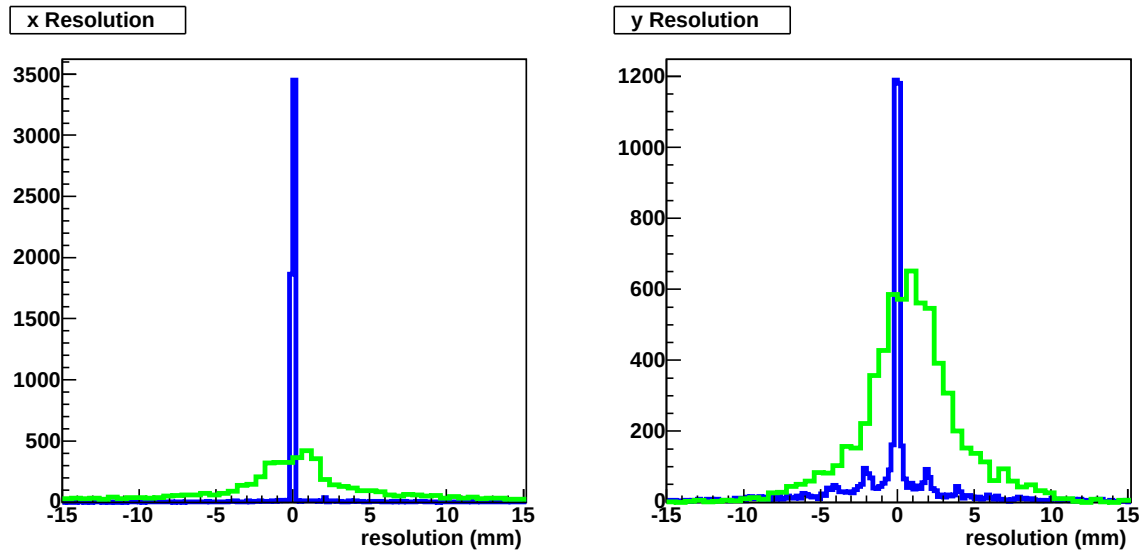

Figure 5.50: *Distribution of the differences in X and Y coordinates between real positions and calculated positions before and after correcting with the equation system method.*

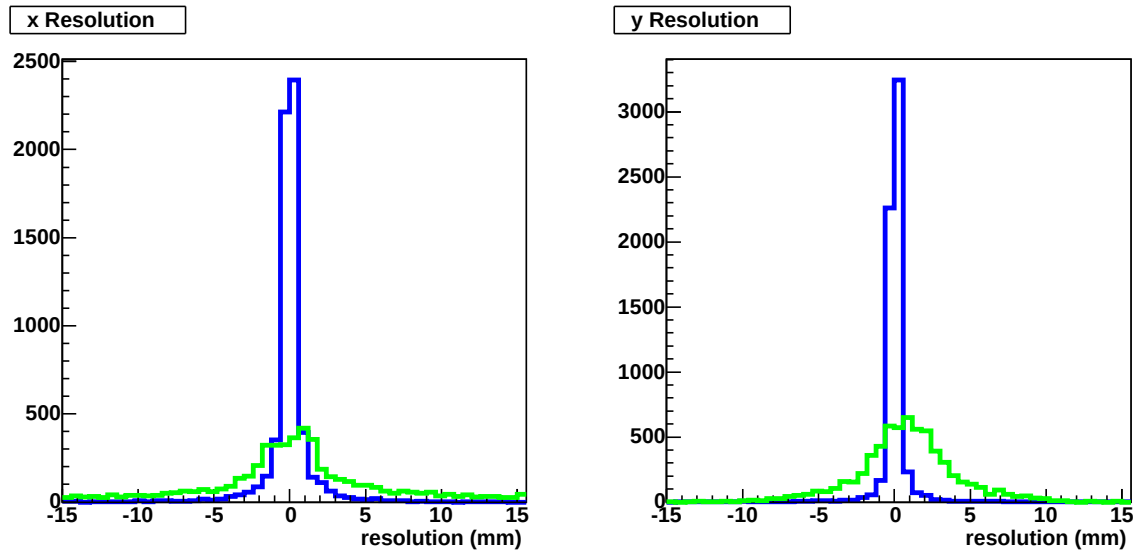

Figure 5.51: *Distribution of the differences in X and Y coordinates between real positions and calculated positions before and after correcting with the interpolation method.*

method	diff X (mm)	diff Y (mm)
system	0.08	0.14
interp	0.45	0.36

Table 5.5: *Standard deviation of the distributions of the differences in X and Y coordinates between real positions and calculated positions corrected with both correction methods.*

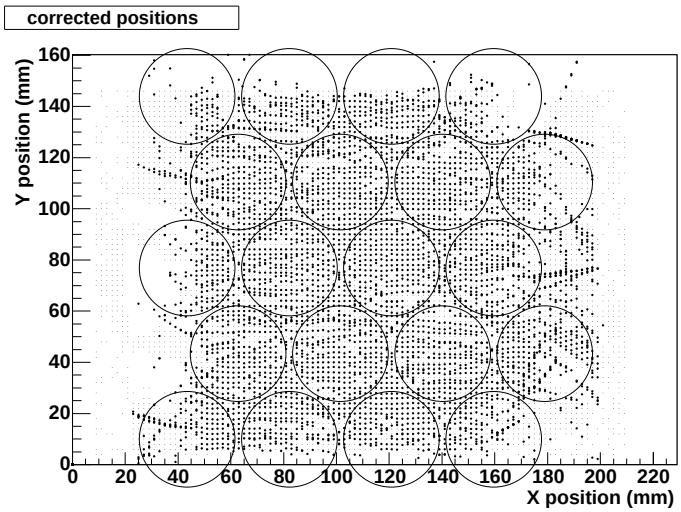

Figure 5.52: *Calculated calibration positions corrected with the equation system method.*

However, the best results were obtained with the *equation system* method, and it is the one that will be employed for data analysis. The reconstructed positions are shown in fig 5.52.

This correction method can also be applied to the positions calculated with the maximum likelihood method, when the calculated positions do not match exactly the real positions. The results are improved, and it has the advantage that events closer to the edges of the scintillator can also be corrected.

5.3 Prototype description

Figure 5.53 shows an exploded view of the prototype where the different components can be seen. The scatter detector, the silicon stack, is surrounded by three scintillator modules, two on the sides and one below, at about 62 mm distance from the silicon centre. The detectors are supported by a metal structure that was specifically designed for this prototype to ensure the correct positioning of the detectors and the grounding of the electronic devices. A cooling circuit for the silicon detectors via air flow has also been incorporated. The source can be located inside or outside the box enclosure, pointing toward the silicon array.

The trigger signal is initiated by the coincidence of the scatter detector and any one of the scintillator modules. This requires a coincidence circuit and the use of the external trigger in the silicon detector readout system. A simplified schematic diagram of the

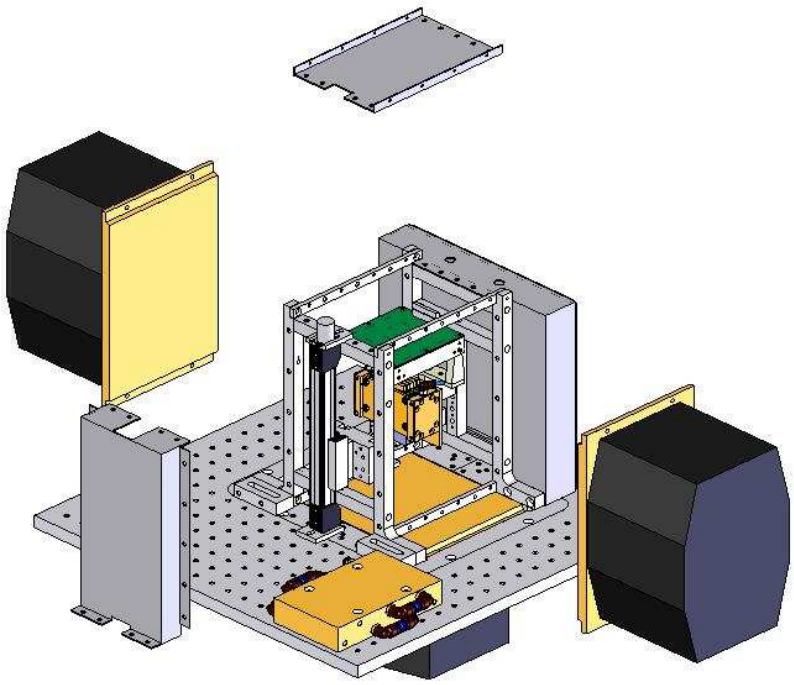

Figure 5.53: *Exploded view of the prototype. The scatter detector, in the centre, is surrounded by three scintillator modules, on both sides and below.*

electronics employed for data acquisition is shown in fig 5.54.

When a coincidence event occurs, a signal is triggered by the coincidence of the silicon detector and one of the scintillators. This signal is sent as a gate to the ADC of the corresponding scintillator, ensuring that only the one that triggered will be read out. The trigger signal is then employed to start the readout of the silicon module. The OR signal of the three possible coincidences is the trigger signal of the prototype and is employed to start the readout of the silicon module. This way, only coincidence events will be read out, reducing dead time and avoiding signal pile-up. It is also employed to prevent the silicon from triggering until the readout is finished. In case there is a trigger in the silicon module but no coincidence, a reset signal must be sent to the silicon. This signal is inhibited in case a coincidence occurs and the silicon is read out.

The coincidence window was set to 200 ns after studying the distribution that results from plotting the time difference between silicon and scintillator triggers in one module (figure 5.55). The peak is fitted with a gaussian function with a sigma of 40 ns, and it has a tail due to the low energies in silicon, for which the trigger signal is delayed due to time-walk. A narrow coincidence window would help to avoid random coincidences, but would also cut the low energy signals in silicon that result in a better resolution of the reconstructed images. The trigger signal of the scintillators was adjusted to have the three peaks at the same position.

The support structure was designed to ensure the maximum possible angular coverage with the available scintillators and enhance the efficiency. This has the disadvantage that the scintillator is placed close to the scatter detector and the spatial resolution influences the prototype resolution as explained in chapter 2. In this configuration it is also harder to

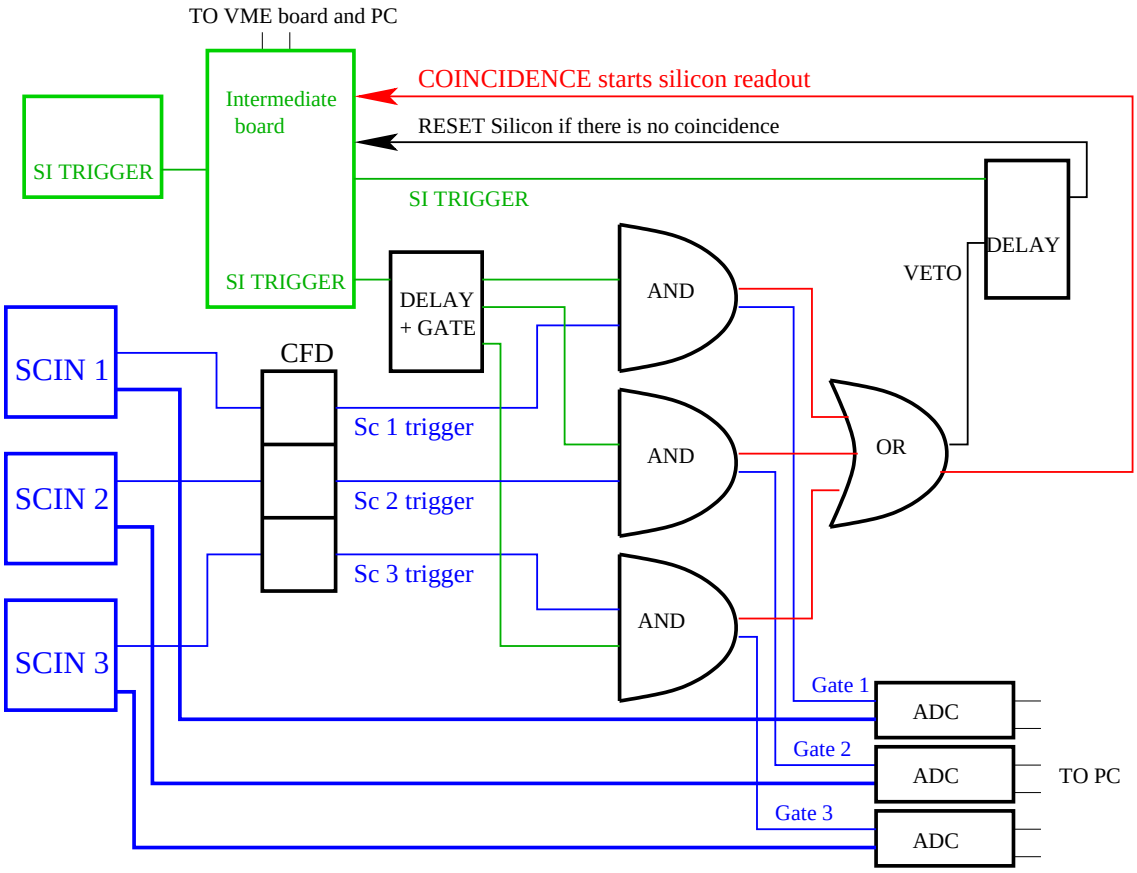

Figure 5.54: *Simplified schematic diagram of the electronics employed for the operation of the prototype.*

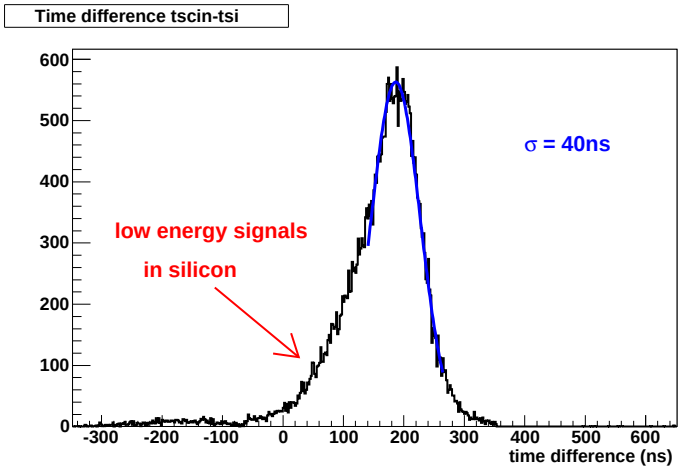

Figure 5.55: *Time difference between the silicon and the scintillator trigger signals obtained with a ^{57}Co source. The tail is due to the time-walk that affects the timing accuracy of low energy signals in the silicon detector.*

shield the detector from direct photons from the source, increasing the amount of random events. Placing the scintillators further from silicon improves the resolution, but restricts the angles detected resulting in an undersampling that affects the image reconstruction, as it will be explained in the following chapter. Larger second detectors designed for this particular application would provide greater flexibility.

Chapter 6

Results

In this chapter the results obtained with the prototype will be summarized. Results from a first test and two different runs of data taking are shown here. The test run (CERN, summer 2003) was intended to assess the possibility of taking coincidence data, and to verify the correct functioning of the coincidence setup and of the data acquisition software. At the same time, it allowed us to investigate the system behaviour for different geometrical configurations. Although the scintillator module was not calibrated and therefore images could not be reconstructed, interesting results were obtained and will be described in this chapter [114, 106].

The development of the prototype was followed by two runs of data taking. A first run (University of Michigan, summer 2004) was the first attempt to operate a stack of thick silicon sensors as scatter detector. Although this possibility was assessed, the performance of the prototype was not optimum [115]. However, the results obtained served to identify the main problems. The second run (CERN, May 2005) tried to correct for these problems and to improve the scatter detector performance. Additional measurements were carried out to verify the improvement of the resolution when the scintillators are placed further from the scatter detector and with high energy sources. Simulations have also been carried out for a better understanding of the prototype response.

The chapter is organized in four sections, that describe and interpret the observed results. The first section explains the data analysis, and includes the results from the first test. The second one gives a brief overview on image reconstruction that aims to facilitate the understanding of the two following sections. In the last two sections, specific results obtained in each run are shown.

6.1 Data analysis

The analysis of Compton data consists of determining the position and energy of the interactions in the scatter and absorption detector, that will be the input of the image reconstruction program. The energy of the scattered photon measured by the scintillator is not necessary for the reconstruction, but its determination can be used to reject accidental coincidences based on the total energy of the event.

Energy (keV)	%
14	9.54
122	85.6
136	10.6
692	0.02

Table 6.1: *Energies and relative intensities of the photons emitted by the ^{57}Co source.*

6.1.1 Silicon data

The interaction positions in the silicon detector are determined from the position of the sensor and the pad that records the signal within the sensor. In order to determine the energy deposited, the detector must be calibrated obtaining the the gain of each channel, as explained in the previous chapter. Since the photopeak is not present when coincidence data are taken, data employing only the silicon sensors to obtain the energy spectrum of the source are acquired each time a modification is made in the setup, in order to determine the gains and an estimate of the noise in the silicon sensors.

The results obtained in the first test illustrate the dependence of the energy spectrum of the coincidence data on the setup geometry. A ^{57}Co source was employed that emits two gamma rays at 122 keV and 136 keV. The emission probability of the second peak is low (see table 6.1.1), and only the 122 keV peak will be considered for the analysis.

Data were taken with one 500 μm thick silicon detector and one scintillator in two different geometrical configurations of the setup. Figure 6.1 shows the relative positions of the scatter and absorption detector in each case. In the 90-deg configuration, the scintillator is positioned to detect the photons with scattering angles around 90^o A 1 cm thick collimator with a single hole of about 1 mm diameter is placed between the source and the silicon detector. The distance from the source to the sensor is around 6 cm. Lead shielding prevents photons from hitting directly the second detector. In the 180-deg configuration, the backscattered photons, with higher energies and scattering angles, are detected. In this case, no collimator is employed, and the source is situated at 2-3 cm from the detector. No shielding is necessary, since the source itself is shielded, and it is pointing downwards.

Figure 6.2 shows a ^{57}Co energy spectrum in the silicon detector, together with the energy spectrum of coincidence events for the 90-deg configuration setup. The cut on the highest energies in the Compton continuum of the coincidence spectrum is due to the angular acceptance determined by the geometry, and it depends on the relative position of the silicon detector and the scintillator. The cut on low energies is set by the threshold. This can be better appreciated in the comparison of the measured spectrum from figure 6.2 with a simulated ^{57}Co spectrum (fig 6.3). The simulations have been performed with GEANT4, and an interface to EGS4-LSCAT was implemented to simulate the electromagnetic interactions at low energies [116]. The background that appears in the spectrum obtained with real data, for energies higher than the Compton edge (40 keV for the 122 keV ^{57}Co) is due to the scattering of photons in the source shielding and surrounding material previous to their interaction in the silicon sensor. The peaks around 80 keV are due to X-rays emitted from lead that surrounds the source when K-shell electrons are ejected

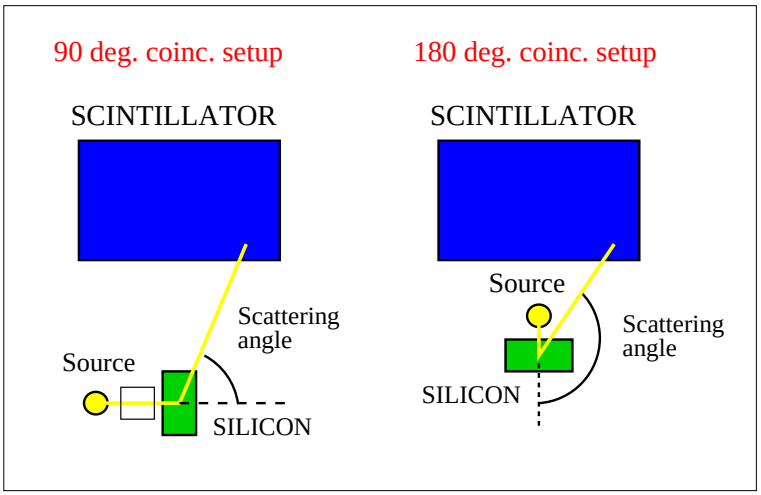

Figure 6.1: *Relative position of the scatter and absorption detector in the two geometrical configurations employed for data taking. In the 90-deg configuration, the scintillator is positioned to detect the photons with scattering angles around 90°. A collimator is employed in this case. In the 180-deg configuration, the backscattered photons, with higher energies and scattering angles, are detected.*

from the atom by the source photons, and an outer shell electron fills the vacancy ($K\alpha_2$ = 72.804 keV, $K\alpha_1$ = 74.969 keV, $K\beta_3$ = 83.450 keV, $K\beta_1$ = 84.936 keV, $K\beta_2$ = 87.3 keV). The fit of the two photopeaks gives a resolution of 1.6 keV FWHM. The hybrid employed at this point was not yet the final version, and the noise is higher than in the following runs.

The influence of the geometry can be better appreciated in the angle distribution. The scattering angle for each event is obtained from the energy measured with a silicon detector, according to equation 2.6. Figure 6.4 shows a simulated and a measured scattering angle distribution, without any restrictions due to geometry. In the simulated spectrum all energies, and therefore all angles, are considered. The cut in angles in the measured spectrum is due to the cut in energies set by the threshold.

If coincidence events are considered, the scattering angles of the events are restricted by the setup geometry. Fig 6.5 shows the angle distributions reconstructed from the measured data. Both setups have also been simulated, and the reconstructed angle distributions from simulated data are shown in the same figure. In the 90-deg configuration, the angles of the measured coincidence events range from 40° to 120°. The cut in low scattering angles is due to the threshold, while the cut in high angles is determined by the setup geometry. In the case of the 180-deg configuration, the cut in low scattering angles is also determined by the geometry, being angles close to 100° the minimum that can be recorded. The photons with angles close to 180° are stopped by the source shielding after backscattering.

The position of the scintillator was not precisely determined, causing the slight disagreement between the simulated and measured angle spectra for coincidence events. However, the very good agreement of the simulated energy and angle spectra in the silicon detector with those obtained from real data serves us to validate the simulation

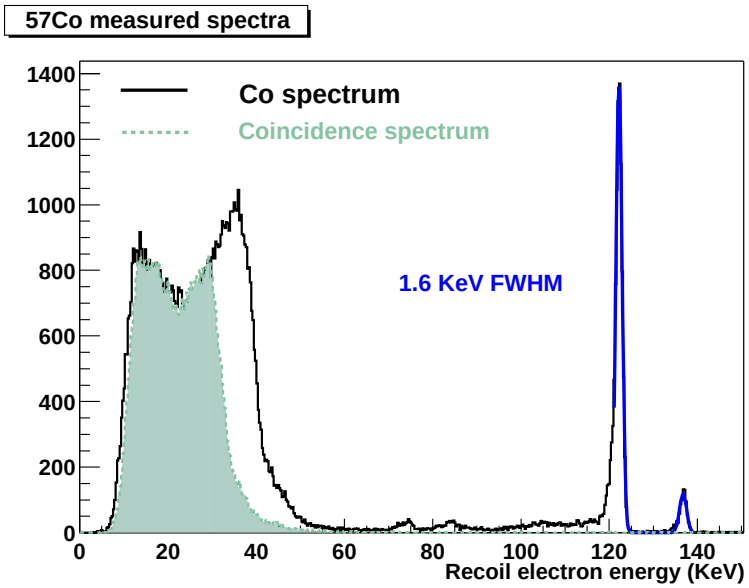

Figure 6.2: *^{57}Co energy spectrum measured with a 500 μm silicon detector, and energy spectrum from coincidence data. The fit of the two photopeaks gives a resolution of 1.6 keV FWHM.*

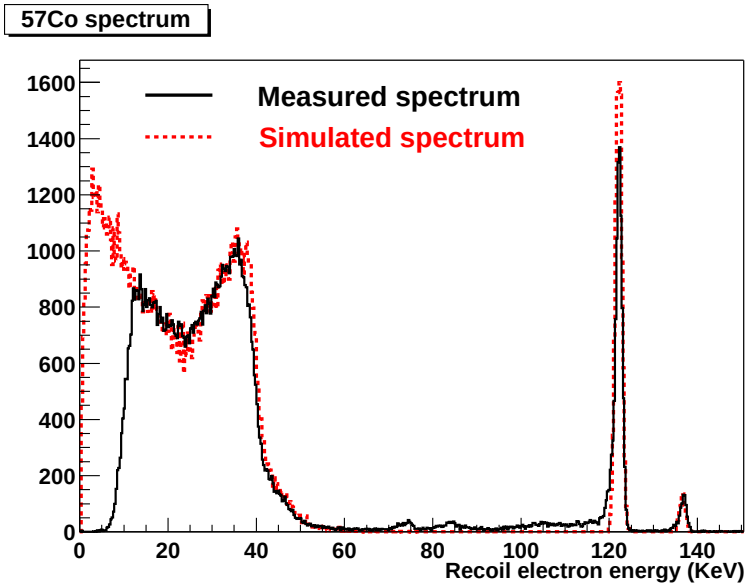

Figure 6.3: *Simulated and measured ^{57}Co energy spectra.*

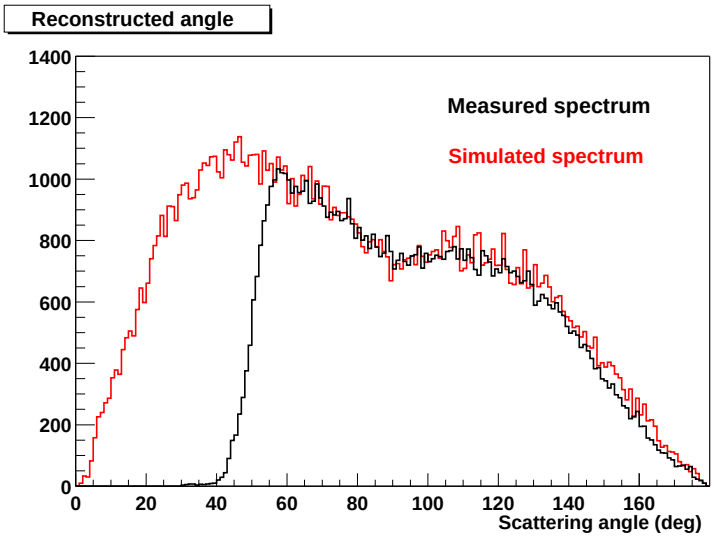

Figure 6.4: *Angle distribution, simulated and measured. For each event, the scattering angle was calculated from the energy measured in the scatter detector.*

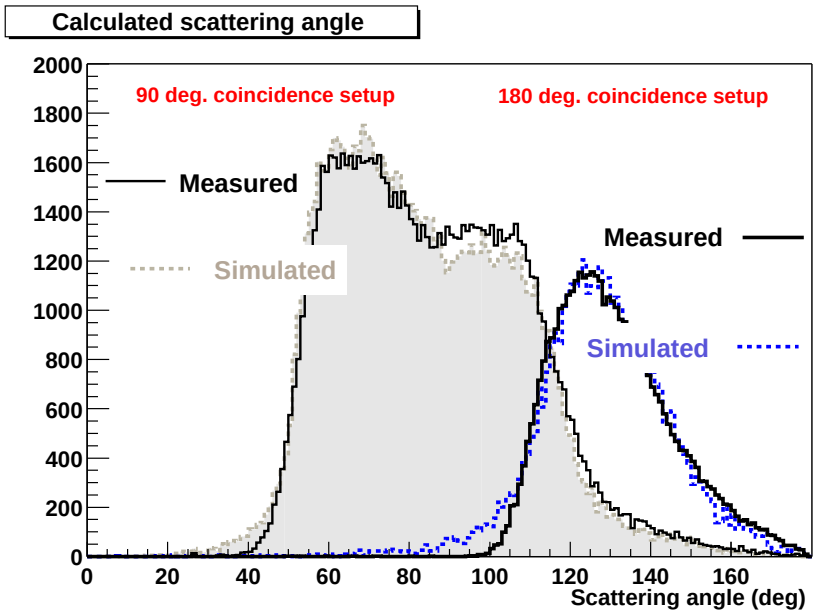

Figure 6.5: *Simulated and measured angle distributions of coincidence events for the 90-deg and 180-deg coincidence setup.*

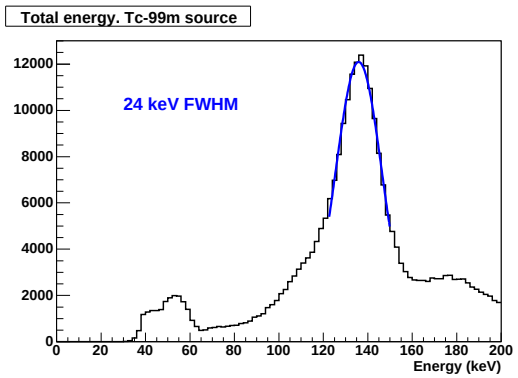

Figure 6.6: *Total energy distribution for ^{99m}Tc, calculated for each event as the sum of energies measured in the scatter and absorption detector. The fit of the peak with a gaussian function gives a resolution of 24 keV FWHM.*

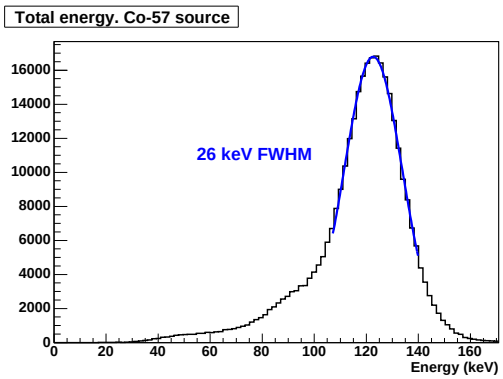

Figure 6.7: *Total energy distribution for ^{57}Co, calculated for each event as the sum of energies measured in the scatter and absorption detector. The fit of the peak with a gaussian function gives a resolution of 26 keV FWHM.*

program, that will be employed in the following sections.

6.1.2 Scintillator data

The determination of positions and energies in the scintillators for the first and second run is done, as explained in chapter 5, based on a previous calibration. Different scintillator modules were employed in the different runs, and the spacing between the points in the mesh for taking the calibration data was not the same in the two cases. In the first run, data were taken in steps of 1 mm in the Y direction, across the scintillator bar width, and 4 mm in the X direction, along the bar length. A ^{99m}Tc source was employed both for calibration and data taking of coincidence events. In the second run, the steps for the calibration are 2 mm both in X and Y coordinates, and a ^{57}Co source was employed. The energy in the scintillator is also determined by the calibration method described in section 5.2.2.

The total energy of the coincidence events is calculated summing the energies measured in both detectors. The results obtained employing ^{57}Co and ^{99m}Tc sources are shown in figs 6.6 and 6.7. In the case of the ^{57}Co source, lead bricks were placed to reduce the rate of direct photons on the second detector and the amount of accidental coincidences is smaller. The total energy resolution is dominated by the energy resolution of the scintillator. During the analysis, cuts are set on the total energy of the event with the aim of rejecting the random events.

The determination of the scintillator positions is done employing different methods due to the different calibrations. In the first run (calibration with steps of 1 mm in the Y direction and 4 mm in the X direction), the positions determined in the calibration procedure with the maximum likelihood (ML) method do not match exactly the real positions. The equation system correction method can be applied once the positions are determined with the maximum likelihood method. The resolution of the reconstructed

images is better if the positions are determined with the ML method and corrected with the equation system method than if just the maximum likelihood method or the corrected centroid method are employed. The results obtained in the three cases are shown in section 6.3. In the second run (calibration with 2 mm steps in both directions), the determination of the calibration positions with the maximum likelihood method matches the real positions almost perfectly. As a result, the resolution of the reconstructed images is very similar when the positions in the scintillator detector are obtained with the ML method or the corrected centroid method. The advantage of the centroid method being faster makes it the option chosen in the second case.

6.2 Image reconstruction

This section describes the image reconstruction and analysis procedure and shows the results of image reconstruction studies performed with simulated data, aiming to a better understanding of the results obtained with real data. The use of simulated coincidence data avoids artifacts and systematic errors that could be caused by the data analysis. Positions and energies can be more accurately determined, and there are no accidental coincidences. In addition, the geometry can be selected to record a 360º sampling on the azimuthal angles (see fig 2.6), and a large coverage on the scattering angle.

The setup selected for the simulations consists of a square silicon detector 4 cm long × 4 cm high and 1 mm thick, surrounded by a cylindric NaI scintillator with 10 cm radius, 2 cm thickness, and 20 cm length. This geometry tries to avoid asymmetries and artifacts in the reconstructed images due to cuts in the scattering angles accepted by the second detector. A ^{57}Co point source was simulated including only the 122 keV and the 136 keV peaks at their relative intensities. The Z axis corresponds to the cylinder axis, and to the line connecting the source and the center of the silicon detector, that is situated in the XY plane at Z=0. Photons are generated isotropically. Very simplified assumptions have been taken into account, since the aim of these simulations is just to understand the general behaviour of image reconstruction results and not to provide accurate results. Only events with a single Compton interaction in the silicon detector are considered for image reconstruction. The energy resolution of the first detector is 1.18 keV FWHM energy, the interaction position is that given by the simulation code, and no pixelation is taken into account. In the case of the scintillator, if more than one interaction occurs, the position of the first interaction is taken without any degradation. The energy measured in the second detector is not necessary for the image reconstruction, and therefore its energy resolution is also not considered.

As explained in section 2.4, the first step in the image reconstruction with the list-mode MLEM algorithm for the Compton data is a backprojection of the data to generate the Compton cone and find the intersection with the image plane. The backprojected image serves as the initial estimation of the image to start the iteration procedure. The image is reconstructed at a given plane, specified by the user. The reconstruction code outputs the resulting image after each iteration, providing the relative intensities for each bin in which the image plane has been divided for the reconstruction. 40000 events were considered in each case to avoid noise due to a low number of counts. Unless otherwise

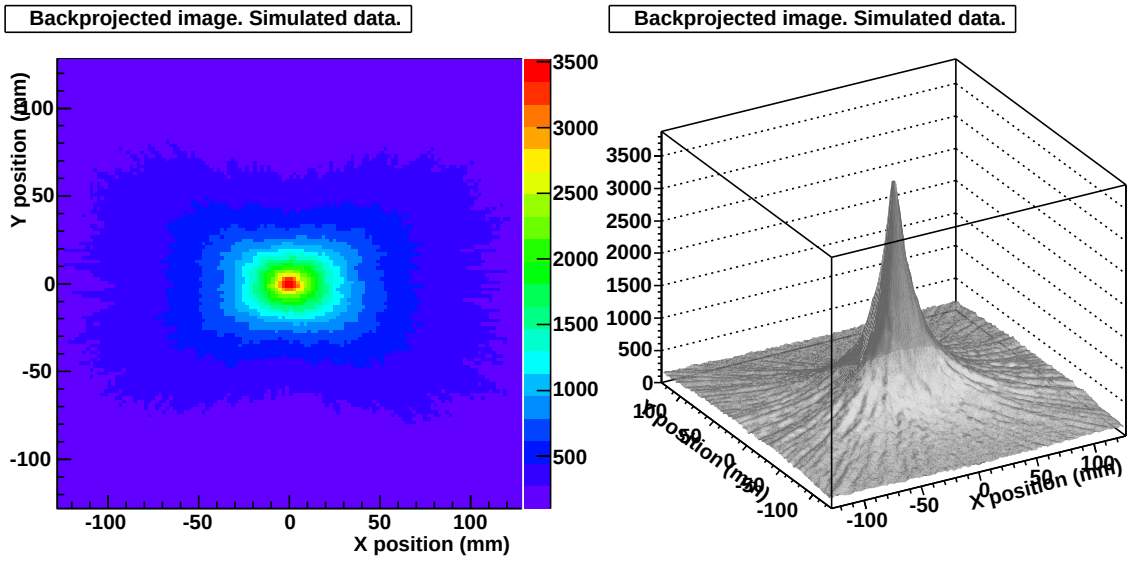

Figure 6.8: *Result of a backprojected image, employed as initial image estimate for the first iteration of the MLEM image reconstruction algorithm.*

indicated, the results shown in this chapter correspond to the image plane where the source was placed, both in the case of simulations and real data. The results can be represented in a 2D or 3D plot to form the image. Fig 6.8 shows the result of the initial backprojection.

To determine the image resolution, a slice through the maximum of the image peak is selected in X and Y directions, and it is fitted with a sum of two gaussian functions. The standard deviation of the narrower gaussian, that fits the upper part of the peak, is taken as the image resolution in the corresponding direction. As the program iterates, the resolution of the reconstructed image improves, until a minimum is achieved. From that point on, the resolution gets worse and if the program continues iterating, the noise starts to dominate. Fig 6.9 shows an example of a resulting image and in fig 6.10 the Y profile is fitted with a sum of two gaussian functions. For the selected geometry, X and Y axis are symmetric and there is no difference in the reconstructed images.

The resolution obtained is strongly dependent on the detector geometry, as explained in section 2.2.1. For a given angular uncertainty, the resolution of the reconstructed images improves with distance from the source to the scatter detector. Fig 6.11 shows the X resolution obtained for different distances from the source to the scatter detector, confirming the expected results.

The scattering angles of the events selected for the reconstruction will also determine the resolution of the reconstructed image, due to the influence of energy resolution and Doppler broadening. The angle distribution of all coincidence events is shown in fig 6.13. The correspondence between the energy and mean scattering angle is given by equation 2.1 and can be seen in fig 6.12 for energies of 122 keV, 140.5 keV and 356 keV, corresponding to photons emitted by ^{57}Co, ^{99m}Tc and ^{133}Ba sources respectively.

Images have been reconstructed selecting energies corresponding to different angle ranges. The resolution obtained for each interval is shown in table 6.2. Figure 6.14 shows

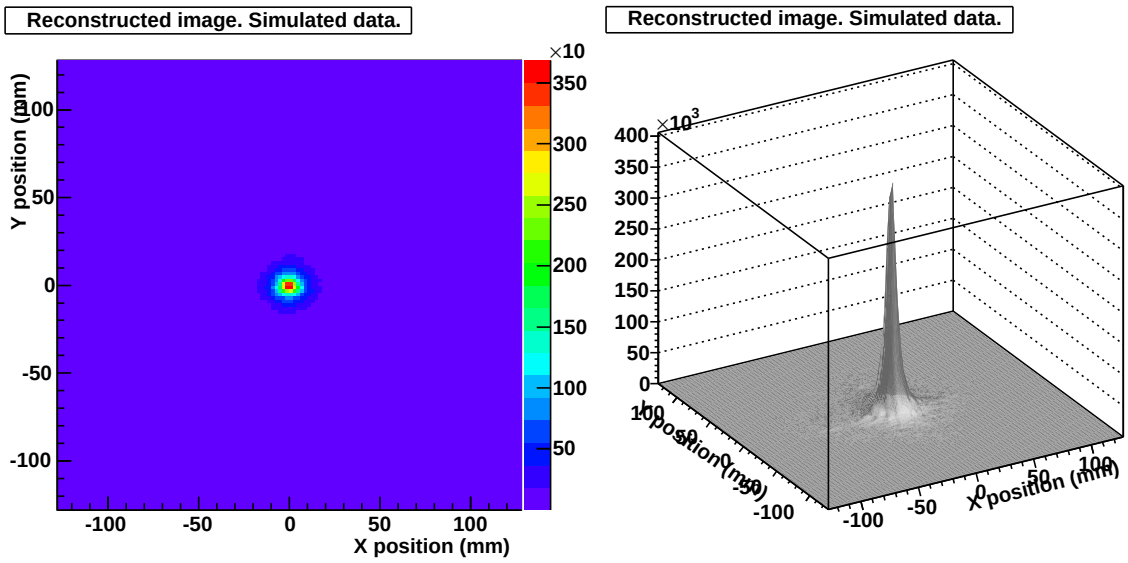

Figure 6.9: *2D and 3D views of the reconstructed image.*

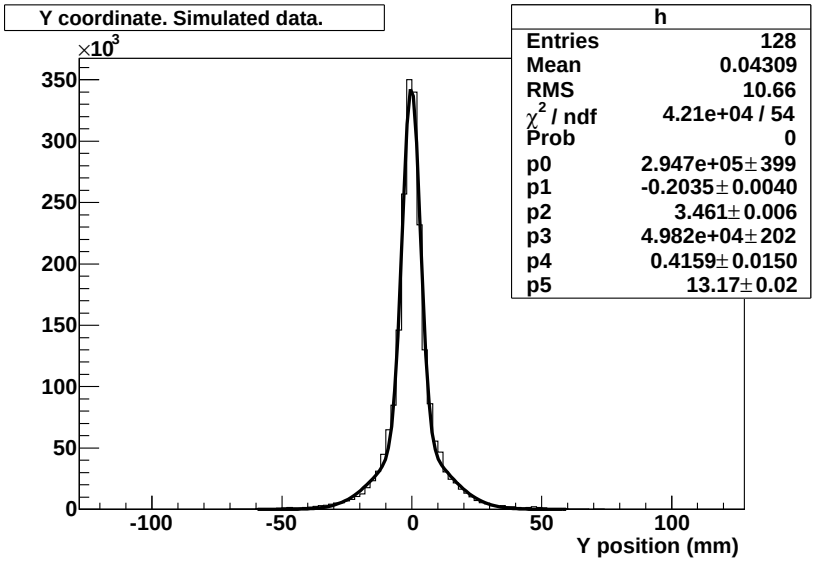

Figure 6.10: *Image slice along the Y direction through the image peak fitted with a sum of two gaussian functions to obtain the image resolution.*

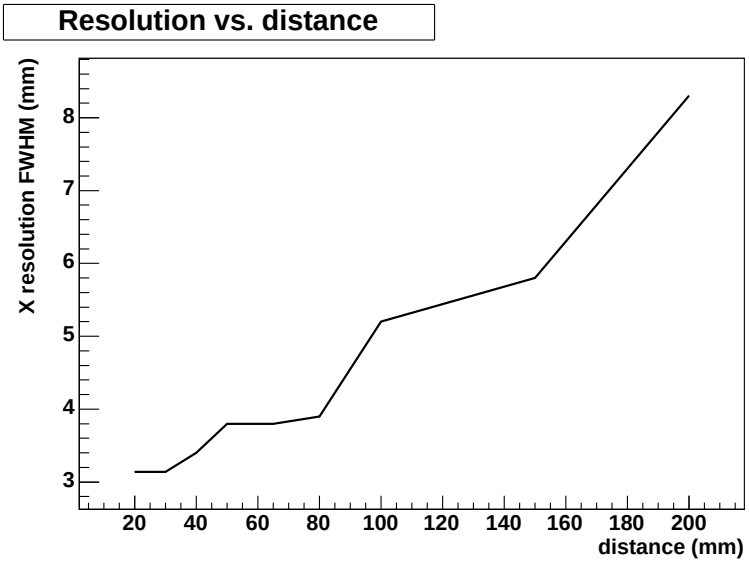

Figure 6.11: *Image resolution as a function of the distance from the source to the scatter detector. The resolution improves for smaller distances.*

Energy interval(keV)	Angle range	X resolution (mm FWHM)
0 - 5	0° - 35°	10.2
5 - 10	35° - 51°	7.4
10 - 15	51° - 66°	7.5
15 - 20	66° - 80°	7.5
20 - 25	80° - 95°	7.5
25 - 30	95° - 112°	8.1
30 - 35	112° - 133°	8.9
35 - 40	133° - 166°	15.0

Table 6.2: *X resolution obtained selecting coincidence events from different energy (angle) intervals.*

the resolution obtained versus the upper value of the energy interval. As expected, the best resolution is obtained for events with low scattering angles, if angles too close to zero are avoided, because of the energy resolution effect explained in section 2.2.1.

The cuts in the azimuthal angle cause distortions on the reconstructed images, already preasent in the backprojected image that is employed to initialize the iterative algorithm. A 180° angle sampling yields perfectly symmetric images and no artifacts can be seen. However, if photons with determined scattering angles are not absorbed in the second detector, the angles selected determine a preferred direction of the cone intersecting with the image plane. As a result, the image is elongated in this direction. Figure 6.15 shows the effect of selecting events with azimuthal angle between 0° and 90°. To obtain the previous results or the ones that will be shown in next section with real data, the parameters of the system matrix in the MLEM algorithm have not been modified according to the selected events. The effect of this restrictions should be studied to avoid possible distortions and

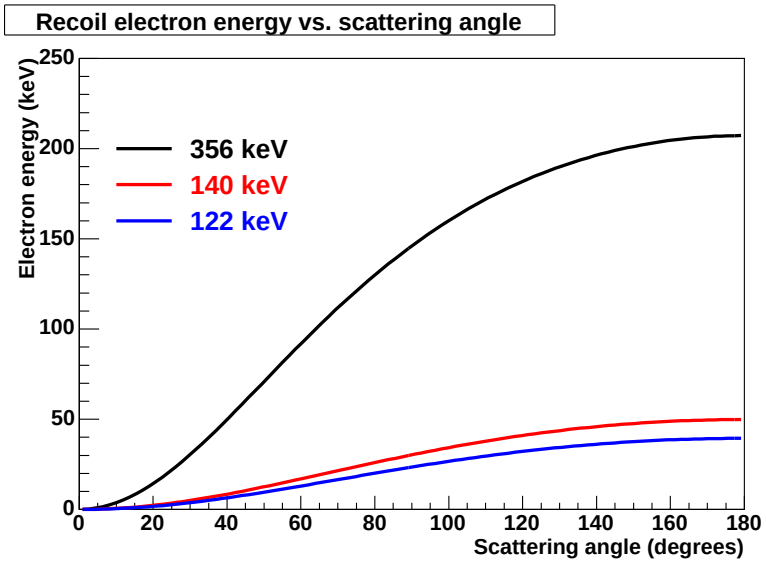

Figure 6.12: *Mean energy of the recoil electron as a function of the scattering angle, for three different energies of the incident photon.*

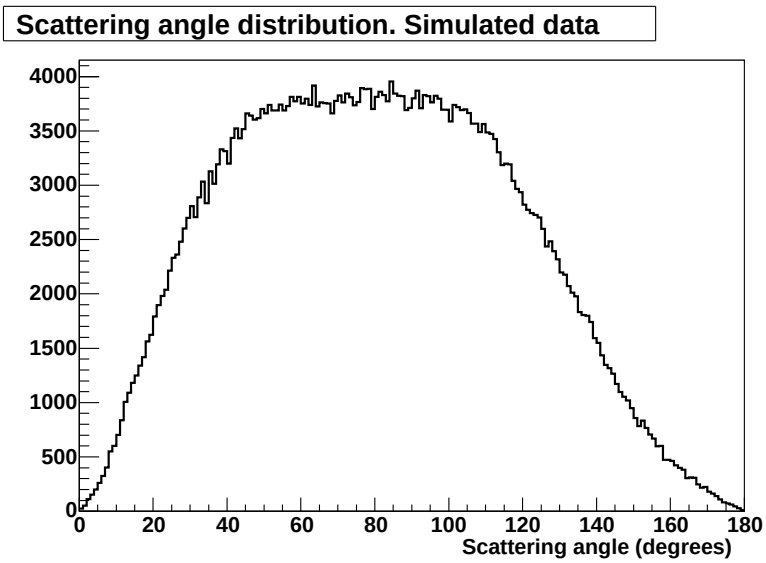

Figure 6.13: *Angle distribution of the simulated coincidence events.*

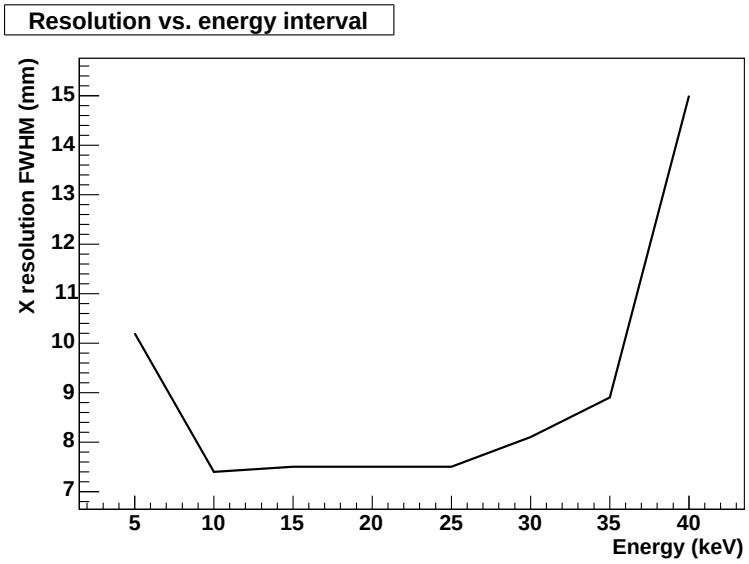

Figure 6.14: *Resolution of the reconstructed image for different energy (angle) intervals.*

artifacts in the reconstructed images.

The size of the first detector has an effect on the depth resolution of the images. When images are reconstructed considering different planes, the best resolution is achieved when the image is reconstructed in the plane where the source is located.

However, the size of the first detector has an effect on the depth resolution. The resolution of the reconstructed images will be closer to the minimum if a large scatter detector is employed. This is due to the fact that the size of the scatter detector determines the incoming angles of the photons emitted by the source that can interact in it (fig 6.16). In the case a smaller detector is employed, the solid angle subtended is restricted, and only photons emitted at smaller angles will hit the scatter detector. This effect is also appreciated if the source is placed further from the silicon sensor.

In figure 6.17, different planes have been considered for image reconstruction. Images reconstructed at planes close to the source plane have a resolution more similar to the minimum if the scatter detector is smaller, resulting in a worse depth resolution.

6.3 Results first run

After the first test, the prototype was constructed as explained in the previous chapter. A mechanical structure is designed to give support and ensure the correct positioning of the detectors. The scatter detector is placed in the middle of the structure. Three scintillator modules can be situated on both sides and below. The source employed sits on a support that allows precise determination of relative changes in its position.

Five silicon modules were assembled, tested and packed in a dense array to conform the scatter detector (fig 5.1). Four of the sensors are 1 mm thick and one is 0.5 mm thick. The spacing between the modules is 6.3 mm.

In this run, two scintillator modules were situated on the sides of the prototype (fig

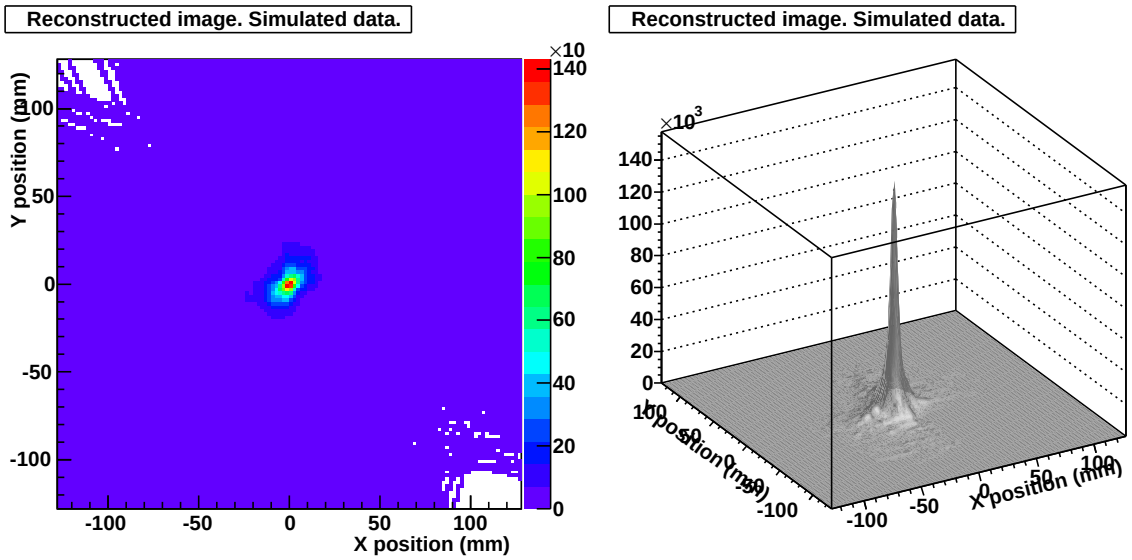

Figure 6.15: *Reconstructed image considering only events with azimuthal angles between 0 and 90º. The resulting image is elongated.*

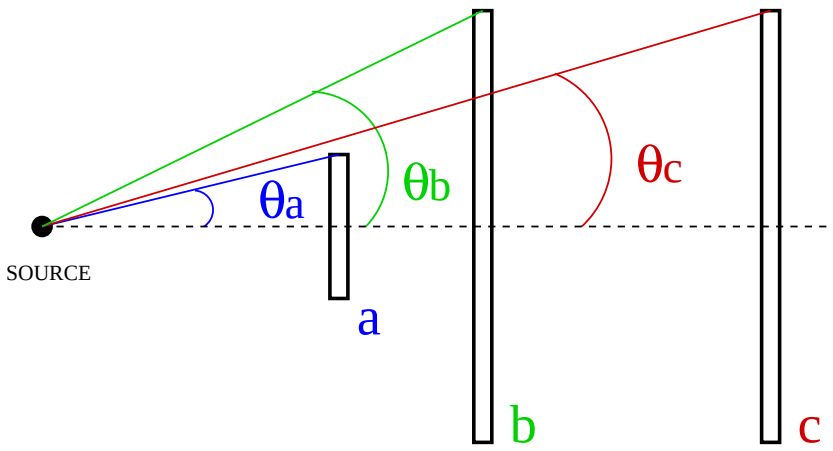

Figure 6.16: *Variation in the maximum angle recorded in the scatter detector due to differences in its size (a and b) or position with respect to the source (b and c).*

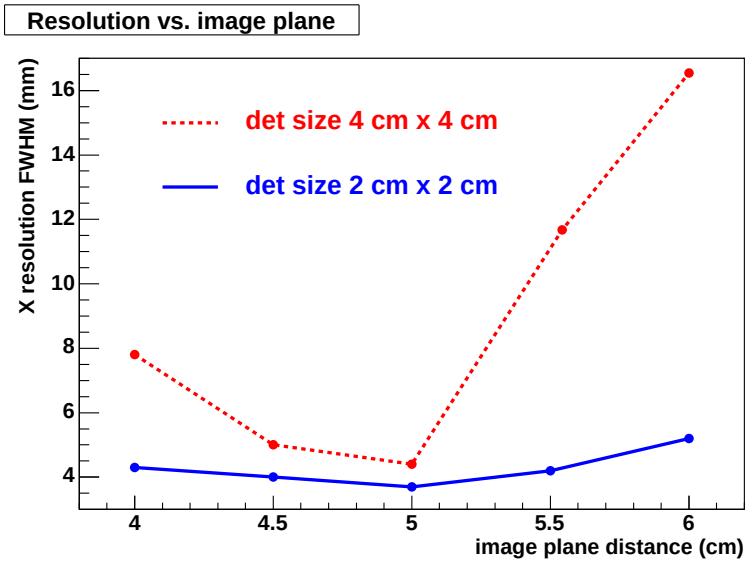

Figure 6.17: *Resolution of the reconstructed image for different image planes and different sizes of the scatter detector.*

6.18), at 62.5 mm from the centre of the silicon detector. The position of the scintillators was thought to provide the maximum possible solid angle coverage. However, due to their close distance to the scatter detector, the influence of their spatial uncertainty on the resolution of the reconstructed images is bigger. The azimuthal angle sampling is also not complete, affecting the image reconstruction. The position of the scintillator modules in this case results in a better resolution of the X coordinate in the reconstructed image.

The calibration of the silicon modules yielded energy resolutions ranging from 1.2 to 1.5 keV FWHM. However, when the five modules were operated together, their performance degraded by about 20%, with energy resolutions up to 1.8 keV FWHM. In addition, the minimum threshold that can be set increases with the number of silicon modules operated. A relatively high threshold had to be set to avoid instabilities in the scatter detector operation.

As explained in section 5.3, a wide coincidence window needs to be set with the current version of the readout electronics due to a non-optimized timing resolution. As a consequence, the rate of random events is higher than it should be with a narrower coincidence window. This is especially a problem if the second detector views the source directly.

The position of the source, inside the box and close to the scatter detector, makes it impossible to shield the source to avoid direct photons on the second detector, without restricting the angles of the photons hitting the scatter detector. Data were therefore taken without any shielding. The high rate of direct photons on the second detector, together with the wide coincidence window set, results in a high amount of accidental coincidences. Figure 6.19 shows a ^{99m}Tc spectrum employed for energy calibration of the silicon modules, and an energy spectrum of coincidence events in silicon. The high amount of events with energies higher than the Compton edge (50 keV for ^{99m}Tc) for the coincidence events is due to accidental coincidences.

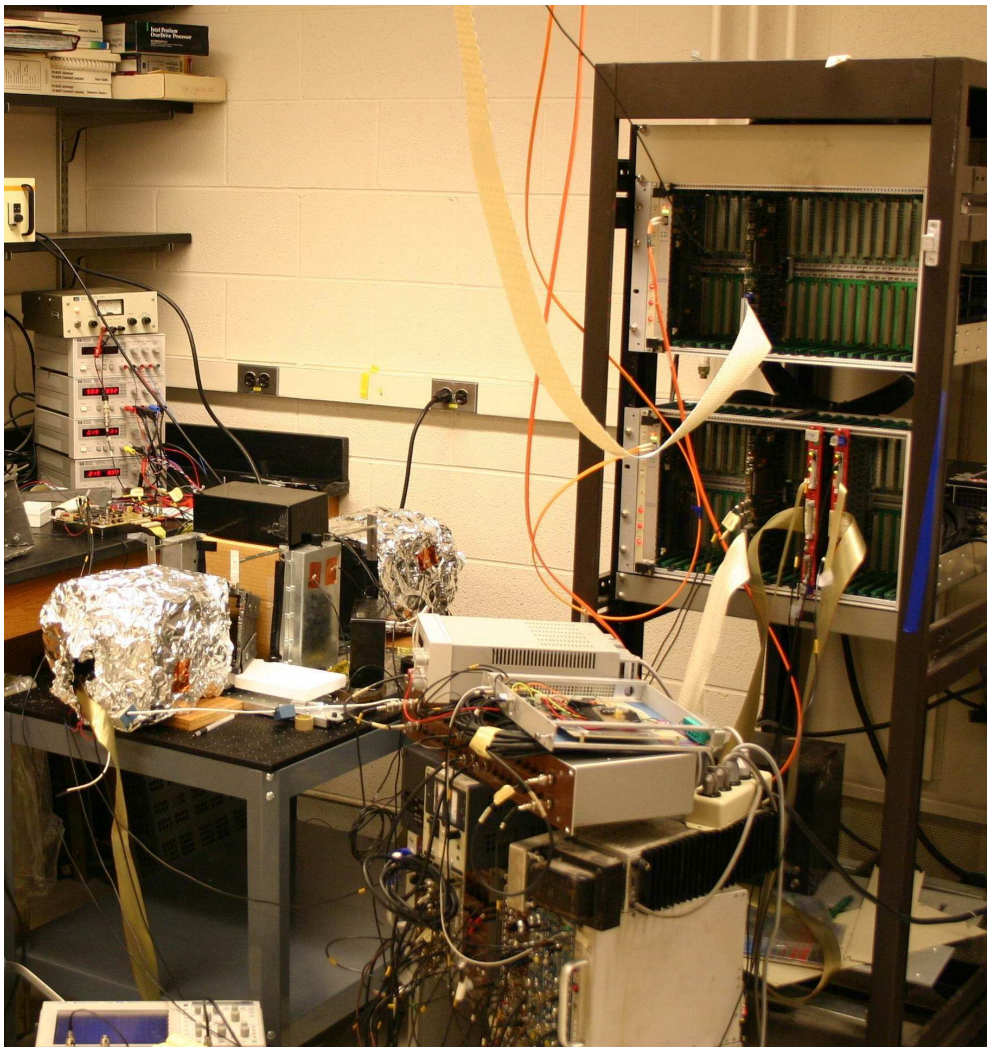

Figure 6.18: *Setup employed in the first run.*

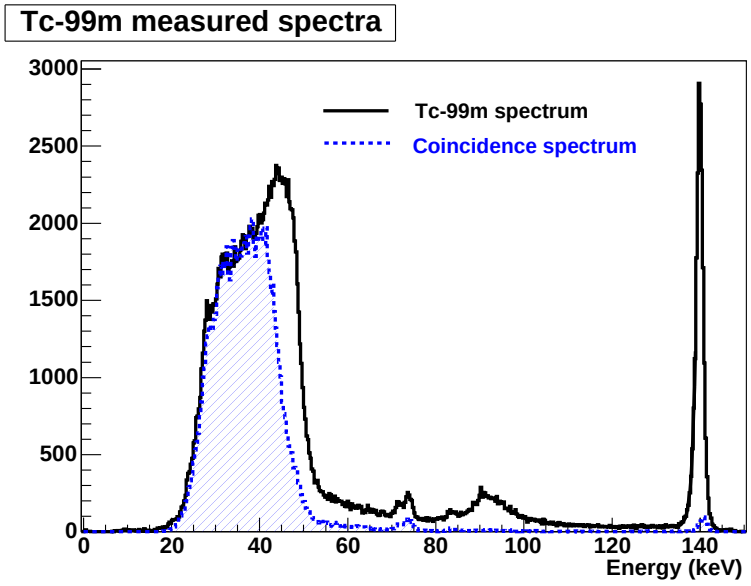

Figure 6.19: *Energy spectra measured in the silicon detector, ^{99m}Tc energy spectrum and energy distribution from coincidence data.*

Method employed	X resolution (mm FWHM)
maximum likelihood (ML)	8.5
corrected centroid	8.35
corrected ML	7.1

Table 6.3: *Image resolution obtained from the same coincidence data employing three different methods to determine the scintillator positions.*

A ^{99m}Tc source emitting a gamma ray of 140.5 keV was employed for data taking. Data were taken with one and two point-like sources situated at 4.5 cm from the first detector, and images were reconstructed. The minimum resolution that could be achieved corresponds to events scattering on a single silicon detector. The best resolution was obtained when the scintillator positions were determined with the corrected maximum likelihood method. The results with the different methods tested (described in section 5.2.2) are shown in table 6.3.

Figure 6.20 shows the reconstructed image of one point source, with a resolution of 7.1 mm FWHM. Figure 6.21 shows the reconstructed image corresponding to two point sources separated 15 mm, with a similar resolution.

In order to ensure a perfect understanding of the results, simulations were carried out. The system geometry was simulated with the same code employed for the simulation results shown in the previous sections.

For a fixed distance from the scatter detector to the source, the spatial resolution is influenced by the uncertainty in the scattering angle, mainly determined by the Doppler broadening uncertainty and the energy resolution, and by the spatial resolution of the detectors.

Simulations enable the study of each effect on the reconstructed image independently.

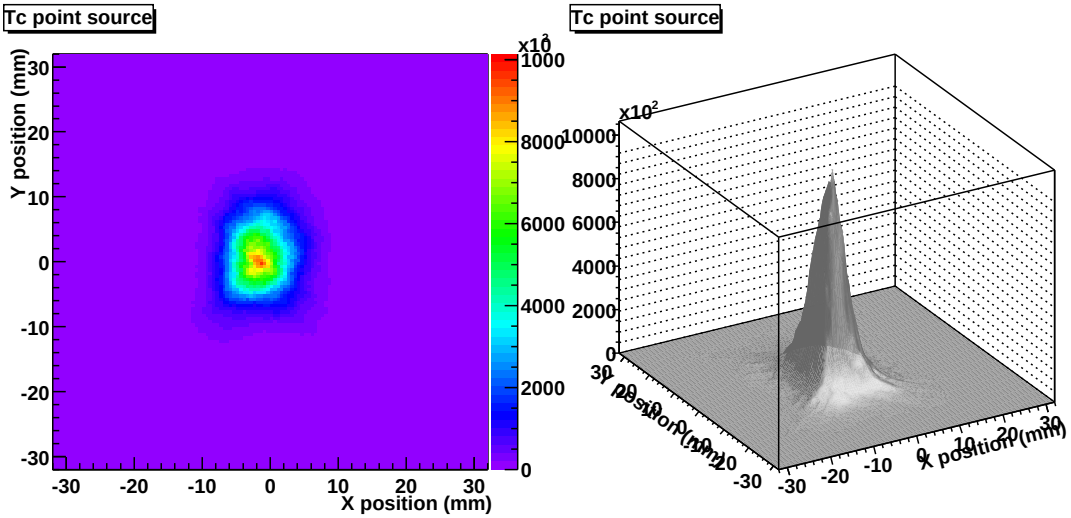

Figure 6.20: *Reconstructed image of a ^{99m}Tc point-like source situated at 4.5 cm from the scatter detector. A resolution of 7.3 mm FWHM is obtained by fitting the peak.*

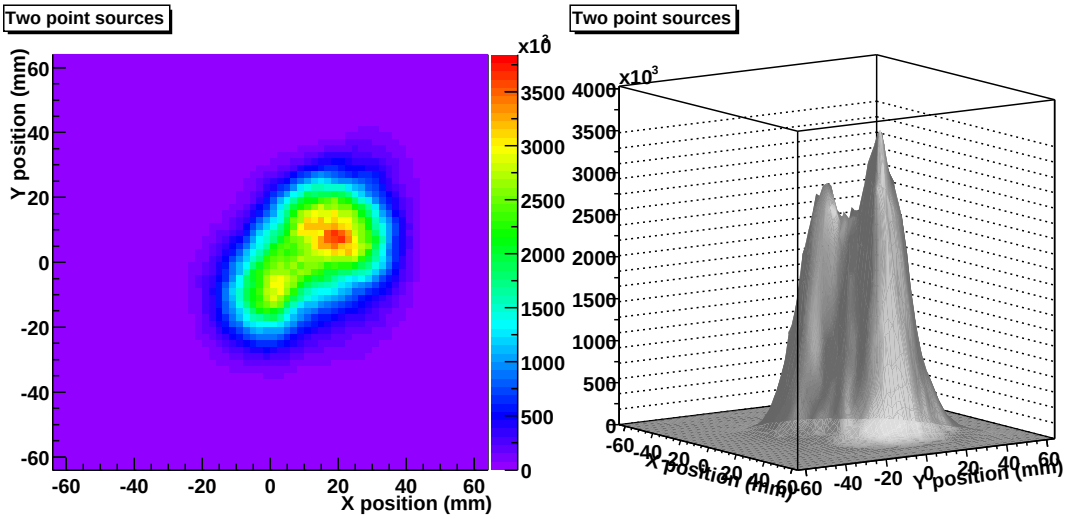

Figure 6.21: *Reconstructed image from two ^{99m}Tc point-like sources situated at 4.5 cm from the scatter detector and separated 15 mm.*

Contribution considered	X resolution (mm FWHM)
Doppler broadening (DB)	3.6
DB + energy resolution (ER)	5.2
DB + ER + spatial resolution (SR)	5.8
DB + ER + SR + 27 keV threshold	6.9

Table 6.4: *Different contributions to the spatial resolution of the Compton detector. Results from simulated data.*

As a first step, the image of a point source in which the only effect considered is Doppler broadening, was reconstructed. Next, the effect of energy resolution of the scatter detector was included, and finally, the contribution due to the spatial resolution was also taken into account. The results obtained are shown in table 6.3. The effect of Doppler broadening cannot be avoided, and imposes a physical limit in the resolution achievable that can only be minimized by selecting the adequate material for the scatter detector, low scattering angles for the image reconstruction, and high energy sources. On top of that, the energy resolution constitutes an important source of degradation of the spatial resolution at low energies, and it must be kept as low as possible. The contribution due to the spatial resolution of the absorption detectors could be minimized by placing them further from the scatter detector. Another effect to consider is the one due to the threshold set on the scatter detector. The high threshold imposed to ensure stability in the scatter detector operation, leaves out the low energies that correspond to low scattering angle, that have higher resolution. Figure 6.22 shows the improvement in the resolution when events at lower energies are considered, for simulated data in the same conditions as the real data taken. The small difference between the simulated and the measured data can be due to the presence of accidental coincidences.

The aim of this experiment, assessing the possibility of taking data and reconstructing the images with a multilayer scatter detector, was accomplished. However, the detector performance was worse than expected. Several problems that degrade the resolution of the reconstructed images were identified. The measured energy resolution when all detectors were operated together was higher than that obtained in the individual measurements of the modules. Furthermore, a high threshold was required to avoid instabilities in the operation of the modules. The high accidental coincidence rate related to the wide coincidence window and direct illumination of the second detector further degraded the resolution.

Fortunately, once these problems have been identified, they can be eliminated with an improved scatter detector operation and optimized geometry.

6.4 Results second run

This experiment run was performed to demonstrate the improved performance of the scatter detector that could be achieved after solving some of the problems identified in the previous set of experiments. Additional experiments were carried out in which the scintillator detector to scatter detector distance was varied and two different radioactive

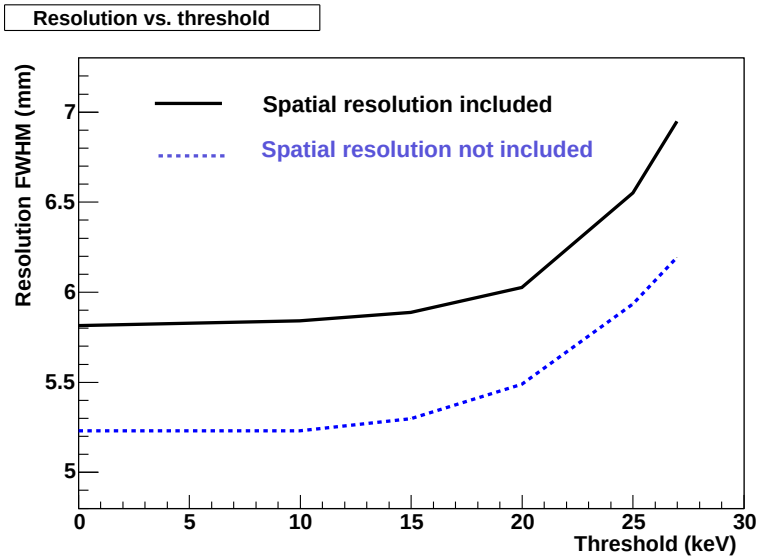

Figure 6.22: *Resolution of the reconstructed image as a function of the threshold set to the silicon detectors for simulated data, with and without the effect of spatial resolution introduced by the detectors*

sources were evaluated.

Reducing the silicon module noise allowed the energy threshold to be lowered. The noise dependence on the number of modules in the scatter detector was also reduced, although not eliminated.

Three scintillator modules, two on the sides and one below, were employed in this case (figs 6.23 and 6.24). The source was placed outside the metal structure, increasing the distance from the source to the scatter detector about 7 cm compared to the previous run, and provided room to add lead shielding in order to reduce the rate of direct photons on the absorption detector without blocking the path of gamma-rays from the source to the scatter detector. In the clinical prototype of the Compton probe, the source will not be shielded. However, better timing performance will make it possible to set a narrower coincidence window, that will reduce the rate of accidental coincidences. In addition, a high countrate second detector will be employed, and a better energy resolution will ensure a more effective rejection of accidental coincidences. Shielding the source therefore aims to reproduce a situation closer to the real one, where the rate of random coincidences will be lower than in our previous run. However, placing the source further from the scatter detector results in a worse resolution, compared to the results obtained in the previous run.

Of the five modules presented in table 5.3, module G had a lower effective threshold than the other modules when the same threshold level was set to all of them. A higher threshold needed to be set to prevent module G from triggering on noise signals. In order to be able to record low energy signals in the scatter detector with all modules, module G was excluded. Data were taken with three scintillator modules. However, one of the scintillators was calibrated in steps of 5 mm in both X and Y directions, and its spatial resolution is worse than that of the other two, that were calibrated with 2 mm steps.

Figure 6.23: *Prototype employed in the second run. Two scintillators are placed on both sides and below the scatter detector, that is inside the metal box.*

Detector	thickness (mm)	Distance from source (mm)	Eres indiv (keV- FWHM)	Eres together (keV- FWHM)
A	0.5	112	1.2	1.32
H	1	118	1.3	1.40
F	1	124	1.4	1.48
B	1	130	1.4	1.46

Table 6.5: *Technical data for the four detectors employed in the second run.*

As a consequence, the resolution of the reconstructed image is worse if data from the third scintillator are included, and only data from the two scintillators with better spatial resolution will be considered for the image reconstruction. The two scintillators employed for data analysis are placed on one side and below the scatter detector. This configuration provides a more adequate angular sampling than the one employed in the previous run, improving the resolution of the Y coordinate.

The energy resolution of the four silicon modules is shown in table 6.5 when operated individually and all together. In this case, the resolution is only slightly degraded when the detectors are operated together, about 10% compared to 20% in the previous run. The distance from each of the detectors to the source is also shown.

In order to test the change in the resolution of the prototype when the distance from the scintillators to the scatter detector is increased, data were taken with the scintillators at three different positions.

Data were also taken with two different sources ^{57}Co and ^{133}Ba. ^{57}Co emits mainly

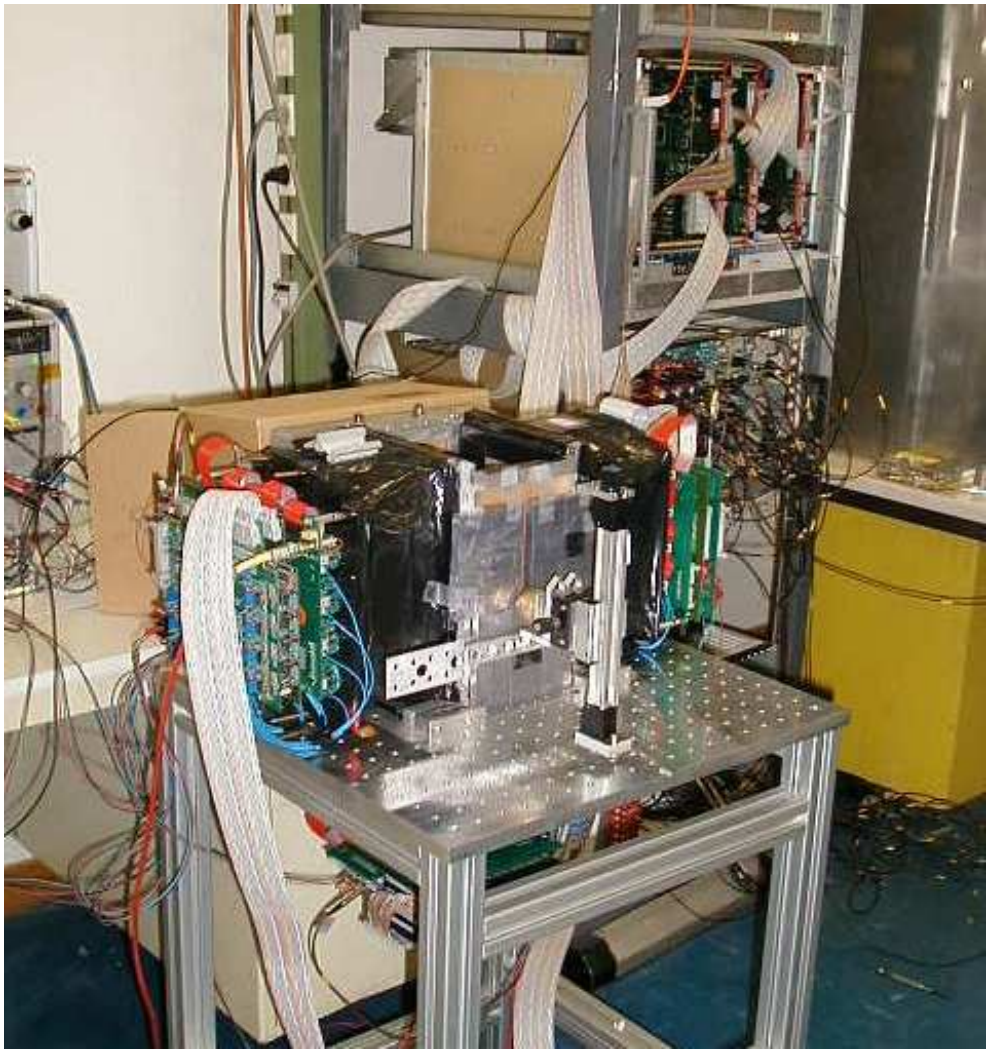

Figure 6.24: *Setup employed in the second run.*

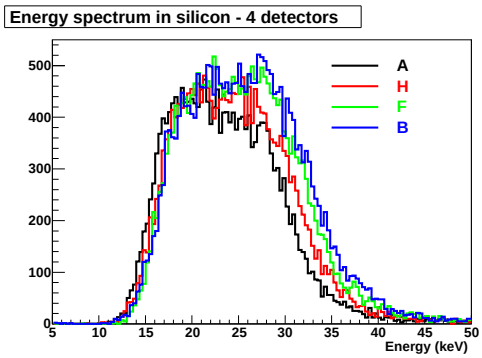

Figure 6.25: *Energy distribution of coincidence events measured in each of the silicon sensors.*

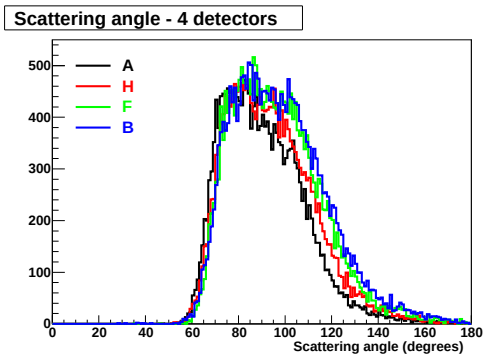

Figure 6.26: *Angle distribution of coincidence events measured in each of the silicon sensors.*

the two peaks previously mentioned, which are not possible to separate given the energy resolution of the scintillator detectors. However, the low intensity of the second peak yields a small amount of events with 136 keV total energy, and their consideration in the analyzed data hardly affects the resolution of the reconstructed images. ^{133}Ba instead has important contributions from several peaks, and the analysis of the data is more complex. In both cases, the active element of the radioactive source is restricted to a 3 mm diameter disk. The comparison of the results obtained with both sources shows that the resolution improves with energy. First, the results obtained with the ^{57}Co source will be presented. Then, the results will be compared to those obtained with the ^{133}Ba source.

6.4.1 Results with the ^{57}Co source

Results have been obtained for each of the modules, and for all together. Detector A has better energy resolution due to its reduced thickness, and the results considering only events in this detector show better spatial resolution. However, the efficiency is lower than that of the 1 mm thick detectors.

The energy and scattering angle distribution of the coincidence events that are measured is different for each distance, since variations in the geometry result in different ranges of recorded scattering angles, as seen in section 6.1.1. For a given position of the scintillation detectors, slightly different distances of the individual scatter detectors introduce slight variations in the energy and angle range distributions as shown in figs 6.25 and 6.26.

To avoid differences in the resolution due to variations in the angle range, the results are compared selecting an energy range with sufficient events in all distances and detectors.

Variation with angle

To confirm the variation of the results with the angle range, images have been reconstructed selecting events with energies corresponding to different angle intervals. The correspondence between energies and angles for the ^{57}Co source is shown in fig 6.12.

Energy interval (keV)	Angles (deg)	X resolution (mm-FWHM)
<16	<68	7.8
16 - 20	68 - 80	10.6
20 - 24	80 - 92	12.2
24 - 28	92 - 104	14.4

Table 6.6: *Resolution obtained for different angle interval.*

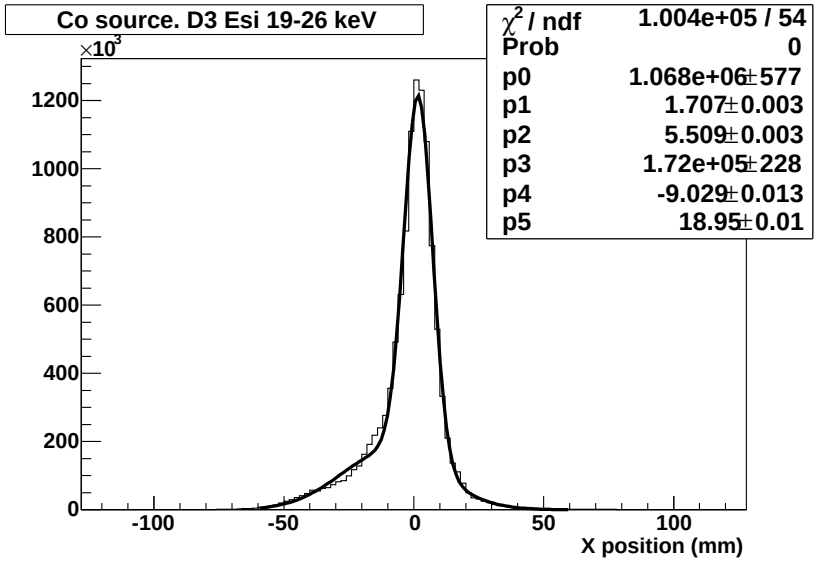

Figure 6.27: *Reconstructed image selecting energies from 19 to 26 keV in the silicon energy spectrum for a scintillator distance of 162.5 mm.*

Table 6.6 shows the results of the X resolution obtained for module H with the scintillators placed at 162.5 mm from the center of the detector. As expected, the resolution improves when lower angles are considered. However, cutting angles results in asymmetries in the images in some cases, as shown in fig 6.27.

Variation with distance

Three different positions of the scintillator modules have been considered for data taking. The distance from the centre of the scatter detector to the scintillator in each case is shown in table 6.7. D0 is the original position for maximum angle coverage, and it is the one employed in the previous run. The other two distances correspond to placing the scintillators 5 cm and 10 cm further.

As previously seen, energy and angle distributions depend on the geometry. Figures 6.28 and 6.29 show the variations of the energy and angle distributions as a function of the distance for detector H. The minimum energy that can be measured is set by the threshold, and this determines the minimum angle. The geometry in each case determines the maximum angle that can be measured, setting a cut on the maximum energy that the coincidence events can have. This maximum angle depends on the distance from the scintillators to the silicon sensor.

	distance (mm)
D0	62.5
D5	112.5
D10	162.5

Table 6.7: *Distance from each of the scintillators to the centre of the scatter detector for the three scintillator positions.*

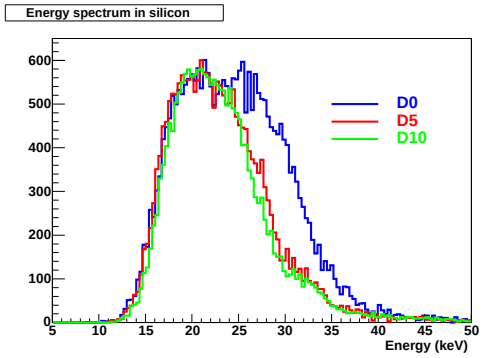

Figure 6.28: *Energy distribution of coincidence events measured for each of the scintillator positions with silicon module H.*

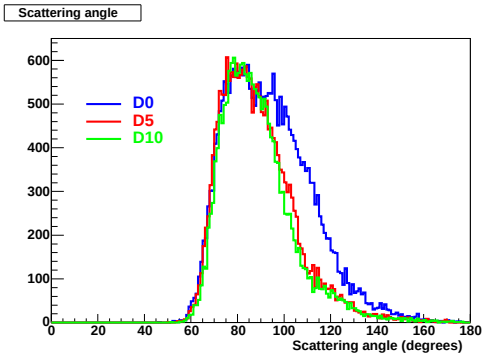

Figure 6.29: *Angle distribution of coincidence events measured for each of the scintillator positions with silicon module H.*

Since the comparison must be done in the same angle interval for the three distances, events with energies up to 24 keV have been selected for the image reconstruction.

The resolution has been calculated for the four detectors individually, and all together. In the last case, events from all detectors are considered equally, and they have not been weighted according to their energy resolution. The results shown in table 6.8 correspond to X/Y coordinates. Similar results were obtained for both coordinates.

If all events are considered for each distance the resolution is worse, in particular for D0. The results are shown in table 6.9.

As the distance is increased, the solid angle coverage of the scintillator modules decreases, and this is reflected in the reconstructed images, that have a diamond shape, with tails in the directions where the scintillators are placed and are bigger for larger scintillator distance. This effect can be seen in the reconstructed images for module H for

Esi <24 keV	X/Y resolution mm FWHM		
Module	D0	D5	D10
A	14.6/15.1	10.7/10.9	10.1/12.6
H	16.1/15.9	13.2/13.6	13.0/13.4
F	18.0/19.6	13.7/14.3	12.0/12.5
B	17.5/16.9	13.7/14.3	13.4/14.13
ALL	16.6/16.8	12.7/12.7	11.8/13.2

Table 6.8: *X and Y resolution obtained for the three distances for the four modules considering events with silicon energy less than 24 keV.*

All Esi	X resolution mm FWHM		
Module	D0	D5	D10
A	15.7	11.6	10.9
H	17.2	13.9	13.1
F	21.0	14.2	13.7
B	20.1	15.5	14.1
ALL	19.1	13.7	12.9

Table 6.9: *X and Y resolution obtained for the three distances for the four modules considering all events.*

	X resolution mm FWHM		
Module	D0	D5	D10
A	10.8	8.7	6.0
H	13.8	10.8	7.8

Table 6.10: *Resolution obtained considering only events with energies lower than 18 keV, and therefore the lowest possible scattering angles with the current setup, improving the resolution.*

each scintillators position, in figures 6.30, 6.31 and 6.32.

Results were also obtained for events with silicon energies below 18 keV, for modules A and H. The resolution, shown in table 6.10, is the minimum that could be achieved.

From the results obtained in this section we see that the resolution of the reconstructed images improves when low scattering angles are considered, and if the distance from the scatter to the absorption detector is increased, minimizing the influence of the spatial resolution of the absorption detector.

6.4.2 Comparison with the ^{133}Ba source

The resolution of the images is expected to improve with increased source energy, mainly due to a smaller contribution of Doppler broadening. A ^{133}Ba source was employed to take coincidence data and compare the results with those obtained for ^{57}Co. The energies of the photons emitted by the ^{133}Ba source and the corresponding value of the Compton edge are listed in table 6.11.

Figure 6.33 shows a measured ^{133}Ba energy spectrum. The photopeaks corresponding to photons with energies above 260 keV fall outside the ADC range. However, the corresponding Compton edges can be clearly seen.

To determine the scattering angle and reconstruct the cone, image resolution relies on the knowledge of the total energy of the event, either by knowing the energy of the photon emitted by the source, or from the sum of energies measured in both detectors. If contributions from different peaks cannot be separated, the resolution of the images will be degraded, since a wrong total energy is being assigned to some of the events.

In our case, the Compton events of different peaks overlap in the energy spectrum. It is possible to select energies from the peak with the highest energy (383 keV), setting the threshold above the Compton edge of the 356 keV peak. However, the emission probability

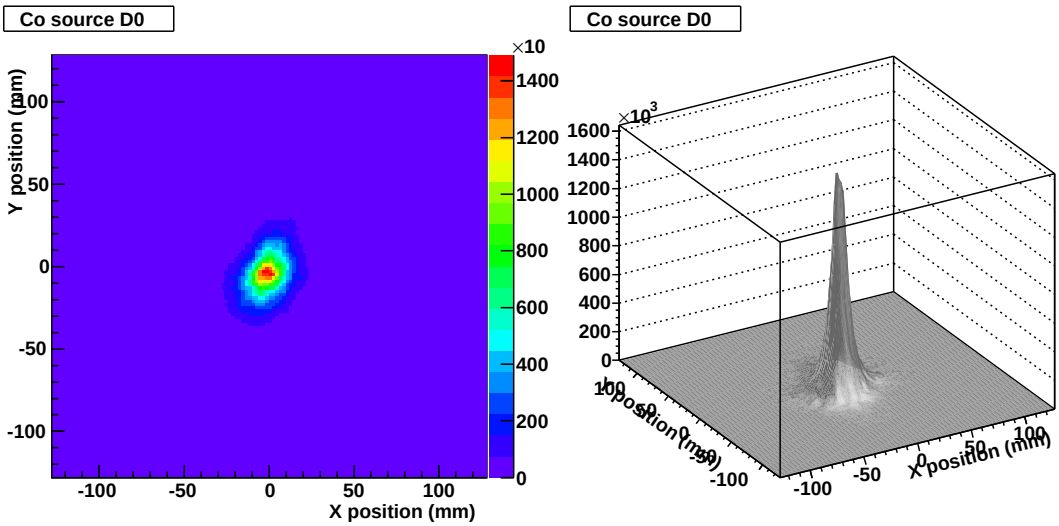

Figure 6.30: *Reconstructed image of a ^{57}Co source with the scintillator modules at distance D0.*

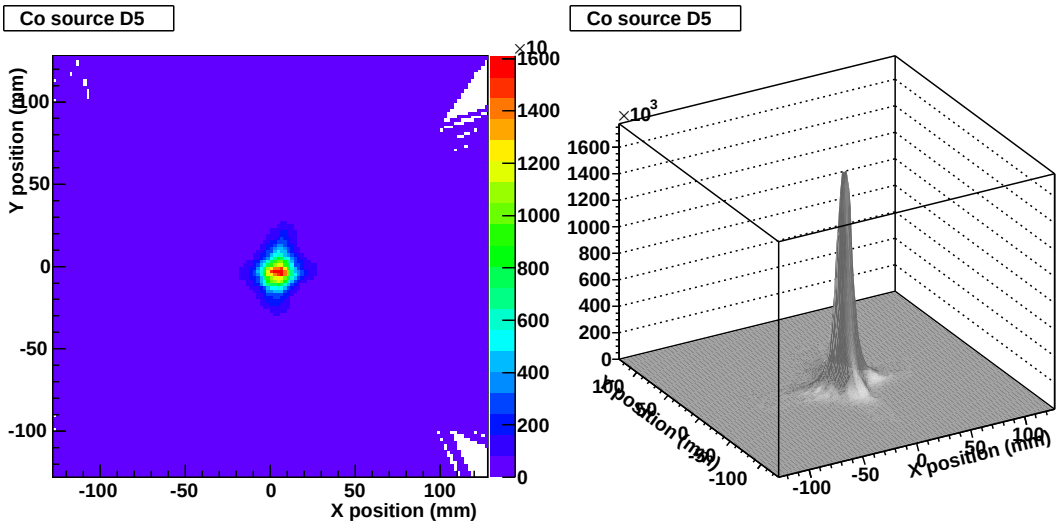

Figure 6.31: *Reconstructed image of a ^{57}Co source with the scintillator modules at distance D5.*

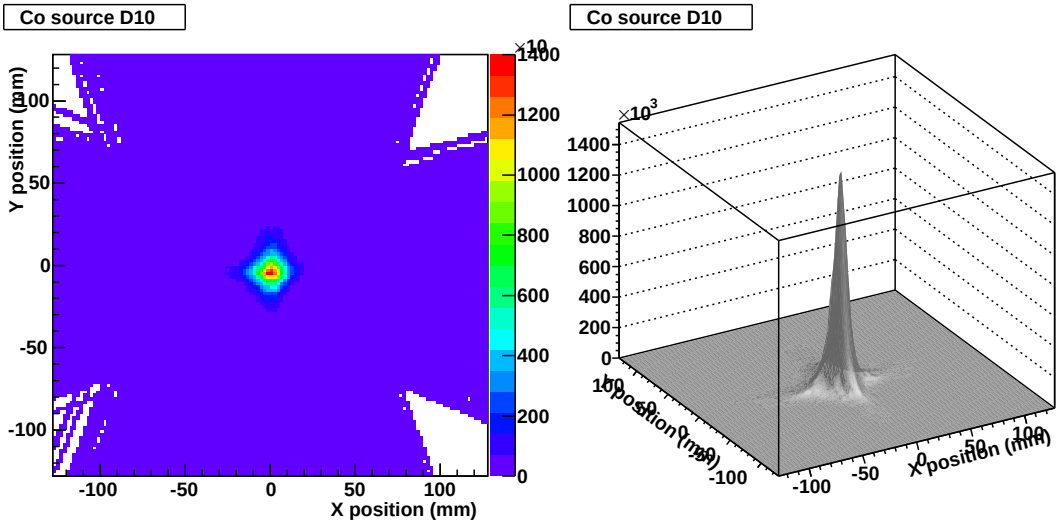

Figure 6.32: *Reconstructed image of a ^{57}Co source with the scintillator modules at distance D10.*

Energy (keV)	%	Compton edge (keV)
Ba	γ	
80	34.1	20
276	7.2	143
303	18.3	164
356	62.1	207
383	8.9	230
Cs	X-rays	
4	17.0	
31	96.2	
33	22.4	

Table 6.11: *Energies and relative intensities of the photons emitted by the ^{133}Ba source.*

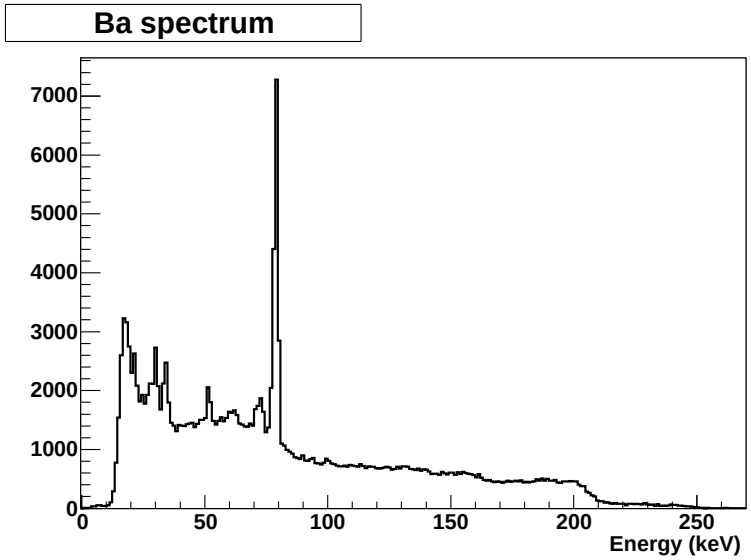

Figure 6.33: *^{133}Ba energy spectrum measured with the scatter detector.*

for the 383 keV peak is very low, and together with the loss of the highest energies due to the limited geometric acceptance of the second detector, it results in an extremely low coincidence rate for those events.

The 356 keV peak provides photons that after scattering have energies up to 207 keV, and has a high enough flux to be employed for image reconstruction. Unfortunately, the energy resolution of the scintillator is not good enough to separate contributions from different peaks by the calculation of the total energy of the event, shown in fig 6.34, and the resolution will be degraded due to the contribution of events with different total energy.

In order to have the minimum possible contribution from other peaks, events with a determined energy range in the silicon detector have been considered. Two ranges have been studied with energies from 150 keV to 178 keV, and from 133 keV to 178 keV, that correspond to angles from 92º to 116º, and from 82º to 116º respectively (see fig 6.12). This restricts the total energy of the photon to two possible values in the first case (383 keV and 356 keV) and three in the second case (383 keV, 356 keV and 303 keV). The total energy distribution for each case is shown in fig 6.35.

In both cases, the analysis is considering events at high scattering angles, and therefore the results obtained will correspond to the worst possible at the source energies considered, and with the current setup. In the second case, lower energies that improve the resolution are being considered, but it includes contributions from a third peak.

The comparison with the ^{57}Co source must be done considering the same angle interval, and those events have been selected for the image reconstruction. For the ^{57}Co source, the energy interval corresponding to 92º-116º is 24-31 keV (see fig 6.12). Since the energies considered are higher than in the cases previously shown, the resolution obtained will be worse.

The results with both sources for the three possible distances considering events in detector H are shown in table 6.12, and in figure 6.37 for the angle range 92º-116º. The

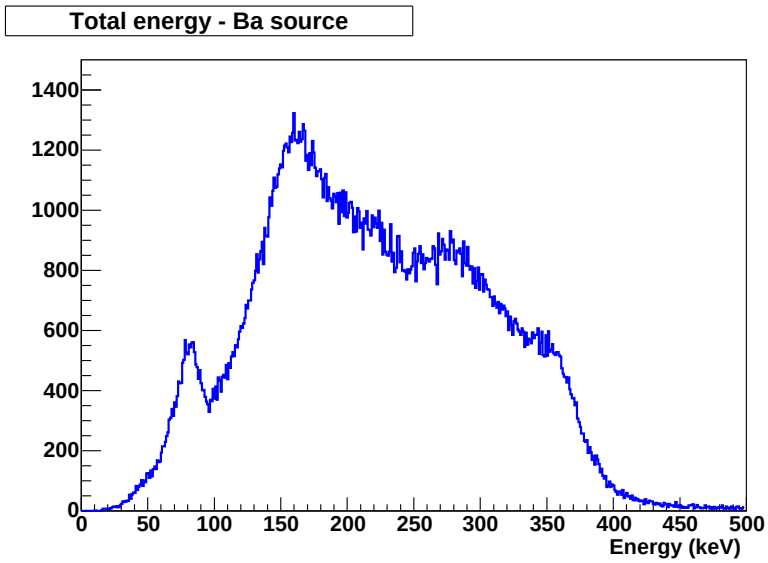

Figure 6.34: *Total energy of coincidence events for the ^{133}Ba source calculated as the sum of the energies measured in the scatter and absorption detectors.*

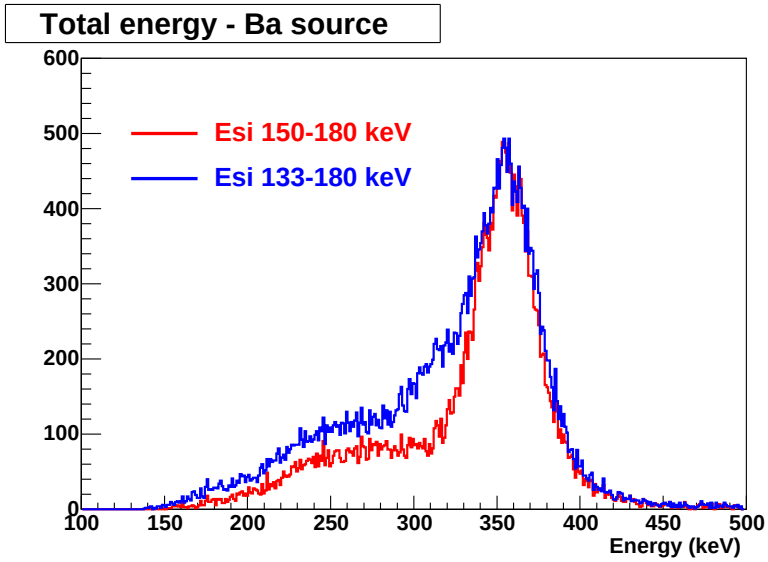

Figure 6.35: *Total energy of coincidence events for two different energy intervals in the scatter detector, including events with two (383 keV and 356 keV) or three (383 keV, 356 keV and 303 keV) different values of the photon energy.*

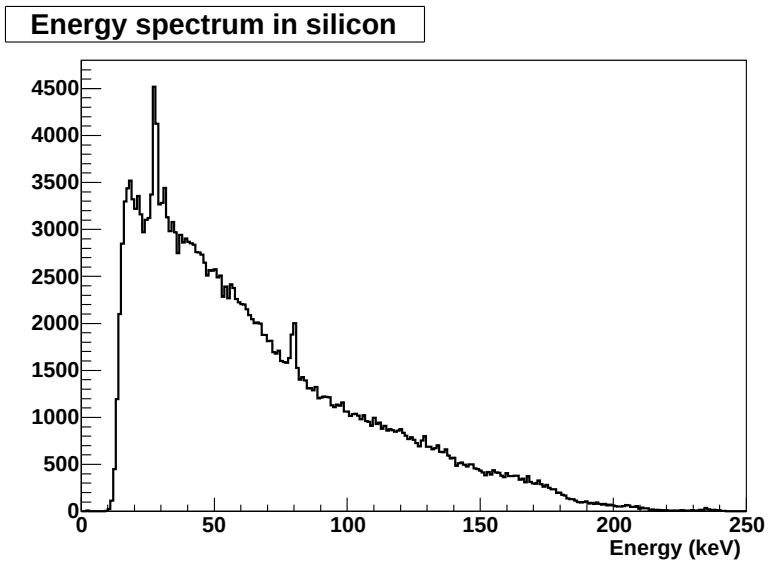

Figure 6.36: *Energy distribution of coincidence events measured with the scatter detector.*

		X resolution (mm FWHM)		
Si energy range	Angle range (degrees)	D0	D5	D10
Co: 24-31 keV	92-116	15.9	14.1	12.2
Ba: 150-178 keV	92-116	13.2	10.8	—
Ba: 133-178 keV	82-116	13.9	11.3	9.9

Table 6.12: *Results comparing the energy resolution obtained with the ^{57}Co source and the ^{133}Ba source for detector H.*

geometric limitations at D10 reduce the event rate to the point that the number of events is too low to reconstruct an adequate image with the data taken.

Although lower angles have been considered in the second range, the fact that data from a third peak are included contributes to worsen the resolution, instead of improving it. The results prove the superior performance at high energies. However, since only events with high scattering angles are being considered, they underestimate the resolution that can be obtained at those energies.

If sources with more than one peak such as ^{111}In are employed, a second detector with better energy resolution should be employed for an adequate determination of the gamma-ray energy.

Results have also been obtained with detector A, that has the best energy resolution and therefore the results obtained, shown in table 6.13, have better spatial resolution.

6.4.3 Efficiency

The efficiency of the current setup is limited by the performance of the scintillator modules in terms of low countrate and detector area. The raw efficiency has been estimated from the rate of coincidence events measured for a 4 MBq ^{133}Ba source placed at about 12 cm

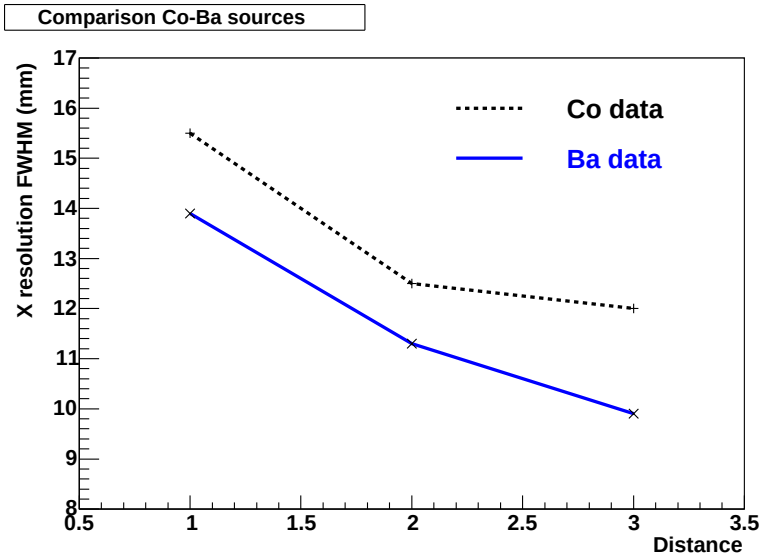

Figure 6.37: *Resolution obtained for the three distances with the two sources in the 92°-116° angle interval.*

	X resolution (mm FWHM)		
Si energy range	D0	D5	D10
Ba: 150-178 keV	11.5	8.5	-

Table 6.13: *Resolution obtained with the ^{133}Ba source for detector A.*

	D0	D5	D10
events rate (Hz)	45	20	15
efficiency	5.1×10^{-3}	2.3×10^{-3}	1.7×10^{-3}

Table 6.14: *Events rate and raw efficiency estimated for the three scintillator positions with the ^{133}Ba source.*

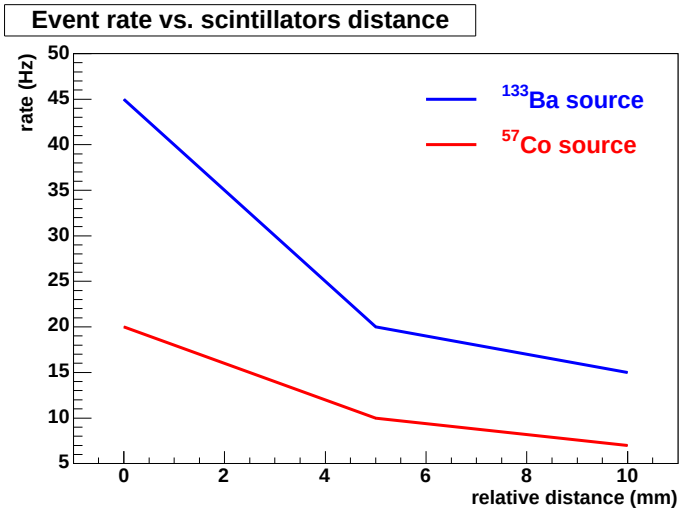

Figure 6.38: *Coincidence event rate measured for the three scintillator positions with the two sources.*

from the scatter detector. Increasing the distance results in a reduction of the solid angle subtended by the second detector, and therefore the efficiency for coincidence events is lower. The results obtained for all distances are shown in table 6.14. Figure 6.38 shows the variation of the coincidence events rate with the scintillators distance for both sources.

6.5 Expected performance

As in the previous run, simulations have been carried out. The aim in this case is to estimate the expected resolution with the current setup placing the source at smaller distances from the scatter detector. The simulations include energy resolution of the scatter detector and position resolution of both detectors, as for the previous run. In this case, the threshold set to the simulated data is 15 keV. A ^{57}Co source and 356 keV gamma rays from a ^{133}Ba source were simulated. Photons originate from a 3 mm diameter disk in both cases. The influence of the energy resolution of the scatter detector in the results with ^{57}Co has also been studied, considering different values of the energy resolution in the simulated data.

Images have been reconstructed for a single silicon sensor and two scintillators on one side and below, placed at 112.5 cm from the center of the silicon detector. The source was located at distances of 120, 70 and 20 mm from the scatter detector. The first case corresponds to the setup employed to obtain the results shown in section 6.4.1 with real data. All events recorded in each case were employed for the image reconstruction,

	X resolution (mm FWHM)		
	Co source distance (mm)		
Si energy resolution (keV FWHM)	20	70	120
1.0	3.0	6.2	10.7
1.4	3.3	8.1	12.8
2.3	3.5	11.2	15.9

Table 6.15: *Resolution obtained with a ^{57}Co source for the three distances from the source to the scatter detector and different values of the energy resolution of the scatter detector.*

	X resolution (mm FWHM)		
	Ba source distance (mm)		
Si energy resolution (keV FWHM)	20	70	120
1.4	2.35	4.11	6.35

Table 6.16: *Resolution obtained for the three distances for a 356 keV gamma-ray and 1.4 keV FWHM energy resolution of the scatter detector.*

without restricting angle intervals.

The results are shown in table 6.15 for ^{57}Co, for three different values of the energy resolution: 1 keV FWHM, 1.4 keV FWHM (similar to that measured with the real data), and 2.3 keV FWHM. The results obtained for a gamma-ray energy of 356 keV at the three distances with 1.4 keV FWHM energy resolution of the scatter detector are shown in table 6.16.

Fig 6.39 shows the results obtained with both sources for 1.4 keV FWHM energy resolution.

These results give an estimate of the improvement in the resolution of the Compton prototype that can be achieved with the current setup if adequate high energy sources are employed and the distance from the source to the scatter detector is minimized. This resolution is close to the one expected for the Compton prostate probe.

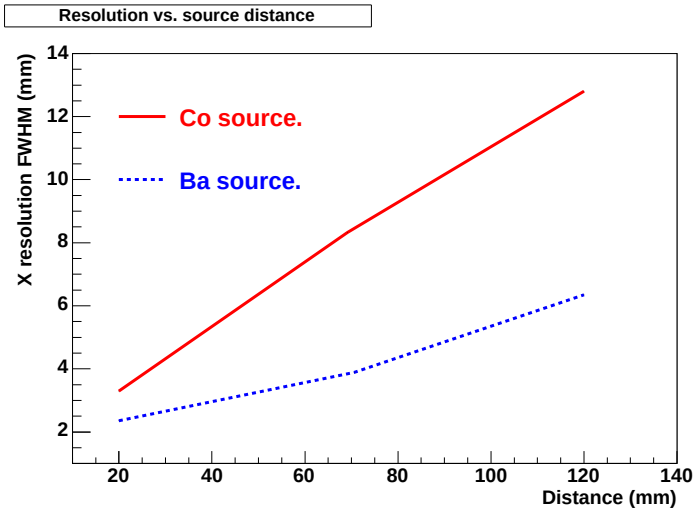

Figure 6.39: *Resolution obtained with simulated data for three different distances from the source to the scatter detector and 1.4 keV FWHM energy resolution of the scatter detector, for* ^{57}Co *and* ^{133}Ba.

Resumen

7.1 Introducción

El descubrimiento de la creación de pares electrón-hueco en uniones de germanio por partículas α en los años 50, constituyó el punto de partida para el uso de detectores semiconductores en física nuclear para medidas precisas de la energía de rayos gamma desde unos keV hasta 10 MeV. Su empleo en física de altas energías comenzó en los años 70, cuando se utilizaron telescopios compuestos por varias filas de detectores de silicio para monitorización de haces. En los años 80, se emplearon por vez primera para la medida de trayectorias de partículas, y desde entonces se han incluido en la mayoría de los experimentos de altas energías de los últimos 20 años, desde grandes colisionadores hasta experimentos de blanco fijo, o espectrómetros para experimentos espaciales. Sus avances se han desarrollado paralelamente a los de la microelectrónica empleada en su lectura, cuyo progreso ha derivado en un procesado de la señal más rápido y con una mejor relación señal-ruido. El éxito de estos detectores se basa en sus características que los convierten en excelentes dispositivos para medidas de energía y posición con gran precisión. Algunas de estas características son linealidad, excelente resolución energética, velocidad del orden de 10 ns, resolución espacial de hasta 2-3 μm, flexibilidad de diseño, buenas propiedades mecánicas y tolerancia a altas dosis de radiación.

La medicina nuclear es un campo que puede verse enormemente beneficiado gracias al empleo de detectores de silicio. Actualmente en la tomografía por emisión de fotones (SPECT por sus siglas en inglés), detectores de centelleo mecánicamente colimados, para los cuales la resolución y la eficiencia se relacionan inversamente, son utilizados para la detección y determinación de la dirección de la que provienen los fotones. El empleo de detectores de silicio permitiría implementar una técnica conocida como *método Compton de obtención de imágenes* que ha sido utilizada con éxito en telescopios Compton. Los colimadores mecánicos son sustituidos por un detector en el que los fotones procedentes de una fuente radiactiva interaccionan por dispersión Compton antes de ser absorbidos por un segundo detector, que puede ser un centelleador. Utilizando esta técnica, tanto la resolución espacial como la eficiencia del centelleador pueden mejorarse simultánemente. Los detectores de silicio resultan ser la mejor opción para el primer detector.

Una posible aplicación de este método, de especial interés, es el desarrollo de una sonda para la obtención de imágenes de la próstata. El cancer de próstata es el segundo más común entre los varones, y sin embargo los métodos actuales de obtención de imágenes no son adecuados en ese campo. Según los resultados de exhaustivas simulaciones que se han llevado a cabo, el desarrollo de una sonda Compton para la próstata supondría un inmenso

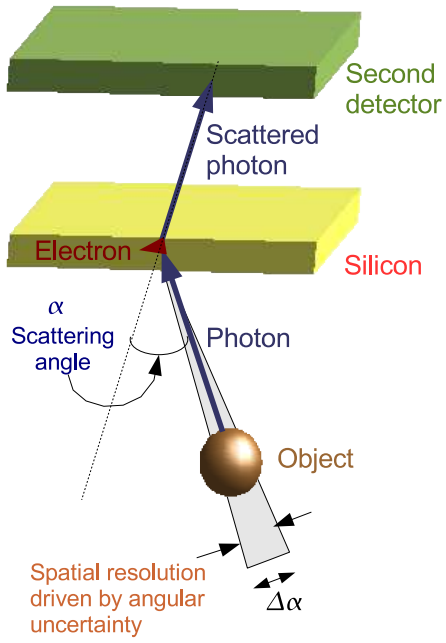

Figure 7.1: *Principio de funcionamiento de un detector Compton. Los fotones incidentes son colimados electrónicamente por dispersión Compton en un primer detector (detector de* scattering*), y posteriormente absorbidos por un segundo detector (detector de absorción).*

avance en detección de tumores en sus primeras etapas de desarrollo en comparación con los métodos empleados en la actualidad.

El desarrollo de un prototipo clínico que permita validar los resultados de las simulaciones está en proceso. Se ha construido un primer prototipo, con el propósito de demostrar la posibilidad de utilizar un primer detector compuesto por una pila de módulos de silicio, para aumentar la eficiencia de detección. Este primer paso es esencial en el desarrollo de la sonda. Se han desarrollado específicamente para esta aplicación detectores de silicio de 1 mm de espesor y su electrónica de lectura asociada.

El trabajo aquí expuesto describe el desarrollo de primer prototipo y los resultados obtenidos con él.

7.2 Método Compton de obtención de imágenes.

El principio de funcionamiento de un detector Compton se ilustra en la figura 7.1. Los fotones procedentes de la fuente radiactiva (un radiotrazador administrado al paciente), interaccionan por dispersión Compton en un primer detector (detector de dispersión o de *scattering*), y son posteriormente absorbidos por un segundo detector (detector de absorción). La determinación de la dirección de los fotones mediante este método recibe el nombre de *colimación electrónica*, y no restringe la dirección de los fotones como sucede con los colimadores mecánicos. Esto permite aumentar la eficiencia en comparación con los detectores colimados mecánicamente, utilizados en SPECT.

Conociendo la energía depositada en el detector de *scattering*, es posible determinar

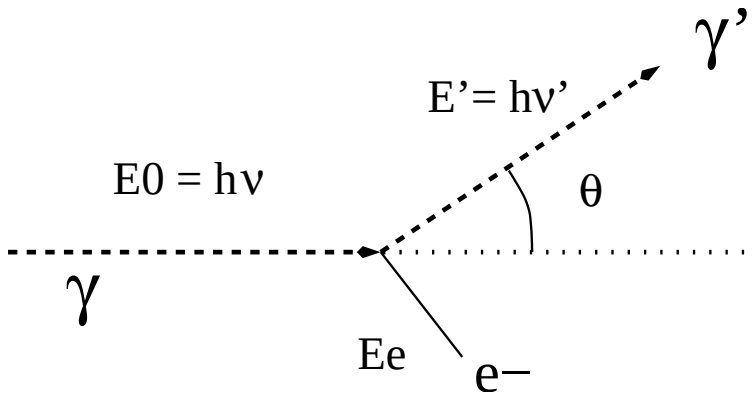

Figure 7.2: *Cinemática de las interacciones Compton.*

el ángulo de dispersión de los fotones a partir de la relación [13, 14]

$$E' = E_0 - E_e = \frac{E_0}{1 + \alpha(1 - cos\theta)}. \tag{7.1}$$

En esta ecuación E_0 es la energía inicial del fotón, E' es la energía del fotón dispersado, θ es el ángulo de dispersión, E_e es la energía del electrón, y $\alpha = \frac{E_0}{m_0 c^2}$, donde m_0c^2=0.511 MeV es la energía del electrón en reposo (ver figura 7.2).

Dado que el vector momento del electrón es desconocido, no es posible determinar la dirección de origen de los fotones. Sin embargo, a partir de los puntos de interacción en los dos detectores y el ángulo de dispersión, es posible reconstruir una superficie cónica en la que debe situarse el punto a partir del cual el fotón fue emitido. La intersección de los conos generados en diferentes sucesos permite la localización de la fuente.

Este método de determinar la posición de la fuente supone una recontrucción de la imagen mucho más compleja que en el caso del SPECT convencional. El posible beneficio en la eficiencia se obtiene por tanto a cambio de un mayor coste computacional.

El rendimiento de los detectores Compton depende en gran medida de las características de los detectores que lo componen, así como de su geometría. La mejora respecto a los detectores convencionales no está por tanto garantizada, y su funcionamiento dependerá de sus características.

7.2.1 Resolución espacial

La resolución espacial de un detector Compton depende de la precisión con que se reconstruye el cono, que depende de la resolución espacial y energética de los detectores que lo componen, así como de su geometría.

La resolución espacial del detector de absorción afecta a la orientación del cono, mientras que la resolución espacial del detector de *scattering* afecta tanto a la orientación del cono, como a la posición de su vértice. Además, la influencia de la resolución espacial del detector de absorción depende de la distancia relativa entre ambos detectores, disminuyendo cuando ésta aumenta.

Cuando la geometría del detector es óptima para minimizar la influencia de la resolución de los detectores, los parámetros clave que determinan la resolución espacial del

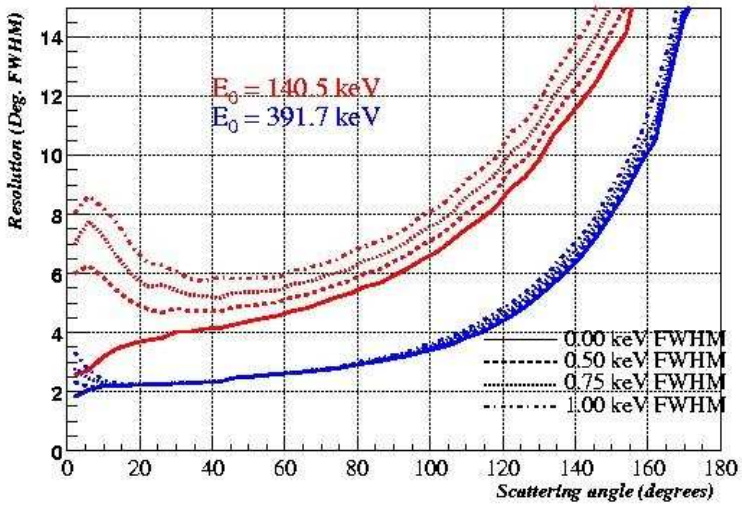

Figure 7.3: *Incertidumbre angular frente al ángulo de dispersión para dos valores de la energía del fotón incidente, y diferentes valores para la resolución energética del primer detector.*

detector son la incertidumbre en el ángulo de dispersión, y la distancia del detector de *scattering* a la fuente radiactiva. Para una resolución angular determinada, la incertidumbre en la resolución espacial es mayor cuanto más alejada se encuentra la fuente del primer detector (ver figura 7.1.).

La incertidumbre en el ángulo de dispersión viene afectada por dos factores, la precisión en la medida de la energía en el primer detector, y el ensanchamiento Doppler. En la deducción de la ecuación 7.1, se ha considerado el electrón libre. Sin embargo, los electrones que intervienen en la interacción están ligados a un núcleo del material y tienen un determinado momento cinético. La distribución de momentos de los electrones da lugar a una distribución de energías alrededor del valor dado por la ecuación 7.1 para un ángulo de dispersión fijo. Este efecto es conocido como ensanchamiento Doppler, y depende del material en que se produce la interacción. Para un material concreto, el efecto es mayor para menores energías del fotón incidente, y para mayores ángulos de dispersión.

La influencia de la resolución energética del detector puede obtenerse a partir de la ecuación 7.1, y viene dada por [5]

$$\Delta\theta = \frac{m_0 c^2}{sin\theta(E_0 - E_e)^2}\Delta E_e$$

La función seno en el denominador hace que la incertidumbre crezca para ángulos próximos a 0º y 180º. La dependencia $\frac{1}{E_0}$ hace que a energías más altas, la incertidumbre disminuya y por tanto la resolución del detector Compton mejore, al contrario que para el SPECT convencional.

La figura 7.3 muestra la incertidumbre en el ángulo de dispersión para dos valores distintos de la energía del fotón incidente (140.5 keV del ^{99m}Tc y 391.7 keV del ^{113m}In), y para diferentes valores de la resolución energética del detector. La influencia del ensanchamiento Doppler también ha sido considerada. La línea continua corresponde a un detector con perfecta determinación de la energía, y por tanto la incertidumbre angular se

debe únicamente al ensanchamiento Doppler. Este efecto es menor para energías mayores, y para ángulos bajos, que son por tanto los más adecuados con vistas a la reconstrucción de imágenes.

Las líneas discontinuas incluyen diferentes valores para la resolución energética del detector. Para energías altas, su efecto es prácticamente despreciable, mientras que para energías más bajas la influencia puede ser significativa.

7.2.2 Eficiencia

La eficiencia de los detectores Compton depende de la probabilidad de que el fotón interaccione por dispersión Compton en el primer detector y a continuación sea absorbido en el segundo detector. Por tanto dependerá del material, tamaño y disposición de ambos detectores.

A la hora de comparar la eficiencia del detector Compton con la del SPECT convencional se ha de tener en cuenta el hecho de que se necesitan varios sucesos para determinar la posición de la fuente. Se han llevado a cabo estudios que permiten determinar la ganancia en eficiencia que debe tener una cámara Compton para ser comparable a SPECT para una determinada geometría. Para una fuente en forma de disco de 7.5 cm de diámetro, la eficiencia de la cámara Compton ha de ser 40 veces mayor si la fuente empleada es de ^{99m}Tc (140.5 keV). Sin embargo, para una fuente de ^{131}I (364.4 keV), la relación es únicamente un factor 2. Si se consideran fuentes de menor tamaño, estos valores disminuyen.

7.2.3 Requisitos de los detectores

La adecuada selección de los detectores y la geometría es esencial para un funcionamiento óptimo del detector Compton.

Para el detector de *scattering*, lo deseable es que se produzca una única interacción Compton, seguida del escape del fotón, junto con una precisa determinación del punto de interacción y del ángulo de dispersión. Los requisitos son, por tanto, elevada probabilidad de interacción, buena resolución espacial y excelente resolución energética que permita una adecuada determinación del ángulo de dispersión.

La probabilidad de que se produzca una interacción Compton aumenta linealmente con el número atómico del material, mientras que la probabilidad de fotoabsorción aumenta como Z^n, donde n toma valores entre 4 y 5. Los materiales adecuados deben tener bajo número atómico. Detectores de estado sólido (Si, Ge) o detectores gaseosos (Ne, Xe, Ar), son buenos candidatos para el detector de *scattering*.

La principal ventaja de los detectores de estado sólido viene dada por su baja energía de ionización (3.6 eV para el Si, 2.9 eV para el Ge) comparado con el valor típico de 30 eV para los gases. El mayor número de portadores generados por unidad de radiación absorbida es mucho mayor, y por tanto las fluctuaciones estadísticas son menores. Como resultado, la resolución energética es mejor.

De entre los detectores de estado sólido, varias razones hacen de los detectores de silicio la opción más adecuada [27].

A pesar de que la sección eficaz Compton es menor que la del Ge, reduciendo la eficiencia, la relación entre la sección eficaz Compton y la total es mayor. Además,

la probabilidad de doble interacción Compton es suficientemente baja. También se ha de considerar el hecho de que los detectores de Ge necesitan ser refrigerados para un correcto funcionamiento, mientras la resolución energética de los detectores de Si es buena a temperatura ambiente. Otro factor a tener en cuenta es el ensanchamiento Doppler, que es menor para el Si que para el Ge. El diamante tiene menor ensanchamiento Doppler, pero la tecnología de detectores de diamante se encuentra aún en fase de desarrollo.

El proceso de fabricación de detectores de silicio ha alcanzado en la acualidad un alto grado de madurez y estabilidad, paralelo al de la electrónica empleada en su lectura. Su empleo cada vez más frecuente en física de altas energías ha disminuido su coste. Todas estas razones hacen de los detectores de silicio la opción óptima para el primer detector.

El objetivo del segundo detector es absorber los fotones dispersados. Los materiales adecuados deben tener alta densidad y número atómico para una adecuada fotoabsorción, evitando interacciones Compton.

Los centelleadores, utilizados comúnmente en física médica, son materiales adecuados para el segundo detector. Además de los más usuales como NaI, CsI o BGO, en la actualidad se investiga una gran variedad de nuevos materiales, tratando de mejorar las propiedades de los ya existentes [30, 29].

Otra posibilidad es la utilización de detectores de estado sólido de número atómico alto, como CdTe o CZT, que tienen una probabilidad de interacción similar a la del NaI(Tl), y excelente resolución espacial y energética. Sus mayores desventajas son su elevado coste y el hecho de que al tener menor grosor, se necesita un mayor número de detectores para lograr una eficiencia similar.

La geometría también desempeña un papel fundamental en el rendimiento de un detector Compton. Como se ha mencionado previamente, la distancia de la fuente al detector de *scattering* influye en gran medida en la resolución espacial. Además, el mayor ángulo sólido subtendido hace que aumente la eficiencia. Aumentar la distancia relativa entre detectores minimiza la influencia de la resolución espacial del segundo detector, y por tanto también contribuye a mejorar la resolución del detector Compton. Sin embargo en este caso el ángulo sólido disminuye, y con él la eficiencia.

Otros factores, como el espesor del detector de *scattering*, también deben ser considerados. Un espesor de 10-12 cm de silicio resulta ser óptimo para maximizar la eficiencia de una única interacción Compton. Lograr el grosor deseado con el espesor típico de 300 μm requeriria el empleo de un excesivo número de detectores.

Por ello es necesario aumentar el grosor de los detectores de silicio, a pesar de que ello supone otros requisitos técnicos.

Otras consideraciones han de tenerse en cuenta en la geometría, como situar el detector de absorción de modo que registre aquellos fotones con menor ángulo de dispersión. También es interesante evitar que el segundo detector reciba fotones procedentes directamente de la fuente, escogiendo una adecuada geometría, o bien añadiendo algún material para bloquear el paso de los fotones.

La geometría del detector también afecta la reconstrucción de la imagen. Limitar el ángulo de dispersión de los sucesos registrados produce artefactos en las imágenes reconstruidas, y restringir el camino de los fotones hacia el primer detector, da como resultado una peor resolución en el eje transversal.

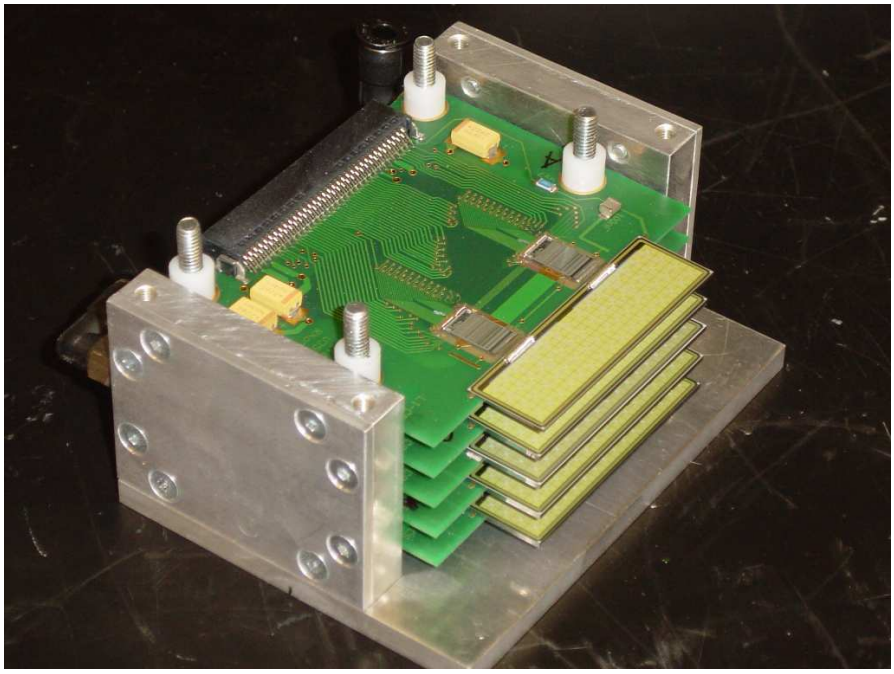

Figure 7.4: *Detector de* scattering *formado por una pila de detectores de silicio, uno de de 0.5 mm y uno de 1 mm de grosor.*

7.3 Desarrollo del prototipo

El principal objetivo en la construcción de este prototipo ha sido desarrollar y comprobar el correcto funcionamiento de detectores de silicio de grosor mayor a las $300\mu m$ habituales para su empleo como detector de *scattering* en el prototipo, asi como lograr el funcionamiento de varios de estos detectores simultáneamente.

El empleo de detectores de silicio de mayor grosor pretende aumentar la eficiencia del detector de *scattering* sin aumentar excesivamente el número de canales de lectura. Sin embargo, el aumento del grosor de un detector de silicio implica otro tipo de dificultades derivadas del incremento de la corriente de fuga, que aumenta el ruido y degrada la resolución energética, el aumento del voltaje de desertización, y el aumento del tiempo de formación de la señal. Por ello, el empleo de detectores de silicio de mayor grosor impone un importante reto tecnológico al desarrollo del prototipo.

7.3.1 Detector de *scattering*

El detector de *scattering* consiste en una pila de hasta un máximo de 5 módulos de silicio (figura 7.4). Cada uno de los módulos está compuesto por un híbrido que da soporte al detector y a la electrónica de lectura. Los detectores son sensores de silicio de *pads*, de dimensiones 46 mm×16 mm, y 500 μm o 1 mm de espesor. Sus 256 *pads* están dispuestos en una matriz de 8×32, y tienen un tamaño de 1.4 mm × 1.4 mm, siendo por tanto su resolución espacial de 0.404 mm, lo que supone una contribución despreciable a la resolución espacial del prototipo. Los sensores han sido desarrollados por SINTEF. La figura 7.5 muestra una sección transversal. Los *pads* son implantes tipo p^+ en silicio n^-

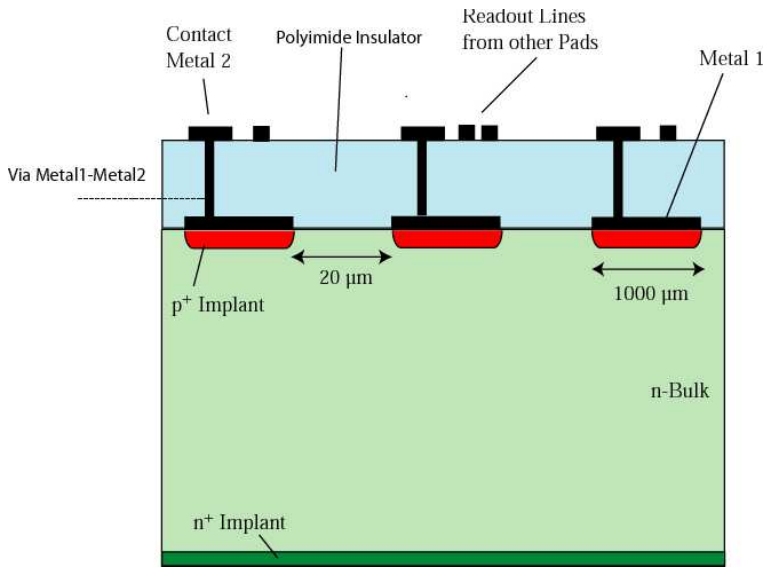

Figure 7.5: *Sección transversal de un detector de silicio.*

de alta resistividad, con una separación de 20 μm respecto a los *pads* adyacentes. Los *pads* de aluminio situados sobre ellos y cubiertos por una capa de poliimida, recogen las señales. La tecnología "doble metal" permite guiar las señales hasta el borde del detector. Una via en la capa de poliimida conecta el *pad* de aluminio con un contacto de metal en la superficie del detector, del cual parten las líneas que guiaran las señales hasta el extremo del detector. Allí se conectan mediante microsoldaduras a la electrónica de lectura.

Las medidas de corriente de fuga dan valores ente 20 y 50 pA por *pad* a 400 V para los distintos detectores de 1 mm de grosor, y el voltaje de desertización es de 140-150 V.

La electrónica de lectura debe ser de bajo ruido y proporcionar la señal que indica la llegada de las partículas (*trigger*). Para la electrónica de lectura se ha escogido el ASIC VATAGP3 de IDEAS [105]. Las señales de los 256 *pads* de un detector son leidas mediante dos chips de 128 canales cada uno. En cada canal, la señal, tras ser amplificada, es dividida en dos partes. Una proporciona el *trigger* en 150 ns a partir de la llegada de la partícula. Otra es la encargada del muestreo de la señal una vez alcanzado su máximo valor, para dar lugar a la salida analógica proporcional a la energía depositada en el detector.

La tabla 7.1 muestra la resolución energética obtenida tras el análisis de los datos para cinco módulos, cuatro de ellos de 1 mm de grosor, y el quinto (A) de 0.5 mm. La figura 7.6 muestra dos espectros, de ^{241}Am y ^{57}Co, con datos de los 256 *pads* de un detector de 1 mm de grosor.

7.3.2 Detector de absorción

El segundo detector lo componen hasta tres detectores de centelleo situados a ambos lados y debajo del detector de *scattering*, obtenidos de un tomógrafo existente. Su elección la viene determinada por la disponibilidad, y no constituyen la mejor opción posible para el segundo detector. Fueron originalmente diseñados para ser utilizados con colimadores

Modulo	resolucion energetica (keV FWHM)
A	1.165 ± 0.009
H	1.278 ± 0.005
F	1.370 ± 0.005
G	1.450 ± 0.009
B	1.511 ± 0.005

Table 7.1: *Resolución energética para 5 módulos de silicio.*

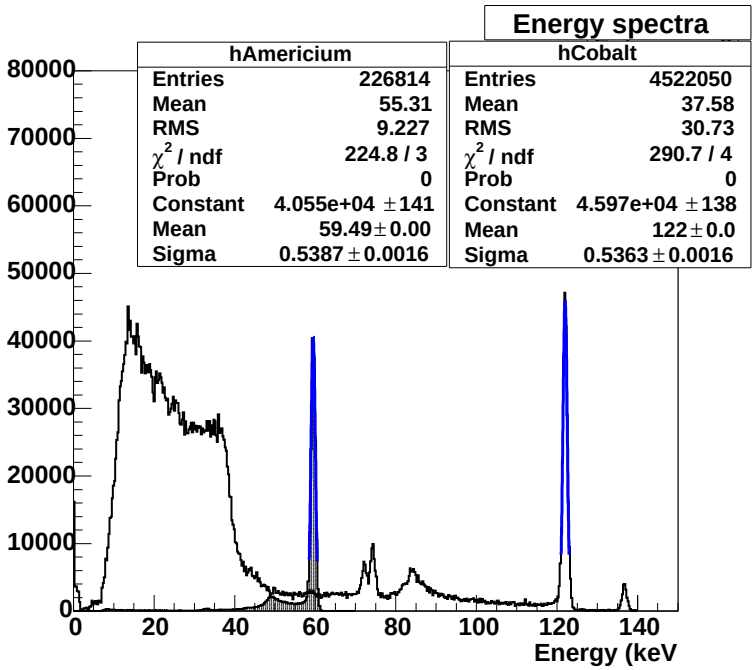

Figure 7.6: *Espectros energéticos de ^{241}Am y ^{57}Co para un detector de 1 mm de grosor, incluyendo datos de los 256* pads.

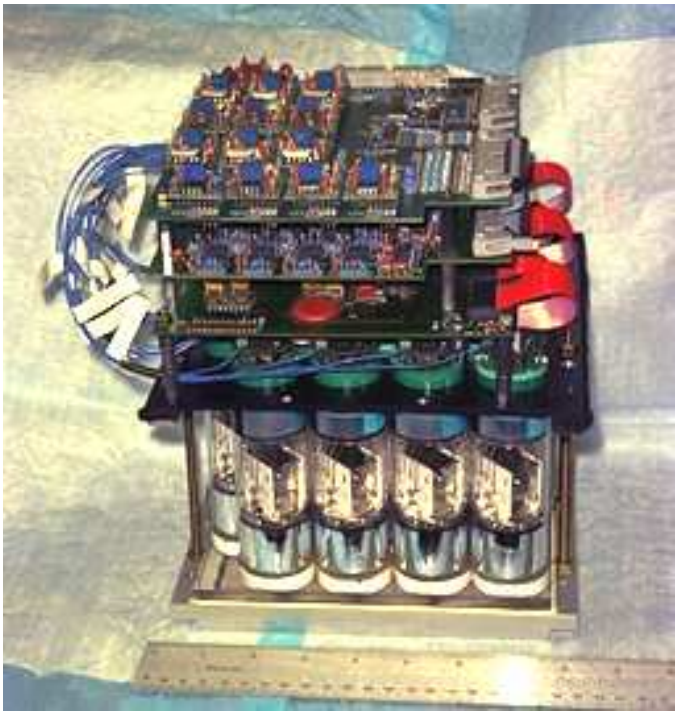

Figure 7.7: *Módulo centelleador*

mecánicos, y su capacidad de contaje es limitada. Su resolución energética también es limitada. Sin embargo, cumplen los requisitos necesarios para ser utilizados como segundo detector, absorber los fotones dispersados en el primer detector y determinar su posición, y nos ha permitido realizar los experimentos previstos satisfactoriamente.

Cada uno de los módulos (figura 7.7) está formado por 44 barras da NaI(Tl) de dimensiones 3 mm×13 mm×150 mm. Veinte tubos fotomultiplicadores (PMTs) de 38 mm de diámetro se acoplan al centelleador cubriendo la mayor área posible, para detectar los fotones de centelleo y formar la señal. Unas tarjetas electrónicas también integradas en los módulos procesan las señales de cada uno de los PMTs, y de la suma, que a través de un discriminador, proporciona la señal de *trigger*. La posición de la interacción se determina con una precisión de 1-2 mm, y la resolución energética es de 16.5 keV FWHM para fotones de 122 keV.

7.3.3 Prototipo

La figura 7.8 muestra un esquema tridimensional del prototipo, donde se aprecian los diferentes componentes. Los detectores de silicio se situan en el centro del prototipo, y los módulos centelleadores a los lados y debajo, a una distancia de unos 62 mm de distancia del centro del detector. Una estructura metálica diseñada expresamente asegura la posición correcta de los detectores con gran precisión. La fuente puede situarse dentro o fuera de la estructura metálica, emitiendo fotones hacia el detector de *scattering*.

La señal generada a partir de la coincidencia del *trigger* de ambos detectores se emplea para iniciar la lectura de los datos del silicio y del módulo centelleador que ha detectado

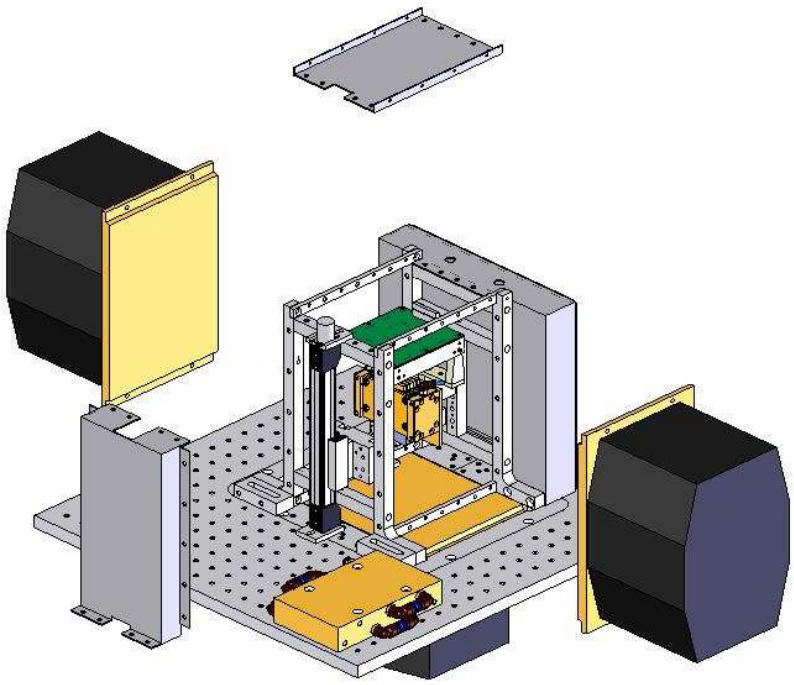

Figure 7.8: *Esquema tridimensional del prototipo. El detector de* scattering*, en el centro, se encuentra rodeado por tres detectores de centelleo, a ambos lados y debajo.*

el fotón. De este modo se logra iniciar la lectura de datos únicamente cuando se produce la coincidencia de las señales, reduciendo el tiempo muerto. Para ello es necesario un circuito electrónico externo al prototipo.

La ventana de coincidencias ha de ser amplia (200 ns) debido a la variación temporal en la generación de la señal de *trigger* con respecto al momento de llegada de la partícula dependiendo de la amplitud de la señal (*time-walk*).

7.4 Resultados

Los resultados que se presentan en esta sección corresponden a un primer test, y dos ejercicios de toma de datos (*runs*) y reconstrucción de imágenes llevados a cabo.

El test (CERN, verano 2003) se realizó con un detector de $500\mu m$ y un solo módulo centelleador, para comprobar el correcto funcionamiento de ambos detectores y el circuito de coincidencias, asi como del programa de adquisición de datos. A pesar de que el centelleador no estaba calibrado y no es posible la reconstrucción de imágenes con precisión, los resultados obtenidos son interesantes y permiten una mayor comprensión del análisis de datos.

Una vez desarrollado el prototipo (figura 7.9), se llevaron a cabo dos *runs*, de toma de datos, análisis de los resultados y reconstrucción de las imágenes. El primero (Ann Arbor, verano 2004) constituye la primera prueba con el detector de *scattering* compuesto por una pila de detectores de silicio. A pesar de haberse probado la posibilidad de funcionar de este modo, el rendimiento del prototipo no fue óptimo. Sin embargo, el análisis

Figure 7.9: *Fotografía del prototipo donde pueden verse los centelleadores a ambos lados y debajo. El detector de silicio está en el interior de la estructura metálica*

de los datos permitió detectar y subsanar algunos de los principales problemas. En el segundo *run* (CERN, Mayo 2005) se intenta corregir estos problemas y mejorar la resolución de las imágenes reconstruidas. Además se realizaron medidas adicionales para comprobar la mejora de la resolución con la energía del fotón incidente, y la distancia de los centelleadores al detector de silicio.

7.4.1 Análisis de datos.

El análisis de los datos consiste en determinar las posiciones y energía de las interacciones en ambos detectores, que coinstituirán la entrada del programa de reconstrucción de imágenes. La energía y la posición en el detector de absorción se determinan con ayuda de una calibración realizada previamente. La medida de la energía en el segundo detector no es necesaria para la reconstrucción de la imagen, si se conoce la energía del fotón incidente, pero resulta útil para descartar aquellos sucesos cuya suma de energías medidas con ambos detectores no coincida con la energía inicial del fotón.

En el caso del silicio, la posición de la intección viene dada por el *pad* en que tiene lugar. Para la determinación de la energía también es necesaria una calibración que determine para cada canal la ganancia que relacione la señal producida con la energía depositada. La distribución de energías medidas en el detector de silicio para los sucesos obtenidos en coincidencia de los dos detectores depende de la geometría del detector. Los resultados del primer test ilustran esta circunstancia. Los datos de coincidencias se tomaron utilizando una fuente de ^{57}Co, que emite fotones con energías de 122 keV y 136 keV. Sin embargo, la probabilidad de emisión de fotones con la energía mas alta es

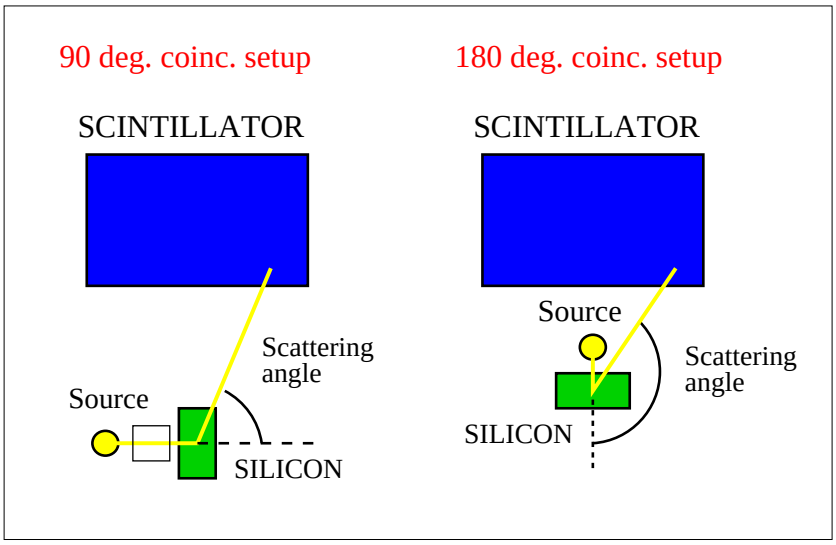

Figure 7.10: *Posición relativa del detector de* scattering *y de absorción en las dos configuraciones geométricas.*

muy reducida en comparación con la de 122 keV, de modo que sólo ésta será tenida en cuenta en el análisis.

Los datos se tomaron con un detector silicio de 500 μm de espesor, y un centelleador en diferentes posiciones relativas (figura 7.10). En la configuración 90-deg, el centelleador está situado de modo que absorbe los fotones con ángulos de dispersión próximos a 90º. En la configuración 180-deg son detectados aquéllos con ángulos cercanos a 180º.

La figura 7.11 muestra un espectro energético de ^{57}Co junto con el de los sucesos de coincidencias registrados en la configuración 90-deg. El corte en las energías más altas se debe a la geometría, que no permite detectar fotones a partir de un determinado ángulo de dispersión. El corte de las energías más bajas viene dado por el umbral energético que es necesario utilizar en el detector de silicio para evitar el ruido. El corte en la energía determina el mínimo ángulo que es posible detectar, según la ecuación 7.1.

La distribución de ángulos correspondiente puede verse en la figura 7.12, para ambas configuraciones. También aparecen distribuciones a partir de datos simulados, que permiten una mejor comprensión de los resultados. En la configuración 90-deg, los ángulos medidos se encuentran entre 40º y 120º. En el caso de la configuración 180-deg, los ángulos medidos vienen determinados por la geometría, y los fotones con ángulos próximos a 180º son absorbidos por el recubrimiento protector de la fuente radiactiva.

La resolución energética, dominada por la del centelleador, es de 26 keV en el caso de datos tomados con ^{57}Co (122 keV). Para los datos de ^{99m}Tc (140.5 keV), la resolución es de 24 keV.

La reconstrucción de imágenes se lleva a cabo mediante el método iterativo MLEM. La imagen obtenida es una matriz de números que representan la intensidad de la fuente en diferentes posiciones en un plano. Para obtener la resolución de la imagen se selecciona una fila o columna de datos, paralela al eje X o Y, que corresponda a la posición de intensidad máxima en la imagen. A la representación del pico así obtenida se le ajusta una función formada por la suma de dos gaussianas que nos permite obtener la anchura

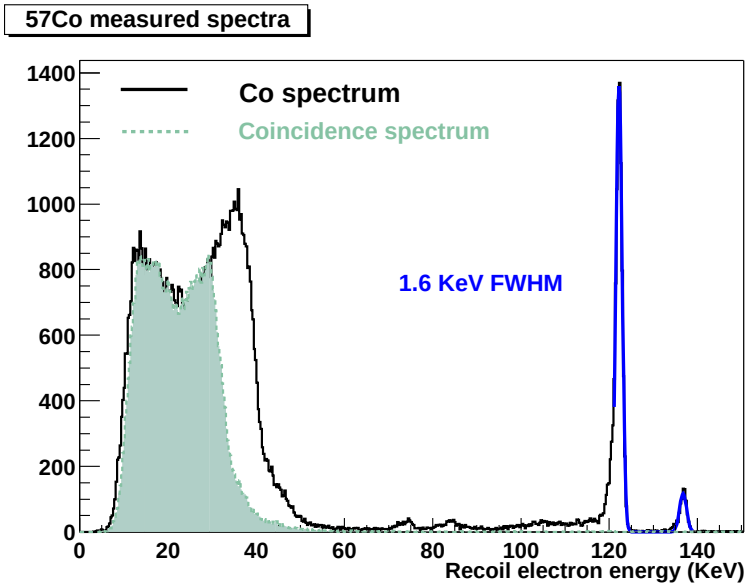

Figure 7.11: *Espectro energético de ^{57}Co medido en el detector de silicio, y energía medida en los datos de coincidencias.*

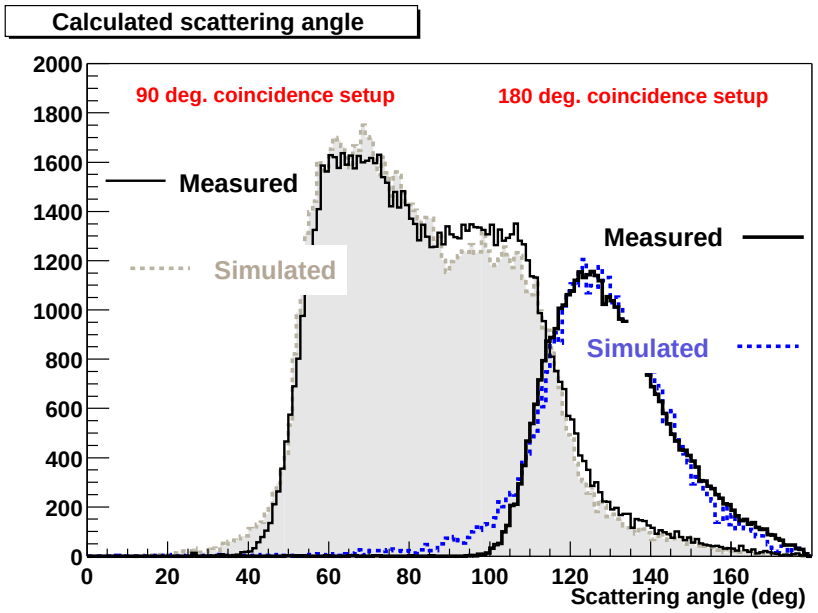

Figure 7.12: *Distribuciones angulares, medidas y simuladas para las configuraciones 90-deg y 180-deg.*

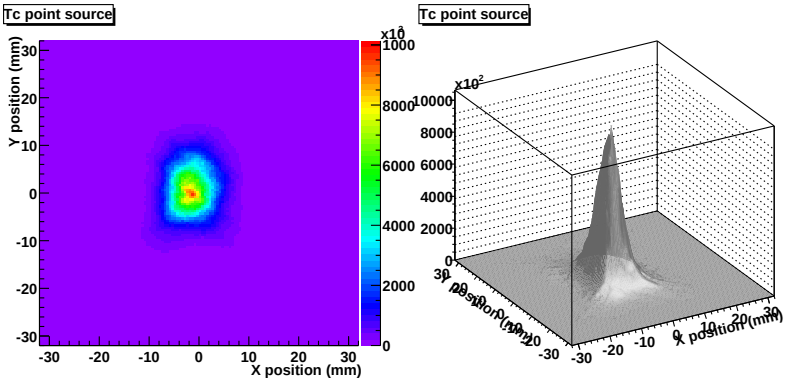

Figure 7.13: *Imagen reconstruida de una fuente puntual de* ^{99m}Tc *situada a 4.5 cm del detector de* scattering*, con una resolución de 7.1 mm FWHM.*

del pico.

7.4.2 Resultados del primer *run*.

Para el primer run se emplearon cinco detectores de silicio en el detector de *scattering* (uno de 0.5 mm de espesor, y los restantes de 1 mm) y dos centelleadores situados a ambos lados. El objetivo primordial era demostrar la posibilidad de tomar datos de coincidencias con un detector de *scattering* compuesto por varios módulos de silicio. Con este equipo se tomaron datos con una fuente de ^{99m}Tc, que tras ser analizados, permitieron la reconstrucción de las imágenes.

La posición de la fuente hace imposible situar plomo entre la fuente y el detector de absorción para evitar que fotones procedentes de la fuente incidieran en él directamente. Esta circunstancia, unida a la de que la ventana de coincidencias ha de ser amplia, hace que se registre un gran número de coincidencias aleatorias que empeoran la resolución de las imágenes.

Además la resolución energética de los módulos de silicio se degrada al ponerlos en funcionamiento simultáneamente y es necesario un umbral alto para evitar inestabilidades en su funcionamiento.

Los datos fueron tomados con una y dos fuentes puntuales, situadas a 4.5 cm del detector de silicio más próximo. La mejor resolución obtenida corresponde a un único detector situado a 4.5 cm de la fuente. La imagen resultante, con una resolución de 7.1 mm FWHM se muestra en la figura 7.13. La figura 7.14 muestra la imagen de dos fuentes puntuales separadas 15 mm.

También se llevaron a cabo simulaciones para asegurar una perfecta comprensión de los resultados obtenidos. La geometría del sistema fue simulada con GEANT4, y se empleó EGS4-LSCAT para las interacciones electromagnéticas a baja energía.

Para una distancia fija del detctor de *scattering* a la fuente, la resolución de la imagen viene determinada principalmente por la incertidumbre en el ángulo de dispersión, dada por la resolución energética del detector y el ensanchamiento Doppler. Las simulaciones permiten el estudio de cada una de las contribuciones independientemente, incluyéndolas por separado en los datos simulados y reconstruyendo las imágenes. Los resultados

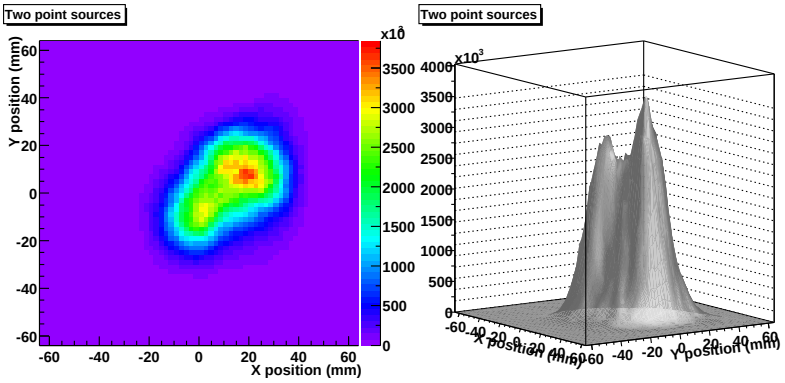

Figure 7.14: *Imagen reconstruida de dos fuentes puntuales de* ^{99m}Tc *situada a 4.5 cm del detector de* scattering *y separadas 15 mm.*

Contribucion	Resolucion (mm - FWHM)
Ensanchamiento Doppler (ED)	3.6
ED + resolución energética (REn)	5.2
ED + REn + resolución espacial (REs)	5.8
ED + REn + REs + umbral 27 keV	6.9

Table 7.2: *Diferentes contribuciones a la resolución espacial de las imágenes. Resultados de datos simulados.*

obtenidos se muestran en la tabla 7.2. En un primer paso, el único efecto considerado es el del ensanchamiento Doppler. A continuación, se incluye también la resolución energética del detector de silicio, que constituye una importante fuente de incertidumbre en el ángulo. La contribución debida a la resolución espacial de los detectores puede ser minimizada si se situan a mayor distancia relativa. Por último se ha tenido en cuenta el efecto del umbral, que corta las energías más bajas, y por tanto los menores ángulos de dispersión, que sufren menor incertidumbre angular al ser menor el ensanchamiento Doppler. Los ángulos menores permiten por tanto una mejor resolución de las imágenes reconstruidas.

El objetivo de este *run*, comprobar el funcionamiento del detector de *scattering*, se ha visto cumplido. Sin embargo, una serie de fallos hace que su funcionamiento sea peor de lo esperado. El análisis de los datos ha permitido identificar los principales problemas, algunos de los cuales pueden ser resueltos.

7.4.3 Resultados del segundo *run*.

El segundo run trata de corregir algunos de los problemas surgidos durante el primer run. En este caso se toman datos con cuatro detectores de silicio y tres centelleadores. El ruido es reducido, permitiendo situar el umbral a energías más bajas, y mejorando la resolución energética. Además se utilizan ladrillos de plomo para impedir la incidencia directa de fotones de la fuente en el detector de absorción. Para ello es necesario situar la fuente más alejada del primer detector, lo que empeora la resolución de las imágenes.

Detector	grosor (mm)	Distancia a la fuente (mm)	resol E indiv (keV- FWHM)	resol E juntos (keV- FWHM)
A	0.5	112	1.2	1.32
H	1	118	1.3	1.40
F	1	124	1.4	1.48
B	1	130	1.4	1.46

Table 7.3: *Datos técnicos de los cuatro detectores empleados en el segundo* run

Intervalo de energía (keV)	Angulos (grados)	Resolucion (mm-FWHM)
<16	<68	7.8
16 - 20	68 - 80	10.6
20 - 24	80 - 92	12.2
24 - 28	92 - 104	14.4

Table 7.4: *Resolución obtenida para datos seleccionados en distintos intervalos angulares.*

Además se han realizado nuevos tests, tomando datos con fuentes de diferente energía (^{57}Co y ^{133}Ba), y con los centelleadores a diferente distancia del primer detector, para comprobar la variación de la resolución.

En este caso se utilizaron cuatro detectores de silicio para la toma de datos. Sus características, resolución energética calculada individualmente y cuando se emplean todos juntos, así como la distancia de cada uno de ellos a la fuente se muestran en la tabla 7.3.

Como se ha visto en la sección 7.4.1, las distribuciones de energía y ángulo varían con la geometría del detector. Para una distancia dada de los centelleadores, se observan pequeñas diferencias debidas a las distintas posiciones de los módulos de silicio.Las diferencias se acentúan cuando se consideran diferentes posiciones de los centelleadores.

Variación con el ángulo

Los datos permiten estudiar la variación de la resolución con el ángulo de dispersión. Para una distancia dada, se han reconstruido las imágenes seleccionando sucesos con energías en determinados rangos, correspondientes a intervalos angulares calculados según la ecuación 7.1.

La tabla 7.4 muestra la resolución obtenida para el módulo H considerando una distancia dada de los centelleadores. Como era de esperar, la resolución mejora cuando se incluyen sucesos con ángulos de dispersión menores.

Variación con la distancia

Para este test se han tomado datos situando los centelleadores en tres posiciones a diferente distancia del primer detector. Las distancias en cada caso se muestran en la tabla 7.5, y las correspondientes distribuciones de energía y ángulo en las figuras 7.15 y 7.16. La energía mínima que puede ser medida viene dada por el umbral, y determina el ángulo mínimo. El ángulo máximo lo fija la geometría en cada caso.

	distancia (mm)
D0	62.5
D5	112.5
D10	162.5

Table 7.5: *Distancia de los centelleadores al centro del detector de* scattering *en cada una de las tres posiciones.*

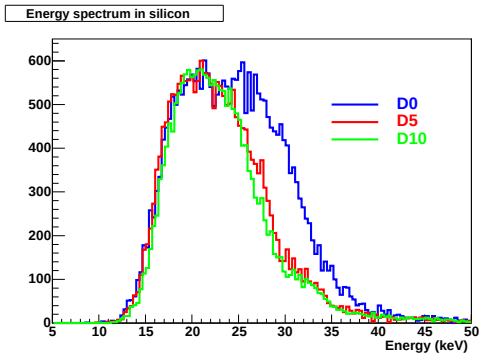

Figure 7.15: *Distribución de energías medidas para los sucesos de coincidencias en cada una de las posiciones de los centelleadores para el módulo H.*

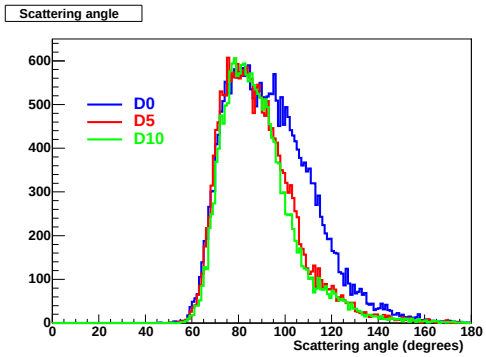

Figure 7.16: *Distribución de ángulos para los sucesos de coincidencias en cada una de las posiciones de los centelleadores para el módulo H.*

La comparación de los resultados a diferente distancia ha de realizarse en el mismo intervalo angular para evitar su influencia en la resolución. Para las tres distancias se han seleccionado datos con energías hasta 24 keV. La resolución ha sido calculada para los cuatro detectores individualmente, y también considerando datos de todos ellos. Los resultados se muestran en la tabla 7.6.

Para mayores distancias, la influencia de la resolución espacial del detector de absorción disminuye, y la resolución de las imágenes reconstruidas es mejor.

Esi <24 keV	resolucion X/Ymm FWHM		
Modulo	D0	D5	D10
A	15.4/16.1	10.4/10.9	10.1/12.6
H	16.6/15.6	13.2/13.6	13.0/13.4
F	18.1/19.6	13.7/14.3	12.0/12.5
B	15.9/15.9	13.7/14.3	13.4/14.13
TODOS	15.6/16.6	12.7/12.7	11.8/13.2

Table 7.6: *Resolución X/Y obtenida para las tres distancias considerando sucesos con energía en el silicio menor que 24 keV.*

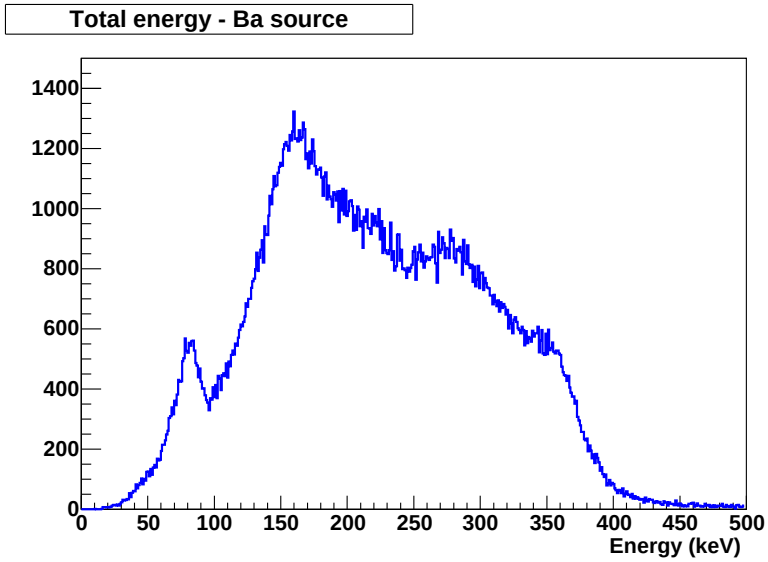

Figure 7.17: *Energía total de los sucesos de coincidencias obtenidos con la fuente de ^{133}Ba, calculada como la suma de energías medidas en ambos detectores.*

Intervalo de energia	intervalo angular (degrees)	D0	D5	D10
Co: Esi 24-31 keV	92-116	15.9	14.1	12.2
Ba: Esi 150-178 keV	92-116	13.2	10.8	—

Table 7.7: *Comparación de los resultados obtenidos con las fuentes de ^{57}Co y ^{133}Ba para el detector H.*

Variación con la energía

Para estudiar la dependencia de la resolución con la energía del fotón incidente se comparan los datos tomados con las fuentes de ^{57}Co y ^{99m}Tc. El ^{133}Ba tiene la desventaja de que emite fotones de diferentes energías. La reconstrucción de imágenes supone el conocimiento de la energía del fotón incidente, bien sea porque se utiliza una fuente monoenergética o porque puede calcularse como la suma de las energías depositadas en ambos detectores. En nuestro caso, la resolución energética del segundo detector no nos permite separar las contribuciones debidas a los fotones de diferentes energías mediante el cálculo de la energía total (ver figura 7.17), y el hecho de asignar una energía total errónea a una parte de los sucesos empeora la resolución de las imágenes.

Para lograr la mínima contaminación posible con sucesos de diferentes energías se ha seleccionado un intervalo de energía en el detector de silicio que incluye únicamente contribuciones de fotones de 356 keV, y 383 keV, siendo la probabilidad de emisión del primero muy superior a la del segundo. El intervalo seleccionado es de 150 keV a 178 keV, que corresponde a un intervalo angular de 92º a 116º. Para comparar con el ^{57}Co se han reconstruido las imágenes con sucesos en el mismo intervalo angular, que en este caso corresponde a energías de 24 keV a 31 keV. Los resultados (tabla 7.7) muestran una mejor resolución para fuentes de mayor energía.

Hay que tener en cuenta que además de incluir contribuciones de diferentes energías,

que degradan la resolución, los sucesos seleccionados corresponden a los mayores ángulos de dispersión medidos, y por tanto a la peor resolución que podía haberse obtenido, de modo que los resultados no demuestran la resolución que es posible lograr a la energía de 356 keV.

7.5 Conclusiones

El trabajo aquí presentado explica los pasos dados para el desarrollo de un primer prototipo de una sonda Compton para la próstata, cuyo principal objetivo es lograr el correcto funcionamiento de un detector de *scattering* formado por varios detectores de silicio funcionando simultáneamente. Su desarrollo, puesta en funcionamiento y análisis de los datos obtenidos con él suponen importantes logros.

En el aspecto tecnológico se han producido dos avances fundamentales. Uno es el desarrollo de detectores de silicio de 1 mm de grosor, con baja corriente de fuga que supone una contribución mínima al ruido de los detectores, y electrónica de lectura de bajo ruido. Con los detectores de silicio de 1 mm de grosor se han ensamblado módulos de silicio que permiten aumentar la eficiencia sin aumentar excesivamte el número de detectores a utilizar. La resolución energética medida en estos detectores se encuentra alrededor de 1.3-1.5 keV FWHM.

Aun así, para obtener el espesor deseado es necesario emplear varias capas de detectores de silicio con un adecuado funcionamiento, un paso decisivo hacia el desarrollo del prototipo clínico.

El prototipo ha podido utilizarse satisfactoriamente para la toma de datos. Los principales problemas que degradan el rendimiento del prototipo han podido ser identificados. La principal limitación que sufre el detector de silicio se debe al *time-walk* en el discriminador de la electrónica de lectura. Este problema ya ha sido corregido en la siguiente versión de la electrónica de lectura, que será empleada en el futuro.

El funcionamiento de este prototipo está limitado principalmente por el detector de absorción. Los módulos centelleadores, obtenidos de una cámara gamma existente, fueron diseñados para ser utilizados con colimadores mecánicos. Un nuevo detector de centelleo se encuentra en vias de desarrollo. La principal mejora viene dada por su mayor capacidad de procesado de datos que permite la llegada de fotones directos de la fuente en el modo en que habrá de funcionar la sonda para la próstata. Una mejor resolución energética permitirá una eliminación de las coincidencias accidentales más eficiente.

Se han tomado datos con fuentes de diferentes energías, y se han reconstruido las imágenes. En el proceso de análisis se han probado diferentes métodos con el fin de utilizar aquél que nos lleve a una mejor resolución de las imágenes en cada caso.

El análisis de datos en diferentes *runs* ha servido para identificar los principales problemas en el funcionamiento del prototipo. Algunos de ellos han podido ser subsanados, mejorando su funcionamiento. Además, los resultados han servido para verificar diversos aspectos del método Compton de formación de imágenes, que es necesario tener en cuenta en cualquier detector Compton. Los resultados reflejan la importancia de la geometría escogida, asi como de la resolución energética del primer detector y la energía de la fuente.

Los resultados del primer y segundo *run* incluyendo todos los ángulos no pueden

compararse directamente, ya que fueron tomados en diferentes condiciones y con fuentes de distinta energía. Los resultados del segundo *run* deberían ser mejores que los del primero, ya que la resolución energética de los detectores es mejor, y el umbral es menor. A pesar del peor funcionamiento del prototipo, la resolución de las imágenes es significativamente mejor en el primer *run* debido a dos motivos. Una causa de la mejora se debe a la mayor energía del ^{99m}Tc respecto al ^{57}Co. Sin embargo, la diferencia de 20 keV no es suficiente para producir tal disparidad. La gran diferencia entre ambos resultados muestra la enorme influencia de la distancia entre la fuente y el primer detector, hecho en que se basa el diseño de la sonda para la próstata para lograr una excelente resolución espacial.

A partir de los resultados de las simulaciones se puede apreciar la importancia de factores como el ensanchamiento Doppler, que impone un límite físico a la incertidumbre angular que solo puede mejorarse escogiendo el material más adecuado para el detector de *scattering*, energías altas y ángulos de dispersión pequeños. Además, la resolución energética del primer detector supone un factor importante de degradación de la resolución espacial, especialmente a energías más bajas, que debe ser minimizado.

De la comparación de los resultados obtenidos con las fuentes de ^{133}Ba y ^{57}Co, y a pesar de que las imágenes no fueron reconstruidas en las mejores condiciones posibles, puede verse la gran mejora que supone la utilización de fuentes radiactivas de energías altas.

Seleccionando ángulos de dispersión bajos mediante una adecuada colocación del detector de absorción se reduce la influencia del ensanchamiento Doppler y se mejora la resolución.

Tanto los resultados obtenidos con ^{57}Co, como los obtenidos con ^{133}Ba, reflejan la mejora que se obtiene minimizando la influencia de la resolución espacial del detector de absorción aumentando su distancia respecto al de *scattering*.

Este ha sido el primer test realizado con el detector de *scattering* compuesto por diversos módulos de silicio. Aún es necesario llevar a cabo una serie de mejoras, y por tanto los resultados no son indicativos del rendimiento esperado en el caso de la sonda para la próstata. En cualquier caso, los resultados son prometedores.

El trabajo en la actualidad se centra en dar solución a las principales limitaciones del prototipo, con vistas a la construcción de un segundo prototipo. Se llevarán a cabo nuevos tests con fuentes extensas e incluyendo material atenuante para simular escenarios más realistas.

Conclusions

The work that has been presented describes the successful construction of a Compton prototype, whose main goal is the development and operation of a scatter detector composed of several layers of thick silicon detectors.

This prototype is a necessary first step towards the development of a Compton probe prototype that will outperform imaging devices currently employed for prostate imaging. A resolution about 2.4 mm FWHM and 1.7 $\times$ 10^{-3} efficiency are expected, compared to the 10-15 mm FWHM spatial resolution and 10^{-3} - 10^{-5} efficiency of conventional SPECT.

The prototype development, operation and analysis of the data taken implies fundamental achievements. In the technological aspect two are the most important goals accomplished. One is the development of 1 mm thick silicon sensors with low leakage current, whose contribution to the energy resolution of the detector is almost negligible, and low noise readout electronics. Silicon detector modules have been developed and tested employing thick silicon sensors, that have the advantage of enhancing the efficiency without increasing the number of readout channels. The energy resolution measured with a ^{241}Am source including data from all detector pads is around 1.3-1.5 keV FWHM.

Still, obtaining the desired thickness of 10-12 mm, requires several detector layers. In this prototype, the successful operation of a stack of silicon sensors as scatter detector has also been achieved. This is an important step towards the development of the Compton probe clinical prototype. In the near future, a larger number of detectors will be employed, and especially in the case of the endorectal probe configuration, dense packaging of the detectors will be required. Tests have been performed with the tab-bonding technique, substituting wire-bonds by direct soldering of the readout electronics to a kapton cable with aluminium traces. Aluminium is more flexible than copper traces and can be bent without being damaged, allowing very close packaging of the sensors.

The first prototype of a prostate probe has been successfully employed for data taking. The main problems that degrade the prototype performance have been identified. The essential limitation concerning the silicon modules is the time-walk in the ASICs discriminator. Time-walk compensation has already been incorporated to the next version of the ASICs, that will be employed for the development of new silicon modules.

The performance of the prototype is mainly limited by the second detector. The absorption detector was obtained from an existing gamma camera, and designed to work with mechanical collimators. A new scintillator detector is being developed to be employed as absorption detector for the second prostate probe prototype. The main improvement is its high countrate capability that will accomodate direct photons from the source with no need of shielding, as necessary for the Compton probe. Improved energy resolution

	Energy (keV)	Distance to source (mm)	resolution (mm FWHM)
First run	140.5	45	7.1
Second run	122	112	15.7

Table 8.1: *Results obtained in the two runs for detector H considering all angles and scintillators position D0.*

will also help to reject accidental coincidences.

Data have been taken with sources of different energies, and images have been reconstructed. In the analysis process, different methods have been tested to employ in each case the one yielding the best image resolution.

Through different tests and runs, the data analysis has helped to identify the main problems in the prototype operation. Some of the problems could be solved and the scatter detector performance has been optimized.

In addition, the results obtained have served to verify several aspects of Compton imaging that can and should be taken into account in future Compton detectors. The results reflect the importance of the geometry chosen, as well as the energy resolution of the first detector.

Results from the first and the second run cannot be directly compared, since data were taken in different conditions and with sources of different energies. The results of the second run should improve with respect to those obtained in the first run, since a better energy resolution was achieved for the first detector, and a lower threshold was set.

In spite of the worse prototype performance, the resolution of the reconstructed images is considerably better in the first run due to two factors. An improvement is due to the higher energy of ^{99m}Tc gamma rays, but the 20 keV energy difference cannot account for the large difference in the image resolution. The significantly better spatial resolution achieved in the first run for events in detector A considering all angles (table 8.1) proves the outstanding importance of the distance from the scatter detector to the source in the spatial resolution of the device. This importance is also clear in the simulation results, that predict a much better resolution if the source can be placed close to the scatter detector. This fact has been profited in the design of the prostate probe to achieve its excellent spatial resolution.

From the simulation results it can be seen that Doppler broadening imposes a limit in the angular uncertainty, that can only be improved by selecting the most adequate material for the scatter detector, high energies and low scattering angles. In addition to this, the energy resolution of the scatter detector is an important factor degrading the spatial resolution, in particular for low energy sources, that should be minimized as much as possible.

From the comparison of the results obtained with ^{57}Co and ^{133}Ba sources, and despite the fact that they were not done in the optimum conditions, it is possible to see that a great improvement of the spatial resolution can be obtained if high energy sources are employed.

Selecting low scattering angles by an adequate positioning of the absorption detector reduces the influence of Doppler broadening and improves the resolution of the recon-

structed images. Resolutions as low as 6 mm FWHM for the 0.5 mm detector, and 7.8 mm FWHM for the 1 mm thick detectors with a ^{57}Co source at about 11 cm from the detectors have been obtained selecting the lowest possible scattering angles.

Both ^{57}Co and ^{133}Ba results reflect the improvement that can be obtained minimizing the influence of the absorption detector spatial resolution by increasing its distance from the scatter detector.

This is the first test performed with the multimodule scatter detector prototype. Some features still need to be improved and therefore the results are not representative of the performance that could be achieved with a Compton prostate probe. However, they are very promising for a first test.

Ongoing work is focused in solving the main problems encountered that limit the prototype performance, in view of the construction of a second prototype.

Further tests with extended sources and including attenuating media trying to simulate a more realistic setup will be carried out.

Bibliography

[1] J.A. Sorenson, M.E. Phelps, and S.C. Cherry. *Physics in Nuclear Medicine.* Saunders, 2003.

[2] H.O. Anger. Scintillation camera. *Rev. Sci. Inst.*, 29:27–33, 1958.

[3] W.W. Moses. Overview of Nuclear Medical Imaging Instrumentation and Techniques. *Proc SCFIF97 Conference on Scintillating and Fiber Detectors*, 450:477–488, 1988.

[4] W.W. Moses. Trends in PET Imaging. *Nucl. Instr. & Meth. A*, 471:209–214, 2001.

[5] W.L. Rogers, N.H. Clinthorne, and A. Bolozdynya. *Compton cameras for nuclear medical imaging in Emission tomograpy. The fundamentals of PET and SPECT.* M.N. Wernick and J. N. Aarsvold. Elsevier academic press, 2004.

[6] T. Ichihara. Ring type single photon emission CT imaging device. *U.S. Patent*, 4:639,599, 1987.

[7] R. Rohe and J. D. Valentine. A novel Compton camera design for in-vivo medical imaging of radiopharmaceuticals. *IEEE Nucl. Sci. Symp. Med. Img. Conf.*, 3:1579–1583, 1995.

[8] R. Rohe and J. D. Valentine. Compton camera design for in-vivo medical imaging of radiopharmaceuticals. *U.S. Patent*, 5:567,994, 1996.

[9] A. Bolozdynya, C. E. Ordonez, and W Chang. A concept for cylindrical Compton camera for SPECT. *IEEE Nucl. Sci. Symp. Med. Img. Conf.*, 2:1047–1051, 1997.

[10] L. Zhang et al. Potential of a Compton camera for high performance scintimammography. *Phys. Med. Biol.*, 49:617–638, 2004.

[11] S. J. Park et al. Experimental setup for very high resolution animal PET based on solid state detector. *IEEE Nucl. Sci. Symp. & Med. Img. Conf. Rec*, 2:1120–1123, 2001.

[12] L. Zhang et al. An innovative high efficiency and high resolution probe for prostate imaging. *J. Nucl. Med.*, 41(5), 2000.

[13] W.R. Leo. *Techniques for Nuclear and Particle Physics Experiments.* Springer-Verlag, 1987.

[14] G. F. Knoll. *Radiation detection and measurement.* John Wiley and Sons, 1999.

[15] R. Ribberfors. Relationship of the relativistic Compton cross section to the momentum distribution of bound electron states. *Phys. Rev. B.*, 12(6):2067–2074, 1975.

[16] R. Ribberfors and K Berggren. Incoherent-X-ray-scattering functions and cross sections by means of a pocket calculator. *Phys. Rev. A.*, 26(6):3325–3333, 1982.

[17] R. Basko, G.L. Zeng, and G.T. Gullberg. Fully three dimensional image reconstruction from V projections acquired by Compton camera with three vertex electronic collimation. *IEEE Nucl. Sci. Symp. Med. Img. Conf.*, 1997.

[18] W. Reed and P. Eisenberg. Gamma-ray Compton profiles of diamond, silicon and germanium. *Phys. Rev. B.*, 6:4598–4604, 1972.

[19] Chia-Ho Hua. *Compton Imaging System Development and Performance Assessment.* PhD thesis, University of Michigan, 2000.

[20] J.W. LeBlanc. *A Compton Camera for Low Energy Gamma Ray Imaging in Nuclear Medicine Applications.* PhD thesis, University of Michigan, 1999.

[21] C. Hua et al. Quantitative information loss for Compton cameras. *IEEE Trans. Nucl. Sci.*, 46(3):587–593, 1999.

[22] C. E. Ordonez, W. Chang, and A. Bolozdynya. Angular uncertainties due to geometry and spatial resolution in Compton cameras. *Phys. Med. Biol.*, 49:1387–1408, 2004.

[23] Lisha Zhang. *Compton gamma-ray imaging probes for prostate and breast.* PhD thesis, University of Michigan, 2001.

[24] S. Vatnitski and H. Jarvinen. Application of a natural diamond detector for the measurement of relative dose distributions in radiotherapy. *Phys. Med. Biol.*, 38:173–84, 1993.

[25] P. Weilhammer et al. Recent results on CVD diamond radiation sensors. *Nucl. Instr. & Meth. A*, 409:264–270, 1998.

[26] M. Zhang et al. CVD diamond photoconductive devices for detection of X-rays. *J. Phys. D: Appl. Phys.*, 37:3198–3201, 2004.

[27] N.H. Clinthorne et al. Choice of scattering detector for Compton scatter cameras. *Nucl. Med. Supp.*, 5:51, 1998.

[28] W.W. Moses et al. Scintillators for positron emission tomography.

[29] W.W. Moses. Current trends in scintillator detectors and materials. *Nucl. Instr. & Meth. A*, 487:123–128, 2002.

[30] C. van Eijk. Inorganic scintillators in medical imaging. *Phys. Med. Biol.*, 47:85–106, 2002.

[31] W.W. Moses. Scintillator Requirements for Medical Imaging. *Proc. SCINT99 International Conference on Inorganic Scintillators and Their applications.*, pages 11–21, 1999.

[32] W.W. Moses et al. Recent Results in a Search for Inorganic Scintillators for X- and Gamma Ray Detection.

[33] W.W. Moses and K. Shah. Potential for $RbGd_2Br_7$:Ce, $LaBr_3$:Ce, $LaBr_3$:Ce, and LuI_3:Ce in nuclear medical imaging. *Nucl. Instr. & Meth. A*, 537:317–320, 2005.

[34] C.L. Melcher. Perspectives on the future development of new scintillators. *Nucl. Instr. & Meth. A*, 537:6–14, 2005.

[35] J.R. Stickel and S.R. Cherry. High resolution PET detector design: modelling components of intrinsic spatial resolution. *Phys. Med. Biol.*, 50:179–195, 2005.

[36] Th. Claesson et al. An X-ray computed tomograph demonstrator using a CZT solid-state detector. *Nucl. Instr. & Meth. A*, 487:202–208, 2002.

[37] C. Scheiber et al. Medical Applications of CdTe and CdZnTe detectors. *Nucl. Instr. & Meth. A*, 458:12–25, 2001.

[38] C. Mestais et al. A new design for a high resolution, high efficiency CZT gamma camera. *Nucl. Instr. & Meth. A*, 458:62–67, 2001.

[39] T. Takahashi and S. Watanabe. Recent Progress on CdTe and CZT detectors. *IEEE Trans. Nucl. Sci.*, 48:950–959, 2001.

[40] F. Zhang, Z. He, and D. Xu. Analysis of Detector Response Using 3-D Position-Sensitive CZT Gamma-Ray Spectrometers. *IEEE Trans. Nucl. Sci.*, 51(6):3098–3104, 2004.

[41] F. Zhang et al. Improved Resolution for 3-D Position Sensitive CdZnTe Spectrometers. *IEEE Trans. Nucl. Sci.*, 51(5):2427–2431, 2004.

[42] M. Singh. An electronically collimated gamma camera for single photon emission computed tomography.Part I: Theoretical considerations and design criteria. *Med. Phys.*, 10(4):421–427, 1983.

[43] T. Conka-Nurdan et al. Impact of the Detector Parameters on a Compton Camera. *IEEE Trans. Nucl. Sci.*, 510:122–125, 2002.

[44] L. Shepp and Y. Vardi. Maximum likelihood reconstruction for emission tomography. *IEEE Trans. Med. Imag*, MI-1:113–122, 1982.

[45] K. Lange and R Carson. EM reconstruction algorithms for emission and transmission tomography. *J. Comput. Assist. Tomogr.*, 8(2):306–316, 1984.

[46] A. Dempster, N. Laird, and D. Rubin. Maximum likelihood from incomplete data via the EM algorithm. *J. Roy. Stat. Soc.*, B 39:1–38, 1977.

[47] S.J. Wilderman et al. List-Mode Maximum Likelihood Reconstruction of Compton Scatter Camera Images in Nuclear Imaging. *IEEE Trans. Nucl. Sci.*, 3:1716, 1999.

[48] L. Parra and H. Barret. List-Mode Likelihood: EM Algorithm and Image Quality Estimation Demonstrated on 2-D PET. *IEEE Trans. Nucl. Sci.*, 17(2):228–235, 1998.

[49] L. Parra, H. Barret, and T. White. List-mode Likelihood. *J. Opt. Soc. Amer. A*, 14(11), 1997.

[50] S.J. Wilderman et al. Fast Algorithm for List-Mode Back-Projection of Compton Scatter Camera Data. *IEEE Trans. Nucl. Sci.*, 45:957–961, 1998.

[51] S.J. Wilderman et al. Improved Modeling of System Response in List Mode EM Reconstruction of Compton Scatter Camera Images. *IEEE Trans. Nucl. Sci.*, 48(1):111–116, 2001.

[52] A.C. Sauve et al. 3D image reconstruction for a Compton SPECT camera model. *IEEE Trans. Nucl. Sci.*, 46(6):2075–2084, 1999.

[53] K. Pinkau. Die messung solarer und atmosphaerischer neutronen. *Zeitschr Fur Naturforschung A*, 21(12):2100–2106, 1966.

[54] R. S. White. An experiment to measure neutrons from the sun. *Bull. Am. Phys. Soc. Ser II*, 13(4):714, 1968.

[55] V. Schonfelder et al. Instrument description and performance of the imaging gamma ray telescope COMPTEL abroad the Compton Gamma-Ray Observatory. *Astroph. Suppl. Series*, 86:657–692, 1993.

[56] P.F. Bloser et al. The MEGA Advanced Compton Telescope Project. *New Astr. Rev.*, 46:611–616, 2002.

[57] G. Kanbach et al. The MEGA Project. *New Astr. Rev.*, 48:275–280, 2004.

[58] D. Bhattacharya et al. Prototype TIGRE Compton gamma-ray balloon-borne telescope. *New Astron. Rev.*, 48((1-4)):287–292, 2004.

[59] T.J. O' Neill et al. Development of the TIGRE Compton telescope for intermediate energy gamma-ray astronomy. *IEEE Trans. Nucl. Sci.*, 50:251–257, 2003.

[60] E. Aprile et al. XENA- A Liquid Xenon Compton Telescope for Gamma-Ray Astrophysics in the MeV regime. *Proc. of SPIE*, 3446(88), 2004.

[61] E. Aprile and M. Suzuki. Development of liquid xenon detectors for gamma ray astronomy. *IEEE Trans. Nucl. Sci.*, 36:311–315, 1989.

[62] E. Aprile et al. Liquid xenon gamma-ray imaging telescope (LXeGRIT) for medium energy astrophysics. *Proc. of SPIE*, 2806:337–348, 1996.

[63] J.D. Kurfess et al. An Advanced Compton Telescope based on thick, position-sensitive solid-state detectors. 2004.

[64] T. Tanaka et al. Development of a Si/ScTe semiconductor Compton telescope. *IEEE Nucl. Sci. Symp. Med. Img. Conf.*, 2004.

[65] T. Kamae, R Enomoto, and N Hanada. A new method to measure energy, direction and polarization of gamma rays. *Nucl. Instr. & Meth. A*, 260:254–257, 1988.

[66] T. Mitani et al. A prototype Si/ScTe Compton Camera and the Polarization Measurement. *IEEE Nucl. Sci. Symp. Med. Img. Conf.*, 2004.

[67] W.N. Kroeger et al. Three-Compton Telescope: Theory, Simulations, and Performance. 2004.

[68] R. W. Todd, J. M. Nightingale, and D. B. Everett. A proposed γ camera. *Nature*, 251:132–134, 1974.

[69] M. Singh and D. Doria. An electronically collimated gamma camera for single photon emission computed tomography. Part II: Image reconstruction and preliminary experimental measurements. *Med. Phys.*, 10(4):421–427, 1983.

[70] M. Singh and R. Brechner. Experimental test-object study of electronically collimated SPECT. *J. Nucl. Med.*, 31(2):178–186, 1990.

[71] A. Bolozdynya et al. High pressure Xenon electronically collimated camera for low energy gamma ray imaging. *IEEE Nucl. Sci. Symp. Med. Img. Conf.*, 2:1157–1161, 1996.

[72] C. J. Solomon and R. J. Ott. Gamma ray imaging with silicon detectors - a Compton Camera for radionuclide imaging in medicine. *Nucl. Instr. & Meth. A*, 273:787–792, 1988.

[73] J.W. LeBlanc et al. C-SPRINT: A Prototype Compton Camera System for low Energy Gamma Ray Imaging. *IEEE Trans. Nucl. Sci.*, 45, 1998.

[74] J.W. LeBlanc et al. Experimental results from the C-SPRINT Prototype Compton Camera. *IEEE Trans. Nucl. Sci.*, 46(3):950–955, 1999.

[75] E.A. Wulf et al. Thick Silicon Strip Detector Compton Imager. *IEEE Trans. Nucl. Sci.*, 51(5):1997–2003, 2004.

[76] T. Conka-Nurdan et al. Compton Camera Coincidences in the Silicon Drift Detector. *IEEE Nucl. Sci. Symp. Med. Img. Conf.*, 2004.

[77] A. Peisert. *Silicon Microstrip Detectors.* DELPHI Collaboration 92-143 MVX2, 1992.

[78] P. Giubelino et al. Silicon detectors. *Instrumentation in High Energy physics:VIII ICFA School*, pages 35–59, 2000.

[79] G.W. Neudeck. *The PN juntion diode (Volume II).* Addison-Wesley Publishing Company, 1989.

[80] Petra Riedler. *Radiation Damage Effects and Performance of Silicon Strip Detectors using LHC Readout Electronics.* PhD thesis, University of Vienna, 1998.

[81] H. Spieler. Front-End Electronics and Signal Processing. *Lectures.*

[82] *US National Cancer Institute. www.cancer.gov.*

[83] A. W. Partin and J.E. Oesterling. The clinical usefulness of prostate specific antigen:update 1994. *Jour. Urol.*, 152(5):1358–1368, 1994.

[84] H.B Carter and U.M. Hamper. Evaluation of thransrectal ultrasound in early detection of prostate cancer. *Jour. Urol.*, 142(4):1008–1010, 1989.

[85] R.L. Waterhouse and M.I. Resnick. The use of transrectal prostatic ultrasonography in the evaluation of patients with prostatic carcinoma. *Jour. Urol.*, 141(2):233–239, 1989.

[86] M.E. Sakarya and H. Arslan. The role of power Doppler ultrasonography in the diagnosis of prostate cancer: a preliminary study. *BJU International*, 82(3):386–388, 1998.

[87] H. Hricak, S. White, and D. Vigneron. Carcinoma of the prostate gland: MR Imaging with pelvic phased-array coils versus integrated endorectal-pelvic phased-array coils. *Radiology*, 193:703–709, 1994.

[88] M. Chen, H. Hricak, and C.L. Kahlben. Hormonal ablation of prostatic cencer: effects on prostate morphology, tumor detection and staging by endorectal coil MR imaging. *Am. J. Roentgenol*, 166:249–311, 1991.

[89] S. White, H. Hricak, and M. Chen. Prostate cancer:effect of post-biopsy hemorrhage on interpretation of MR images. *Radiology*, 195:385–390, 1995.

[90] K.K. Yu. Prostate Cancer: Prediction of Extracapsular Extension with Endorectal MR Imaging and Three-dimensional Proton MR Spectroscopic Imaging. *Radiology*, 213:481–488, 1999.

[91] H.M. Lamb and D. Faulds. Capromab pendetide: a review of its use as an imaging agent in prostate cancer. *Drugs Aging*, 12:293–304, 1998.

[92] M.A. Seltzer et al. Comparison of helical computerized tomography, positron emission tomography and monoclonal antibody scans for evaluation of lymph node metastases in patients with prostate specific antigen relapse after treatment for localized prostate cancer. *Jour. Urol.*, 162:1322–1328, 1999.

[93] H. Jadvar, J. K. Pinski, and P. S. Conti. FDG PET in suspected recurrent and metastatic prostate cancer. *Oncology reports*, 10:1485–1488, 2003.

[94] T. Hara, N. Kosaka, and H. Nishi. PET Imaging of prostate cancer using carbon-11 choline. *J. Nucl. Med.*, 39:990–995, 1998.

[95] N. Oyama et al. ^{11}C-Acetate PET imaging of Prostate Cancer. *J. Nucl. Med.*, 43(2):181–186, 2002.

[96] J.S. Huber et al. Conceptual Design of a Compact Positron Tomograph for Prostate Imaging. *IEEE Trans. Nucl. Sci.*, 48:1506–1511, 2001.

[97] J. S. Huber et al. The development of a Compact Positron Tomograph for Prostate Imaging. *IEEE Nucl. Sci. Symp. Med. Img. Conf.*, 2004.

[98] T.G. Turkington et al. PET Prostate Imaging with Small Planar Detectors. *IEEE Nucl. Sci. Symp. Med. Img. Conf.*, 2004.

[99] L. Zhang et al. An anthropomorphic phantom integrated EGS4 Monte Carlo code and its application in Compton Probe. *IEEE Trans. Nucl. Sci.*, pages 119–122, 2000.

[100] L. Zhang, W.L. Rogers, and N.H. Clinthorne. Complete Tomographic Data for Compton Imaging Probes. *IEEE Nucl. Sci. Symp. Med. Img. Conf.*, 2004.

[101] D. Meier. Report on Silicon Detector. *Technical Report (CERN)*, 2000.

[102] *www.sintef.no.*

[103] D. Meier. Silicon Detector for a Compton Camera in Nuclear Medical Imaging. *CERN.EP/2001-009*, 2001.

[104] *VATAGP3 specifications. www.ideas.no.*

[105] *Integrated Detectors and Electronics AS. www.ideas.no.*

[106] A. Studen et al. First Coincidences in Pre-Clinical Compton Camera Prototype for Medical Imaging. *Nucl. Instr. & Meth. A*, 531 I(1-2):258–264, 2004.

[107] A. Studen et al. Development of silicon pad detectors and readout electronics for a Compton camera. *Nucl. Instr. & Meth. A*, 501:273–279, 2003.

[108] W. L. Rogers et al. SPRINT II: A second generation single photon ring tomograph. *IEEE Trans. Med. Im.*, 7(4):291–297, 1988.

[109] S. Huh et al. High Countrate Anger Camera Design for Electronically Collimated SPECT. *IEEE Nucl. Sci. Symp. Med. Img. Conf.*, 2004.

[110] R.M. Gray and A. Macovski. Maximum a posteriori estimation of position in scintillation cameras. *IEEE Trans. Nucl. Sci.*, NS-23:849–852, 1976.

[111] Berta Escat. *Desarrollo, carcterización y evaluación clínica de una mini cámara gamma portátil para aplicaciones médicas.* PhD thesis, Universidad de Valencia, 2003.

[112] M. Abramowitz and I. A. Stegun. *Handbook of mathematical functions.* Dover publications, 1968.

[113] W.H. Press et al. *Numerical Recipes in C.* Cambridge University Press, 1999.

[114] G. Llosá et al. First results in the development of a Compton probe prototype for prostate imaging. *World Sci. Proc 8th ICATPP*, pages 396–401, 2004.

[115] G. Llosá et al. Development of a Pre-Clinical Compton Probe Prototype for Prostate Imaging. *IEEE Nucl. Sci. Symp. & Med. Img. Conf. Rec*, 2004.

[116] Y. Namito, S. Ban, and H. Hirayama. Implementation of the Doppler broadening of a Compton-scattered photon into the EGS4 code. *Nucl. Instr. & Meth. A*, 349:489–494, 1994.